

# Metal Catalysts for the Electrochemical Reduction of CO<sub>2</sub>

Présentée le 14 juillet 2023

Faculté des sciences de base  
Laboratoire des matériaux pour les énergies renouvelables  
Programme doctoral en chimie et génie chimique

pour l'obtention du grade de Docteur ès Sciences

par

**Cedric David KOOLEN**

Acceptée sur proposition du jury

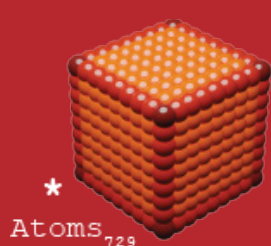
Prof. B. Smit, président du jury  
Prof. A. Züttel, directeur de thèse  
Prof. S. Skrabalak, rapporteuse  
Prof. B. Endrödi, rapporteur  
Dr M. Nachtegaal, rapporteur



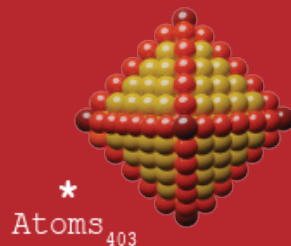




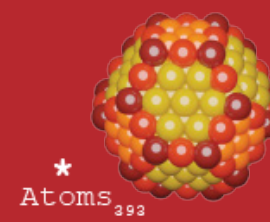
# Metal Catalysts for the Electrochemical Reduction of CO<sub>2</sub>



Corner (100)  
Edge



Corner (111)  
Edge



Corner (111)  
Edge (100)

## Cedric David Koolen

Doctoral Candidate and Safety Engineer  
Ecole Polytechnique Fédérale de Laussane (EPFL)

MSc. Physical Chemistry & MSc. Chemistry

e-mail: [cedric.koolen@epfl.ch](mailto:cedric.koolen@epfl.ch)

phone: +41762025649 | +31613015890

Adress: Rue de conthey 6, 1950 Sion, Switzerland

LinkedIn: <https://www.linkedin.com/in/cedric-koolen/>

Laboratory of Materials for Renewable Energy (LMER), Institute of Chemical Sciences and Engineering (ISIC), Basic Science Faculty (SB), École polytechnique fédérale de Lausanne (EPFL) Valais-Wallis, Energypolis, Sion, 1951, Switzerland.

Empa Materials Science & Technology, Dübendorf, 8600, Switzerland.



# Acknowledgements

## Management of the Laboratory of Materials for Renewable Energy

I would like to extend my deepest gratitude to my thesis director, Prof. Dr. Andreas Züttel, full professor of Physical Chemistry at EPFL, director of the Laboratory of Materials for Renewable Energy (LMER), joint-laboratory of EPFL and Empa and president of the Swiss Hydrogen Association, Hydropole.

*Dear Andreas,*

*your encouragement to explore the unexplored, backing on the most challenging of endeavors and nourishment of a drive to lead, humble me. My appreciation of the trust you have placed in me during my time here at LMER cannot be expressed. I strive to emulate your leadership throughout my career. Thank you.*

I would like to extend my deepest gratitude to our secretary, friend and colleague, Ivana Suter.

*Chère Iva,*

*If Andreas can be seen as our academic father, you would certainly be our mother. I have with great admiration taken note of your commitment to each and every doctoral candidate at LMER. Personally speaking, I have taken your advice to heart.*





## Management of the Chemistry and Chemical Engineering doctoral school

I would like to extend my deepest gratitude to my thesis jury president and mentor, Prof. Dr. Berend Smit, full professor of Chemical Engineering at EPFL, director of the Laboratory of Molecular Simulations (LSMO) and former program director of Chemistry and Chemical Engineering of EPFL.

*You were instrumental both at the beginning and the end. As if it was designed that way.  
Thank you, Berend.*

I would like to extend my deepest gratitude to the secretary of the Chemistry and Chemical Engineering doctoral school of EPFL, Anne Lene Odegaard.

*Anne Lene, I could not imagine an person better suited for the role than you. I hope many more students may get to enjoy your care.*

I would like to thank the current program director of the Chemistry and Chemical Engineering school, Prof. Dr. Anne-Clémence Corminbeouf, full professor of Chemical Engineering at EPFL, director of the Laboratory for Computational Molecular Design.



## Host institution

I would like to extend my deepest gratitude to my host, friend and collaborator, Prof. Dr. Andreas Schmidt-Ott, Emeritus professor of the Technical University of Delft and co-founder of VSParticle B.V.

*Dear Andreas,*

*Luck is when preparation meets opportunity. This is certainly how I see us meeting. It has been a pleasure and a privilege to share ideas with you in the world of cluster catalysis.*



## Thesis defense jurors

I would like to extend my deepest gratitude to the internal examiner of my defense, Dr. Maarten Nachtegaal, head of the SuperXAS and the Debye beamlines of the Swiss Light Source at the Paul Scherrer Institute, first external examiner, Prof. Dr. Sara Skrabalak, James H. Rudy Professor at Indiana University – Bloomington and director of the Center for Single-Entity Nanochemistry and Nanocrystal Design, and the second external examiner, Prof. Dr. Balázs Endródi, assistant professor at the University of Szeged.



## Colleagues and collaborators

I would like to thank my friend and colleague, Prof. Dr. Wen Luo, former member of LMER and professor at the University of Shanghai.

*Wen, it has simply been a pleasure working and writing with you. I am mindful of a reunion in China.*

I would like to thank my colleague and not just yet collaborator, Pr. Dr. Christian Ludwig, adjunct professor at EPFL and head of the Chemical Processes and Materials group of the Paul Scherrer Institute.

*Dear Christian,*

*I would like to thank you for your openness during our many exchanges. It is rare that one is so inclusive towards a non-team member. I cherish that. I look forward to what lies ahead.*

I would like to thank my friend and collaborator, Laura Torrent, Postdoc in the Chemical Processes and Materials group of the Paul Scherrer Institute.

*It has been great to have a true analytical chemist on board. I look forward to working together again. I treasure to have experienced true Catalan hospitality.*

I would like to thank my friend and colleague, Ayush Agarwal, PhD student in the Chemical Processes and Materials group of the Paul Scherrer Institute and EPFL.

*I am impatient for our future ventures.*

I would like to thank my friend and colleague, Dr. Emad Oveisi, senior scientist at Centre for Electron Microscopy, EPFL.

*Emad, it has been great collaborating with you over the years. You are an excellent microscopist full of ingenious ideas. It is a pleasure and a privilege to see our names side by side in the Nature Portfolio.*

I would like to thank my friend and colleague, Dr. Natalia Gasilova, scientist at the Mass Spectrometry and Elemental Analysis Platform, EPFL.

*Natalia, thank you for introducing me to inductively coupled plasma mass spectrometry. It has brought me so much. I look forward to working with you in the future.*

I would like to thank my friend and collaborator, Dr. Olga Borovinskaya, project manager at TOFWERK AG.

*Olga, you have paved the way for much future success. For this I am grateful. I wish you the best of luck in all your endeavors and I look forward to our business paths crossing again.*

I would like to thank my friend and collaborator, Prof. Dr. Jan Rossmeisl, full professor in Chemistry at the University of Copenhagen and director of the Center for High Entropy Alloy Catalysis.

*Quote: "I think that's probably right."*



I would like to thank my friend and collaborator, Dr. Jack Kirk Pedersen, Postdoc at the Center for High Entropy Alloy Catalysis at the University of Copenhagen.

*I have had my fair share of collaborations, but ours is the crown jewel. We seem to understand one another, Jack. I look forward to what the future holds.*

I would like to thank my friend and collaborator, Dr. Olga Safonova, senior scientist of the SuperXAS beamline of the Swiss Light Source at the Paul Scherrer Institute.

*We share a common trait, Olga. And that is to always deliver. This is a great good. I look forward to seeing your career develop further.*

I would like to thank my friend and collaborator, Dr. Tobias Pfeiffer, co-founder and Chief Technology Officer of VSParticle B.V.

*A small world indeed.*

I would like to thank my friend and collaborator, Bernardus Zijlstra, former VSparticle B.V. engineer.

*Immensely skilled. I wish you the best of luck in your future endeavors. I am sure our paths will cross again.*

I would like to thank my friend and colleague, Marie-Valentine Florin, executive director of the Risk and Governance Center of EPFL.

*Dear Marie-Valentine,*

*Thank you for the opportunity to contribute to workshops and reports of the IRGC. You have opened my eyes to the world of risk management.*

I would like to thank my friend and mentor, Prof. Dr. Gadi Rothenberg, Chair of Heterogeneous Catalysis and Sustainable Chemistry at the University of Amsterdam, my Alma Mater.

*Dear Gadi,*

*Your continued support long after graduation means the world to me. Thank you.*

I would like to thank my friend and colleague, Prof. Dr. Raffaella Buonsanti, associate professor in Chemical Engineering at EPFL and director of the Laboratory of Nanochemistry for Energy.

*Dear Raffaella,*

*I wish you all the best in your future endeavors.*

I further would like to acknowledge and express gratitude for contributions from Dr. Laure Menin, head of the Mass Spectrometry and Elemental Analysis Platform of EPFL, Dr. Aurélian Bornet, leader of the NMR platform of EPFL, Dr. Marco Cantoni, senior scientist and operational director of the Interdisciplinary Center for Electron Microscopy of EPFL, Dr. Rita Therisod and Dr. Victor Bureau of the Interdisciplinary Center for Electron Microscopy of EPFL, Dr. Juan Herranz Salaner and Maximilian Winzely, of the Electrochemistry Laboratory of the Paul Scherrer Institute, Bart Boshuizen of the Technical University of Delft, (former-)members of the Laboratory of Materials for Renewable Energy, Dr. Mo Li, Dr. Jie Zhang, Dr. Yunting Wang, Dr. Youngdon Ko, Dr. Liping Zhong, Dr. Kun Zhao, Yasemen Kuddusi, Zohreh Akbari, Thi Ha My Pham, Manhui Wei, Chongnan Ye, former VSParticle B.V. engineer Dr. Wilbert Vrijburg and Sumant Padhke of the Paul Scherrer Institute, Cedric Passerini and Jean Perruchoud of the IT department of EPFL, Stéphane Voeffray, Robin Délèze and Dennis Ellersiek, of the Electronic and Mechanical Engineering Workshop Platform of EPFL, Laurent Seydoux and Annabelle Coquoz of the Chemical Store Platform of EPFL. I would also like to thank my previous supervisors Prof. Dr. Peter Schurtenberg, full professor in Physical Chemistry at Lund University and Prof. Dr. Céilia Fonseca Guerra, full professor of Applied Theoretical Chemistry at VU University.



## Family and Friends.

Ik zou graag mijn familie en vrienden bedanken. Mijn ouders, Erigone en Reidar, voor hun onvoorwaardelijke steun. Mijn broer, Sven en zijn partner Linda en mijn zus, Lotte. Onze band is werkelijk fenomenaal. Mijn Oma uit Delft en haar metgezel Riet. Dankbaarheid is een groot goed. Mijn Oma Koolen. De familie Koolen, Breda. Wilma, Peter, Micha en Daniel. Ik zou graag de gehele familie Penris, Rob (RIP), Henriette, Paul, Erik, Bart en Robert en de familie Pater: Emile, Sasha, Julian en Rinske willen bedanken. De zomers op Terschelling zijn onvergetelijk. De vormende jaren. De broeders van andere moeders, Paul, Steffan, Nino en Yannick. The ABC boys, Phillip, Robin en Julian. ECL, Pip, Abel, Frank, Jules en Jacob. Jaco, de voormalig dienaar van de stad. De familie Hemelrijk, Rob, Karin en Nars. Ignatianen: Noah en Lotte. My friends from Switzerland, Laia, James, Nadja and all my fellow toastmasters. My friends from Lund, Irene, Fabien, Monalisa, Tiago, Tommy, Simon, Marija. A special thanks goes out to Pip (Maurits) van Bremen, a young and talented architect, for editing this thesis.

And finally,

Моей дорогой Настя,

я люблю тебя дорогая. Лучшей команды не существует.



# Abstract

The world by and large has adopted the The Paris Agreement, which commits any signing party to cut greenhouse emissions drastically and prevent global heating above 2 °C beyond pre-industrial levels. For this ambitious goal to be met, ratifying states need to undergo a rapid energy transition away from fossil fuels to renewables for which large scale energy storage is needed.

Fuels such as acetaldehyde and ethanol offer a cost-effective measure to store low-energy-density renewable energy in the form of chemical bonds. One promising technology that achieves both CO<sub>2</sub> emissions reduction and energy storage is the electrochemical CO<sub>2</sub> reduction reaction (CO<sub>2</sub>RR). In here, CO<sub>2</sub> is converted using electricity into value added chemicals. Although promising, several hurdles will need to be taken for this technology to become competitive: 1) catalysts with high product selectivity will need to be designed, 2) reactor design will need to be optimized for specific products, 3) reactors will need to run >10,000 of hours at high conversion.

In this thesis, great attention was spent to the design, synthesis, characterization and CO<sub>2</sub>RR performance of electrocatalysts on the lab scale. Special focus was placed on Cu-based catalysts for their unique capabilities to make carbon-carbon bonds, required to produce energy-dense fuels. Design strategies to fashion selective metal catalysts were discussed in depth based on experimental data spanning three decades. Based on this discussion, two size regimes were selected that could yield promising potential catalysts, and lacked previous investigations.

The first regime is that of the bulk, where in particular the role of the catalyst surface, i.e., the facet exposed and the electronic structure, affects the selectivity in CO<sub>2</sub>RR. These effects were investigated by synthesizing Cu-M with M = Ag and Ag-Pd nanoparticles >10 nm of specific shapes having, therefore, specific facets, i.e., (100) and (111), exposed at the surface and a specific electronic structure as based on their relative composition.

To achieve this, a new wet-chemistry synthesis was developed that allowed to produce facet-controlled surface alloys independent of component miscibility. Further, a new characterization method based on inductively coupled plasma mass spectrometry was established to determine the composition distribution of said alloys with ensemble representative statistics. Based on the deconvolution of composition, i.e., electronic structure and facet, a clear trend in the selectivity for liquid fuels in CO<sub>2</sub>RR could be discerned.

The second regime is that of clusters in which electrocatalyst performance is governed to a large degree by the total number of atoms in the cluster and composition and to a lesser degree by the cluster-support interaction. To probe the effect of cluster size, composition and support in CO<sub>2</sub>RR, Cu(-Ag) clusters <1 nm were synthesized using spark ablation and immobilized on heteroatom doped carbonaceous supports. A remarkable high selectivity towards acetaldehyde (>90%) was observed for the Cu clusters independent of support.

Finally, we draw conclusions and offer perspectives on the further improvement of the technological readiness level of promising electrocatalysts beyond the lab scale. And propose avenues based on reactor design that are considered most promising in bringing CO<sub>2</sub>RR technologies to fruition.

## Keywords

CO<sub>2</sub> reduction, electrochemistry, model catalysts, wet-chemistry, inductively-coupled plasma mass spectrometry, spark ablation



# Résumé

Le monde entier a adopté l'accord de Paris, qui engage toutes les parties signataires à réduire considérablement les émissions de gaz à effet de serre et à empêcher le réchauffement de la planète de dépasser de 2 °C les niveaux de l'ère préindustrielle. Pour atteindre cet objectif, les États doivent opérer une transition énergétique rapide, pour lesquelles un stockage de l'énergie à grande échelle est nécessaire.

Les carburants tels que l'acétaldéhyde et l'éthanol constituent une mesure rentable pour stocker l'énergie renouvelable sous forme de liaisons chimiques. La réaction électrochimique de réduction du CO<sub>2</sub> (CO<sub>2</sub>RR) est une technologie prometteuse qui permet à la fois de réduire les émissions de CO<sub>2</sub> et de stocker de l'énergie. Dans ce cas, le CO<sub>2</sub> est converti en produits chimiques à valeur ajoutée grâce à l'électricité. Bien que prometteuse, plusieurs obstacles devront être surmontés pour que cette technologie devienne compétitive.

Dans cette thèse, une grande attention a été portée à la conception, synthèse, et performance CO<sub>2</sub>RR des électrocatalyseurs à l'échelle du laboratoire. Une attention particulière a été accordée aux catalyseurs à base de Cu pour leurs capacités uniques à établir des liaisons carbone-carbone, nécessaires à la production de carburants. Les stratégies de conception de catalyseurs métalliques sélectifs ont été discutées. Sur la base de cette discussion, deux régimes de taille ont été sélectionnés qui pourraient produire des catalyseurs potentiels prometteurs et qui n'ont pas fait l'objet d'études antérieures.

Le premier régime est celui du bulk, où en particulier le rôle de la surface du catalyseur, c'est-à-dire la facette exposée et la structure électronique, affecte la sélectivité en CO<sub>2</sub>RR. Ces effets ont été étudiés en synthétisant des nanoparticules Cu-M avec M = Ag et Ag-Pd >10 nm de formes spécifiques ayant, par conséquent, des facettes spécifiques exposées à la surface et une structure électronique spécifique en fonction de leur composition relative.

Pour y parvenir, une nouvelle synthèse par chimie humide a été mise au point, qui a permis de produire des alliages de surface à facettes contrôlées, indépendamment de la miscibilité des composants. En outre, une nouvelle méthode de caractérisation basée sur la spectrométrie de masse à plasma inductif a été établie pour déterminer la distribution de la composition. Sur la base de la déconvolution de la composition et de la facette, une tendance claire de la sélectivité pour les carburants dans le CO<sub>2</sub>RR a pu être discernée.

Le deuxième régime est celui des clusters dans lequel la performance est régie dans une large mesure par le nombre total d'atomes dans le cluster et la composition et dans une moindre mesure par l'interaction entre le cluster et le support. Pour étudier l'effet de la taille, de la composition et du support, des clusters de Cu(-Ag) <1 nm ont été synthétisés par ablation par étincelle et immobilisés sur des supports carbonés dopés à l'hétéroatome. Une sélectivité élevée remarquable envers l'acétaldéhyde (>90%) a été observée pour les clusters de Cu indépendamment du support.

Enfin, nous tirons des conclusions et offrons des perspectives sur l'amélioration du niveau de maturité technologique des électrocatalyseurs prometteurs au-delà de l'échelle du laboratoire. Et nous proposons des pistes basées sur la conception des réacteurs qui sont considérées comme les plus prometteuses pour faire fructifier les technologies CO<sub>2</sub>RR.

## Mots clés

Réduction du CO<sub>2</sub>, électrochimie, catalyseurs modèles, chimie humide, spectrométrie de masse à plasma inductif, ablation par étincelle





# Table of Contents

<b>Chapter 1: Research Background</b>	<b>40</b>
1.1. Energy transition	40
1.2. World energy demand, GHG emissions, climate change	41
1.3. Renewable energy: storage capacity	43
<b>Chapter 2: Introduction: metal catalysts in different size regimes for CO<sub>2</sub> electroreduction</b>	<b>52</b>
2.1. Introduction	54
2.2. Bulk regime: single-crystal electrodes	61
2.2.1 Non-Cu-based single crystals	62
2.2.2. Low index Cu single crystals	64
2.2.3. High index Cu single crystals	66
2.3. Nanoparticle catalysts	69
2.3.1. Nanoparticles: facet dominated regime	75
2.3.2. Nanoparticles: undercoordinated sites dominated regime	76
2.4. Metal cluster catalysts	85
2.4.1. Ligand effect in metal clusters	86
2.4.2. Atomicity in metal clusters	88
2.5. Atomically dispersed catalysts.	92
2.5.1 Effect of the metal center	93
2.5.2 Ligation effect	100
2.6. Conclusions and perspectives	102
2.6.1 Deconvolution of ligand/support effects from chemical nature of the active site	104
2.6.2. Dynamic nature of the catalysts demands in situ and in operando characterization	105
2.6.3. Theory-guided catalysts design	106
2.6.4. Reactor and electrolyte design	107
2.6.5. Scalable synthesis	108
2.7. References	110
2.8. Supporting Information	127
<b>Chapter 3: Research Objectives</b>	<b>140</b>
3.1. Objectives of the thesis	141
3.2. Overview of the research work	144

<b>Chapter 4: High-throughput sizing, counting and elemental analysis of anisotropic multimetallic nanoparticles with single-particle inductively-coupled plasma mass spectrometry</b>	<b>146</b>
4.1. Introduction	148
4.2. Instrument calibration and data processing	153
4.3. Results and Discussion	157
4.3.1. NP concentration optimization	157
4.3.2. Reliability of the method	159
4.3.3. Applications	160
4.4. Conclusion	164
4.5. Methods	164
4.5.1. Chemicals	164
4.5.2. Synthesis of anisotropic copper crystals	165
4.5.3. Synthesis of multimetallic NPs	166
4.5.4. Preparation of aqueous dispersions	166
4.5.5. Characterization	167
4.6. References	170
4.7. Supporting Information	175
<b>Chapter 5: Low-temperature non-equilibrium synthesis of anisotropic multimetallic nanosurface alloys for the electrochemical CO<sub>2</sub> reduction reaction</b>	<b>198</b>
5.1. Introduction	200
5.2. Results and Discussion	203
5.2.1 Low-temperature non-equilibrium synthesis of Cu-Ag anisotropic nanosurface alloys.	203
5.2.2. Facet dependent selectivity of Cu-Ag nanosurface alloys in CO <sub>2</sub> RR.	209
5.2.3. Phase-segregation induced selectivity shift	212
5.2.4. Theory-guided Cu-Ag-Pd catalyst selection for stable C <sub>2</sub> + liquid fuel electrosynthesis.	214
5.3. Conclusion	216
5.4. Materials and Methods	217
5.4.1. Chemicals	217
5.4.2. Non-equilibrium synthesis	217
5.4.2. Annealing experiments	218
5.4.3. Cathode preparation	218
5.4.4. Characterization	219
5.4.5. Density Functional Theory simulations	221
5.5. References	222
5.6. Supporting Information	226

<b>Chapter 6: Scalable synthesis of Cu(Ag) oxide clusters for the highly selective electrochemical conversion of CO<sub>2</sub> to acetaldehyde</b>	<b>252</b>
6.1. Main	254
6.2. Catalyst synthesis and characterization.	256
6.3. Electrochemical screening of the Cu(-Ag) oxide cluster carbonaceous support composite electrodes.	260
6.4. Resistance against potential cycling	263
6.5. Conclusions	265
6.6. References.	266
6.7. Supporting Information.	269
<b>Chapter 7: Conclusions and perspectives</b>	<b>302</b>
7.1. Conclusions	303
7.2. Perspectives	305
7.2.2. Catalyst stability as a function of reaction environment	305
7.2.3. Electrolyzer design	306
7.3. References	309
<b>Curriculum Vitae</b>	<b>310</b>





# List of Figures

- Figure 1.** (A) Development of the world population since 1800. Indicated by the colored lines are the filing dates of the patent for relevant technologies that have helped advance civilization. Data extracted from Ref. <sup>2</sup> (B) The energy demand in TWh since 1800 on the left ordinate. Contribution of coal, oil and gas dominate the energy mix starting the 1900s. Global CO<sub>2</sub> emissions in megaton since 1957 as estimated by BP. 41
- Figure 2.** A) Climate spiral showing the increase in atmospheric CO<sub>2</sub> concentration in ppm starting 1958 as measured at the Mauna Loa Observatory established by C.D. Keeling.<sup>5,6</sup> B) The average global temperature change compared to 1850 levels.<sup>9</sup> Each complete convolution construes one year. Reprinted with permission from Ref.<sup>5</sup> 42
- Figure 3.** Daily production of solar and wind energy in Germany in 2021. Both large daily fluctuations as well as seasonal can be distinguished. 43
- Figure 4.** Schematic of the catalytic hydrogenation of CO<sub>2</sub>.<sup>25</sup> 45
- Figure 5.** Electrochemical CO<sub>2</sub> reduction reaction. The schematic shows the conversion of CO<sub>2</sub> and water using renewable electricity to produce various gaseous and liquid products of the CO<sub>2</sub>RR with the current market size and value. Mt = megaton; Gt = gigaton; B = billion, M = million. Note that formate (HCOO<sup>-</sup>) is the direct reduction product of CO<sub>2</sub>RR when neutral or basic electrolyte is used, and thus further conversion is needed to yield formic acid.<sup>8</sup> 55
- Figure 6.** Classification of metal catalysts for CO<sub>2</sub>RR based on the particle size. With the decrease of the catalyst size, the electronic structure changes, and different structural factors can be used to describe the reactivity 57
- Figure 7.** The most common products of CO<sub>2</sub>RR for typical metal catalysts in different size regimes: single-crystal and facet dominated nanoparticle (>10 nm), ultra-small particle (1<x≤10 nm), cluster (≤1 nm), and SAC. The metal utilized to obtain the results is indicated by shape, and the product is indicated by color. The 'others' series includes Cu alloys and other metals. Each point represents a published study, where studies covering different size regimes are included in the gray box. For a list of the publications, see Note S2 of the Supporting Information. Note that publications in Figure 7 have been selected for their investigation of metal catalysts of different sizes using the same synthesis technique. Further, to highlight the differing performance of metal catalysts versus their SAC counterparts, we have included a selection of those as well. 60
- Figure 8.** OLEMS data of CORR of (a) Cu(100) and (b) Cu(111) single-crystals in neutral (blue, KH<sub>2</sub>PO<sub>4</sub> pH=7) and basic conditions (green, NaOH pH = 13) reproduced from ref. <sup>76</sup>. Copyright 2012, American Chemical Society. Both the total current as well as the ion specific current are provided. Note the roughly 200 mV earlier onset potential of C<sub>2</sub>H<sub>4</sub> on Cu(100) vs Cu(111) as well as the 200 mV shift towards the equilibrium potential when switching electrolyte on Cu(100). 65
- Figure 9.** (a) The selectivity triangle of Cu single-crystal electrode in the CO<sub>2</sub>RR summarizing data reported by Hori and co-workers and Koper and co-workers.<sup>13,23,24,76,84</sup> (b-d) Cu(100), Cu 5(100)x(110) and Cu 3(100)x(110). (e-f) Selectivity for H<sub>2</sub>, C<sub>1</sub> products, C<sub>2</sub>H<sub>4</sub> and C<sub>2+</sub> oxygenates on a Cu(100) surface with increasing (111) and (110) step-density.(g) Selectivity on a Cu(111) surface with increasing (111) step-density. (h-j) Cu(111), Cu 3(111)x(111) and Cu(110). Circle, star and square in (b-d) correspond to (f) and in (h-j) to (g). Black inset denotes the proposed active site for the majority product.<sup>85</sup> Note that the electrochemical performances were reported at the most selective potential (ΔU ~200 mV). All reactions were carried out in 0.1 M KHCO<sub>3</sub> at 5 mA cm<sup>-2</sup>. 68

**Figure 10.** Evolution of the relative contribution of the surface atoms (denoted as corner (in rust-brown), edge (in red), and facet ((111) in yellow and (100) in orange)) versus the bulk atoms (in grey) as a function of the particle edge-length, spanning three different geometries: cubic, octahedral and truncated octahedral. The asterisk in each figure indicates the edge-length of the particle depicted by the corresponding ball-model. For particles >5nm, independent of the geometry, the major contribution to the surface atoms is from the facets. The in-house developed geometrical model is based on the definition of various subsurfaces, see Note S3 of the Supporting Information.<sup>86</sup> 70

**Figure 11.** (a-c) TEM images of geometrical Cu octahedra of size 75, 150 and 310 nm, respectively. (d-f) TEM micrographs of Cu single-crystal nanocubes of size 24, 44 and 63 nm. (g) Deconvoluted size and shape effect on the product distribution, determined at -1.1 V vs. RHE in 0.1 M KHCO<sub>3</sub>, polycrystalline Cu is added as a reference. Whereas the activity increases with size, the selectivity to the major product, C<sub>2</sub>H<sub>4</sub>, reaches an optimum near 44 nm. (h) Effect of the applied potential deconvoluted from the size and shape-effect in the facet dominated regime of Cu showing that both the selectivity and activity towards CH<sub>4</sub> increases with decreasing size. Reproduced from ref. <sup>44,87</sup>. Copyright 2016 Wiley-VCH and 2019 RSC Publishing, respectively. 73

**Figure 12.** (a-d) SEM images of 1, 5, 70, and 200 nm silver NPs, respectively. (e) Volcano trend in the activity of ultrasmall to bulk Ag NPs in the CO<sub>2</sub>RR towards CO in CO<sub>2</sub> saturated 1-ethyl-3-methylimidazolium tetrafluoroborate (EMIM-BF<sub>4</sub>) electrolyte.<sup>31</sup> Reproduced from <sup>31</sup>. Copyright 2013 ACS Journals. Current densities for CO and H<sub>2</sub> formation reported are the differences in the current density with CO<sub>2</sub> and Argon at -0.75 V vs SHE and -1.14 V vs SHE, respectively. (f) CO partial current density for Ag NP samples and control samples. (g) Effect of anchoring agents on COOH and CO binding energies examined using Ag<sub>(147-n)</sub>Cys<sub>n</sub> (n = 0,1,2,4) models. Reproduced from ref. <sup>39</sup>. Copyright 2015 American Chemical Society. 77

**Figure 13.** (a-b) TEM images of the 6 nm sized Au NPs as well as the composite material used as cathode of NP-decorated activated carbon, respectively. (c) Size-dependent CO selectivity of Au NPs as a function of applied potential (V vs. RHE) in 0.1 M KHCO<sub>3</sub>. (d) CO specific mass current as a function of size and potential. (e) DFT calculation using the computational hydrogen electrode showing the free-energy diagram at a potential of -0.11 V vs RHE on Au(211), Au(111) and Au<sub>3</sub> clusters for the conversion of CO<sub>2</sub> into CO as well as the parasitic HER. (f) Schematic representing the conversion of CO<sub>2</sub> to CO on Au clusters. Reproduced from ref. <sup>35</sup>. Copyright 2013 American Chemical Society. (g-h) AFM images of the Au NPs of 1.1±1.0 nm and 7.7±2.3 nm produced via the encapsulated-micelle approach. (i) Size-dependent current density of Au NPs at -1.2 V vs. RHE in 0.1 M KHCO<sub>3</sub>. (j) Faradaic efficiency as a function of size at -1.2 V vs. RHE. Reproduced from ref. <sup>37</sup>. Copyright 2014 American Chemical Society. 79

**Figure 14.** (a-f) TEM and HRTEM micrographs of the 2.4, 6.2 and 10.3 nm Pd NPs. (g) Effect of size in the ultrasmall particle regime of Pd on the selectivity towards CO as a function of potential in 0.1 M KHCO<sub>3</sub>. (h) CO partial current density as a function of size and potential in the ultra-small particle regime of Pd. Reproduced from ref. <sup>38</sup>. Copyright 2015 American Chemical Society. (i-k) HRTEM micrographs of the 3.8, 6.5 and 10.7 nm Pd NPs. (h) HCOO<sup>-</sup> FE as a function of particle size at -0.1 V vs RHE in 0.5 M NaHCO<sub>3</sub>. Reproduced from ref. <sup>40</sup>. Copyright 2017 Wiley-VCH. 81

**Figure 15.** (a-f) AFM images of 2-15 nm Cu NPs on glassy carbon. (g) Enhanced overall activity of Cu NPs as a function of particle size at -1.1 V vs RHE in 0.1 M KHCO<sub>3</sub>. (h) Evolution of the product distribution on Cu NPs as a function of size at -1.1 V vs. RHE in 0.1 M KHCO<sub>3</sub> showing that most of the current enhancement reported goes towards the parasitic HER. Reproduced from ref. <sup>36</sup>. Copyright 2014 American Chemical Society. 83

- Figure 16.** (a-b) Size-distributions of Au<sub>25</sub> nanosphere and nanorods, respectively. (c-d) STEM HAADF micrographs of the Au<sub>25</sub> clusters supported on carbon black. (e) Total current density of CO<sub>2</sub> reduction as function of potential vs RHE of rods (in black) and spheres (in red) in 0.1 M KHCO<sub>3</sub>. (f) Faradaic efficiency of the Au<sub>25</sub> cluster pair as a function of potential vs RHE (nanosphere: red, nanorod: black). (g) Atom packing schematic of the conversion of Au nuclei into clusters of nanosphere and nanorod geometry as the result of the ligand shell. Reproduced from ref. <sup>34</sup>. Copyright 2018 American Chemical Society. 87
- Figure 17.** (a) EXAFS data of Cu-N<sub>4</sub>-C SACs. (b) Aberration-corrected STEM-HAADF image of the SAC. (c) Faradaic efficiency as a function of potential vs RHE in 0.1 M KHCO<sub>3</sub>. (d) Change in FE at -1.2 V vs. RHE in 0.1 M Li-, Na-, K-, CsHCO<sub>3</sub> as well as under CO flow. (e) Schematic showing the in-operando changes of the SAC towards metal clusters as determined by EXAFS explaining the selectivity towards C<sub>2</sub>H<sub>5</sub>OH. Reproduced from ref. <sup>116</sup>. Copyright 2019 Wiley-VCH. (f) HAADF-STEM image of Cu/C-0.4, showing the presence of isolated Cu species marked by yellow circles (Scale bar: 2 nm). (g) The product distribution at different polarization potentials for Cu/C-0.4. (h) DFT simulated reaction pathway of CO<sub>2</sub>RR to C<sub>2</sub>H<sub>2</sub>OH on the supported Cu cluster catalyst at 0 and -0.41V. Reproduced from ref. <sup>117</sup>. Copyright 2020 Springer Nature. 89
- Figure 18.** (a) Predicted \*CO binding strengths to various electrocatalysts obtained with DFT explaining the strong tendency towards CO production of SACs in the CO<sub>2</sub>RR. M@G, M-N<sub>4</sub>-C and MPc, denote metal on graphene, metal N-doped carbon with 4 N bonds and metal phthalocyanine, respectively. Reproduced from ref. <sup>160</sup>. Copyright 2021 American Chemical Society. Free energy diagram of CO<sub>2</sub> to CO for, (b) CoPc adsorbed on graphene, (c) FeNC, and (d) NiNC with N<sub>1</sub>, N<sub>2</sub>, N<sub>3</sub> and N<sub>4</sub> the N coordination number. Reproduced from ref. <sup>165</sup>. Copyright 2021 Springer Nature. 93
- Figure 19.** (a) Schematic of the various N-sites present in the M-X-Cs, in which M=Fe, Mn, FeMn. (b) CO FEs as a function of potential for the various M-X-Cs center in which M=Fe, Mn, FeMn. in 0.1 M KHCO<sub>3</sub> (c) FEs of CH<sub>4</sub> for the various electrocatalysts. Reproduced from ref. <sup>57</sup>. Copyright 2015 Wiley-VCH. (d) CO production turnover frequency (TOF) of the M-N-Cs as a function of potential for the various M-X-Cs in which M= M=Mn, Fe, Co, Ni, Cu. Reproduced from ref. <sup>66</sup>. Copyright 2017 Nature Springer. 96
- Figure 20.** (a) Schematic of the production process of the electrospun ZIF-8 derived porous single-atom Cu catalyst (CuSAs/CNFs). (b) HAADF-STEM images of CuSAs/CNFs. (c) Product distribution as a function of applied potential for CuSAs/TCNFs in 0.1 M KHCO<sub>3</sub>. (d) Free energies for conversion of \*CO to CH<sub>3</sub>OH on Cu-N<sub>4</sub> structure. Orange, gray, dark blue, red, and light blue spheres stand for Cu, C, N, O, and H atoms, respectively. Reproduced from ref. <sup>140</sup>. Copyright 2019 American Chemical Society. (e) HAADF-STEM images of SA-Zn/MNC. (f) FEs for CO<sub>2</sub>RR to CH<sub>4</sub> as a function of applied potential for SA-Zn/MNC. (g) Free energy diagrams for CO<sub>2</sub>RR to CH<sub>4</sub> on Zn-N<sub>4</sub>-graphene structure. Reproduced from ref. <sup>149</sup>. Copyright 2020 American Chemical Society. 98
- Figure 21.** Overview of the major products obtained on various Cu-based electrodes in the different size regimes of the CO<sub>2</sub>RR. 103
- Figure 22.** Selectivity vs activity plots of Cu based alloys of up to five components as based on predicted values via a supervised machine algorithm trained with adsorption energies of key intermediates, H\* and CO\*. Reprinted with permission from ref. <sup>2</sup> 142
- Figure 23.** Schematic diagram of the general approach for obtaining size distribution of NP dispersions using SP-ICP-MS. (A) Nebulized NPs formed after nebulization of the sample dispersions. (B) Plasma torch of the ICP-MS instrument used for the desolvation, vaporization, atomization, and ionization of the particles present in the aerosol. (C) SP-ICP-MS raw data containing both background signal (e.g., dissolved ions) and particle events (ion plumes). A snapshot of 100 ms is depicted for representation. (D) Histogram of the raw data obtained via a sorting algorithm after background subtraction equating the intensity to the number of observations (events). (E) Final solution of SP-ICP-MS data processing pipeline, e.g., size distributions. 149

**Figure 24.** (A1-A3) Low resolution transmission electron microscopy (LR-TEM) micrographs of cubic (C), truncated octahedral (TOh), and tetrahedral (Th) Cu NPs synthesized using a phosphine-derivative mediated wet-chemical procedure. (B1-B3) Size distributions of the C-, TOh- and Th-Cu NPs obtained using SP-ICP-MS. The particle most frequently observed has an edge-length of: 77, 15 and 77 nm, respectively. Edge-length is defined as the center-to-center distance between two corner atoms of a particle (depicted in deep red in the ball models in the inset). The total number of particles observed in a single experiment was as high as 1100 for a measurement of 100 s duration with a dwell time of 50  $\mu$ s. Excellent agreement exists between the SP-ICP-MS and LR-TEM (C1-C3) measurements. Aggregates in the sample that are missed by the LR-TEM can be observed (events at the far end of the distributions in (B1-B3), giving a more complete picture of the ensemble. (C1-C3) Size distributions of 100 C-, TOh- and Th-Cu NPs using particle counting of LR-TEM micrographs. 152

**Figure 25.** (A) Time resolved plot of the SP-ICP-MS raw data of a calibrant (yellow). Only 100 ms is depicted for clarity. (B) Intensity-versus-events histogram of a calibrant (yellow). (C) Transport efficiency ( $\eta_t$ ) calibration curve of particle dispersions of known size and number concentration (in the present study Au NP (see Methods, Figure S1 and S2). (D) Dissolved standard solutions calibration curve (Cu in the present study). (E) Converted  $\mu$ g  $s^{-1}$  calibration curve of the dissolved ion standards (Cu in the present study). (F) Time resolved plot of the SP-ICP-MS raw data of an analyte (red). (G) Intensity-versus-events histogram of an analyte (red). A snapshot of 100 ms is depicted for representation. (H) Various geometrical models to extract dimensional parameters such as edge-length including but not limited to spheres, cubes, truncated octahedra and tetrahedra. (I) Final solution of the SP-ICP-MS data processing pipeline representing a NP size distribution. 154

**Figure 26.** Size distributions of a dilution series of TOh-Cu NPs. (A) NP number concentration (N):  $10^5$   $mL^{-1}$ , (B) NP number concentration (N):  $1/3 \times 10^5$   $mL^{-1}$ , (C) NP number concentration (N):  $1/6 \times 10^5$   $mL^{-1}$ . Shift of the average size, thus mass, to lower values. upon dilution highlights the significant effect of the dissolved analyte concentration on data quality. If the dissolved analyte concentration is too high, ion plumes derived from initial particles of intensities close to the dissolved analyte cannot be distinguished from the background. Optimization and calibration of N is instrumental to correct distribution determination. This feature perseveres even with an independent instrument calibration used (Figure S3). The gain in the number of events is evidence that all particle events can be extracted. 158

**Figure 27.** SP-ICP-MS as a method to characterize anisotropic NSAs.<sup>39</sup> The C-Cu NPs synthesized in the present study were coated with an ultrathin shell of Ag using a galvanic exchange reaction (see Methods). (A1-A2) LR-TEM micrograph of the Cu cubic core and the CuAg cubic NSA, respectively. (B1-B2) Cu and Ag mass flux calibration curve used to convert the intensity measured to the mass of the particle. (C1) Using a subsurface model (Note S2, Figure S5), the Cu particle mass distribution obtained with SP-ICP-MS can be converted into an ensemble distribution of surface atoms. (C2) Distribution of Ag atoms obtained via SP-ICP-MS. By taking the ensemble average, we deduce that 0.59 monolayer of Ag has been deposited. Inset shows the normally distributed doping concentration of Ag by superimposing the Cu and Ag spectra, respectively. 161

**Figure 28.** (A1-A3) TEM micrographs of the C-CuAg, C-CuPd, and C-CuPdAg multimetallic NPs, respectively. (B1-B3) STEM-EDX elemental maps of C-CuAg, C-CuPd, and C-CuPdAg NPs. (C1-C3) Normalized composition distributions of C-CuAg, C-CuPd, and C-CuPdAg multimetallic NPs obtained with a TOF mass analyzer. The C-CuAg and C-CuPdAg distributions were normalized by the number of events. The C-CuPd distribution was normalized so that the probability density function integral equaled to one. (C1) The C-CuAg distribution shows that Ag is normally distributed around the mean, corroborating the results obtained using the quadrupole (Gaussian fit:  $R^2 = 0.9723$ , see Note S4). The maximum lies at  $\sim 2.2$  Ag at. %, a four-fold reduction with respect to the SP-ICP-MS determined composition distribution (Figure 5C2), which can be explained by the higher number concentration at a fixed mass loading (see Figure S8 and S12). (C2) The C-CuPd is lognormally distribution evidenced by the positive skew ( $R^2 = 0.9816$ , see Note S4). (C3) The C-CuPdAg distribution shows again a normal distribution ( $R^2 = 0.9467$ , see Note S4). **Figure 31.** Determination of the penetration depth of Ag on the C-Cu<sub>0.97</sub>Ag<sub>0.03</sub> NSA. (A) High-resolution STEM- 163

**Figure 29.** (A) Schematic illustration of the conventional and non-equilibrium galvanic replacement reaction, 202 where phase-separated heterostructures and homogeneous surface alloys were formed, respectively. (B) STEM-EDXS elemental maps of cubic Cu-Ag, Cu-Ag-Pd, Cu-Pd and Cu-Au NSAs prepared by using the non-equilibrium method showing the random nature of the added component(s) and increased intensity at the particle edges.<sup>33</sup>

**Figure 30.** Characterization of the anisotropic Cu-Ag NSAs obtained via the non-equilibrium synthesis. Inductively 205 coupled plasma optical emission spectroscopy (ICP-OES) determined particle bulk composition provided in the title. (A-C) BF-TEM images of C-, Th- and TOh-Cu-Ag NSAs. (D-F) STEM-EDXS elemental maps of C-, Th- and TOh-Cu-Ag NSAs with Cu in orange and Ag in turquoise showing normally distributed Ag and increased intensity at the particle edges. (G-I) Distribution of the number of atoms in the surface for N single particles of the C-, Th- and TOh-Cu-Ag NSAs as determined with single particle-inductively coupled plasma mass spectrometry (SP-ICP-MS) with N>500, with an equivalent of 1.4, 1.1 and 1.5 ML of Ag deposited, respectively. (J) Valence band spectra of pure Cu and Ag references and three C-Cu-Ag particles synthesized at different reaction times using the non-equilibrium synthesis (1, 5 min and 2 hrs). The point-of-gravity of the valence band construed exactly half the area-under-the-curve of the spectra (denoted by the dotted line), which was determined by numerically integrating the spectra with fixed bounds at 0 and 9 eV, respectively. The shift of the valence band towards the Fermi level as compared to pure Cu confirms the random alloy nature of the C-Cu<sub>0.99</sub>Ag<sub>0.01</sub> and C-Cu<sub>0.97</sub>Ag<sub>0.03</sub> NSAs as charge-transfer occurs from Cu to Ag. Instead, for a phase-segregated material (C-Cu<sub>0.13</sub>Ag<sub>0.87</sub>), the valence band spectrum is a linear combination of the Cu and Ag reference spectra showing no charge-transfer. The asterisk (\*) in (J) indicates the valence band spectra of the same ensemble of particles indicated in (H). HAADF image of a 40 nm slice of a Cu-Ag NSA NP embedded in an epoxy resin. (B) Atomic resolution HAADF image of the Cu-Ag NSA edge. (C, D) Cu and Ag EDXS elemental maps of (B). (E) EDX spectra of the core and edge regions of the Cu-Ag NSA (indicated in B-D) showing the presence of the characteristic Ag L<sub>α</sub> and L<sub>β</sub> EDXS peaks at edge regions only, corresponding to the first 6 MLs of the particle. (F) Line scan of intensity over the image in (B).

**Figure 31.** Determination of the penetration depth of Ag on the C-Cu<sub>0.97</sub>Ag<sub>0.03</sub> NSA. (A) High-resolution STEM- 207 HAADF image of a 40 nm slice of a Cu-Ag NSA NP embedded in an epoxy resin. (B) Atomic resolution HAADF image of the Cu-Ag NSA edge. (C, D) Cu and Ag EDXS elemental maps of (B). (E) EDX spectra of the core and edge regions of the Cu-Ag NSA (indicated in B-D) showing the presence of the characteristic Ag L<sub>α</sub> and L<sub>β</sub> EDXS peaks at edge regions only, corresponding to the first 6 MLs of the particle. (F) Line scan of intensity over the image in (B).

**Figure 32.** Electrocatalytic screening of the as-synthesized (an)isotropic Cu-Ag NPs, error bars represent 211 the standard deviation of three independent measurements. Ball models in the title indicate the geometrical description of the anisotropic particles consisting of Cu(100) facets in orange, Cu(111) facets in yellow, edge sites in red and corner sites in red brown. (B) Product distribution of the anisotropic Th-Cu<sub>0.97</sub>Ag<sub>0.03</sub>, C-Cu<sub>0.97</sub>Ag<sub>0.03</sub> and TOh-Cu<sub>0.97</sub>Ag<sub>0.03</sub> NSA. (C) C<sub>2+</sub> selectivity as a function of facet and composition. (D) C<sub>2+</sub> liquid fuel selectivity as a function of facet and composition. The interface between Cu-Ag(111) and Cu-Ag(100) offers evidently the best C<sub>2+</sub> liquid fuel producing active site(s).

**Figure 33.** (A, D, G) Time evolution of the product distributions of the Th-,C- and TOh-Cu-Ag NSA at -1.1 V vs RHE 213 in CO<sub>2</sub> saturated 0.1 M KHCO<sub>3</sub>. C<sub>1</sub> products including HCOO<sup>-</sup>, CO and CH<sub>4</sub> are depicted in orange. C<sub>2+</sub> liquid fuels products including CH<sub>3</sub>COO<sup>-</sup>, CH<sub>3</sub>CHO, CH<sub>3</sub>CH<sub>2</sub>OH, C<sub>3</sub>H<sub>7</sub>OH are depicted in blue. C<sub>2</sub>H<sub>4</sub> is depicted in purple and H<sub>2</sub> in grey. Error bars indicate the standard deviation of three-independent measurements (Table S5). Liquid products are collected under operation from a gas-tight H-cell using a clean syringe. (B, E, H) BF-TEM images of the pristine anisotropic Cu-Ag NSAs. (C, F, I) Negatives of BF-TEM images of the electrocatalysts after 30 min of CO<sub>2</sub>RR offered as a visual-aid to observe the extrusions with higher contrast at the particle surfaces (indicated with arrows) assigned to the Ag phase. Note that the alternating bright/dark areas in the BF-TEM images are the result of thickness-fringes.

**Figure 34.** Theory-guided optimization of the ternary alloy for extended phase-stability. (A) Activity-selectivity 215 plot of CO<sub>2</sub>RR/CORR of the ternary alloy system. Orange colored dots indicate compositions with ≥74 at.% Cu, light blue and purple colored with <74 at.% Cu and >13 at.% Ag and Pd, respectively. Black symbols (circle, star and square) denote the predicted values from the machine learning-based algorithm. Blue symbols and error bars indicate molar yields as calculated from experimental data in (C) and Table S7 and S8. (B) STEM-EDXS elemental map of as-synthesized C-Cu-Ag-Pd NSA with Ag:Pd equals 1:3. (C) Time averaged FEs of C<sub>2+</sub> liquid fuels, C<sub>2</sub>H<sub>4</sub> and H<sub>2</sub> of the C-Cu<sub>79</sub>Ag<sub>21</sub>, C-Cu<sub>79</sub>Ag<sub>16</sub>Pd<sub>5</sub> and C-Cu<sub>79</sub>Pd<sub>16</sub>Ag<sub>5</sub> NSAs, respectively. Electrochemical test was performed for 30 min at -1.1 V vs. RHE in 0.1 M KHCO<sub>3</sub>. Square, circle and star insets reflect matching composition in (A)-(C). Error bars indicate the standard deviation of three independent measurements. ....

**Figure 35.** Schematic of the spark ablation (A) and immobilization (B) of Cu(-Ag) oxide clusters on heteroatom 257 doped carbonaceous support GDL composites.

**Figure 37.** (A-B) Selectivity screening of Cu-NCB and Cu-GO GDL composites, respectively. (C-D) Selectivity 261 screening of Cu-Ag-NCB and Cu-Ag-GO GDL composites, respectively. All electrochemical reactions were carried out in CO<sub>2</sub> saturated 0.1M KHCO<sub>3</sub> electrolyte in Nafion® membrane separated H-cell. Chronoamperometry was carried out in a cathodic potential window of -0.5 to -1.1 V vs RHE (half-cell potential) with 100 and lastly 200 meV increment (iR-drop corrected) using an Ag/AgCl reference electrode. A Pt foil (1 cm<sup>2</sup>) was used as counter electrode. Gaseous products were quantified via gas chromatography. Liquid products were detected using H-NMR and quantified using the Kuhl et al. protocol.<sup>10</sup> For the lower overpotential experiments (<800 meV), liquid products were collected for at least 3 hrs for reasonable statistics. For all other potentials, FEs were averaged for a minimum of 30 min. Error bars represent standard deviations of at least two independent measurements. The less than 100% FE observed for the Cu-Ag-GO-GDL at -0.5 V vs RHE stems from unquantifiable gaseous products due to dilution of the CO<sub>2</sub> stream (H<sub>2</sub> most likely).

**Figure 38.** (A) Stress test of the Cu-NCB GDL at -0.6 V vs RHE in 0.1 M KHCO<sub>3</sub>. (B-C) Radial distribution functions 264 extracted from the EXAFS spectra of the Cu-NCB and -GO catalyst, respectively, after catalysis and exposure to air. Cu, CuPc and Cu(acac)<sub>2</sub> were used as a reference. (D-E) XANES spectra of the Cu-NCB and -GO catalyst, respectively, after catalysis and exposure to air. A linear combination fit (LCF) of the Cu and CuPc and Cu(acac)<sub>2</sub> reference spectra puts the contribution of the ligation sites to catalyst structure at 40% and 30%, respectively.

**Figure 39.** (A) Zero-gap cell with the ion exchange membrane either cation exchange membrane (CEM) or 306 anion exchange membrane (AEM). (B) A solid-state device in which ions shuttling occurs through a solid-state electrolyte (SSE). Adapted and reprinted with permission from Ref. <sup>2</sup> and Ref. <sup>3</sup>.







## Chapter 1

# Research Background

## 1.1. Energy Transition

The rapid pace of human civilization's development in the last century is literally and figuratively fueled by fossil fuels. Energy demand is by an overwhelming majority supplied by the consumption of fossil fuels such as coal, oil and natural gas. For instance, in the Netherlands in 2022, a shocking 87% of the total energy demand was covered by fossil fuels. Further, many products and commodities of modern-day life find their origin in refinery as well. Naturally, fossil fuels are a finite commodity and as such, obtaining them is becoming increasingly difficult. Further, their widespread consumption has led to the massive release of carbon in to the atmosphere in the form of  $\text{CO}_2$ . And heaps of evidence implicate this greenhouse gas (GHG) in the acceleration of climate change with rising global temperatures, higher frequency of extreme weather events, rising sea levels and the melting of our polar ice caps and glaciers, as a result. Therefore, in order to sustain our development in the long term, and to reduce carbon emissions in the short term, we need a rapid transformation of our economic model towards circularity.

- We need to transition away from fossil fuel-based energy consumption to renewable energy instead
- We need to find substitutes for the fossil fuel originated products and commodities of modern-day life.

On this roadmap towards sustainable growth, the first milestone is to reach net neutrality. Thankfully, most countries have pledged to do so as early as 2050 adhering to the goals set in The Paris Agreement. However, the road towards a complete energy transition is far from obvious. The electrochemical  $\text{CO}_2$  reduction reaction ( $\text{CO}_2\text{RR}$ ), in which electricity is used to convert  $\text{CO}_2$  in value added chemicals, using renewable energy is a promising solution to help mitigate climate change, integrate renewables into our traditional carbon-based economy, and achieve net neutrality.

In the coming sections, we will discuss the issue of the global energy demand, associated  $\text{CO}_2$  emissions, induced climate change and highlight the challenges ahead to achieve a complete energy transition. Then, we will discuss the potential of  $\text{CO}_2\text{RR}$  as a proposed tool to catalyze this transition.

## 1.2. World energy demand, GHG emissions, climate change

Since the dawn of time, man has used technology to improve upon his condition. Such improvements led to increases in life expectancy, lower child mortality and higher birthrate and therefore, the opportunity for the population to grow. However, for the vast majority of man's existence, his industrious nature was energy limited. Notably, until the last 1800s, the world population was stagnant. Not until a continuous conversion of thermal energy into mechanical motion was achieved, which greatly facilitated the taming of the elements (i.e. steam engine),<sup>1</sup> did the population start to develop (**Figure 1A**).<sup>2</sup> Notably, the world's energy demand and the appearance of fossil fuels (coal) in the energy mix and its subsequent dominion over the world's energy supply is in step

with this development (**Figure 1B**).<sup>3</sup> Then, from the last 1950s, the world population shows clear signs of exponential growth doubling from 2.5 to 5 billion in less than 40 years. The Green revolution, facilitated by the Haber-Bosch process, enabled in feeding this ever-growing population.<sup>4</sup> Spanning the same period, and brought forth by the heaps of new humans added daily and their desire to improve upon their way of life, the global energy demand soared by 350% to ~100,000 TWh by 1984. Until now, energy demand has grown even further to staggering 170,000 TWh. And with the global population projected to reach 9.7 billion by 2050, it is expected to show sustained growth for the foreseeable future.

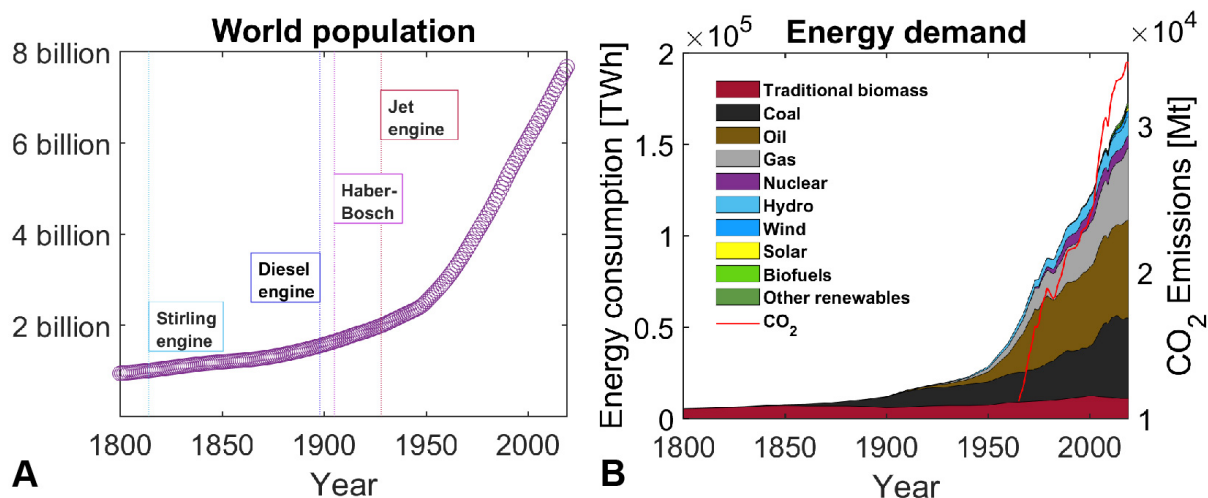


**Figure 1.** (A) Development of the world population since 1800. Indicated by the colored lines are the filing dates of the patent for relevant technologies that have helped advance civilization. Data extracted from Ref. <sup>2</sup> (B) The energy demand in TWh since 1800 on the left ordinate. Contribution of coal, oil and gas dominate the energy mix starting the 1900s. Global CO<sub>2</sub> emissions in megaton since 1957 as estimated by BP.

Unsurprisingly, massive emissions of CO<sub>2</sub> accompanied this rapid increase in fossil fuel consumption (**Figure 1B**, right ordinate). Interestingly, in the same period, the atmospheric CO<sub>2</sub> levels started to rise as well (**Figure 2A**).<sup>5,6</sup> And with a staggering pace. In less than 60 years the average concentration had increased by 130% from ~316 ppm in 1958 to ~418 ppm by 2017 (the fastest rate in last 66 million years).<sup>7</sup> Since CO<sub>2</sub> is a GHG, it is suggested as a major contributing factor in inducing climate change. Indeed, the average global temperature has spiked ever since the consumption of fossil fuels started to rise, hovering around the +1.2°±0.1 in 2020 (above 1850 levels, **Figure 2B**).<sup>8</sup>

With the most severe adverse effects of

climate change predicted to occur for global warming of >1.5°,<sup>9,10</sup> countries that ratified The Paris Agreement have committed to keeping the temperature rise below this value.

Thankfully, efforts in curbing CO<sub>2</sub> emissions already seem to be taking effect, with the year-to-year change in emission from 2016 to 2020: +1.1%, -1.8%, +0.1%, and -5.9%, respectively (effects of COVID-19 not considered). However, this still distances away from commitments to reach net zero. Therefore, to achieve this ambitious goal, a rapid switch from fossil fuel-based energy consumption to renewables is required. In the next section we will see what is putting the brakes on this transition and how this can be mitigated.

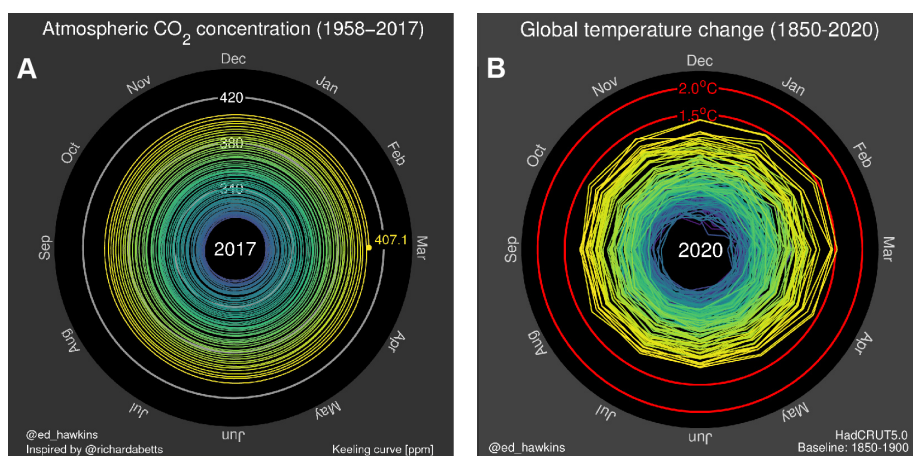


**Figure 2.** A) Climate spiral showing the increase in atmospheric CO<sub>2</sub> concentration in ppm starting 1958 as measured at the Mauna Loa Observatory established by C.D. Keeling.<sup>5,6</sup> B) The average global temperature change compared to 1850 levels.<sup>8</sup> Each complete convolution construes one year. Reprinted with permission from Ref.<sup>5</sup>.

### 1.3. Renewable energy: storage capacity

Countries, including developed and developing ones, are now heavily investing in renewable energy generation, such as hydro-power, solar energy and wind energy etc. In the last 10 years, the installed capacity of solar and wind generated electricity has increased ~17- and ~4-fold, respectively, for instance.<sup>11</sup> However, the availability is often intermittent. In example, for solar power, peak consumption takes place during the night whereas peak production, depending on the geolocation, happens around midday. Further, seasonal variation, which is again location bound, significantly thwarts mass-deployment (**Figure 3**).

In order for the energy transition to reach completion, large-scale energy storage must thus be achieved. Battery technology is often suggested as a likely candidate for this purpose.

However, the associated low energy density, relatively short lifetime and high costs puts doubts on scalability (**Table 1**).<sup>12</sup> Never mind the enormous amounts of raw materials it would require. Consider the global energy demand in 2019 ( $1.8 \times 10^5$  TWh, **Figure 1**). With an energy density of  $0.16 \text{ kWh kg}^{-1}$  for the Li ion battery (the most energy dense on the market), and a typical battery containing ~7% Li,<sup>13</sup> back of the envelope calculation puts the required amount of Li at ~80 Gt if storage capacity is to meet consumption. With the total Li reserves estimated at ~14 Mt, the supply of raw material misses the mark by four orders of magnitude. The case for Co is even worse (7.1 Mt reserve). Even if only a fraction of the global energy consumption is to be stored (1%), not nearly enough raw material can be mined to reach capacity.

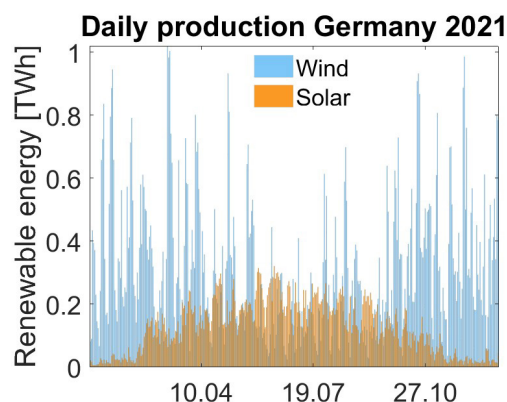


**Figure 3.** Daily production of solar and wind energy in Germany in 2021. Both large daily fluctuations as well as seasonal can be distinguished.<sup>5</sup>

Synthetic fuels offer a much cheaper and more facile approach instead. For one, their calorific value is much better as energy is stored in covalent bonds instead of through a chemical potential difference (**Table 1**). Further, they can be produced catalytically and require, therefore, little to no raw material for their production. Also, since the infrastructure is for the most part already in place (from fossil fuels), transitioning should be more cost-efficient. Further, electricity generation is expected to become fully *green* by 2050,<sup>14,15</sup> putting tremendous pressure on pricing. Pathways towards electricity prices as low as 0.03 USD kWh<sup>-1</sup> have already been proposed.<sup>16,17</sup> That, and the possibility of a carbon tax put into place,<sup>18</sup> greatly benefits the business case of synthetic fuels.

Two roadmaps can be foreseen towards the utilization of CO<sub>2</sub> in the form of synthetic fuels. The first, and the most advanced, is the catalytic hydrogenation of CO<sub>2</sub> towards value-added products such as CO, CH<sub>4</sub>, and CH<sub>3</sub>OH (**Figure 4**).<sup>19,20,21</sup> This, of course, requires first the splitting of H<sub>2</sub> from H<sub>2</sub>O.

Certainly, polymer electrolyte membrane (PEM) electrolyzers have reached maturity with efficiencies of 50% and >30 years of operation.<sup>22</sup> In case of the Sabatier reaction for the production of CH<sub>4</sub>, overall power-to-gas efficiencies of ~35% can be achieved in this way.<sup>23</sup> However, the low natural gas price (not considering relevant geopolitical tensions) and volumetric energy density puts constraints on this reaction.

Synthesis of the more energy dense light-olefins such as octane, which can be produced from CH<sub>3</sub>OH instead using zeolite-catalysts or via the Fischer-Tropsch process, is more promising.<sup>24</sup> Such processes can achieve up to 57% energy efficiency of the energy stored in H<sub>2</sub> (power-to-fuel efficiency of 28.5%).<sup>22</sup> Recently, the first industrial scale CO<sub>2</sub> hydrogenation plant has been commissioned, With the aim to produce methanol.

Fuel	Calorific value	
	[kWh kg <sup>-1</sup> ]	[MJ L <sup>-1</sup> ]
Octane	13.0	34.7
Kerosene	12.8	37.9
Ethanol	8.2	23.4
Methane	14.85	0.04
Li ion	0.16	0.68

**Table 1.** Energy density of a selection of synthetic fuels. Data extracted from Ref.<sup>12</sup>

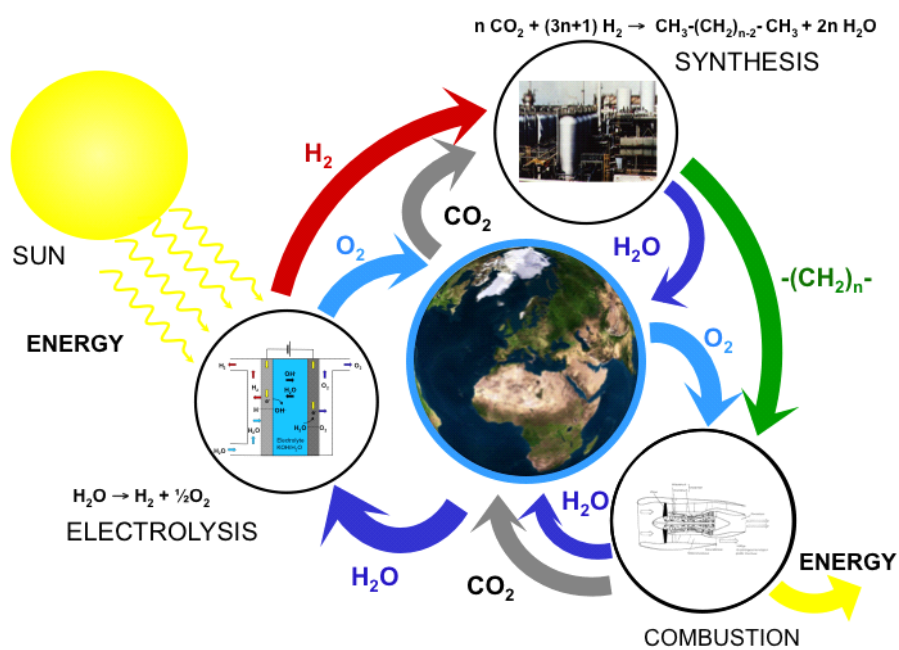


**Figure 4.** Schematic of the catalytic hydrogenation of CO<sub>2</sub>.<sup>25</sup>

The second, is the direct electrochemical conversion of CO<sub>2</sub> into products such as CO, HCOOH, CH<sub>4</sub>, CH<sub>3</sub>OH, CH<sub>3</sub>CHO, C<sub>2</sub>H<sub>4</sub>, C<sub>2</sub>H<sub>5</sub>OH, C<sub>3</sub>H<sub>7</sub>OH, etc.<sup>26,27,28,29,30</sup> Naturally, CO<sub>2</sub>RR has the advantage of producing fuels directly, without the need of first H<sub>2</sub> production (which in many cases would require storage at additional capital cost) followed by a thermal or biocatalytic process. Especially, the two-birds-one stone CO<sub>2</sub> to C<sub>2+</sub> products such as C<sub>2</sub>H<sub>5</sub>OH and C<sub>3</sub>H<sub>7</sub>OH is highly attractive. Not only are H<sup>+</sup> and CO<sub>2</sub> reduced simultaneously, C-C coupling is achieved as well greatly improving the energy stored per pass. This would dramatically reduce cost of operation (if CO<sub>2</sub> electrolyzer can be made as cost-efficiently as PEM electrolyzers). For the CO<sub>2</sub>RR to compete with CO<sub>2</sub> hydrogenation, comparable energy efficiencies need to be achieved. For the case of C<sub>2</sub>H<sub>5</sub>OH, with 0.69 the calorific value of octane, this would mean >41% power-to-fuel efficiency.

Considering that the next generation of H<sub>2</sub> electrolyzers (alkaline electrolyzers) run at an efficiency of 88% this number jumps to ~73%.<sup>31</sup> Recent techno economic analysis put the breakeven point for CO<sub>2</sub>RR to C<sub>2+</sub> products at ~50% for an electricity price of 0.01 USD kWh<sup>-1</sup>.<sup>11</sup> Unfortunately, CO<sub>2</sub>RR to C<sub>2+</sub> suffers from poor selectivity (<50%) putting energy efficiencies in the 15% range.<sup>32</sup> For this reaction to become competitive more selective electrocatalysts need to be designed. In the following chapter, we will introduce design concepts based on a vast survey of the literature of CO<sub>2</sub>RR to optimize catalyst design and improve the selectivity towards C<sub>2+</sub> products and in particular liquid fuels.





## 1.3 References

- (1) R, S. Improvements for Diminishing the Consumption of Fuel and in Particular an Engine Capable of Being Applied to the Moving of Machinery on a Principle Entirely New. *English Patent 4081* **1816**.
- (2) *Population | Gapminder*. <https://www.gapminder.org/data/documentation/gd003/> (accessed 2022-05-05).
- (3) Ritchie, H.; Roser, M. Energy. *Our World in Data* **2020**.
- (4) *Yields vs. Land Use: How the Green Revolution enabled us to feed a growing population*. Our World in Data. <https://ourworldindata.org/yields-vs-land-use-how-has-the-world-produced-enough-food-for-a-growing-population> (accessed 2022-05-05).
- (5) Meinshausen, M.; Vogel, E.; Nauels, A.; Lorbacher, K.; Meinshausen, N.; Etheridge, D. M.; Fraser, P. J.; Montzka, S. A.; Rayner, P. J.; Trudinger, C. M.; Krummel, P. B.; Beyerle, U.; Canadell, J. G.; Daniel, J. S.; Enting, I. G.; Law, R. M.; Lunder, C. R.; O'Doherty, S.; Prinn, R. G.; Reimann, S.; Rubino, M.; Velders, G. J. M.; Vollmer, M. K.; Wang, R. H. J.; Weiss, R. Historical Greenhouse Gas Concentrations for Climate Modelling (CMIP6). *Geoscientific Model Development* **2017**, *10* (5), 2057–2116. <https://doi.org/10.5194/gmd-10-2057-2017>.
- (6) US Department of Commerce, N. *Global Monitoring Laboratory - Carbon Cycle Greenhouse Gases*. <https://gml.noaa.gov/ccgg/trends/> (accessed 2021-08-16).
- (7) Zeebe, R. E.; Ridgwell, A.; Zachos, J. C. Anthropogenic Carbon Release Rate Unprecedented during the Past 66 Million Years. *Nature Geosci* **2016**, *9* (4), 325–329. <https://doi.org/10.1038/ngeo2681>.
- (8) Morice, C. P.; Kennedy, J. J.; Rayner, N. A.; Jones, P. D. Quantifying Uncertainties in Global and Regional Temperature Change Using an Ensemble of Observational Estimates: The HadCRUT4 Data Set: THE HADCRUT4 DATASET. *J. Geophys. Res.* **2012**, *117* (D8), n/a-n/a. <https://doi.org/10.1029/2011JD017187>.
- (9) *Global Warming of 1.5 °C* —. <https://www.ipcc.ch/sr15/> (accessed 2021-08-16).
- (10) *Fourteenth Session of Working Group I and Fifty-Fourth Session of the IPCC — IPCC*. <https://www.ipcc.ch/meeting-doc/ipcc-wgi-14-and-ipcc-54/> (accessed 2021-08-16).
- (11) Shin, H.; Hansen, K. U.; Jiao, F. Techno-Economic Assessment of Low-Temperature Carbon Dioxide Electrolysis. *Nat Sustain* **2021**, *4* (10), 911–919. <https://doi.org/10.1038/s41893-021-00739-x>.
- (12) Hafemeister, D. Sustainable Energy—Without the Hot Air. *American Journal of Physics* **2010**, *78* (2), 222–223. <https://doi.org/10.1119/1.3273852>.
- (13) *Lithium mining: What you should know about the contentious issue*. <https://www.volkswagenag.com/en/news/stories/2020/03/lithium-mining-what-you-should-know-about-the-contentious-issue.html> (accessed 2022-05-04).

- (14) *Renewable Power Generation Costs in 2020*. /publications/2021/Jun/Renewable-Power-Costs-in-2020. <https://www.irena.org/publications/2021/Jun/Renewable-Power-Costs-in-2020> (accessed 2021-11-15).
- (15) *Electricity network economic regulatory framework review 2019*. AEMC. <https://www.aemc.gov.au/market-reviews-advice/electricity-network-economic-regulatory-framework-review-2019> (accessed 2020-01-31).
- (16) Jones-Albertus, R.; Feldman, D.; Fu, R.; Horowitz, K.; Woodhouse, M. Technology Advances Needed for Photovoltaics to Achieve Widespread Grid Price Parity. *Progress in Photovoltaics: Research and Applications* **2016**, *24* (9), 1272–1283. <https://doi.org/10.1002/pip.2755>.
- (17) Haegel, N. M.; Margolis, R.; Buonassisi, T.; Feldman, D.; Froitzheim, A.; Garabedian, R.; Green, M.; Glunz, S.; Henning, H.-M.; Holder, B.; Kaizuka, I.; Kroposki, B.; Matsubara, K.; Niki, S.; Sakurai, K.; Schindler, R. A.; Tumas, W.; Weber, E. R.; Wilson, G.; Woodhouse, M.; Kurtz, S. Terawatt-Scale Photovoltaics: Trajectories and Challenges. *Science* **2017**, *356* (6334), 141–143. <https://doi.org/10.1126/science.aal1288>.
- (18) *Speech by the President on carbon pricing*. European Commission - European Commission. [https://ec.europa.eu/commission/presscorner/detail/en/speech\\_21\\_5764](https://ec.europa.eu/commission/presscorner/detail/en/speech_21_5764) (accessed 2022-05-04).
- (19) Su, X.; Xu, J.; Liang, B.; Duan, H.; Hou, B.; Huang, Y. Catalytic Carbon Dioxide Hydrogenation to Methane: A Review of Recent Studies. *Journal of Energy Chemistry* **2016**, *25* (4), 553–565. <https://doi.org/10.1016/j.jechem.2016.03.009>.
- (20) Chen, X.; Chen, Y.; Song, C.; Ji, P.; Wang, N.; Wang, W.; Cui, L. Recent Advances in Supported Metal Catalysts and Oxide Catalysts for the Reverse Water-Gas Shift Reaction. *Frontiers in Chemistry* **2020**, *8*.
- (21) Jiang, X.; Nie, X.; Guo, X.; Song, C.; Chen, J. G. Recent Advances in Carbon Dioxide Hydrogenation to Methanol via Heterogeneous Catalysis. *Chem. Rev.* **2020**, *120* (15), 7984–8034. <https://doi.org/10.1021/acs.chemrev.9b00723>.
- (22) Future Swiss Energy Economy: The Challenge of Storing Renewable Energy. *Frontiers In Energy Research* **2022**. <https://doi.org/10.3389/ferng.2021.785908>.
- (23) Chapter 5.3.3 - Application of Hydrogen by Use of Chemical Reactions of Hydrogen and Carbon Dioxide. In *Science and Engineering of Hydrogen-Based Energy Technologies*; de Miranda, P. E. V., Ed.; Academic Press, 2019; pp 279–289. <https://doi.org/10.1016/B978-0-12-814251-6.00013-7>.
- (24) Maev, S.; Blinderman, M. S.; Gruber, G. P. 13 - Underground Coal Gasification (UCG) to Products: Designs, Efficiencies, and Economics. In *Underground Coal Gasification and Combustion*; Blinderman, M. S., Klimenko, A. Y., Eds.; Woodhead Publishing, 2018; pp 435–468. <https://doi.org/10.1016/B978-0-08-100313-8.00013-X>.

- (25) Züttel, A.; Remhof, A.; Borgschulte, A.; Friedrichs, O. Hydrogen: The Future Energy Carrier. *Philosophical Transactions of the Royal Society A: Mathematical, Physical and Engineering Sciences* **2010**, 368 (1923), 3329–3342. <https://doi.org/10.1098/rsta.2010.0113>.
- (26) Hori, Y.; Kikuchi, K.; Suzuki, S. Production of Co and CH<sub>4</sub> in Electrochemical Reduction of CO<sub>2</sub> at Metal Electrodes in Aqueous Hydrogencarbonate Solution. *Chem. Lett.* **1985**, 14 (11), 1695–1698. <https://doi.org/10.1246/cl.1985.1695>.
- (27) Hori, Y.; Murata, A.; Takahashi, R.; Suzuki, S. Electroreduction of Carbon Monoxide to Methane and Ethylene at a Copper Electrode in Aqueous Solutions at Ambient Temperature and Pressure. *J. Am. Chem. Soc.* **1987**, 109 (16), 5022–5023. <https://doi.org/10.1021/ja00250a044>.
- (28) *Progress and Perspectives of Electrochemical CO<sub>2</sub> Reduction on Copper in Aqueous Electrolyte | Chemical Reviews*. <https://pubs.acs.org/doi/10.1021/acs.chemrev.8b00705> (accessed 2020-02-29).
- (29) Yu, J.; Wang, J.; Ma, Y.; Zhou, J.; Wang, Y.; Lu, P.; Yin, J.; Ye, R.; Zhu, Z.; Fan, Z. Recent Progresses in Electrochemical Carbon Dioxide Reduction on Copper-Based Catalysts toward Multicarbon Products. *Advanced Functional Materials* **2021**, 31 (37), 2102151. <https://doi.org/10.1002/adfm.202102151>.
- (30) Liu, J.; Cai, Y.; Song, R.; Ding, S.; Lyu, Z.; Chang, Y.-C.; Tian, H.; Zhang, X.; Du, D.; Zhu, W.; Zhou, Y.; Lin, Y. Recent Progress on Single-Atom Catalysts for CO<sub>2</sub> Electroreduction. *Materials Today* **2021**. <https://doi.org/10.1016/j.mattod.2021.02.005>.
- (31) Gallandat, N.; Romanowicz, K.; Züttel, A. An Analytical Model for the Electrolyser Performance Derived from Materials Parameters. *Journal of Power and Energy Engineering* **2017**, 5 (10), 34–49. <https://doi.org/10.4236/jpee.2017.510003>.
- (32) Zhang, J.; Luo, W.; Züttel, A. Crossover of Liquid Products from Electrochemical CO<sub>2</sub> Reduction through Gas Diffusion Electrode and Anion Exchange Membrane. *Journal of Catalysis* **2020**, 385, 140–145. <https://doi.org/10.1016/j.jcat.2020.03.013>.



## Chapter 2: Introduction

# Metal catalysts in different size regimes for CO<sub>2</sub> electroreduction

**Post print version:** this section has been published as a full-length review in *ACS Catal.* **2023**, 13, 2, 948–973

**Edit:** caption numbers of figures, tables, and equations were edited to match the thesis chapter number.

**Permission to reproduce:** reproduced with permission from the publisher.

**Cedric David Koolen,<sup>a,b</sup> Wen Luo<sup>c\*</sup>, Andreas Züttel<sup>a,b</sup>**

<sup>a</sup>Laboratory of Materials for Renewable Energy (LMER), Institute of Chemical Sciences and Engineering (ISIC), Basic Science Faculty (SB), École polytechnique fédérale de Lausanne (EPFL) Valais/Wallis, Energypolis, Sion, 1951, Switzerland.

<sup>b</sup>Empa Materials Science & Technology, Dübendorf, 8600, Switzerland.

<sup>c</sup>School of Environmental and Chemical Engineering, Shanghai University, Shanghai, 200444, China.

\*Corresponding author: wenluo@shu.edu.cn

### Keywords

CO<sub>2</sub> electrochemical reduction, metal catalysts, review, size, reaction mechanism

## Abstract

With the electrochemical CO<sub>2</sub> reduction reaction (CO<sub>2</sub>RR), CO<sub>2</sub> can be used as a feedstock to produce value-added chemicals and fuels whilst storing renewable energy. For its enormous potential, an extensive research effort has been launched to find the most active electrocatalyst. The reduction of catalyst size has been tested and proven as a key approach to increase the activity of CO<sub>2</sub>RR whilst reducing capital cost. However, the catalytic selectivity is not linearly related to the catalyst size due to the influence of many other structural factors. Thus, in-depth knowledge of structure-performance relationships of metals catalysts with different sizes aid in designing efficient electrocatalysts for CO<sub>2</sub>RR. This review surveys three decades worth of research on CO<sub>2</sub>RR and categorizes various metal catalysts into four size regimes, namely bulk materials in the form of single-crystals, nanoparticles, clusters, and single-atom catalysts. The effect of different structural factors, including crystal facet, coordination environment, and metal-support interactions etc. are discussed for metal catalysts in each size regime. Finally, general conclusions are provided with perspectives on future directions for better understanding and further development of active and selective catalysts for CO<sub>2</sub>RR.

## 2.1. Introduction

Since the rapid industrialization of the 19<sup>th</sup> century, the world energy demand has shown exponential growth, which in large has been met by the consumption of fossil fuels.<sup>1</sup> The associated emission of various greenhouse gases such as CO<sub>2</sub> have led to the steady increase of the global average temperature inducing climate change.<sup>2,3</sup> In the last 200 years, global atmospheric concentrations of CO<sub>2</sub> have risen from 280 ppm to over 400 ppm, and the global temperature has increased by more than 1 °C. In their latest report, the International Panel for Climate Change (IPCC) issued its starkest warning yet.<sup>4</sup> If emissions are not cut drastically within the decade, rising sea levels and extreme weather events, amongst others, will no longer be an anomaly. Facing the energy and environmental crisis, countries, including developed and developing ones, are now shifting their energy mix from fossil fuels towards renewable energies, such as hydro-power, solar energy and wind energy etc. In the last 10 years, the installed capacity of solar and wind generated

electricity has increased ~17- and ~4-fold, respectively, and price is projected to drop as low as 0.03 USD·kWh<sup>-1</sup> in the near future.<sup>5</sup> However, compared to fossil fuels, the energy density of renewables is much lower and the availability is often intermittent. In the past decade, the electrochemical CO<sub>2</sub> reduction reaction (CO<sub>2</sub>RR) has emerged as a promising solution in tackling the above-mentioned issues. By bringing CO<sub>2</sub>RR to scale, in which CO<sub>2</sub> is converted into fuels and chemicals using renewable electricity, net zero emissions are within reach and low density renewable energy can be stored at high capacity in chemical bonds.<sup>6</sup> With its major products including drop-in fuels and base-chemicals such as C<sub>2</sub>H<sub>5</sub>OH, C<sub>2</sub>H<sub>4</sub> and CH<sub>4</sub> (**Figure 5.**), its industrial potential is enormous.<sup>7</sup>

Although promising, several significant challenges remain before this technology can become economically competitive. First, despite that CO<sub>2</sub>RR is thermodynamically feasible (**Table S1**), large kinetic barriers exist in the activation of CO<sub>2</sub> and the following reaction intermediates, resulting in high overpotentials (the potential needed on top of the equilibrium potential for the reaction to take place) and low energy efficiency.<sup>9,10,11</sup> In addition, in aqueous solutions, the hydrogen evolution reaction (HER) is in competition with CO<sub>2</sub>RR, which decreases the faradaic efficiencies for

CO<sub>2</sub>RR products (see **Note S1** for a list of equilibrium potentials of CO<sub>2</sub>RR products and other relevant reactions). Further, up to 16 products have been produced from CO<sub>2</sub>RR, resulting in low selectivity towards certain products, especially multi-carbon products.<sup>12,13</sup> Therefore, the design of advanced electrocatalysts is needed to activate the CO<sub>2</sub> molecule and accelerate the desired reaction pathways for an increased conversion rate and product selectivity.

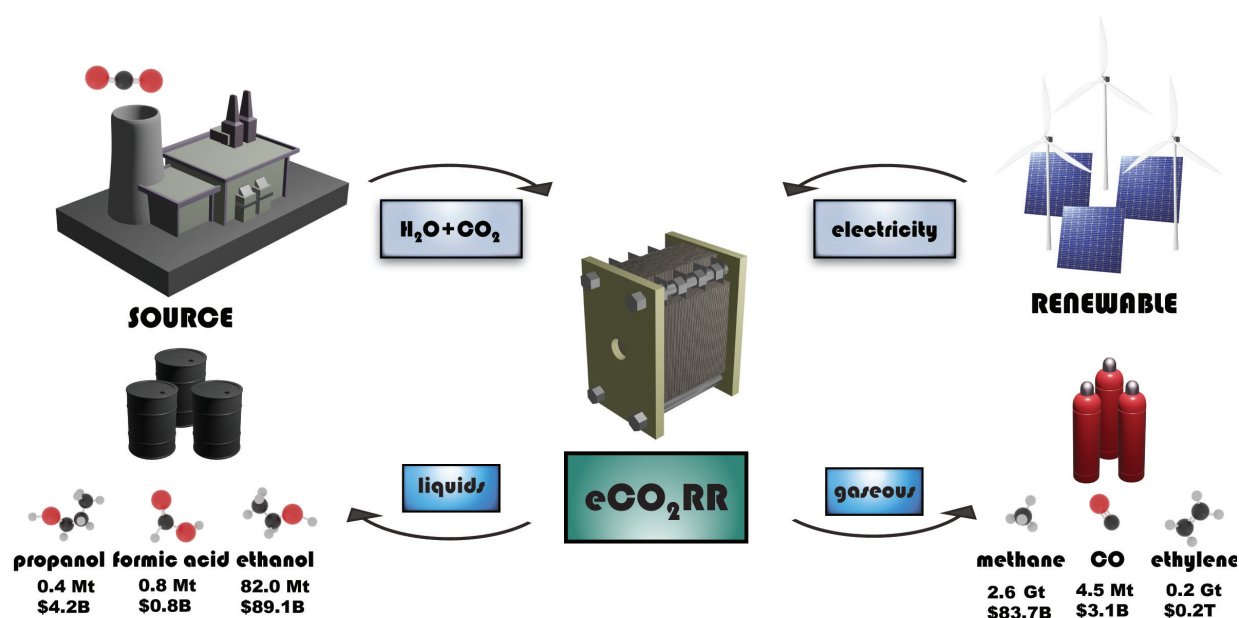


**Figure 5.** Electrochemical CO<sub>2</sub> reduction reaction. The schematic shows the conversion of CO<sub>2</sub> and water using renewable electricity to produce various gaseous and liquid products of the CO<sub>2</sub>RR with the current market size and value. Mt = megaton; Gt = gigaton; B = billion, M = million. Note that formate (HCOO<sup>-</sup>) is the direct reduction product of CO<sub>2</sub>RR when neutral or basic electrolyte is used, and thus further conversion is needed to yield formic acid.<sup>8</sup>



Over the past three decades, various types of materials, such as metals, oxides, and carbon-based materials have been used for CO<sub>2</sub>RR.<sup>10,14,15,16,17</sup> Of which, a comprehensive body of work has been dedicated to metal catalysts for CO<sub>2</sub>RR.<sup>18,19,20,21,22,23,24,13,25,26,27,28,29,30,31,32,33,34,35,36,37,38,39,40,41,42,43,44,45</sup>

Among them, one of the most important contributions came from Hori and co-workers. Based on systematic studies using bulk single-crystal and polycrystalline electrodes, metal catalysts were classified into four groups based on their selectivity: HCOO<sup>-</sup> selective metals (e.g., Pb, Hg, Tl, In, Sn, Cd, and Bi), CO selective metals (e.g., Au, Ag, Zn, Pd, and Ga), H<sub>2</sub> selective metals (e.g., Ni, Fe, Pt, and Ti), and Cu, which is selective for a number of hydrocarbons and oxygenates.<sup>6,18,19,20,21,22,23,24,46</sup> Guided by this early classification, researchers have searched for catalysts with better activity and selectivity ever since. An elegant attempt has been to reduce catalyst size to retain or improve selectivity but increase the gravimetric active site density (mass activity) thereby improving upon atom economy (active sites per catalyst mass). With the

development of synthesis methods, i.e., in colloidal chemistry, dip-pen nanolithography and pyrolysis,<sup>47,48,49,50,51,52</sup> ever more precise catalyst have been produced. For example, nanoparticles of Au, Ag, Pd, and Cu etc. have been synthesized with sizes ranging from several hundreds of nanometers down to a single nanometer, showing significant performance improvements in CO<sub>2</sub>RR.<sup>31,35,36,37,44,40,53</sup> Recently, catalysts with sizes beyond the nanometer regime, such as clusters (< 1 nm) and single-atom catalysts on conductive supports (SACs, with maximum atom utilization), have also been designed and applied for CO<sub>2</sub>RR with superior catalytic activity.<sup>54,55</sup> These recent studies show, however, that not only the activity, but also the product selectivity may vary with decreasing catalyst dimensions. For example, while bulk Ni is not selective for CO<sub>2</sub>RR due to its high HER activity, Ni SACs are proven to be highly selective for the conversion CO<sub>2</sub> to CO.<sup>56,57</sup> This is not entirely unexpected however, as the electronic properties of the metal particles change significantly at sub-nanometer range, and in the case of Ni, its single atom

form can have oxidation states of  $\text{Ni}^+$  and  $\text{Ni}^{2+}$  (Figure 6).<sup>58,59</sup> Indeed, the distinct catalytic performance of nanoparticles in different size ranges for several important thermal reactions have been systematically

studied and thoroughly discussed.<sup>60,61</sup> However, a comprehensive review of how metal catalysts in different sizes catalyze  $\text{CO}_2\text{RR}$  is still missing.

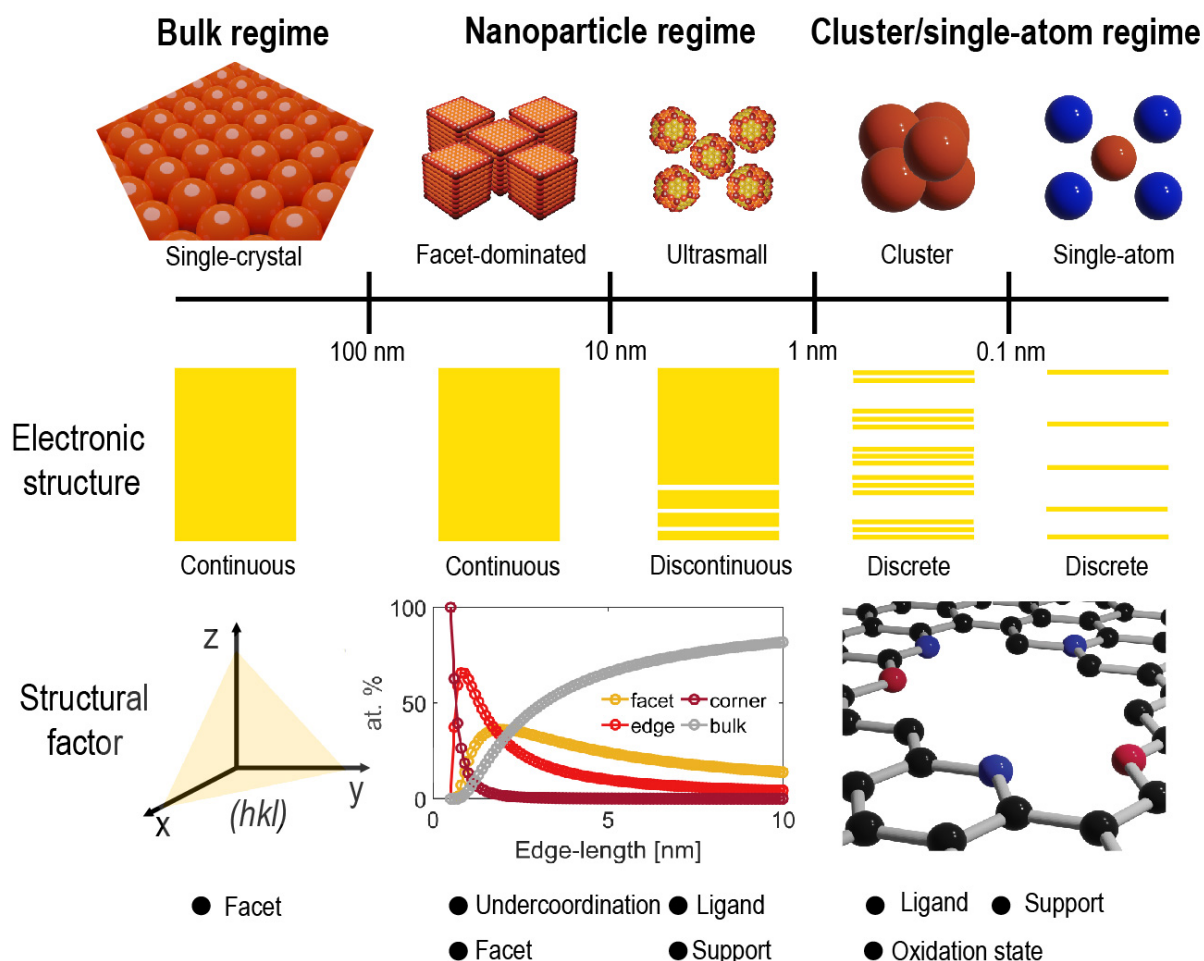


**Figure 6.** Classification of metal catalysts for  $\text{CO}_2\text{RR}$  based on the particle size. With the decrease of the catalyst size, the electronic structure changes, and different structural factors can be used to describe the reactivity.

Revealing a complete catalytic mechanism for CO<sub>2</sub>RR is extremely challenging due to the various material properties and diverse mechanistic steps involved.<sup>10</sup> Thus, most studies have simplified this task and instead tried to find key descriptors to predict the activity of the catalysts or to explain the observed results. Nørskov and co-workers performed pioneering work herein based on density functional theory (DFT) calculations, where the adsorption energies of \*COOH, \*CO, and \*OH were identified as key descriptors.<sup>62,63,64,65</sup> Although the adsorption energy of different intermediates on a model surface can be determined via vacuum techniques (e.g., temperature programmed desorption and XPS), it is still challenging to identify the reaction intermediates and quantify their adsorption energies on a real catalytic surface during the electrochemical process. Thus, experimentalists have tried to tie the catalytic performance to the structural properties of catalysts instead, including crystal facet, coordination environment, and metal-support interactions etc.<sup>44,66,45</sup> For example, the CO<sub>2</sub>RR selectivity can be dramatically affected by the facet

orientation of bulk Cu: whereas the Cu(111) facet is more selective for CH<sub>4</sub>, Cu(100) favors C<sub>2</sub>H<sub>4</sub> production.<sup>18,23,46,44</sup> As another example, CO<sub>2</sub>RR activity has been found to be closely related to the grain boundary density of Au and Cu.<sup>67,68,69</sup> Yet, it is worth noting that with the decrease of particle size, the structural properties of the catalyst vary (**Figure 6**), which in turn changes the CO<sub>2</sub>RR performance. Also, we note the importance of accurate electrochemical active surface area (ECSA) determination to exclude surface area effects with decreasing particle size to thoroughly and unequivocally study the intrinsic activity of metal catalysts.<sup>10</sup>

To better understand the catalytic behavior of metal catalysts in CO<sub>2</sub>RR, we propose a new classification system based on the size of the catalyst as the key structural factors change with catalyst dimension (**Figure 6**): (i) the bulk regime, exemplified by single-crystals (i.e., sizes >100 nm), (ii) the nanoparticle regime, subdivided into large nanoparticles (i.e. 10 nm < sizes ≤100 nm) and ultrasmall particles (i.e., 1 nm < sizes ≤10 nm), (iii) the cluster regime (sizes

≤1nm.), and (iv) the single-atom regime. To cover all structural properties of metal catalysts in all size regimes is neither possible nor advisable. Instead, we have selected for experimentally accessible factors that dominate the reaction kinetics of CO<sub>2</sub>RR, including the element, crystal-facet, the coordination number, the ligand effect, the metal-support interaction, and the coordination environment (**Figure 6**). Where appropriate, we have extended on our discussion of structural factors to include computational activity descriptors. **Figure 7** provides an overview of the studies reported in the literature, in which the majority product of CO<sub>2</sub>RR (and HER)

is related to the element(s) of the metal catalysts and the size-class. In the following chapters, we will use ample representative examples to show how structural properties influence the catalytic performance and moreover, change with decreasing catalyst dimensions. Finally, we will present a general conclusion and an outlook on the challenges and opportunities in catalyst selection and screening in CO<sub>2</sub>RR. We hope this review will provide the reader with insights on improving the selectivity of CO<sub>2</sub>RR over HER, the selectivity towards specific CO<sub>2</sub>RR products, the overall catalytic activity and atom economy.

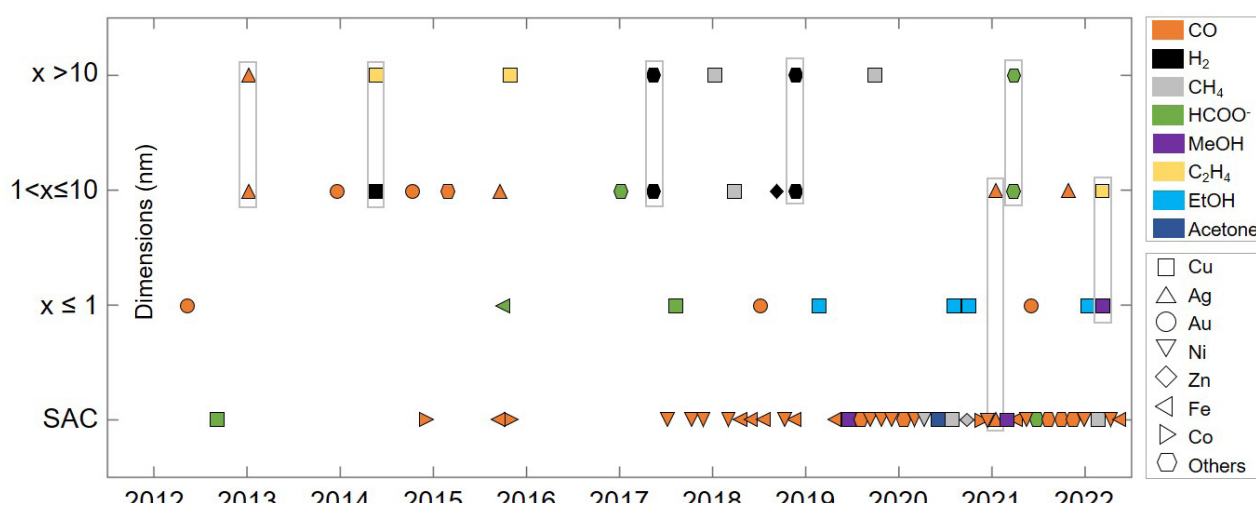


**Figure 7.** The most common products of CO<sub>2</sub>RR for typical metal catalysts in different size regimes: single-crystal and facet dominated nanoparticle ( $>10$  nm), ultra-small particle ( $1 < x \leq 10$  nm), cluster ( $\leq 1$  nm), and SAC. The metal utilized to obtain the results is indicated by shape, and the product is indicated by color. The ‘others’ series includes Cu alloys and other metals. Each point represents a published study, where studies covering different size regimes are included in the gray box. For a list of the publications, see **Note S2** of the Supporting Information. Note that publications in **Figure 7** have been selected for their investigation of metal catalysts of different sizes using the same synthesis technique. Further, to highlight the differing performance of metal catalysts versus their SAC counterparts, we have included a selection of those as well.

## 2.2. Bulk regime: single-crystal electrodes

In bulk systems, polycrystalline metal foils are often used as reference samples and are therefore, the most widely used electrodes for CO<sub>2</sub>RR. However, it is difficult to gain mechanistic insights with such crudely defined catalysts. Various types of facets, steps, and defects collectively contribute to the activity, which cannot be deconvoluted. Single-crystals, on the other hand, are of preferential orientation, and can thus be used to study the relationship between CO<sub>2</sub>RR performance and crystal facet.<sup>6,18,19,20,21,22,23,24,46</sup> Single-crystals can be prepared by different methods. For example, they can be manufactured through controlled cooling from a liquid phase, which are then cut and polished with respect to a specific crystallographic orientation. Alternatively, single-crystal thin films can be prepared via epitaxial growth on other single-crystal surfaces (e.g., Si wafers) with the same crystallographic

orientations.<sup>28</sup> Characterization of their bulk crystal orientation can be achieved via X-ray diffraction (XRD), while the atomic surface structure can be examined by the reversible adsorption of probing ions (e.g., Cl<sup>-</sup> and OH<sup>-</sup>) using cyclic voltammetry.<sup>28</sup> A number of single-crystal electrodes have been prepared and used for CO<sub>2</sub>RR. Among them, face centered cubic metals (FCC, such as Cu, Pd, Au, and Ag) are most frequently studied. This includes low-index *hkl* surfaces, such as (100), (111), and (110) planes, as well as higher-ordered *hkl* planes, which have various degrees of undercoordination. Based on these studies, important insights about the CO<sub>2</sub>RR mechanism have been gained. In the following, the effect of crystal structure will be discussed in detail starting with non-Cu based transition metals, followed by Cu-based low and high-index *hkl* surfaces.

## 2.2.1. Non-Cu-based single crystals

In the last 90s, Hori and co-workers carried out a series of studies on CO<sub>2</sub>RR using metal single-crystals including Pt group metals (Pt, Ir, Rh, and Pd) and Ag to reveal the relation between the atomic arrangement and the catalytic activity. For example, a remarkable activity dependence was observed for Pd single-crystals, i.e., (110)>(111)>(100), with the (110) stepped-surface reaching a 3-fold enhanced rate over the (111) surface at the same potential (-1.0 V vs RHE).<sup>20</sup> Similarly, the (110) plane of Ag also showed the highest activity, showing a 5-fold higher partial current density for CO versus the (111) surface and with the (100) plane the least active (-1.44 V vs. SHE).<sup>22</sup> Much later, the high activity of stepped surface facets was further verified by extended experimental studies congruently with DFT.<sup>27</sup> The high activity of Ag(110), for example, is attributed to its binding of the key intermediate \*COOH and an enhanced electric field stabilization on undercoordinated surface atoms of step sites. The same conclusions were also reached on another CO selective catalyst, Au and Zn. The stepped Au surfaces (e.g.,

Au(211) and Au(110)) better stabilize the \*COOH intermediate than the Au(100) and Au(111) facets and are thus more active. The enhanced activity has been shown to be at least a factor of 20 for undercoordinated Au i.e. Au(110) and steps of Au(211) versus Au(100) by Chorkendorff and co-workers.<sup>70</sup> Similarly, the \*COOH intermediate binding strength inversely scales with the coordination number of Zn surfaces explaining faster CO evolution on undercoordinated Zn.<sup>71</sup> Note that strong evidence exists that for the production of CO on Au and Ag, the rate limiting step is the formation of \*CO<sub>2</sub><sup>-</sup> and that the proton-electron transfer to form \*COOH is actually decoupled.<sup>72</sup> However, modelling a decoupled proton-electron transfer step is challenging and since the following formation of \*COOH from \*CO<sub>2</sub><sup>-</sup> is anyhow a non-electrochemical step and fast, \*COOH is often used as a descriptor to predict relative rates instead.<sup>73</sup>

The above studies on non-Cu-based single-crystals indicate that although the catalytic activity of CO<sub>2</sub>RR is facet-dependent, the selectivity towards CO<sub>2</sub>RR products is less sensitive to the crystal orientation. This is due to the fact that these metals typically reduce CO<sub>2</sub> to CO (or HCOO<sup>-</sup> as a minor product), which involve only a 2e<sup>-</sup> transfer and a limited number of intermediates (e.g., \*COOH and \*OCHO), and that changes in the surface atomic arrangement and thus adsorption energies are not large enough to switch between pathways but do influence the specific rates.<sup>74</sup> Instead, Cu surfaces can bind a multitude of intermediates (e.g., \*COOH, \*OCHO, \*CO, \*CHO, and \*COH etc.) with comparable strength, making it especially sensitive to the facet orientation, as we will see in the following sections.



## 2.2.2. Low index Cu single crystals

As mentioned in the introduction, Cu is the sole metal to produce any meaningful currents towards multi-carbon products. This was first quantitatively presented by Hori and co-workers in their seminal works on CO<sub>2</sub>RR on polycrystalline Cu.<sup>6,18,62</sup> To reveal the unique properties of Cu, fundamental studies using low index Cu single-crystals followed.<sup>23,13,75</sup> Hori and co-workers found that the selectivity of CO<sub>2</sub>RR is highly sensitive to the crystal facet of Cu. Specifically, Cu(100) produced C<sub>2</sub>H<sub>4</sub> most selectively (FE of 31.7 % at -1.44 V vs. NHE and 1.6 mA cm<sup>-2</sup>), Cu(111) produced CH<sub>4</sub> predominantly (21.8% at -1.41 V vs. NHE and 1.1 mA cm<sup>-2</sup>),<sup>65</sup> and Cu(110) showed a mixed product distribution with CH<sub>4</sub> and C<sub>2</sub>H<sub>4</sub> FEs of 23.3% and 18.9% (-1.35 V vs. NHE and 0.9 mA cm<sup>-2</sup>), respectively. Note that these experiments were performed at a constant current with relatively long reaction times, thus detailed information on the origin of the facet-dependent selectivity is missing.

Much later, Koper and co-workers gave insightful explanations through experimental and theoretical methods based on a series of studies on CORR (CO is the key intermediate to C<sub>2+</sub> products).<sup>76,77</sup>

Using non-quantitative time-resolved online electrochemical mass spectrometry (OLEMS), they observed two distinctive pathways for the formation of C<sub>2</sub>H<sub>4</sub> (**Figure 8**). One, which is catalyzed on both Cu(100) and Cu(111), where the rates differ not too strongly and occurs at high-overpotential (**Figure 8a,b**). The other, occurs at much lower overpotential and is only observed on the Cu(100) surface (**Figure 8a**). They proposed that the rate-determining step in the latter involves a chemisorbed CO dimer (i.e., \*C<sub>2</sub>O<sub>2</sub>). Instead, in the former, an intermediate is shared with the reaction pathway for CH<sub>4</sub> (most likely via CHO\*). These assumptions were later supported by their DFT calculations and *in situ* Fourier transform infrared spectroscopy (FTIR) results.<sup>78,77</sup> And the unique ability of Cu(100) for reducing CO to C<sub>2</sub>H<sub>4</sub> at low overpotential was attributed to two factors. First, square-like sites on Cu(100) allow for suitable conformation of \*C<sub>2</sub>O<sub>2</sub>, and second, sites formed by four atoms donate more charges to facilitate the C–C coupling than sites of hexagonal-symmetry formed by three atoms.<sup>79</sup>

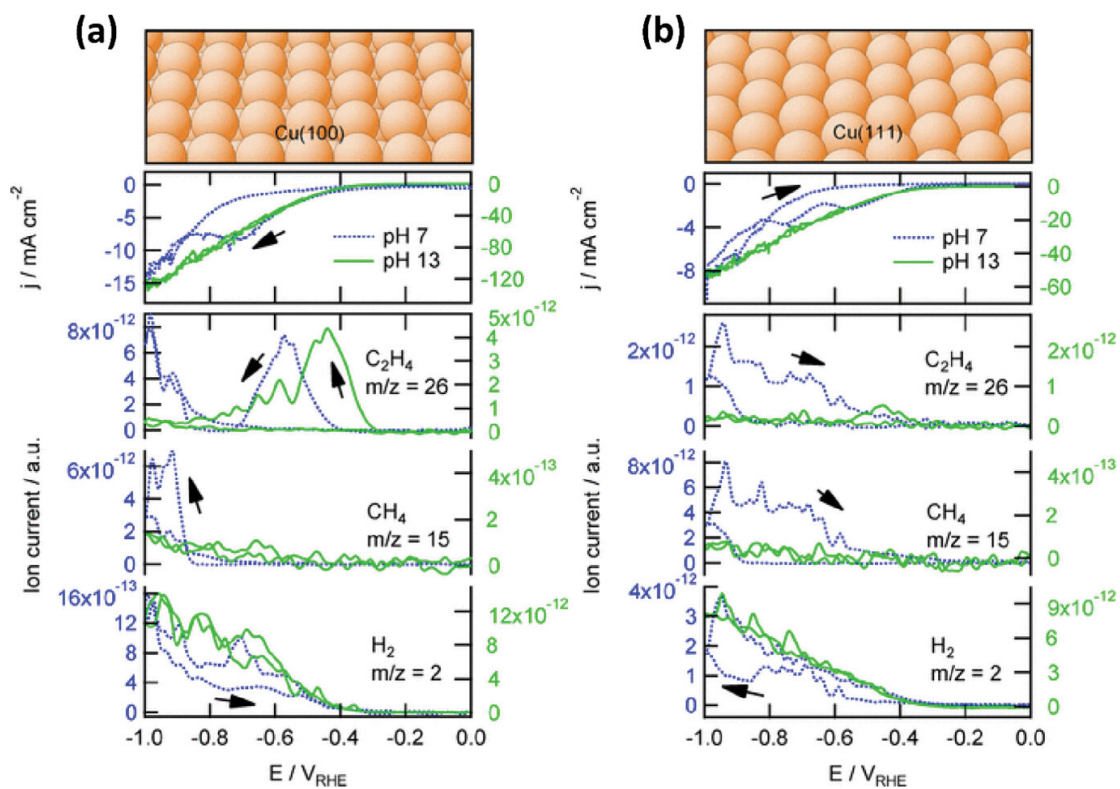


**Figure 8.** OLEMS data of CORR of **(a)** Cu(100) and **(b)** Cu(111) single-crystals in neutral (blue,  $\text{KH}_2\text{PO}_4$  pH=7) and basic conditions (green,  $\text{NaOH}$  pH = 13) reproduced from ref. <sup>76</sup>. Copyright 2012, American Chemical Society. Both the total current as well as the ion specific current are provided. Note the roughly 200 mV earlier onset potential of  $\text{C}_2\text{H}_4$  on Cu(100) vs Cu(111) as well as the 200 mV shift towards the equilibrium potential when switching electrolyte on Cu(100).

### 2.2.3. High index Cu single crystals

Apart from low-index Cu single-crystals, Hori and co-workers further prepared high-index Cu single-crystals for CO<sub>2</sub>RR to investigate the influence of undercoordinated sites on the product distribution.<sup>13</sup> These crystals consisted of  $n$  atomic rows of (100) terraces and one atomic height of (111) or (110) steps, namely Cu(S)-[ $n(100) \times (111)$ ] and Cu(S)-[ $n(100) \times (110)$ ], respectively. They found that introduction of (111) steps to a Cu(100) basal plane can dramatically enhance the C<sub>2</sub>H<sub>4</sub> selectivity and suppress the production of CH<sub>4</sub> (**Figure 9**). The Cu(711) surface ( $n = 4$ ) showed the highest selectivity for C<sub>2</sub>H<sub>4</sub> (FE 58.5% at -1.37 V vs. SHE and 2.9 mA cm<sup>-2</sup>) and the highest ratio of C<sub>2</sub>H<sub>4</sub>/CH<sub>4</sub> (~8.5).<sup>23,24,13</sup> Interestingly, the introduction of (110) steps into (100) terraces, also promoted C<sub>2</sub>H<sub>4</sub> formation and suppressed CH<sub>4</sub>. Additionally, it was shown that by increasing the step-density of Cu(S)-[ $n(111) \times (111)$ ] surfaces an increased selectivity to oxygenates followed (H<sub>3</sub>CCOO<sup>-</sup>, H<sub>3</sub>CCHO and C<sub>2</sub>H<sub>5</sub>OH, **Figure 9**).<sup>13</sup> The Cu(110) surface, with the Cu(S)-[ $2(111) \times (111)$ ] orientation, showed the best H<sub>3</sub>CCOO<sup>-</sup> FE well over 20% (-1.6 V vs. SHE and 1.0 mA cm<sup>-2</sup>). The Cu(S)-[ $n(100) \times (110)$ ]

electrodes showed the inverse trend with respect to H<sub>3</sub>CCOO<sup>-</sup> formation (**Figure 9**). These results indicate that stepped facets on the Cu surface can improve the selectivity to multi-carbon products compared to the planar single crystals. Later on, stepped surfaces such as Cu (211) facet have also been computationally determined to be more active in comparison to flat surfaces (similar to that of Ag and Au).<sup>64,27</sup>

Based on the reported results, a relatively clear performance trend can be distinguished in CO<sub>2</sub>RR on Cu single-crystals (**Figure 9**). Cu(111) surface is selective for CH<sub>4</sub> and portrays a limited rate towards C-C coupling, especially at low overpotential. The Cu(100) surface, in turn, shows especially strong C-C coupling reactivity, with the main product being C<sub>2</sub>H<sub>4</sub>. Introduction of (111) or (110) step sites further enhances the C-C coupling rate. Cu(110) shows mixed selectivity towards hydrocarbons, but does

show a clear trend in the production of oxygenates: the higher the number of (111) steps on (111) terraces, the higher the oxygenate production rates. Interestingly, in a recent publication by Cuenya and co-workers, pristine Cu(111) and Cu(100) surfaces produced via UHV techniques showed no meaningful activity for CO<sub>2</sub>RR.<sup>29</sup> The majority of the current (80%) went towards HER instead. Hydrocarbons only became the majority product after the introduction of defects. Also, significant restructuring under the applied potential was observed. Even though defects in Cu single crystals have both experimentally and computationally been shown to improve CO<sub>2</sub>RR to hydrocarbons,<sup>80,81,82,83</sup> the inactivity of the clean Cu(100) and Cu(111) as well as the significant restructuring of the catalyst under operation is a non-trivial result. It begs the question, if single crystals in general, under applied potential and *in operando*, reconstruct. Therefore, the use of single-crystals for CO<sub>2</sub>RR mechanistic studies should be further investigated and validated in combination with operando techniques to monitor the catalytic surface in real time.

To conclude, the crystal orientation of metals greatly affects the binding energy to the reactants, i.e., CO<sub>2</sub> and H<sub>2</sub>O, and various intermediates, e.g., \*CO, \*H, and \*COOH etc., thus affecting both catalytic activity and the selectivity in CO<sub>2</sub>RR. Despite those different metals (e.g., Pt, Ag, Au and Cu etc.) show distinct product distributions in CO<sub>2</sub>RR, stepped-surfaces of these metals are generally more active than planar surfaces. Although inducing changes to adsorbate binding energies, crystal facets of most metals (e.g., Pt, Ag and Au) do not change their inherent selectivity for specific products. Cu is the sole exemption i.e., Cu(111) is CH<sub>4</sub> selective, Cu(100) is C<sub>2</sub>H<sub>4</sub> selective and Cu(110) shows a mixed selectivity but enhanced production of oxygenates such as C<sub>2</sub>H<sub>5</sub>OH and H<sub>3</sub>CCOO<sup>-</sup>. Finally, single-crystals, due to their large surface energy, may reconstruct under operation possibly making them proto-catalysts.

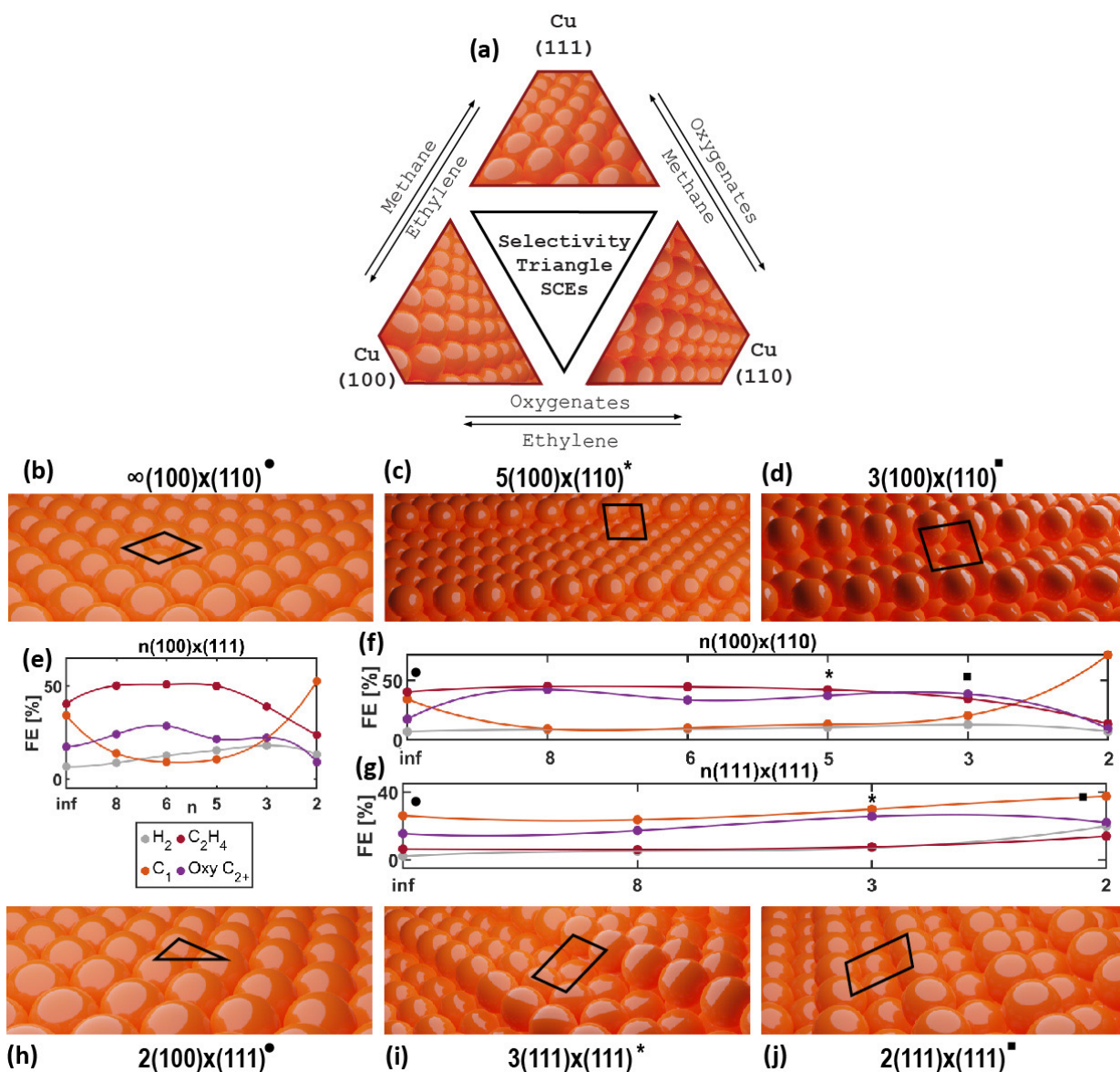


**Figure 9.** (a) The selectivity triangle of Cu single-crystal electrode in the  $CO_2RR$  summarizing data reported by Hori and co-workers and Koper and co-workers.<sup>13,23,24,76,84</sup> (b-d) Cu(100), Cu 5(100)x(110) and Cu 3(100)x(110). (e-f) Selectivity for  $H_2$ ,  $C_1$  products,  $C_2H_4$  and  $C_{2+}$ , oxygenates on a Cu(100) surface with increasing (111) and (110) step-density. (g) Selectivity on a Cu(111) surface with increasing (111) step-density. (h-j) Cu(111), Cu 3(111)x(111) and Cu(110). Circle, star and square in (b-d) correspond to (f) and in (h-j) to (g). Black inset denotes the proposed active site for the majority product.<sup>85</sup> Note that the electrochemical performances were reported at the most selective potential ( $\Delta U \sim 200$  mV). All reactions were carried out in 0.1 M  $KHCO_3$  at  $5$  mA  $cm^{-2}$ .

## 2.3. Nanoparticle catalysts

### 2.3.1. Nanoparticles: facet dominated regime

With a well-defined surface structure, single-crystals are excellent systems to understand the CO<sub>2</sub>RR mechanism. However, due to their low surface area, and thus poor atom economy, their potential is limited in real-world applications. To improve this, nanocrystals that expose specific facets but with a higher degree of surface atom density have been synthesized and used for CO<sub>2</sub>RR. For example, as an FCC metal, Cu nanocrystals can be prepared with a cubic shape exposing (100) facet and a tetrahedral shape exposing (111) facets. However, with the decrease of catalyst size from extended surface to nanoparticles, other factors besides the crystal facet begin to play a role (or even a dominant role) in the catalytic reaction. For instance, the increased number of low coordinated atoms (**Figure 10**), the interactions between

NPs and support materials, and the organic ligands used in synthesis, etc. In this section, we will summarize some representative examples that use NPs larger than 10 nm, of which the facet still dominates the surface and, thus the reactivity. We lay emphasize on examples that include particles in a size range produced with the same method to deconvolute contributing factors. Through this section, we can better understand the synergistic effect of crystal facet, edge and corner on the catalytic performance, as well as other key factors that influence the reactivity.

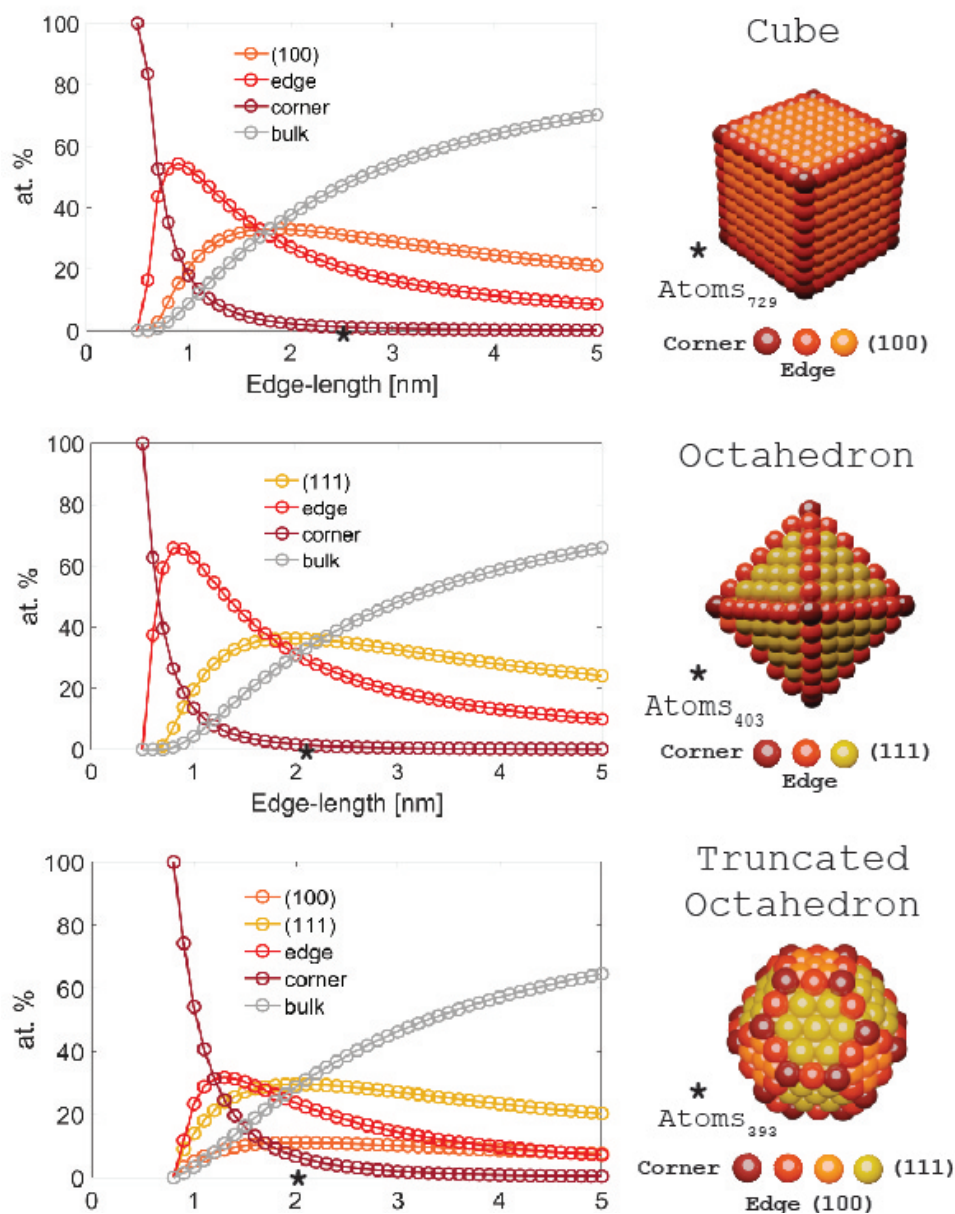


**Figure 10.** Evolution of the relative contribution of the surface atoms (denoted as corner (in rust-brown), edge (in red), and facet ((111) in yellow and (100) in orange)) versus the bulk atoms (in grey) as a function of the particle edge-length, spanning three different geometries: cubic, octahedral and truncated octahedral. The asterisk in each figure indicates the edge-length of the particle depicted by the corresponding ball-model. For particles >5nm, independent of the geometry, the major contribution to the surface atoms is from the facets. The in-house developed geometrical model is based on the definition of various subsurfaces, see **Note S3** of the Supporting Information.<sup>86</sup>

Motivated by the work on single-crystals, a few research groups have synthesized Cu NPs that expose certain facets for CO<sub>2</sub>RR. Buonsanti and co-workers prepared Cu octahedra particles that expose predominately (111) facets (75, 150 and 310 nm) for CO<sub>2</sub>RR (**Figure 11a-c**).<sup>87</sup> In agreement with the results obtained from single crystals (**Figure 10**), these particles are CH<sub>4</sub> selective. In addition, both the CO<sub>2</sub>RR partial current density and the CH<sub>4</sub> selectivity increased with the decrease of particle size (**Figure 11h**). Alternatively, the same group used a different colloidal synthesis to yield (100) faceted Cu cubes of various sizes (24, 44 and 62 nm edge-length) (**Figure 11d-f**). However, they found that the 44 nm particles, not the smallest one, showed the highest C<sub>2</sub>H<sub>4</sub> selectivity, with an FE of 42% at -1.1V vs. RHE and 2.3 mA cm<sup>-2</sup> (**Figure 11g**). Here, the authors argue that an optimal ratio of edge-sites over (100) facet-sites for the 44 nm Cu cube particle is key for the high C<sub>2</sub>H<sub>4</sub> selectivity. Later, in collaboration with theoreticians, the same group explained these results through DFT simulations: the C-C coupling step does not take place through the CO-CO dimerization mechanism typical of the Cu(100) facet, but exploits through the COH-CO coupling at the interfaces of the terraces and the

edges.<sup>88</sup> The notion that edges improve C<sub>2</sub>H<sub>4</sub> selectivity is in agreement with that observed by Hori and co-workers on high-index Cu single-crystals, as cube edges are chemically equivalent to Cu(110) steps (i.e., coordination number of 7). Notably, this mechanism does not explain why 44 nm particles exhibited the best C<sub>2</sub>H<sub>4</sub> selectivity, as smaller particles (24 nm) have higher numbers of interfacial sites at the same catalyst loading. It is speculated that the *in operando* restructuring of the Cu NPs may instead have contributed to the poor performance of the smallest particle.<sup>89,90</sup> Indeed, with operando electrochemical atomic force microscopy (ECAFM), Cuenya and co-workers have observed morphology changes of Cu nanocubes during CO<sub>2</sub>RR.<sup>45</sup> Similarly, Buonsanti and co-workers performed ex situ TEM analysis of three different sized Cu nanocubes (16 nm, 41 nm, and 65 nm) and found that the cubic structure became ill-defined during CO<sub>2</sub>RR and the CO<sub>2</sub>RR activity decreased.<sup>91</sup> Both studies concluded that smaller Cu nanocubes suffer from faster morphology changes, and more importantly, degradation immediately starts at the edges where C-C coupling is argued to take place. Therefore, these results indicate that it is still worthwhile to conduct more controlled



studies to understand the synergistic effects of different facets. Further, it is important to note the challenges involved in normalization of the ECSA. Roughness factors can have tremendous influence on the current densities and techniques to determine it vary widely.<sup>10</sup> Therefore, the effect of the enhanced surface area by particle size reduction are far from excluded in this size-regime.

Another important factor that can affect the CO<sub>2</sub>RR performance of NP catalyst is the support material. In contrast to the self-standing single-crystals, a suitable support material (i.e., glassy carbon or carbon paper) is required to ensure good dispersion, conductivity, and mechanical stability of the NPs. In such case, the interactions between NPs and supports can change the electronic and geometric structures of the NP, and therefore the catalytic properties. In example, wetting behavior of transition metals varies on different supports and, thereby influence particle shape.<sup>92</sup> However, studies focusing on the impact of support in CO<sub>2</sub>RR are scarce. Cuenya and co-workers reported that CO<sub>2</sub>RR selectivity of Cu cubes is indeed both size- and support-dependent.<sup>45</sup> In here, Cu cubes of 220, 320 and 580 nm were electrodeposited on

carbon paper and tested at -1.1 V vs. RHE. The smallest cubes were most selective for CH<sub>4</sub>, reaching a maximum FE of 50% (~5 mA cm<sup>-2</sup>). When the Cu cubes were electrodeposited on Cu foil, C<sub>2</sub>H<sub>4</sub> was the major product (~50% FE). Furthermore, the authors observed fast dynamic changes on particles with small size and with carbon support. The dynamic changes, including the roughening and the disappearance of the (100) facets, loss of Cu, and reduction of Cu(I) species, are suggested to be the origin of the decreased selectivity for C<sub>2</sub> products versus CH<sub>4</sub>. Finally, what only is starting to be considered to affect the CO<sub>2</sub>RR performance is adsorbed organic molecules and ligands on the surface of NPs. To synthesize NPs, particularly the ones with orientated facets, organic ligands are often required. Broekmann and co-workers showed that polyvinylpyrrolidone (PVP) present at the surface of 100 nm Ag cubes (used as a shape-directing agent) thwarted the performance. The FE for CO became poor (<50% at >-0.75 V vs RHE and ~45 mA cm<sup>-2</sup>) when PVP was present at the surface. Instead, when they applied briefly a cathodic potential of -1.1 V vs. RHE desorbing the PVP, FE well over 70% could be maintained up to -0.65 V vs. RHE (~85 mA cm<sup>-2</sup>). On the other hand, organic

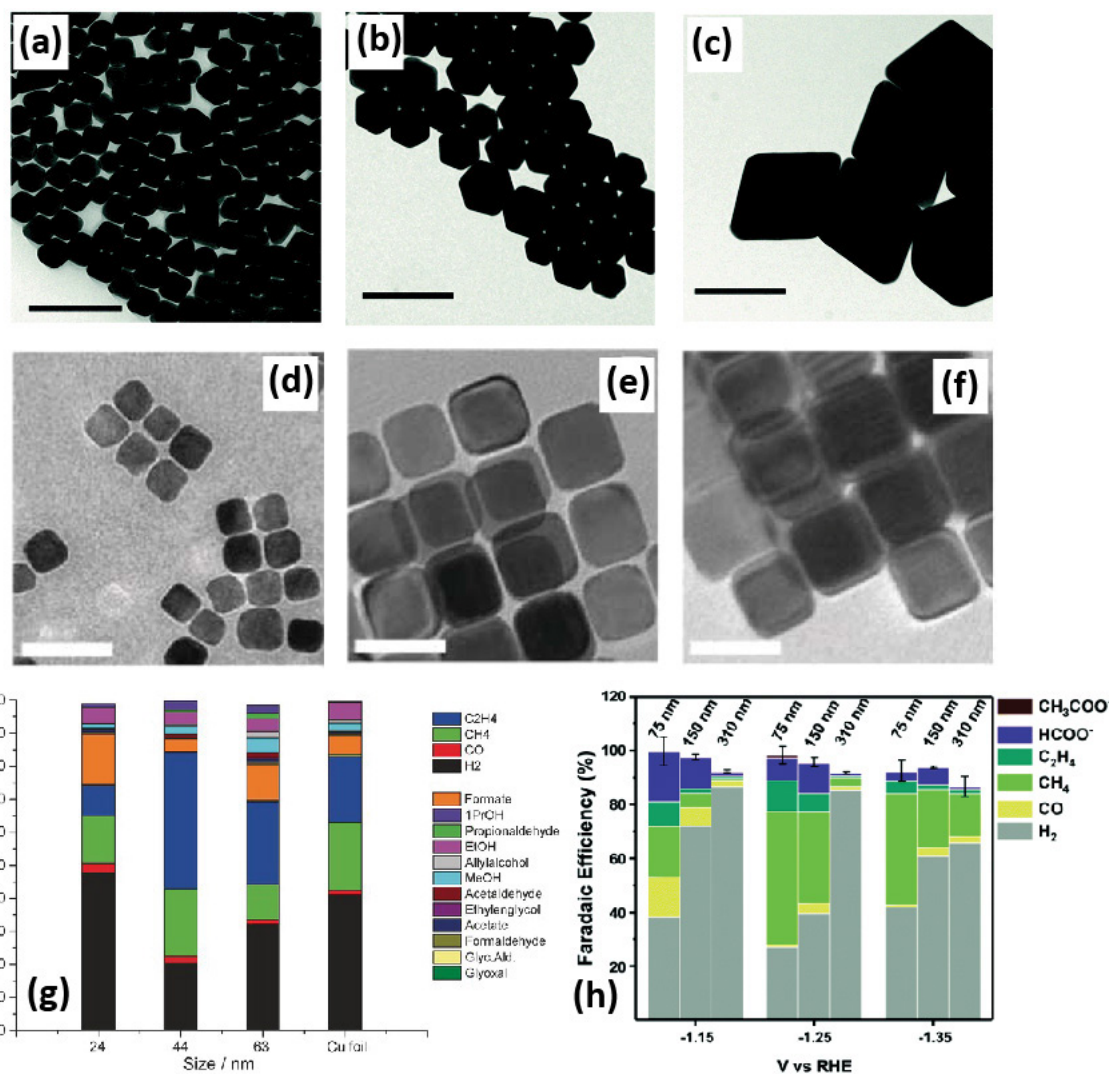


**Figure 11.** (a-c) TEM images of geometrical Cu octahedra of size 75, 150 and 310 nm, respectively. (d-f) TEM micrographs of Cu single-crystal nanocubes of size 24, 44 and 63 nm. (g) Deconvoluted size and shape effect on the product distribution, determined at -1.1 V vs. RHE in 0.1 M KHCO<sub>3</sub>, polycrystalline Cu is added as a reference. Whereas the activity increases with size, the selectivity to the major product, C<sub>2</sub>H<sub>4</sub>, reaches an optimum near 44 nm. (h) Effect of the applied potential deconvoluted from the size and shape-effect in the facet dominated regime of Cu showing that both the selectivity and activity towards CH<sub>4</sub> increases with decreasing size. Reproduced from ref. <sup>44,87</sup>. Copyright 2016 Wiley-VCH and 2019 RSC Publishing, respectively.

molecules can also be introduced onto the surface of NPs to improve the performance. For instance, Kim and co-workers showed that the presence of cysteamine on their 5 nm Ag NPs immobilized on carbon black lowered the overpotential by 300 mV in the CO<sub>2</sub>RR to CO.<sup>39</sup> DFT calculation pointed towards a stronger affinity of the anchoring agent capped Ag NPs for the \*COOH intermediate fastening the rate. In fact, recent studies have begun to use organic molecules or polymers to modulate the electronic structure and/or the local environment of the catalyst to tune the catalytic performance.<sup>93,94,95</sup> These examples further indicate that the chemical nature of the surfactant of colloiddally synthesized NPs needs to be considered in CO<sub>2</sub>RR, something that is not often addressed.

Overall, for NPs with size of 10-1000 nm, most of the atoms are still in the bulk region (**Figure 10**). Therefore, like single-crystals, these NPs are mainly used for fundamental studies for understanding the structure-performance relationships and their selectivity is largely governed

by the crystal facets exposed. In contrast to single-crystals, however, studies propose that the edges and corners of the NPs in this size range already played an important role in the catalytic reaction, despite, according to our model (**Figure 10**), that the ratios of edge/facet and corner/facet are still very low. Since other factors, such as catalyst-support and catalyst-ligand interactions, also start to play a role, we would like to highlight the need for more fundamental studies on nanoparticles in this size regime to decouple the effects of crystal facet from other effects. In addition, similar to single-crystals, the surface energy of these nanoparticles is high, thus restructuring of the surface under CO<sub>2</sub>RR condition can easily take place and should be further studied.

### 2.3.2. Nanoparticles: undercoordinated sites dominated regime

For NPs with any given geometry, the density of undercoordinated surface atoms grows with decreasing particle size as can be seen from **Figure 10**. Therefore, as we continue to go down in particle size, the contribution of the edges and corners starts to dominate the reaction kinetics. Rates may be enhanced several orders of magnitude on increasingly undercoordinated sites, meaning that minor contributions to the surface can actively impact the reaction. However, as HER and the different reaction pathways of CO<sub>2</sub>RR take place over a similar potential range, simply increasing the number of undercoordinated sites will not necessarily enhance the production of specified products from CO<sub>2</sub>. Thus, it is essential to understand the geometrical effect on CO<sub>2</sub>RR for NPs with size of 2-10 nm, where the ratio of undercoordinated sites to coordinated sites becomes significant.

Actually, most NP-catalysts used for CO<sub>2</sub>RR are in this size-class, because they can easily be prepared with various methods, and still remain stable whilst improving the activity. As factors like facets, metal-support interactions and organic ligands have been discussed in **Section 2.3.1**, herein, we will focus especially on the size dependent catalytic behavior of both non-Cu based catalysts and Cu-based catalysts.

### 2.3.2.1. Non-Cu based nanoparticle catalysts

For Ag-based CO<sub>2</sub>RR catalysts, size-dependent catalytic behavior has been observed in several studies, however, the origin of the size effect remains controversial. Kenis and co-workers found that Ag NPs of 5 nm size showed a 10-fold higher CO partial current density than both the bulk sample and the 1 nm sample (**Figure 12a-e**).<sup>31</sup> They suggested that an optimized adsorption strength of reaction intermediates on 5 nm sized Ag NP is the key, however, why the binding energy varies was not explained. While the above results were obtained in organic electrolyte, Hwang and co-workers studied the size effect of Ag NPs in aqueous electrolyte (**Figure 12f-g**).<sup>39</sup> Despite that they also found 5 nm Ag NPs to be the most active ones (**Figure 12f**), DFT simulation showed that the binding energy difference of \*COOH is marginal for NPs larger than 3 nm. Thus, the cysteamine used for the synthesis of Ag NP was considered as the dominating factor. With an optimal coverage of the 5 nm sized Ag

NPs with the cysteamine anchoring agent, a suitable amount of Ag-S bonds are formed which enhanced the stabilization of \*COOH (**Figure 12g**). Very recently, Kaufmann and co-workers synthesized a series of Ag NPs with average diameters of 2 to 6 nm through physical vapor deposition to avoid the influence of organic ligands, and the best CO activity and selectivity were observed on NPs of ~4 nm.<sup>96</sup> Combining DFT simulation and microkinetic modeling, the authors found that CO<sub>2</sub>RR and HER activity was dominated by Ag(100) and Ag edge sites, respectively. The high prevalence of Ag edge sites on NPs smaller than 4 nm leads to a higher HER activity. Unfortunately, the highly oriented pyrolytic graphite was used as a support for Ag NPs and the weak Ag-C bond may lead to rapid aggregation of Ag NPs, which was not considered in this work.

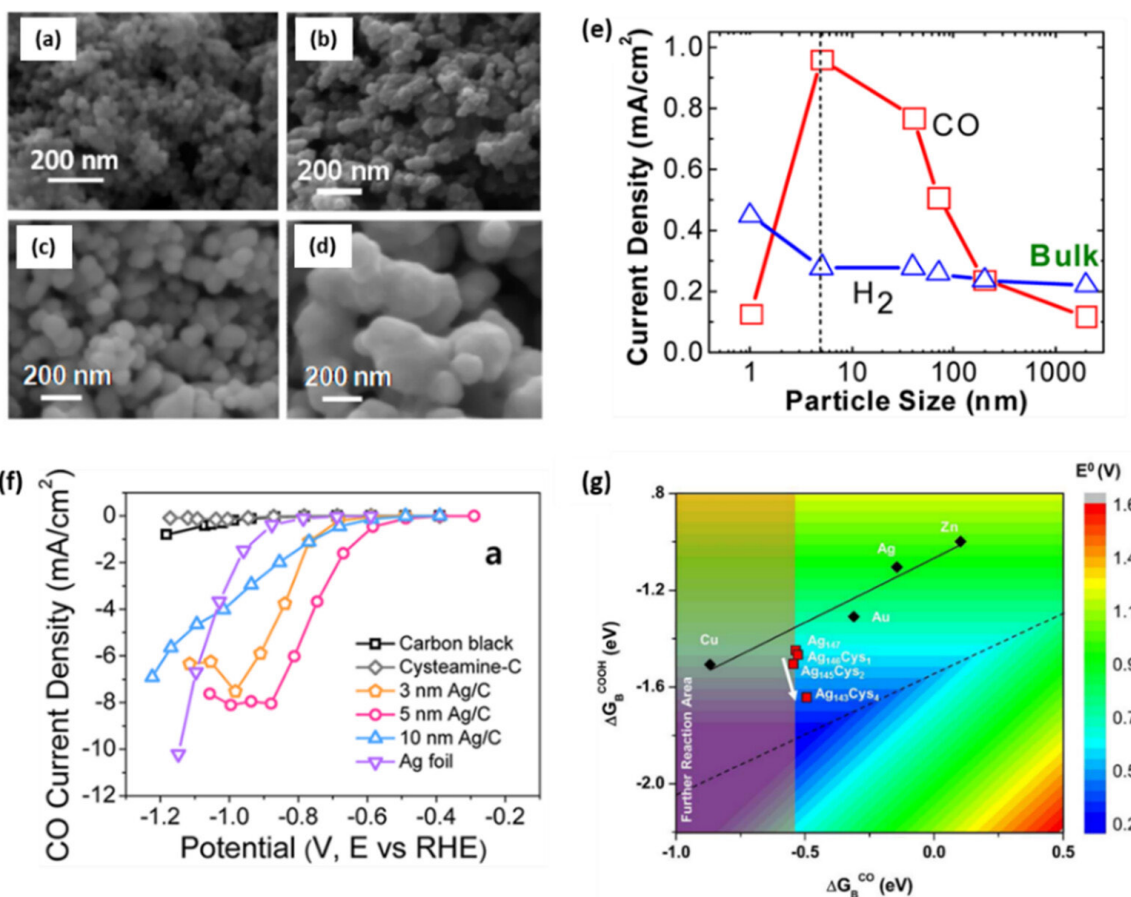


**Figure 12.** (a–d) SEM images of 1, 5, 70, and 200 nm silver NPs, respectively. (e) Volcano trend in the activity of ultrasmall to bulk Ag NPs in the CO<sub>2</sub>RR towards CO in CO<sub>2</sub> saturated 1-ethyl-3-methylimidazolium tetrafluoroborate (EMIM-BF<sub>4</sub>) electrolyte.<sup>31</sup> Reproduced from <sup>31</sup>. Copyright 2013 ACS Journals. Current densities for CO and H<sub>2</sub> formation reported are the differences in the current density with CO<sub>2</sub> and Argon at –0.75 V vs SHE and –1.14 V vs SHE, respectively. (f) CO partial current density for Ag NP samples and control samples. (g) Effect of anchoring agents on COOH and CO binding energies examined using Ag<sub>(147–n)</sub>Cys<sub>n</sub> (n = 0,1,2,4) models. Reproduced from ref. <sup>39</sup>. Copyright 2015 American Chemical Society.

The size effect of Au NPs was studied by Sun and co-workers using 4, 6, 8 and 10 nm particles (**Figure 13a**).<sup>35</sup> Notably, the NPs were immobilized on carbon black and the organic ligands were removed through annealing before the reaction (**Figure 13b**). The authors found that the CO partial mass current increased with decreasing particle size (**Figure 13d**), but the selectivity followed a volcano trend, peaking at the 8 nm particle (**Figure 13c**). After calculating the CO<sub>2</sub>-to-CO and the HER pathways on Au (211), Au (111) and Au<sub>13</sub> cluster, the authors concluded that the highest CO production rate for the 8 nm particles is due to the presence of an optimum ratio of the edge sites. It must be noted that the crystalline size determined by XRD was much smaller than the one reported based on TEM, suggesting the existence of different types of uncoordinated sites on the surface of Au NPs, making the Au (211) surface possibly too simple to simulate the real surface. Cuenya and co-workers also investigated the size effect of Au NPs in CO<sub>2</sub>RR (**Figure 13g-i**), however, they found that the majority of the current went towards

H<sub>2</sub>, especially at large overpotential (**Figure 13j**).<sup>37</sup> The authors argued, based on DFT, that while the formation of \*COOH is increasingly favored with decreasing particle size, H<sup>+</sup> is as well and to a higher degree. This explains both the enhanced activity on smaller Au NPs as well as the change in selectivity, similar to that from Sun and co-workers.<sup>37</sup> Note that the particles were produced with the inverse-micelle encapsulation method, and that the influence of the polymer was not considered. Another fact worth mentioning is that the standard deviation of particle diameter is in the order of ±1 nm, the reactivity reported is actually the average of an ensemble. It would therefore, be very interesting to see these measurements repeated with better size-selection.

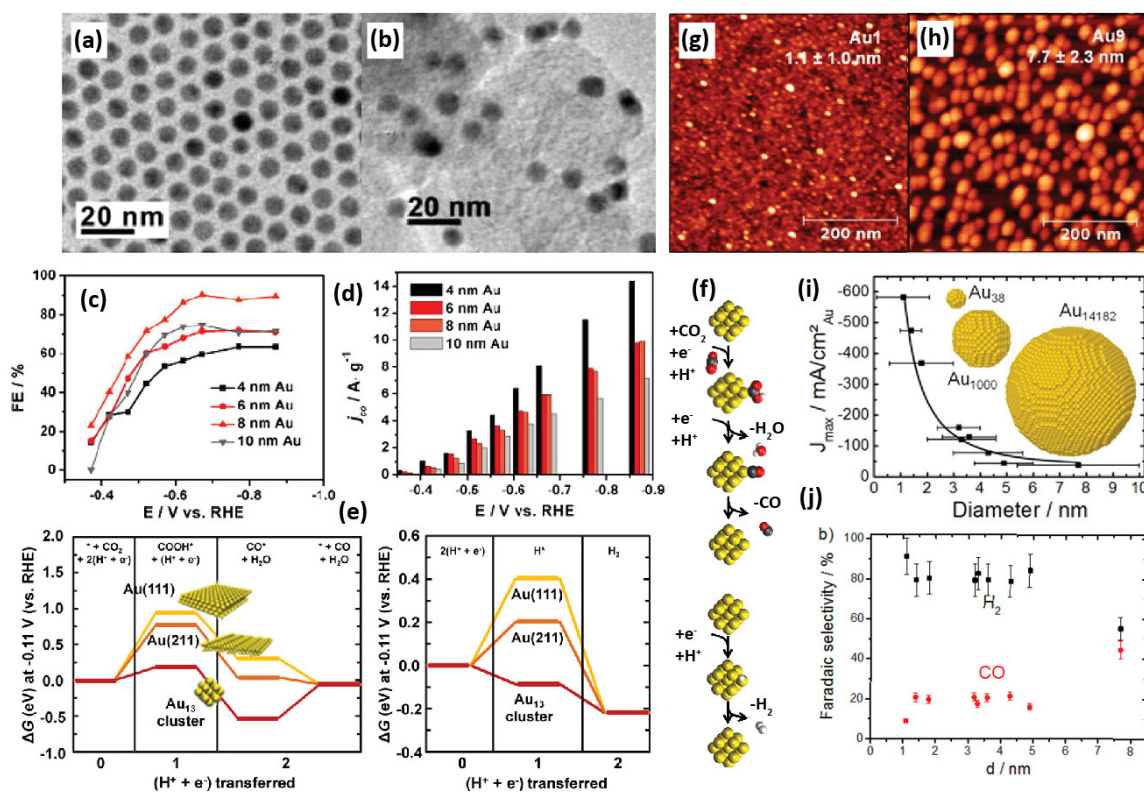


**Figure 13.** (a-b) TEM images of the 6 nm sized Au NPs as well as the composite material used as cathode of NP-decorated activated carbon, respectively. (c) Size-dependent CO selectivity of Au NPs as a function of applied potential (V vs. RHE) in 0.1 M  $\text{KHCO}_3$ . (d) CO specific mass current as a function of size and potential. (e) DFT calculation using the computational hydrogen electrode showing the free-energy diagram at a potential of -0.11 V vs RHE on Au(211), Au(111) and  $\text{Au}_{13}$  clusters for the conversion of  $\text{CO}_2$  into CO as well as the parasitic HER. (f) Schematic representing the conversion of  $\text{CO}_2$  to CO on Au clusters. Reproduced from ref. <sup>35</sup>. Copyright 2013 American Chemical Society. (g-h) AFM images of the Au NPs of  $1.1 \pm 1.0$  nm and  $7.7 \pm 2.3$  nm produced via the encapsulated-micelle approach. (i) Size-dependent current density of Au NPs at -1.2 V vs. RHE in 0.1 M  $\text{KHCO}_3$ . (j) Faradaic efficiency as a function of size at -1.2 V vs. RHE. Reproduced from ref. <sup>37</sup>. Copyright 2014 American Chemical Society.



As has been mentioned before, Zn is another CO selective metal. Interestingly, oxidized Zn NPs (1.7 to 6.8 nm) showed a similar trend to that of Au and Ag:<sup>42</sup> while the overall activities increased with the decrease of particle size, the CO selectivity did not. Here, Zn NPs in the size regime of 3 to 5 nm benefited the most from undercoordinated atoms, maintaining a high CO selectivity (>70% FE) at a relatively high current density (3.5–5.6 mA cm<sup>-2</sup>). Notably, the authors also suggested that Zn(OH)<sub>2</sub> species could be directly involved in the mechanism as a partial reduction of oxidized-Zn was observed using *operando* XAS.

Besides CO-selective metals, other size-selected particles in CO<sub>2</sub>RR have also been reported. In a study by Li and co-workers, In<sub>2</sub>O<sub>3</sub> nanocrystals were investigated covering both isotropic and cubic crystals.<sup>97</sup> In, being a typical HCOO<sup>-</sup> selective catalyst, showed improved selectivity when switching from the bulk to the nanoscale. However, similar to results obtained for CO selective NPs, smaller did not necessarily mean better. The highest FE (>90% and 6.3 mA cm<sup>-2</sup>) for HCOO<sup>-</sup> was observed for the 15-nm In<sub>2</sub>O<sub>3</sub> cubes from -0.71 to -0.9 V vs.

RHE. Instead, the 5-nm spheres peaked at 83% at -0.71 V vs. RHE and rapidly became H<sub>2</sub> selective at larger overpotentials (FE HER >70%). DFT calculations of In(101), In<sub>165</sub> and In<sub>85</sub> clusters, showed \*H adsorption gradually approached thermoneutrality as the particle size decreased. Thereby, the acceleration in HER for the 5-nm NP could be explained.

While all the above examples showed the effects of structural factors on a single product from CO<sub>2</sub> (e.g., CO or HCOO<sup>-</sup>), the selectivity of Pd NPs is tunable towards CO and HCOO<sup>-</sup>.<sup>38</sup> By the reduction of PdCl<sub>2</sub> with citrate as capping agent, 2–10 nm Pd NPs were obtained and tested (**Figure 14a–f**).<sup>38</sup> Similar to other metal NPs, the overall activity increases with decreasing size of Pd NPs, but the difference is that the selectivity is also improved (**Figure 14h**). An excellent CO FEs over 90% could be obtained between -0.7 and -1.0 V vs. RHE for particles <5 nm (**Figure 14g**). Based on a DFT model, the authors use \*CO poisoning to explain the deceleration of the rate for the 2.4 nm Pd NP. Further, it was shown that \*H binding did not benefit equally from the reduction of size versus the \*COOH intermediate. This made CO<sub>2</sub>RR the preferred pathway.

Interestingly, Broekmann and co-workers showed that  $\text{HCOO}^-$  was the main product for Pd NPs of the same size range (3.8, 6.5 and 10.7 nm) but synthesized with a PVP capping strategy (**Figure 14i-k**).<sup>40</sup> The highest selectivity of 98.3% was obtained at a strikingly low overpotential (-0.1 V vs. RHE and  $\sim 1.5 \text{ mA cm}^{-2}$ ) for the 6.5 nm sized NPs. Noteworthy is the equilibrium potential of  $\text{HCOO}^-$  at -0.12 V vs. RHE (**Table S1**), which seems at odds with

the values reported by Broekmann and co-workers reported. The authors claimed that the active phase was PdH, not metallic Pd, providing a likely explanation for this discrepancy.

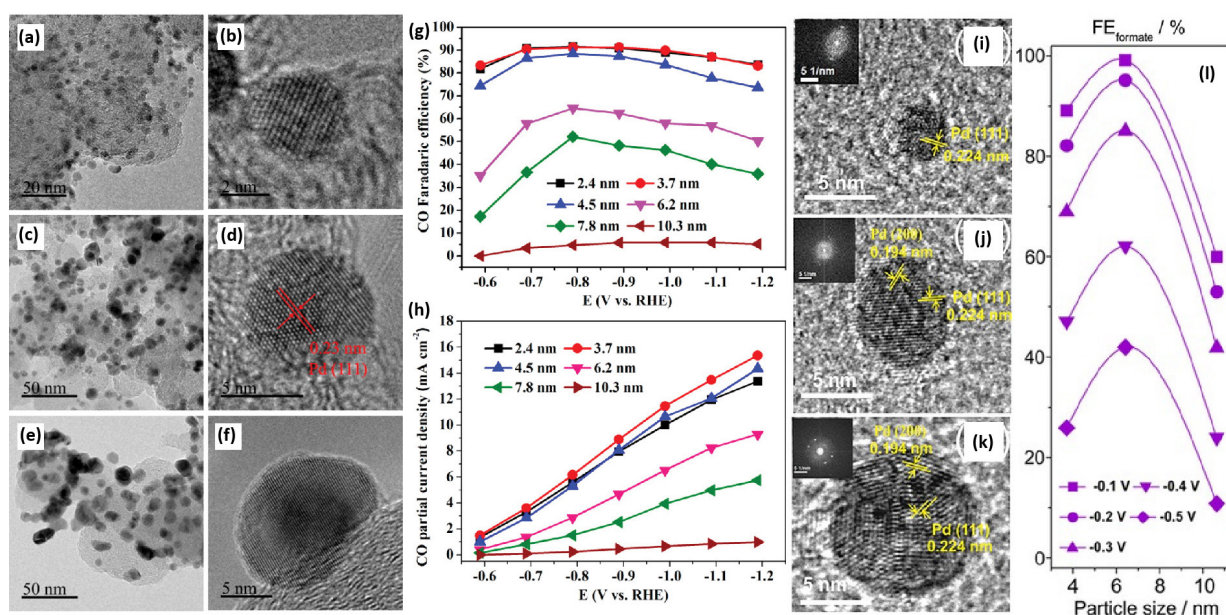


**Figure 14.** (a-f) TEM and HRTEM micrographs of the 2.4, 6.2 and 10.3 nm Pd NPs. (g) Effect of size in the ultrasmall particle regime of Pd on the selectivity towards CO as a function of potential in 0.1 M  $\text{KHCO}_3$ . (h) CO partial current density as a function of size and potential in the ultra-small particle regime of Pd. Reproduced from ref. <sup>38</sup>. Copyright 2015 American Chemical Society. (i-k) HRTEM micrographs of the 3.8, 6.5 and 10.7 nm Pd NPs. (h)  $\text{HCOO}^-$  FE as a function of particle size at -0.1 V vs RHE in 0.5 M  $\text{NaHCO}_3$ . Reproduced from ref. <sup>40</sup>. Copyright 2017 Wiley-VCH.

### 2.3.2.2. Cu-based nanoparticle catalysts

As discussed above, tuning the facet and particle size of non-Cu based catalysts generally changes the activity of CO<sub>2</sub>RR, and, therefore the ratio of CO<sub>2</sub> reduction products to H<sub>2</sub>. However, for Cu-based catalysts, due the large variance in products generated, the product distribution is very sensitive to the facet and particle size. For example, Cuenya and co-workers investigated size selected Cu NPs deposited on glassy carbon (2 to 15 nm) and observed a clear activity trend as a function of particle size (**Figure 15**).<sup>36</sup> The formation of hydrocarbons decreased drastically with decreasing particle size, with the FE for C<sub>2</sub>H<sub>4</sub> and CH<sub>4</sub> reaching a plateau at <15 nm (**Figure 15h**). At particle sizes <5 nm, at least an order higher currents for H<sub>2</sub> and CO in comparison to the bulk were produced (**Figure 15g**). The authors explained this trend for the fact that the number of undercoordinated sites goes up exponentially in this size regime suggesting much stronger binding to intermediates.

Different catalytic behaviors for Cu NPs in this size regime have been observed. Kibsgaard

and co-workers showed that 5 nm sized Cu NPs prepared using magnetron sputtering exhibited excellent C<sub>2</sub>H<sub>4</sub> selectivity (FE >40% at -0.8 V vs RHE and 4 mA cm<sup>-2</sup>) in CORR.<sup>98</sup> Further, Cu-phthalocyanine derived 2±1 nm sized Cu NPs showed high FEs towards CH<sub>4</sub> in CO<sub>2</sub>RR (66% at -1.06 V vs. RHE and ~15 mA cm<sup>-2</sup>).<sup>99</sup> It is possible that the inverse-micelle encapsulation method used by Cuenya and co-workers introduces carbonaceous material to the particle surface that interferes with the reaction. Especially when considering the behavior of the extended library of Cu-based bimetallic electrodes produced via the same method, this seems plausible. For example, Cuenya and co-workers investigated composition controlled Cu<sub>x</sub>Co<sub>100-x</sub> NPs (size of 1.2-21 nm) and showed that HER was favored over CO<sub>2</sub>RR.<sup>43</sup> Later, they also studied AuCu alloys in the 1.4 to 24 nm size regime and reported again high H<sub>2</sub> FE independently of the size.<sup>41</sup> Contrarily, Yang and co-workers showed at least 40% CO FE under the same conditions for 10 nm AuCu NPs of various compositions prepared using a co-reduction method.<sup>41,100</sup> As we have seen

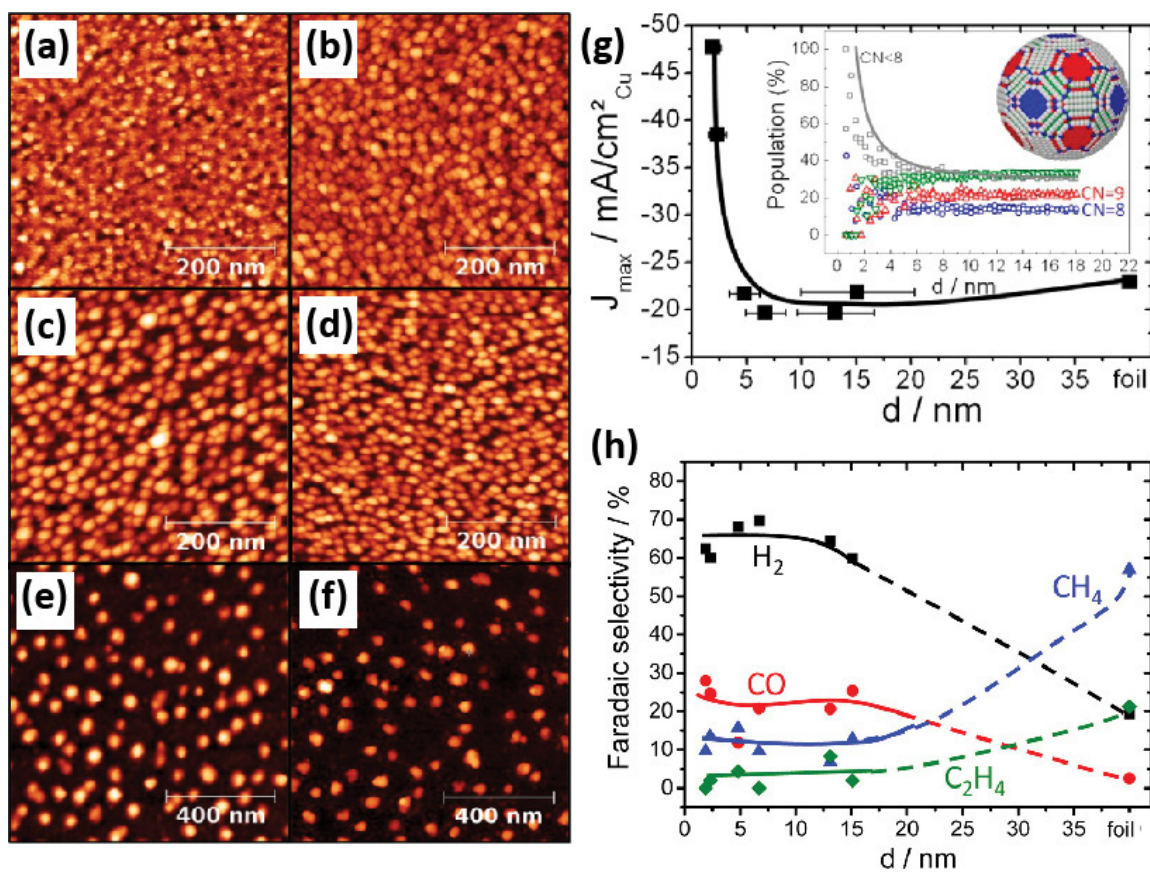


**Figure 15.** (a-f) AFM images of 2-15 nm Cu NPs on glassy carbon. (g) Enhanced overall activity of Cu NPs as a function of particle size at -1.1 V vs RHE in 0.1 M  $\text{KHCO}_3$ . (h) Evolution of the product distribution on Cu NPs as a function of size at -1.1 V vs. RHE in 0.1 M  $\text{KHCO}_3$  showing that most of the current enhancement reported goes towards the parasitic HER. Reproduced from ref. <sup>36</sup>. Copyright 2014 American Chemical Society.

that adsorbed organic molecules and ligands can dominate the reaction, with size only of minor influence, care should be taken by interpreting these results. Thus, further experiments excluding some of the possible contributing factors should be performed, to precisely evaluate the intrinsic performance of Cu NPs this size regime. Magnetron sputtering under UHV such as reported by Kibsgaard and co-workers is good method for this, although the low loading of NPs makes the accurate quantification of products harder. We would like to point out that much higher deposition rates have been reported for spark ablation (1 g/h for 5 nm NPs).<sup>101</sup> Although its application in catalysis is still in its infancy, the high production rates reported and absence of ligands make it an interesting candidate to investigate this size-class further.<sup>102,103</sup>

From the above-mentioned examples of non-Cu and Cu-based ultras-small particles, it is clear that decreasing the particle size is an effective way to tune the catalytic performance. However, smaller particle size, although enhancing overall reaction rates due to a higher degree of undercoordination,

does not necessarily result in better CO<sub>2</sub>RR performance. An intricate balance between adsorption strengths of intermediates determines the selectivity often resulting in volcano-like selectivity trends as competing reaction (i.e., HER) sway the performance. Further, the effect of support and ligation-shell cannot be excluded from performance assessments as they may dominate the reaction kinetics. It is worthwhile to note that although our discussions have been focused on single-element metal catalysts, most of the bimetallic catalysts (e.g., alloys, tandem catalysts) can be devised in this particle regime.<sup>104,105</sup> In the framework of systematic investigations of structure-performance relationships in combination with composition effects, we see opportunities for these types of studies in the future. Our discussions of single-elemental particles may help as a guideline to place such studies in context.

## 2.4. Metal cluster catalysts

Below a certain particle size, <1.5 nm for Au for instance, common structural factors useful to determine reactivity of NPs become meaningless.<sup>106</sup> In this regime, metallicity breaks down and clusters behave more like molecules than particles. Localized electron density, e.g., in the form of molecular orbitals, now dictate the reactivity. Clusters, namely, occupy discrete energy levels (**Figure 2**), which are directly related to the number of atoms bonded, their spatial arrangement and charge.<sup>107,108,109,110</sup> Metal clusters that contain a small number of atoms have shown great advantages in heterogeneous catalysis. For example, the activity and selectivity of the catalytic reaction can be well tuned by precisely controlling the size of the clusters. Furthermore, clusters of a single and well-defined mass can facilitate the understanding of reactivity as it allows for computational studies at the highest level of theory. As early as the 1980s have metal clusters been produced using physical deposition methods, such as thermal evaporation or magnetron sputtering, and applied in catalysis.<sup>111,112,113</sup> <sup>114</sup> However, few

studies have used such clusters for CO<sub>2</sub>RR, possibly due to their low production rates and loading, as well as the consequent difficulties in quantifying reaction products. Metal clusters can also be synthesized through chemical methods, where atomically precise clusters are protected with organic ligands. These materials have found their applications in CO<sub>2</sub>RR in the last few years, showing promising catalytic performances, as will be discussed in the following section. Even more recently, metal clusters have also been produced *in situ* from dispersed metal catalysts upon applied cathodic potential of which sparse examples will be discussed as well.

## 2.4.1. Ligand effect in metal clusters

Metal clusters, either produced colloiddally or SAC-derived are all bonded to some type of ligand. In the case of colloidal clusters, ligands are molecular compounds such as thiols and phosphines, and are necessary to control atomicity (number of atoms bonded) and geometry and ensure colloidal stability. Instead, in the case of SAC-derived clusters, stability originates from ligation sites in the support (often heteroatoms). Without the ligands, agglomeration would occur upon the slightest perturbation, let alone under applied potential. Beyond stability, however, ambiguity exist about the actual role of ligands in reactivity itself as many convoluted effects may be present.

Thiol-capped icosahedral  $\text{Au}_{25}$  clusters were first synthesized and used for the  $\text{CO}_2$ RR by Jin and co-workers.<sup>30</sup> An extremely low CO onset potential of -0.193 V vs. RHE was observed, indicating the exceptional intrinsic activity of the Au clusters (i.e., 200-300 mV earlier than for 2 nm Au NPs and polycrystalline Au). Also, near unity FEs could be obtained at more cathodic potentials (-1.0 V vs. RHE), albeit at low partial current densities (0.1 mA

$\text{cm}^{-2}$ ). The authors argued based on DFT simulations that strong physisorbed  $\text{CO}_2$  bonded through the S atoms of the thiol, explained the enhanced reactivity. However, since the reference Au NPs were citrate capped, the effect of the ligand could not be deconvoluted from the reduction in size. In a later study of the same group, icosahedral  $\text{Au}_{25}$  clusters were compared with rods of the same mass produced using different sets of ligands (**Figure 16**).<sup>34</sup> In this way, it became possible to exclude the effect of atomicity and determine instead to what degree ligation affected cluster reactivity. Interestingly, it was shown that the CO production rate was 2.8 times higher for the near-to-spheres than for the rods at -1.17 V vs. RHE (**Figure 16a**). Further, the icosahedra were 1.5 times more selective for CO than the rods. However, in contrast to physisorption via the ligands reported before, adsorption of  $\text{CO}_2$  was expected to proceed through a ligand exchange process instead. And  $\text{CO}_2$  adsorption was more facile for the near-to-sphere than the rod explaining the difference in rates. Experimental evidence has been reported

that such atomically precise clusters are partially dethiolated when they undergo  $\text{CO}_2\text{RR}$  and that the active site resides on an uncapped Au atom.<sup>115</sup> This suggests that the ligand does not play a direct role in the catalysis but the fast dissociation of those ligands does facilitate rapid conversion. On top of that, the type of ligand also determined the geometry of the clusters. And it was shown that a partial negative charge on the near-to-spheres improved the formation of the  $^*\text{COOH}$  intermediate, which enhances the rate further. Note how

the charge influences the geometry similar to what has been observed for  $\text{Au}_{<14}$  clusters produced with UHV methods.<sup>110</sup> Although ligands here are not directly involved in the conversion of  $\text{CO}_2$ , they do affect the rates of reaction through exchange rates and charge stabilization. Unfortunately, deconvolution of the rates induced by the ligand and the atomicity of the cluster have not yet been reported. And as we will see in the following section, atomicity may have massive impacts.

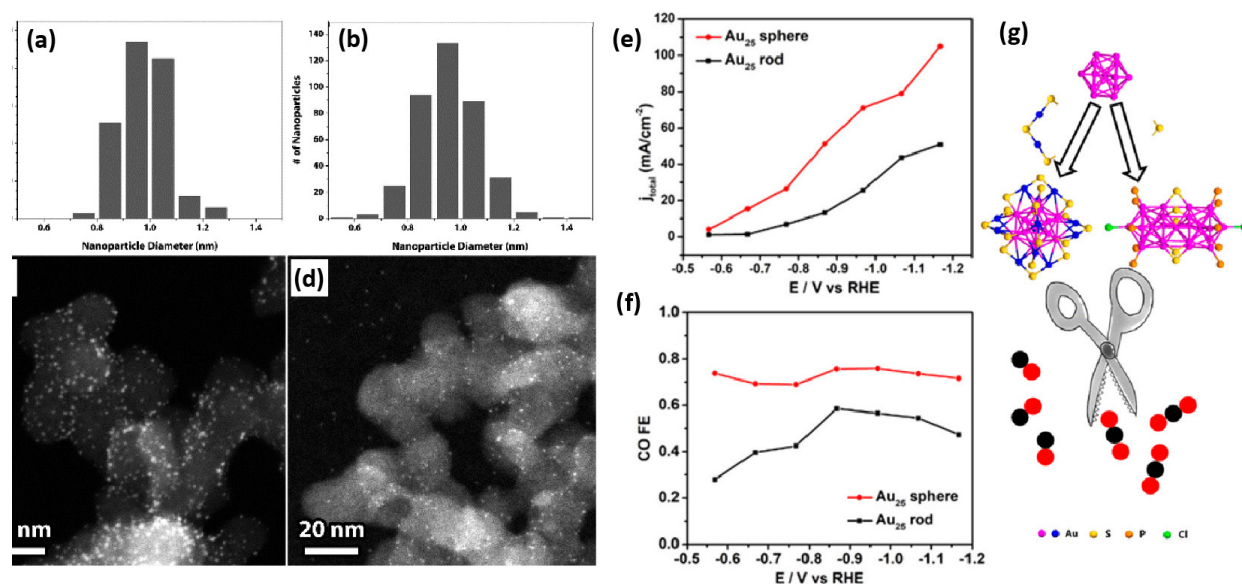


**Figure 16.** (a-b) Size-distributions of  $\text{Au}_{25}$  nanosphere and nanorods, respectively. (c-d) STEM HAADF micrographs of the  $\text{Au}_{25}$  clusters supported on carbon black. (e) Total current density of  $\text{CO}_2$  reduction as function of potential vs RHE of rods (in black) and spheres (in red) in 0.1 M  $\text{KHCO}_3$ . (f) Faradaic efficiency of the  $\text{Au}_{25}$  cluster pair as a function of potential vs RHE (nanosphere: red, nanorod: black). (g) Atom packing schematic of the conversion of Au nuclei into clusters of nanosphere and nanorod geometry as the result of the ligand shell. Reproduced from ref. <sup>34</sup>. Copyright 2018 American Chemical Society.



## 2.4.2. Atomicity in metal clusters

While both physical deposition and chemical synthesis methods require careful control of synthesis parameters, metal clusters have also been obtained through the dynamic evolution of SACs. Here, the instability of atomically dispersed catalysts is used to produce clusters *in situ*. Fontecave and co-workers, showed that fully oxidized Cu(II)-N-doped carbon SAC (N-C, **Figure 17**) formed metallic Cu clusters of  $0.47 \pm 0.04$  nm under cathodic potential (-1.2 V vs. RHE).<sup>116</sup> The *in situ* generated clusters showed an impressive C<sub>2</sub>H<sub>5</sub>OH FE of 43% at a stable average current density of 16.2 mA cm<sup>-2</sup>. Interestingly, the

formation of the Cu clusters was completely reversible as through potential cycling the Cu(II) SAC reformed. Remarkably, other than CO and H<sub>2</sub>, no additional products could be detected highlighting how Cu clusters can catalyze reaction pathways with a high degree of specificity. Instability against potential in Cu-hydroxyl SACs was also shown, which interestingly was also C<sub>2</sub>H<sub>5</sub>OH selective.

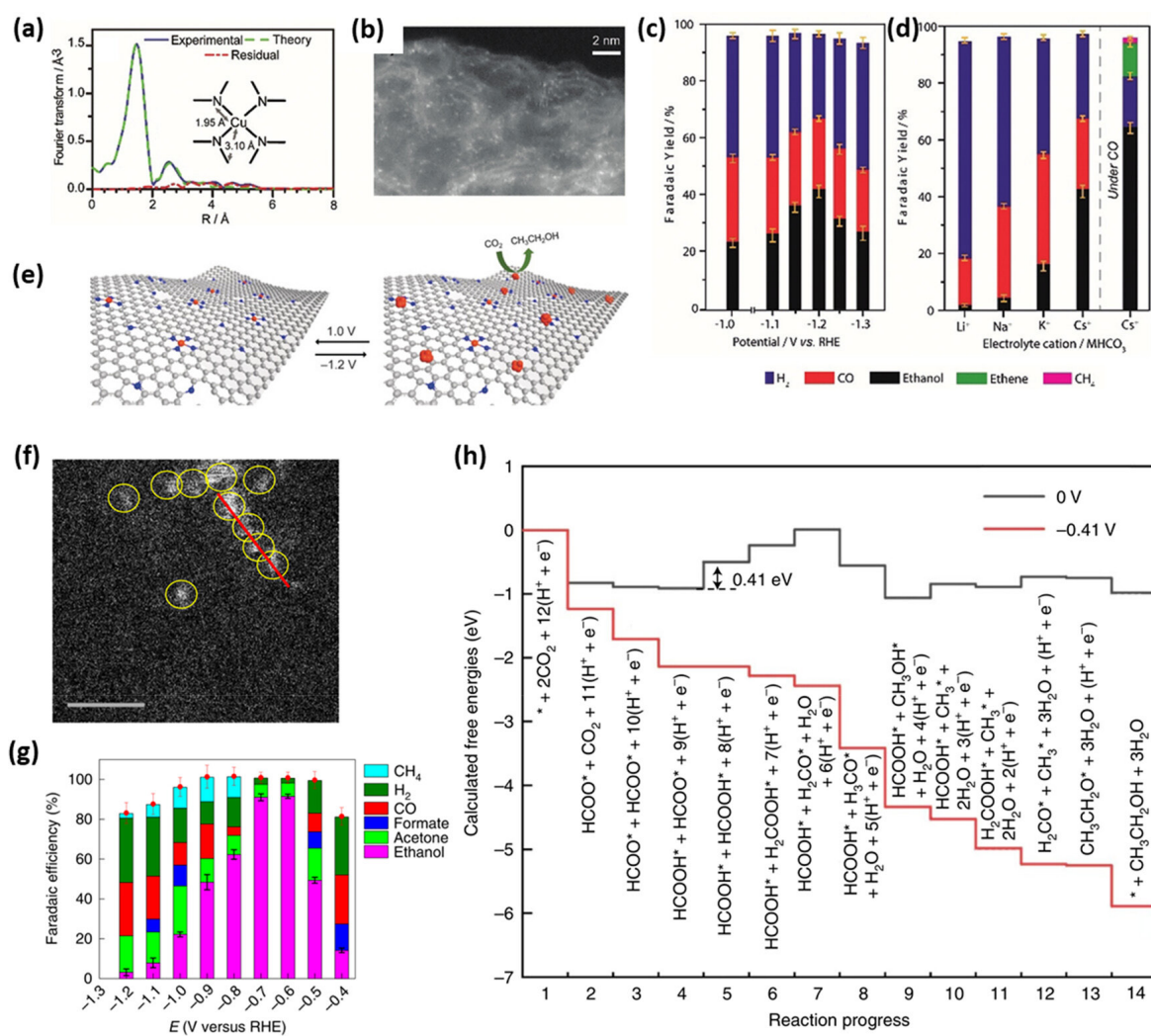


**Figure 17.** (a) EXAFS data of Cu-N<sub>4</sub>-C SACs. (b) Aberration-corrected STEM-HAADF image of the SAC. (c) Faradaic efficiency as a function of potential vs RHE in 0.1 M KHCO<sub>3</sub>. (d) Change in FE at -1.2 V vs. RHE in 0.1 M Li-, Na-, K-, CsHCO<sub>3</sub> as well as under CO flow. (e) Schematic showing the in-operando changes of the SAC towards metal clusters as determined by EXAFS explaining the selectivity towards C<sub>2</sub>H<sub>5</sub>OH. Reproduced from ref. <sup>116</sup>. Copyright 2019 Wiley-VCH. (f) HAADF-STEM image of Cu/C-0.4, showing the presence of isolated Cu species marked by yellow circles (Scale bar: 2 nm). (g) The product distribution at different polarization potentials for Cu/C-0.4. (h) DFT simulated reaction pathway of CO<sub>2</sub>RR to C<sub>2</sub>H<sub>5</sub>OH on the supported Cu cluster catalyst at 0 and -0.41V. Reproduced from ref. <sup>117</sup>. Copyright 2020 Springer Nature.

Xu and co-workers developed an amalgamation method to obtain atomically dispersed Cu on a hydroxylated-graphene that showed an even better selectivity towards  $C_2H_5OH$  (although with a rotating disc electrode, which does not suffer from mass-transport limitations).<sup>117</sup> The  $C_2H_5OH$  onset potential is, to our knowledge, the lowest ever reported (-0.4 V vs. RHE). Further, the highest FE to date (92%) was achieved at -0.7 V vs. RHE and  $1.2 \text{ mA cm}^{-2}$  (**Figure 17g**). Fitting of operando EXAFS spectra showed that the initially ligated Cu(II) species had reduced and (reversibly) formed  $Cu_n$  (with  $n=3,4$ ) clusters, similarly to what was observed for the N-doped material of Fontecave and co-workers. The authors found through DFT that the HO-ligation sites did not play an active role in the catalytic cycle and, interestingly, that a  $HCOO^*$  mediated pathway has an overall lower energy than via  $*CO$  (**Figure 17h**). The observation of  $HCOO^-$  at the onset potential of  $C_2H_5OH$  makes this hypothesis plausible. However, it is in stark contrast with what is known for metallic Cu, as  $HCOO^-$  is considered a terminal product.<sup>10</sup>

Unfortunately, Fontecave and co-workers did not include DFT calculation in their study. However, the difference in onset potential of 0.6 V suggests entirely different pathways are being catalyzed.

It is known that metal clusters of specific atomicity, differing only by a single atom, can have tremendously different reactivities.<sup>118</sup> In the above examples, we possibly see such an event unfold. Using our simplistic model as outlined in **Figure 10** and assuming a 3D geometry of the  $0.47 \pm 0.04 \text{ nm}$  clusters reported by Fontecave, we calculate an atomicity of 5. This means that the subtraction of 1-2 atoms from the catalyst resulted in a 0.6 V shift in onset potential. A mere 310 mV off the equilibrium potential (**Table S1**). Strong differences in reactivity upon substitution of 1-2 atoms in colloiddally produced Au clusters have also been reported. For example, by substituting one atom of the  $Au_{25}$  near-to-sphere clusters with Pd, not only was the CO FE enhanced to 100% over a 600 mV potential range, an order larger CO partial current density could be achieved as well ( $35 \text{ mA cm}^{-2}$  at -1.2 V vs. RHE).<sup>119</sup> Further, substituting two Au atoms

in Au<sub>23</sub> with Cd nearly doubled the TOF to CO at the same potential.<sup>120</sup>

Metal clusters provide a new and exciting materials synthesis platform. In example, several orders of magnitude enhanced activities can be achieved with Au<sub>n</sub> clusters in the CO<sub>2</sub>RR over their bulk metallic counterpart. Further, Cu<sub>n</sub> clusters may show enhanced selectivity towards C<sub>2+</sub> products and specifically oxygenates with respect to their metallic counterparts and are strongly speciating as only specific pathways are catalyzed and the active site is much better defined than for bulk materials. However, to establish the effects of atomicity, charge, geometry and ligand shell on the performance in the CO<sub>2</sub>RR, more systematic studies are needed. In the case of SAC-derived clusters, the dynamic nature of these clusters makes it extremely difficult to predict *a priori* what ligation site (density) would lead to what atomicity. Much more

systematic studies are needed in order to gain control over the formation of these clusters and determine the effect of the potential. Lastly, due to the significantly reduced number of bonding electrons in metal clusters with respect to their metallic counterparts, the activity and selectivity of clusters can be modelled at the highest level of theory allowing for theory-guided candidate catalysts selection. For instance, in a combined study by a computational and experimental group, Lee and Jiang and co-workers<sup>33</sup> predicted with DFT and validated experimentally that a CuH catalyst was HCOO<sup>-</sup> selective at low overpotential but produced H<sub>2</sub> at high overpotential. Such cross-discipline collaborations will become increasingly valuable in this field of research.

## 2.5. Atomically dispersed catalysts

In the final reduction of the number of atoms comprising an active catalyst, we arrive at isolated metal atoms that are stabilized by the ligands. This type of atomically dispersed catalysts has attracted increasing attention in CO<sub>2</sub>RR in recent years. They not only exhibit nearly 100% atom utilization efficiency, but also show high activity, selectivity, and stability. Further, their activity and selectivity can be optimized via tuning of the metal center and the coordination structure.<sup>121,56,122</sup> However, studies show that SACs behave differently than their bulk and NP forms. This is not surprising as their electronic structure is quite different: NPs have a single valence band, SAC show discrete energy levels (**Figure 6**).<sup>60</sup> Therefore, the classification of SACs according to the selectivity of their metal centers based on the element is no longer appropriate.

In recent years, various types of SACs have been tested in CO<sub>2</sub>RR, including immobilized molecular catalysts, metal organic frameworks (MOFs), metal containing covalent organic frameworks (mCOFs), metal and heteroatom co-doped

carbon materials (M-X-Cs in which M=metal and X=N, O and S etc.), as well as single-atoms anchored on host metals/oxides.<sup>123,124,125,126,127,128,129,130,131,132,57,133,66,134,59,135,136,137,138,139,140,141,142,143,144,145,146,147,148,149,150,54</sup> Moreover, as a further expansion of the SACs, diatomic catalysts (active sites of two metal atoms close to each other) have also been designed to introduce synergistic effects.<sup>151,152,153,154</sup> Many excellent reviews regarding synthesis, characterizations, and applications of SACs exist in the literature.<sup>155,156, 157,158,159,160,161,162,163</sup> As this review focuses on the influence of structural properties of metal catalysts in various size-regimes, in this chapter, we will review the influence of the metal center and the coordination environment on the catalytic performance, as they are the two most important factors that determine the properties of SACs (**Figure 18**). We note, however, that the conductivity of the support can also play a substantial role in performance especially at high current densities.

## 2.5.1. Effect of the metal center

### 2.5.1.1 CO selective SACs

With an overview of the published works on SACs for CO<sub>2</sub>RR, we find that various types of SACs have been used, and most of them are selective for CO production (**Figure 7 and Figure 18**).<sup>124,125,126,127,128,129,130,131,132,57,133,66,134,59,135,136,137,138,139,140,141,143,144,145,146,147,148</sup>

Further, even the usually HCOO<sup>-</sup> selective elements show a tendency towards CO as SACs.<sup>164</sup>

The influence of metal centers, organic ligands, supporting materials and reaction conditions have been extensively studied to explain selectivity and activity trends. Herein, we would first like to emphasize the influence of metal centers on the activity of SACs for CO.

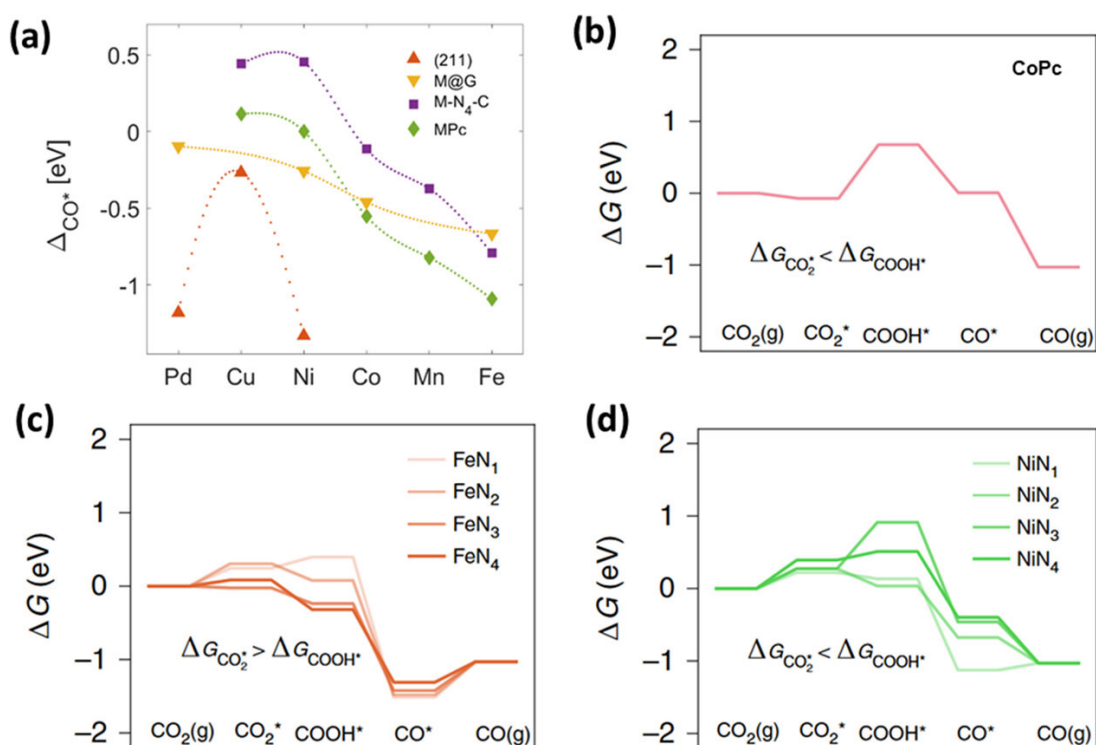


**Figure 18.** (a) Predicted \*CO binding strengths to various electrocatalysts obtained with DFT explaining the strong tendency towards CO production of SACs in the CO<sub>2</sub>RR. M@G, M-N<sub>4</sub>-C and MPc, denote metal on graphene, metal N-doped carbon with 4 N bonds and metal phthalocyanine, respectively. Reproduced from ref.<sup>160</sup>. Copyright 2021 American Chemical Society. Free energy diagram of CO<sub>2</sub> to CO for, (b) CoPc adsorbed on graphene, (c) FeNC, and (d) NiNC with N<sub>1</sub>, N<sub>2</sub>, N<sub>3</sub> and N<sub>4</sub> the N coordination number. Reproduced from ref.<sup>165</sup>. Copyright 2021 Springer Nature.

M–X–C materials are likely the most studied SACs for CO<sub>2</sub>RR in the past few years, due to the ease of preparation, high tunability, and high activity and selectivity. Various studies using these types of SACs have investigated the effect of the metal center on catalysts activity and selectivity for CO.<sup>57,66,142</sup> However, some ambiguity exists on the nature of the most active and selective metal. For example, Strasser and co-workers prepared a series of metal- and N-doped porous carbon materials (M–N<sub>x</sub>–C) through pyrolyzing Co, Mn, Fe, Ni and Cu coordinated bipyridine-based polymers.<sup>66</sup> They found that Mn–N–C and Fe–N–C showed the earliest CO onset potentials, while Ni was more selective and active at higher overpotentials (**Figure 18d**). In contrast, Co–N–C produced mostly H<sub>2</sub> for the entire potential window. The authors performed DFT simulations of CO<sub>2</sub>RR and HER pathways using single-site motif M–N<sub>4</sub> as active sites (approximation). Then, they correlated the CO activity to the adsorption energy of key reaction intermediates (\*COOH, \*CO and \*H). The results show that Ni–N<sub>4</sub> adsorbs \*COOH, \*H and \*CO weakly,

and thus requires a high overpotential to produce CO. On the other hand, Ni–N<sub>4</sub> resists \*CO poisoning. By contrast, Co–N<sub>4</sub> is energetically favorable for \*H adsorption and is, therefore active for HER. Contrarily, Jaouen and co-workers also prepared M–N<sub>x</sub>–C catalysts with Mn, Fe, Co, Ni, and Cu but found Co–N–C the most active for CO and least selective for H<sub>2</sub>.<sup>142</sup> The authors proposed that the best compromise between \*CO and \*CO<sub>2</sub><sup>–</sup> binding energies on the Co–N–C site was responsible for the high CO activity, and the competing adsorption of \*CO<sub>2</sub><sup>–</sup> and \*H determined the selectivity.

The different catalytic behavior with respect to the metal center and the lack of insight in the catalytic mechanism of the above-mentioned works could be explained by possible inhomogeneities in the materials and changes of the catalyst's properties induced by the reaction conditions. Deng and co-workers showed that for well-defined M–N<sub>4</sub> (M=Mn, Fe, Co, Ni and Cu) phthalocyanine-based SACs, DFT could be used to predict the most active metal center.<sup>166</sup> Optimal binding of \*COOH and \*CO

suggested Co-N<sub>4</sub> to be the most selective. Indeed, when phthalocyanine-carbon paper composite materials were tested for the CO<sub>2</sub>RR, an excellent selectivity of 99% was obtained for the Co-N<sub>4</sub> based material. This could form a possible explanation of the ambiguity observed for Co-N-Cs reported by Strasser and Jaouen. In homogeneous molecular catalysts, the active site is well-defined. However, SACs produced via pyrolysis, for example, show various kinds of ligation sites (**Figure 19a**). Observed reactivity is therefore, an ensemble average of the active sites that are present in the material.

Finally, Strasser and co-workers also showed that for the Fe containing composites, small amounts of CH<sub>4</sub> could be observed in the exhaust stream (<1%, **Figure 19b-c**).<sup>57</sup> This once again showed the relevance of homogeneous catalysts regarding the nature of the active site in SACs, as molecular Fe-based catalyst also show activity towards the production of CH<sub>4</sub> from CO<sub>2</sub>.<sup>167</sup> Not much later, Koper and co-workers also observed CH<sub>4</sub> as by-product in the CO<sub>2</sub>RR on a SAC but in this case on an immobilized Co porphyrin complex catalyst.<sup>168</sup> Interestingly, the methane pathway showed correlation with adsorbed formaldehyde, which is not an expected intermediate for the production of CH<sub>4</sub> on metallic Cu for instance.<sup>26</sup> These studies provided the first evidence that with specific metal centers of SACs, hydrocarbons could be produced as well. We will now turn to the effect of the metal center for the formation of CO<sub>2</sub>RR products beyond CO.



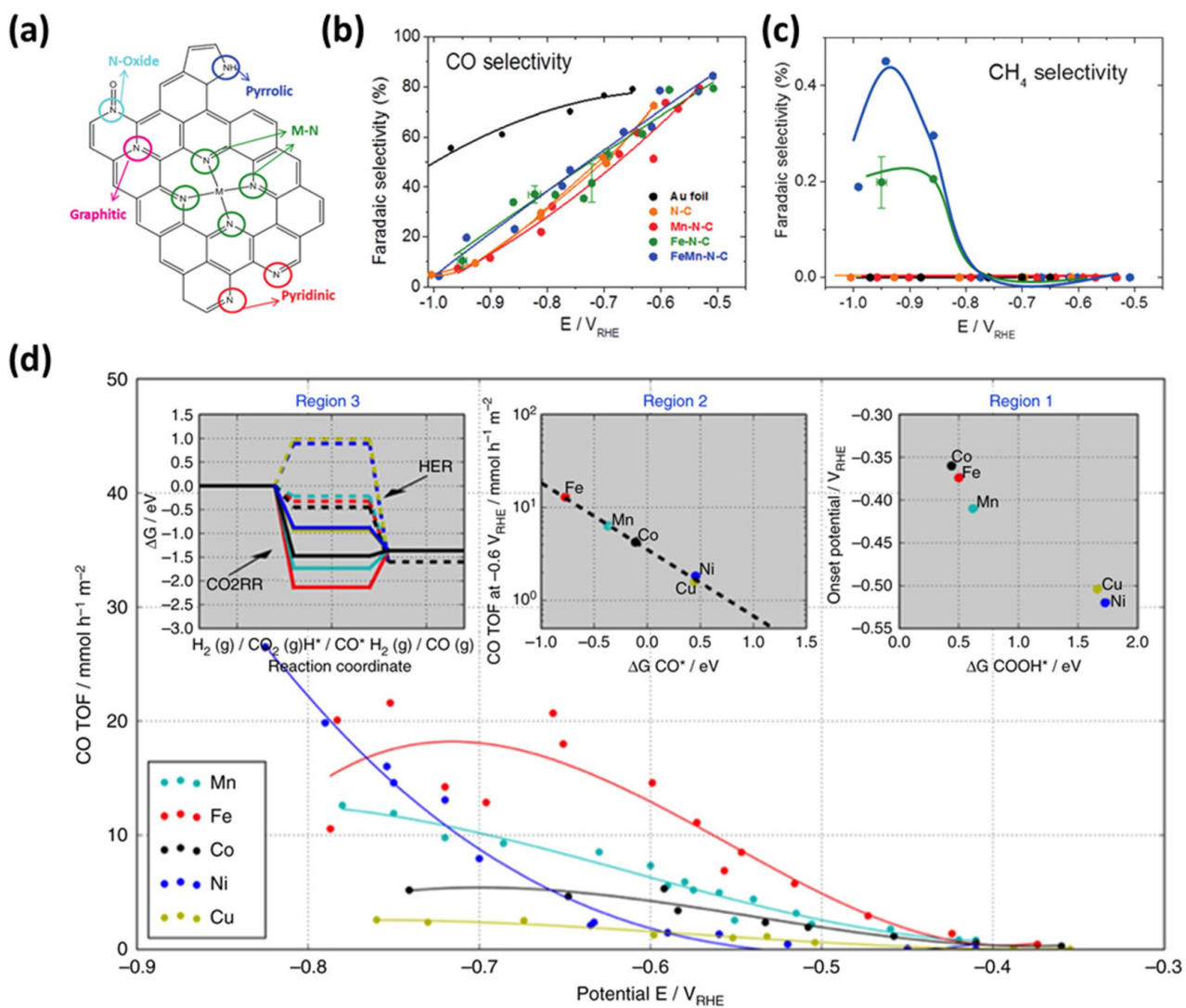


**Figure 19.** (a) Schematic of the various N-sites present in the M-X-Cs, in which M=Fe, Mn, FeMn. (b) CO FEs as a function of potential for the various M-X-Cs center in which M=Fe, Mn, FeMn. in 0.1 M KHCO<sub>3</sub> (c) FEs of CH<sub>4</sub> for the various electrocatalysts. Reproduced from ref. <sup>57</sup>. Copyright 2015 Wiley-VCH. (d) CO production turnover frequency (TOF) of the M-N-Cs as a function of potential for the various M-X-Cs in which M= M=Mn, Fe, Co, Ni, Cu. Reproduced from ref. <sup>66</sup>. Copyright 2017 Nature Springer.

### 2.5.1.2. C<sub>1</sub> products beyond CO

As discussed previously, the metal center of SACs affects the activity to produce CO, but also includes the possibility to produce further reduced C<sub>1</sub> products, as evidenced by Strasser and co-workers.<sup>57</sup> In this section, we will discuss how the nature of the metal center may lead to surprising electrochemistry with respect to their bulk counterparts. In a very interesting study by Yang and co-workers, pyrolyzed electrospun carbon nanofibers consisting of single-atom Cu-N-C catalysts achieved a high selectivity for CH<sub>3</sub>OH (44% and 41 mA cm<sup>-2</sup>, **Figure 20**), a product metallic Cu shows only limited activity for.<sup>140,169</sup> The absence of the competing CH<sub>4</sub> reaction, which does share intermediates with CH<sub>3</sub>OH, was explained using first principle calculations. Therein it was shown that the reduction of the <sup>\*</sup>COH intermediate to <sup>\*</sup>CHOH was much more favorable than towards <sup>\*</sup>C (relevant to the production of CH<sub>4</sub>). Further, C-C coupling was deemed unlikely *a priori* due to the absence of Cu-Cu moieties in the material as excluded through XPS. One must note, however, that under applied potential Cu ions can become labile in SAC resulting in the formation of Cu clusters *in situ*, which in effect function as the active catalyst as discussed in the previous chapter. Since the absence of clusters was reported based on ex situ characterization, reversible

cluster formation cannot be excluded as an alternative explanation of the observed performance.

Possibly due to a comparable boiling point of Zn and pyrolysis temperatures required to achieve carbonization, the excellent performance of Zn-N-C in the CO<sub>2</sub>RR went unnoticed until 2020.<sup>149</sup> Via a low temperature evaporation-carbonization approach, SACs of Zn supported on N-doped graphite were synthesized and showed a CH<sub>4</sub> selectivity of 85% at -1.8 V vs. RHE with a partial current density as high as -38.5 mA cm<sup>-2</sup>. Note that both Zn and partially oxidized Zn cathodes convert CO<sub>2</sub> to CH<sub>4</sub> with FEs <1%.<sup>42,170</sup> Interestingly, other than CH<sub>4</sub>, the only other CO<sub>2</sub>RR product observed was CO and the authors invoke a HCOO<sup>-</sup> mediated pathway to explain its high selectivity. This is a very interesting although controversial claim as HCOO<sup>-</sup> is generally considered a terminal product.<sup>10</sup> More studies towards the behavior and performance of Zn-based SACs are needed to elucidate such questions. Nevertheless, it is clear that entirely new chemistry can be achieved on the molecule-like active sites of SACs.

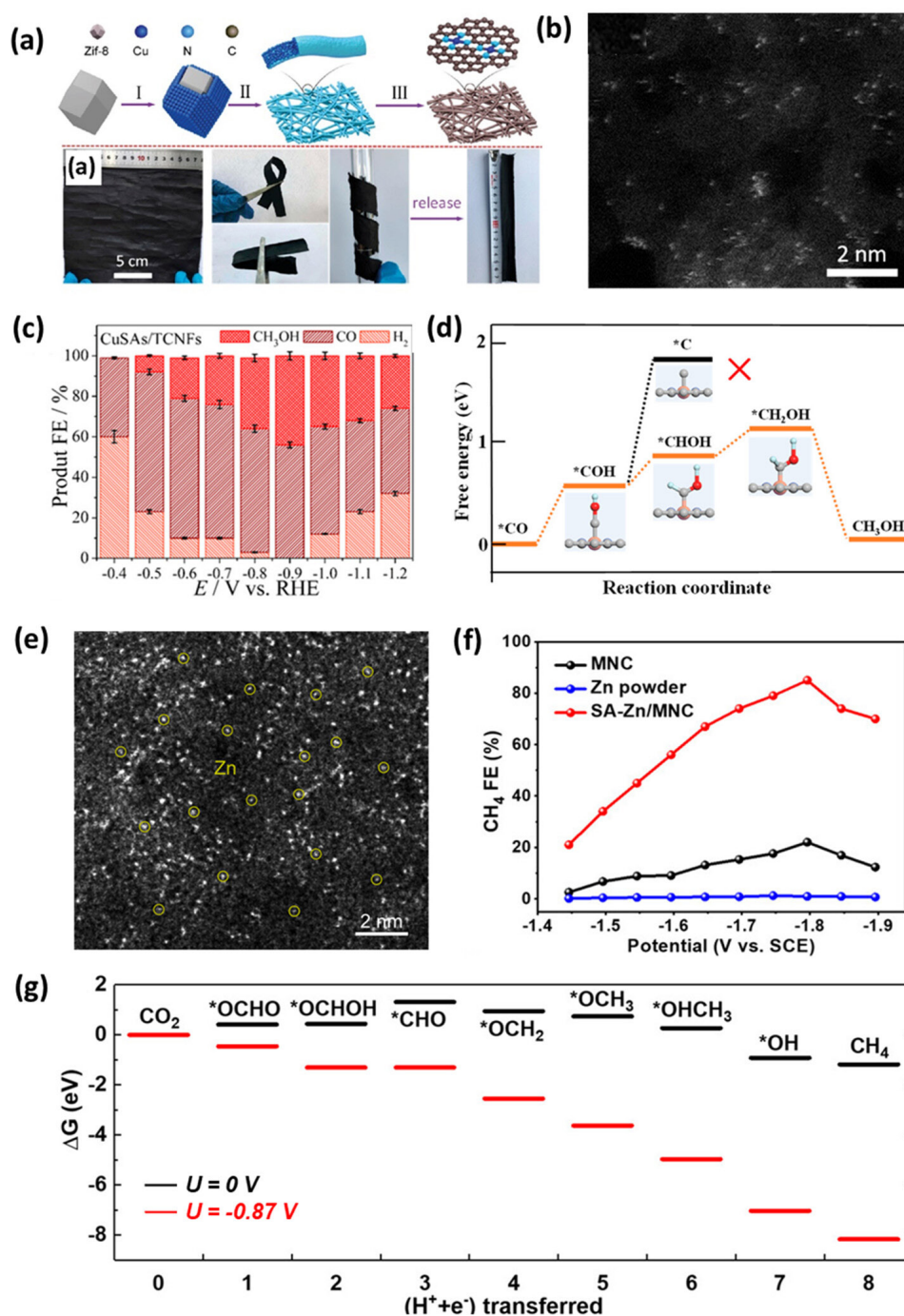


**Figure 20.** (a) Schematic of the production process of the electrospun ZIF-8 derived porous single-atom Cu catalyst (CuSAs/CNFs). (b) HAADF-STEM images of CuSAs/CNFs. (c) Product distribution as a function of applied potential for CuSAs/TCNFs in 0.1 M KHCO<sub>3</sub>. (d) Free energies for conversion of \*CO to CH<sub>3</sub>OH on Cu-N<sub>4</sub> structure. Orange, gray, dark blue, red, and light blue spheres stand for Cu, C, N, O, and H atoms, respectively. Reproduced from ref. <sup>140</sup>. Copyright 2019 American Chemical Society. (e) HAADF-STEM images of SA-Zn/MNC. (f) FEs for CO<sub>2</sub>RR to CH<sub>4</sub> as a function of applied potential for SA-Zn/MNC. (g) Free energy diagrams for CO<sub>2</sub>RR to CH<sub>4</sub> on Zn-N<sub>4</sub>-graphene structure. Reproduced from ref. <sup>149</sup>. Copyright 2020 American Chemical Society.

### 2.5.1.3. SACs for C<sub>2+</sub> products

It is generally understood that in order for C-C coupling to be possible, at least two metal centers need to be in proximity to one another.<sup>171</sup> Zheng and co-workers showed that the same is true for Cu-N-C SACs.<sup>147</sup> Where Cu-N-Cs produced at temperatures higher than 900 °C were mostly selective for CH<sub>4</sub>, C<sub>2</sub>H<sub>4</sub> became the major product when the temperature used was as low as 800 °C. Using EXAFS, it was shown that the relative distance between Cu-N<sub>x</sub> species was greatly suppressed by increasing the pyrolysis temperature. The absence of Cu-Cu bonds in either material could be deduced from the same results.

Finally, an opposing view that C-C coupling can take place on single metal centers, can be found in the description of Chen and co-workers of their single-atom Cu anchored on porous N-doped carbon electrocatalyst Cu-SA/NPC, which was selective for acetone (36.7% at -0.74 V vs. RHE and ~3.7 mA cm<sup>-2</sup>).<sup>148</sup> DFT calculation showed that on pyrrolic N-Cu sites, C-C coupling forming the \*COCOH intermediate involved an exothermic step, which the authors, therefore determined as facile. STEM-HAADF analysis after electrochemistry showed neither Cu cluster nor particle formation. However, *operando* measurements were not reported and as we saw before, this can prove essential as SACs can reduce reversibly to metal clusters under an applied potential.<sup>116,117</sup>

## 2.5.2. Ligation effect

Ambiguity exists in the literature in the determination of the most active metal center in M-X-Cs, which may originate from inhomogeneities in the support material and respective ligation sites. Presently, we discuss studies using M-X-Cs that excellently determine the effect of the ligand showing the strong influence coordination number may have on catalyst performance. In a study by Xie and co-workers, atomically dispersed Co based M-N-Cs with N<sub>2</sub>-, N<sub>3</sub>- and N<sub>4</sub>-coordination were synthesized and their performance assessed.<sup>172</sup> Interestingly, selectivity and activity increased with decreasing coordination number. DFT calculations showed that low coordination resulted in faster electron transfer to form \*CO<sub>2</sub><sup>-</sup> explaining the enhanced rate. This makes sense from a chemical intuition point of view and may remind the reader of the effect of undercoordination in our discussion of NP catalysts. Metal centers coordinated to fewer ligation sites, will have undergone less back bonding interaction with the support. Therefore, it may donate more charge to an adsorbate. Indeed, in another study, the same behavior was

discerned for Ni-containing M-N<sub>x</sub>-Cs in which X=2, 3 and 4.<sup>173</sup> Ni-N<sub>2</sub>-C showed the highest selectivity (98% at 10 mA cm<sup>-2</sup>) and the earliest onset potential for CO (-0.6 V vs RHE). Here, DFT identified the formation of \*COOH as the potential-determining step,<sup>174</sup> which became increasingly energetically favorable with decreasing coordination number. This offers a roadmap to enhance the catalytic rate in SACs. By actively engineering low number coordination site into the catalyst support, better performances can be achieved.

Overall, it has been clear that M-X-C based SACs can show entirely different reactivities than their metallic counterparts. Explanations for these discrepancies in reactivity have for the most part been based on computational efforts. For M-N-Cs, for example, enlarged adsorbate dipoles due to the discrete and narrow d-states of these molecule like active sites can shift the rate-determining step from CO<sub>2</sub>\* adsorption found in their transition metal counterparts to \*COOH formation strongly accelerating the reaction.<sup>165</sup> More generally, activation barriers insurmountable at

room temperature on metals ( $>1$  eV), can become facile on the SACs. This shows the tremendous potential of these materials. Entirely new pathways could be opened up to the more valuable products of the  $\text{CO}_2\text{RR}$ . With SACs active sites being treatable at the highest level of theory, collaborations between theorists and experimentalists may yield exceptional results. Nevertheless, the lone nature of the metal center, will most likely limit its performance to  $\text{C}_1$  products. Metal clusters rather, with multiple metal centers in one active site, can benefit from both worlds: the tremendously rich chemistry of SACs, and the C-C coupling capabilities of metals. Further, such properties can be envisioned for dual-atom catalysts as well although presently only CO selective catalysts have been reported.<sup>151,152,153,154</sup> We expect major developments in both fields, however.

## 2.6. Conclusions and perspectives

The CO<sub>2</sub>RR powered by renewable electricity can convert CO<sub>2</sub> to valuable chemical and fuels and is therefore a promising strategy for achieving a sustainable global energy economy. Metals have been used as electrocatalysts for CO<sub>2</sub>RR for more than three decades, showing distinct selectivity towards a variety of products. Decreasing the size of the metal particle is an effective way to increase the number of atoms exposed to the reactant, thus the activity. Further, with the decrease of the particle size, geometric and electronic structures also change, which in turn influences the catalytic behavior of the metal. As an example, **Figure 21** illustrates the variation of the major products from CO<sub>2</sub>RR with the decrease of Cu particle size. Here, we have reviewed representative studies of metal catalysts for CO<sub>2</sub>RR and categorized them according to the particle size. We have discussed how key structural factors, including crystal facet, particle size, undercoordination sites, ligands, and support, influence the catalytic behavior of metal catalysts in different size regimes. And determined for each size regime the most relevant structural factors governing the reactivity. This may help researchers determine the parameters that are most relevant to the type of metal catalyst they are interested in or provide direction for catalyst target selection. Moreover, as we have seen

that research groups often operate in only one of the defined size regimes, and that challenges and opportunities differ hugely between these disciplines, we hope our classification system will help researcher effectively communicate their findings between fields.

In brief, it is shown that the crystal facet dominates the activity and selectivity of metal single crystals and nanocrystals with particle size larger than 10 nm. While undercoordination sites start to dominate the performance of particles smaller than 10 nm (but > 1 nm), the role of ligands and support should not be ignored. Finally, for clusters and SACs, their electronic structure is distinct from bulk metals, and the catalytic performance are mainly determined by the ligands/support and the number of atoms. Although much progress has been made in understanding the structure-performance relationships and finding efficient electrocatalysts for CO<sub>2</sub>RR, some significant challenges remain in the field both from fundamental and applied perspectives. Now we discuss some of the challenges and opportunities researcher may want to focus on.

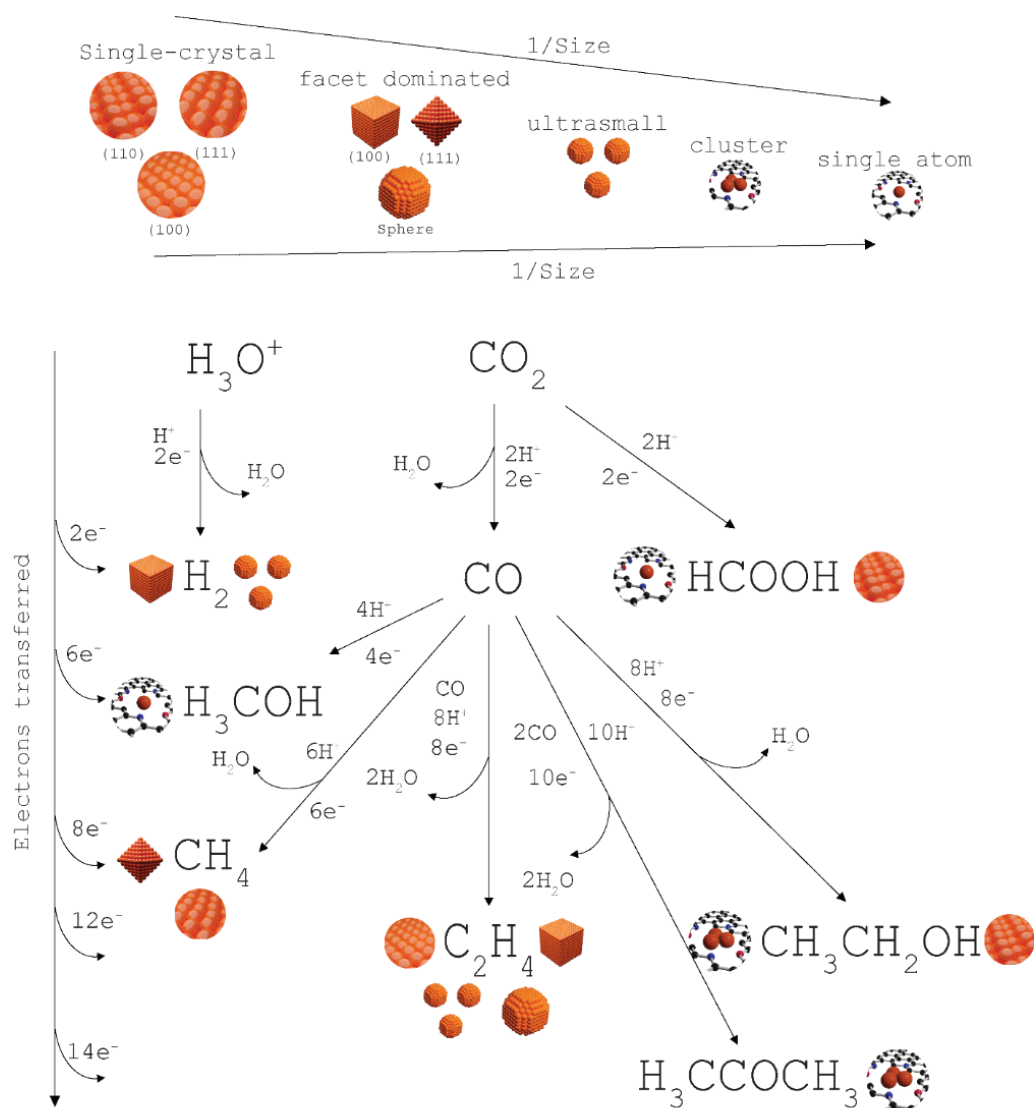


**Figure 21.** Overview of the major products obtained on various Cu-based electrodes in the different size regimes of the CO<sub>2</sub>RR.



## 2.6.1. Deconvolution of ligand/support effects from chemical nature of the active site

Despite the large number of studies reported for size-selected catalysts spanning multiple size regimes, the non-homogeneity of catalysts production methods and the presence of other often overlooked factors (e.g., effects of the ligand and support), still leaves us without a unified theory to explain and predict catalytic performance. Only by fully dissecting and deconvoluting the intricacy of the parameters governing the CO<sub>2</sub>RR within a given synthesis platform, will it be possible to not only qualitatively but also quantitatively compare between them. This calls for more benchmark studies with precise control over the structural factors influencing the performance. Researchers may want to produce metal catalysts of different sizes via the same synthesis method

and stabilize them using different types of conductive supports such as (heteroatom doped) carbonaceous supports (e.g., graphene, reduced-graphene oxide, carbon nanodots, carbon black etc.), MOFs, COFs and metal oxides and determine catalyst performance in relation to the support and or ligand. Further, one may want to include control experiments of particle systems of the same size but using different synthesis methods to elucidate the role of synthesis parameters.

## 2.6.2. Dynamic nature of the catalysts demands *in situ* and *in operando* characterization of the active site

For cross-discipline, comparative studies to become fully reliable, it is of utmost importance that structure-performance relationships are assessed under practically relevant conditions. As shown in several examples, electrocatalysts greatly undergo rearrangement under laboratory testing conditions. For example, Cu single crystal have been shown to significantly change their morphology under applied potential and over time, which has further been correlated to changes in performance. Similarly, for Cu nanocrystals, applied potential and the binding of adsorbed species progressively damaged particles and resulted in loss in product selectivity. Also, the dramatic switch from CO to H<sub>2</sub> selectivity for Ag NPs <5nm could potentially be assigned to rapid agglomeration under reaction conditions. It is therefore, of utmost important to better understand restructuration processes. Thus, more effort must be invested in the use and further development of *in situ* and *operando* techniques to determine the dynamic nature of the catalysts and its effect on determined structure-performance relationships and long-term stability. This must include both inhouse-developed techniques as well as at large scale research

facilities. For example, performance tests of SACs and or clusters should include *in situ* and preferably *operando* XANES and EXAFS studies to probe the chemical nature of the catalyst. This may involve oxidation state, coordination number and bond length to couple chemical structure with CO<sub>2</sub>RR activity. Further, *in situ/operando* IR and Raman spectroscopy could offer insight in the transient nature of the catalyst (e.g., adsorbed species and phase) and reaction intermediates relevant in CO<sub>2</sub>RR towards value added chemicals. The use of shiners (plasmonic nanoparticles made electrochemically inactive by surface modifications) can help to enhance Raman scattering in case of low signal strength. Further, corrosion of the electrodes may start to play a role during prolonged electrolysis, *in situ/operando* monitoring of the electrolyte using analytical techniques such as inductively coupled plasma mass spectrometry to determine ion contaminations could prove of value as well.

### 2.6.3. Theory-guided catalysts design

With structure–property relationships well-established and benchmarked, it should become possible to build up unified reaction mechanisms across the size regimes in the CO<sub>2</sub>RR.<sup>165</sup> Having overarching mechanistic insights conjoining several size regimes would be of tremendous value to catalyst candidate selection as theory could guide performance-optimization *in silico*. Incorporation of multi-scale modelling at the device level would be a prerequisite to translate such computational studies to real-world applications, however.

A great opportunity lies here for the incorporation of artificial intelligence (AI) in reaction parameter optimization.<sup>85,175,176</sup> The autonomous learning capabilities of AI based-algorithms offer improved predictability at a fraction of the (computational) cost. Stronger ties between experimentalists and theorists could reap the benefit of symbiotic efforts in which theory guides catalysts design and experiment offers data for the improvement of the predictive power of the algorithm.

## 2.6.4. Reactor and electrolyte design

For the large part, our discussions have considered performance tests in the conventional H-cell and in aqueous electrolyte, as most studies have evaluated the performance of catalysts under such conditions. However, due to the low solubility of CO<sub>2</sub> (350 ppm in water), its local concentration at the catalyst surface will be limited. This limits the partial current densities <100 mA cm<sup>-2</sup>, which are far from industrially relevant (> 1 A cm<sup>-2</sup>). Further, the low solubility may also result in the CO<sub>2</sub>RR becoming mass-transport limited, which may in turn affect performance parameters such as selectivity. Thus, the catalytic behavior of metal catalysts in different size regimes will require validation at more industrially applicable current densities, i.e., in flow cell or membrane electrode assemblies. Further, to achieve unitary selectivity's and keep energy losses at a minimum, the parasitic HER will need to be suppressed in order for CO<sub>2</sub>RR electrolyzer technology to reach market maturity. This may be achieved by introducing hydrophobic polymers and or molecular adsorbates at the catalyst interface, reducing the local proton flux and increase CO<sub>2</sub>/CO concentration.<sup>95,177</sup> Further, beyond

catalyst design and interface modification, reactor and electrolyte design may be used to this affect as well. High-pressure devices that enhance the CO<sub>2</sub> concentration at the catalyst surface can play an important role herein. Early work from the last century in this direction by Sakata and co-workers have shown promising results in aqueous electrolyte.<sup>178,179</sup> High CO<sub>2</sub> local partial pressures may as well be achieved by increasing its relative solubility by switching to non-aqueous electrolyte, i.e., ionic liquids. Also, since cations such as Na<sup>+</sup>, K<sup>+</sup>, Cs<sup>+</sup> have shown to be essential in the catalytic CO<sub>2</sub> reduction and influences the selectivity in aqueous electrolyte, molecular cation engineering could be considered to tune selectivity towards desired products further.<sup>180</sup> Finally, issues associated with liquid electrolyte based-devices such as carbon losses and thus low conversion due to formation and cross-over of CO<sub>3</sub><sup>2-</sup> to the anode side, can be solved by switching to an all solid-state device as has been reported by Wang and co-workers.<sup>181</sup>

## 2.6.5. Scalable synthesis

Finally, leaps have been taken in the synthesis of various electrocatalysts of well-defined structure ranging from wet-synthesis (i.e., colloidal) to production of aerosols and physical deposition (i.e., magnetron sputtering). However, other than some SACs and a handful of atomically-precise clusters, most catalysts are produced with a broad distributions of sizes and/or geometries and/or active sites making it hard to formulate unifying postulations.

Therefore, more precise, scalable

production of particles and clusters could unlock a treasure trove of new information regarding performance optimization, as the most active and selective candidates can be identified and selected. In this way, cost-efficient electrocatalyst for all the relevant products of the CO<sub>2</sub>RR, which in the near-future may start uprooting the petroleum industry, can be unveiled with the speed necessary to tackle one of the biggest challenges mankind faces: the energy transition.



## 2.7. References

- (1) Ritchie, H.; Roser, M. Energy. *Our World in Data* **2020**.
- (2) US Department of Commerce, N. *Global Monitoring Laboratory - Carbon Cycle Greenhouse Gases*. <https://gml.noaa.gov/ccgg/trends/> (accessed 2021-08-16).
- (3) Stips, A.; Macias, D.; Coughlan, C.; Garcia-Gorriz, E.; Liang, X. S. On the Causal Structure between CO<sub>2</sub> and Global Temperature. *Sci Rep* **2016**, *6* (1), 1–9. <https://doi.org/10.1038/srep21691>.
- (4) *Fourteenth Session of Working Group I and Fifty-Fourth Session of the IPCC — IPCC*. <https://www.ipcc.ch/meeting-doc/ipcc-wgi-14-and-ipcc-54/> (accessed 2021-08-16).
- (5) Shin, H.; Hansen, K. U.; Jiao, F. Techno-Economic Assessment of Low-Temperature Carbon Dioxide Electrolysis. *Nat Sustain* **2021**, *4* (10), 911–919. <https://doi.org/10.1038/s41893-021-00739-x>.
- (6) Hori, Y.; Kikuchi, K.; Suzuki, S. Production of Co and CH<sub>4</sub> in Electrochemical Reduction of CO<sub>2</sub> at Metal Electrodes in Aqueous Hydrogencarbonate Solution. *Chem. Lett.* **1985**, *14* (11), 1695–1698. <https://doi.org/10.1246/cl.1985.1695>.
- (7) Jouny, M.; Luc, W.; Jiao, F. General Techno-Economic Analysis of CO<sub>2</sub> Electrolysis Systems. *Ind. Eng. Chem. Res.* **2018**, *57* (6), 2165–2177. <https://doi.org/10.1021/acs.iecr.7b03514>.
- (8) Verma, S.; Lu, S.; Kenis, P. J. A. Co-Electrolysis of CO<sub>2</sub> and Glycerol as a Pathway to Carbon Chemicals with Improved Technoeconomics Due to Low Electricity Consumption. *Nature Energy* **2019**, *4* (6), 466–474. <https://doi.org/10.1038/s41560-019-0374-6>.
- (9) Nitopi, S.; Bertheussen, E.; Scott, S. B.; Liu, X.; Engstfeld, A. K.; Horch, S.; Seger, B.; Stephens, I. E. L.; Chan, K.; Hahn, C.; Nørskov, J. K.; Jaramillo, T. F.; Chorkendorff, I. Progress and Perspectives of Electrochemical CO<sub>2</sub> Reduction on Copper in Aqueous Electrolyte. *Chemical Reviews* **2019**, *119* (12), 7610–7672. <https://doi.org/10.1021/acs.chemrev.8b00705>.
- (10) Liu, Y.; Yu, W.; Raciti, D.; Gracias, D. H.; Wang, C. Electrocatalytic Oxidation of Glycerol on Platinum. *J. Phys. Chem. C* **2019**, *123* (1), 426–432. <https://doi.org/10.1021/acs.jpcc.8b08547>.
- (11) Hori, Y.; Takahashi, R.; Yoshinami, Y.; Murata, A. Electrochemical Reduction of CO at a Copper Electrode. *J. Phys. Chem. B* **1997**, *101* (36), 7075–7081. <https://doi.org/10.1021/jp970284i>.
- (12) Hori, Y.; Takahashi, I.; Koga, O.; Hoshi, N. Electrochemical Reduction of Carbon Dioxide at Various Series of Copper Single Crystal Electrodes. *Journal of Molecular Catalysis A: Chemical* **2003**, *199* (1), 39–47. [https://doi.org/10.1016/S1381-1169\(03\)00016-5](https://doi.org/10.1016/S1381-1169(03)00016-5).
- (13) Zhai, Q.; Pan, Y.; Dai, L. Carbon-Based Metal-Free Electrocatalysts: Past, Present, and Future. *Acc. Mater. Res.* **2021**, *2* (12), 1239–1250. <https://doi.org/10.1021/accountsmr.1c00190>.
- (14) Gao, D.; Zhang, Y.; Zhou, Z.; Cai, F.; Zhao, X.; Huang, W.; Li, Y.; Zhu, J.; Liu, P.; Yang, F.; Wang, G.; Bao, X. Enhancing CO<sub>2</sub> Electroreduction with the Metal–Oxide Interface. *J. Am. Chem. Soc.* **2017**, *139* (16), 5652–5655. <https://doi.org/10.1021/jacs.7b00102>.
- (15)

- (17) Franco, F.; Rettenmaier, C.; Jeon, H. S.; Cuenya, B. R. Transition Metal-Based Catalysts for the Electrochemical CO<sub>2</sub> Reduction: From Atoms and Molecules to Nanostructured Materials. *Chem. Soc. Rev.* **2020**, *49* (19), 6884–6946. <https://doi.org/10.1039/D0CS00835D>.
- (18) Hori, Y.; Murata, A.; Takahashi, R. Formation of Hydrocarbons in the Electrochemical Reduction of Carbon Dioxide at a Copper Electrode in Aqueous Solution. *J. Chem. Soc., Faraday Trans. 1* **1989**, *85* (8), 2309–2326. <https://doi.org/10.1039/F19898502309>.
- (19) Hori, Y.; Wakebe, H.; Tsukamoto, T.; Koga, O. Adsorption of CO Accompanied with Simultaneous Charge Transfer on Copper Single Crystal Electrodes Related with Electrochemical Reduction of CO<sub>2</sub> to Hydrocarbons. *Surface Science* **1995**, *335*, 258–263. [https://doi.org/10.1016/0039-6028\(95\)00441-6](https://doi.org/10.1016/0039-6028(95)00441-6).
- (20) Hoshi, N.; Noma, M.; Suzuki, T.; Hori, Y. Structural Effect on the Rate of CO<sub>2</sub> Reduction on Single Crystal Electrodes of Palladium. *Journal of Electroanalytical Chemistry* **1997**, *421* (1), 15–18. [https://doi.org/10.1016/S0022-0728\(96\)01023-6](https://doi.org/10.1016/S0022-0728(96)01023-6).
- (21) Hoshi, N.; Suzuki, T.; Hori, Y. Catalytic Activity of CO<sub>2</sub> Reduction on Pt Single-Crystal Electrodes: Pt(S)-[n(111)×(111)], Pt(S)-[n(111)×(100)], and Pt(S)-[n(100)×(111)]. *J. Phys. Chem. B* **1997**, *101* (42), 8520–8524. <https://doi.org/10.1021/jp971294m>.
- (22) Hoshi, N.; Kato, M.; Hori, Y. Electrochemical Reduction of CO<sub>2</sub> on Single Crystal Electrodes of Silver Ag(111), Ag(100) and Ag(110). *Journal of Electroanalytical Chemistry* **1997**, *440* (1), 283–286. [https://doi.org/10.1016/S0022-0728\(97\)00447-6](https://doi.org/10.1016/S0022-0728(97)00447-6).
- (23) Hori, Y.; Takahashi, I.; Koga, O.; Hoshi, N. Selective Formation of C<sub>2</sub> Compounds from Electrochemical Reduction of CO<sub>2</sub> at a Series of Copper Single Crystal Electrodes. *J. Phys. Chem. B* **2002**, *106* (1), 15–17. <https://doi.org/10.1021/jp013478d>.
- (24) Takahashi, I.; Koga, O.; Hoshi, N.; Hori, Y. Electrochemical Reduction of CO<sub>2</sub> at Copper Single Crystal Cu(S)-[n(111)×(111)] and Cu(S)-[n(110)×(100)] Electrodes. *Journal of Electroanalytical Chemistry* **2002**, *533* (1), 135–143. [https://doi.org/10.1016/S0022-0728\(02\)01081-1](https://doi.org/10.1016/S0022-0728(02)01081-1).
- (25) Schouten, K. J. P.; Kwon, Y.; Ham, C. J. M. van der; Qin, Z.; Koper, M. T. M. A New Mechanism for the Selectivity to C<sub>1</sub> and C<sub>2</sub> Species in the Electrochemical Reduction of Carbon Dioxide on Copper Electrodes. *Chem. Sci.* **2011**, *2* (10), 1902–1909. <https://doi.org/10.1039/C1SC00277E>.
- (26) Schouten, K. J. P.; Pérez Gallent, E.; Koper, M. T. M. Structure Sensitivity of the Electrochemical Reduction of Carbon Monoxide on Copper Single Crystals. *ACS Catal.* **2013**, *3* (6), 1292–1295. <https://doi.org/10.1021/cs4002404>.
- (27) Todoroki, N.; Tei, H.; Tsurumaki, H.; Miyakawa, T.; Inoue, T.; Wadayama, T. Surface Atomic Arrangement Dependence of Electrochemical CO<sub>2</sub> Reduction on Gold: Online Electrochemical Mass Spectrometric Study on Low-Index Au(Hkl) Surfaces. *ACS Catal.* **2019**, *9* (2), 1383–1388. <https://doi.org/10.1021/acscatal.8b04852>.



- (28) Clark, E. L.; Ringe, S.; Tang, M.; Walton, A.; Hahn, C.; Jaramillo, T. F.; Chan, K.; Bell, A. T. Influence of Atomic Surface Structure on the Activity of Ag for the Electrochemical Reduction of CO<sub>2</sub> to CO. *ACS Catal.* **2019**, *9* (5), 4006–4014. <https://doi.org/10.1021/acscatal.9b00260>.
- (29) Scholten, F.; Nguyen, K.-L. C.; Bruce, J. P.; Heyde, M.; Roldan Cuenya, B. Identifying Structure–Selectivity Correlations in the Electrochemical Reduction of CO<sub>2</sub>: A Comparison of Well-Ordered Atomically Clean and Chemically Etched Copper Single-Crystal Surfaces. *Angewandte Chemie International Edition* **2021**, *60* (35), 19169–19175. <https://doi.org/10.1002/anie.202103102>.
- (30) Kauffman, D. R.; Alfonso, D.; Matranga, C.; Qian, H.; Jin, R. Experimental and Computational Investigation of Au<sub>25</sub> Clusters and CO<sub>2</sub>: A Unique Interaction and Enhanced Electrocatalytic Activity. *J. Am. Chem. Soc.* **2012**, *134* (24), 10237–10243. <https://doi.org/10.1021/ja303259q>.
- (31) Salehi-Khojin, A.; Jhong, H.-R. M.; Rosen, B. A.; Zhu, W.; Ma, S.; Kenis, P. J. A.; Masel, R. I. Nanoparticle Silver Catalysts That Show Enhanced Activity for Carbon Dioxide Electrolysis. *J. Phys. Chem. C* **2013**, *117* (4), 1627–1632. <https://doi.org/10.1021/jp310509z>.
- (32) Taheri, A.; Thompson, E. J.; Fettinger, J. C.; Berben, L. A. An Iron Electrocatalyst for Selective Reduction of CO<sub>2</sub> to Formate in Water: Including Thermochemical Insights. *ACS Catal.* **2015**, *5* (12), 7140–7151. <https://doi.org/10.1021/acscatal.5b01708>.
- (33) Tang, Q.; Lee, Y.; Li, D.-Y.; Choi, W.; Liu, C. W.; Lee, D.; Jiang, D. Lattice-Hydride Mechanism in Electrocatalytic CO<sub>2</sub> Reduction by Structurally Precise Copper-Hydride Nanoclusters. *J. Am. Chem. Soc.* **2017**, *139* (28), 9728–9736. <https://doi.org/10.1021/jacs.7b05591>.
- (34) Zhao, S.; Austin, N.; Li, M.; Song, Y.; House, S. D.; Bernhard, S.; Yang, J. C.; Mpourmpakis, G.; Jin, R. Influence of Atomic-Level Morphology on Catalysis: The Case of Sphere and Rod-Like Gold Nanoclusters for CO<sub>2</sub> Electroreduction. *ACS Catal.* **2018**, *8* (6), 4996–5001. <https://doi.org/10.1021/acscatal.8b00365>.
- (35) Zhu, W.; Michalsky, R.; Metin, Ö.; Lv, H.; Guo, S.; Wright, C. J.; Sun, X.; Peterson, A. A.; Sun, S. Monodisperse Au Nanoparticles for Selective Electrocatalytic Reduction of CO<sub>2</sub> to CO. *J. Am. Chem. Soc.* **2013**, *135* (45), 16833–16836. <https://doi.org/10.1021/ja409445p>.
- (36) Reske, R.; Mistry, H.; Behafarid, F.; Roldan Cuenya, B.; Strasser, P. Particle Size Effects in the Catalytic Electroreduction of CO<sub>2</sub> on Cu Nanoparticles. *J. Am. Chem. Soc.* **2014**, *136* (19), 6978–6986. <https://doi.org/10.1021/ja500328k>.
- (37) Mistry, H.; Reske, R.; Zeng, Z.; Zhao, Z.-J.; Greeley, J.; Strasser, P.; Cuenya, B. R. Exceptional Size-Dependent Activity Enhancement in the Electroreduction of CO<sub>2</sub> over Au Nanoparticles. *J. Am. Chem. Soc.* **2014**, *136* (47), 16473–16476. <https://doi.org/10.1021/ja508879j>.
- (38) Gao, D.; Zhou, H.; Wang, J.; Miao, S.; Yang, F.; Wang, G.; Wang, J.; Bao, X. Size-Dependent Electrocatalytic Reduction of CO<sub>2</sub> over Pd Nanoparticles. *J. Am. Chem. Soc.* **2015**, *137* (13), 4288–4291. <https://doi.org/10.1021/jacs.5b00046>.

- (39) Kim, C.; Jeon, H. S.; Eom, T.; Jee, M. S.; Kim, H.; Friend, C. M.; Min, B. K.; Hwang, Y. J. Achieving Selective and Efficient Electrocatalytic Activity for CO<sub>2</sub> Reduction Using Immobilized Silver Nanoparticles. *J. Am. Chem. Soc.* **2015**, *137* (43), 13844–13850. <https://doi.org/10.1021/jacs.5b06568>.
- (40) Rahaman, M.; Dutta, A.; Broekmann, P. Size-Dependent Activity of Palladium Nanoparticles: Efficient Conversion of CO<sub>2</sub> into Formate at Low Overpotentials. *ChemSusChem* **2017**, *10*(8), 1733–1741. <https://doi.org/10.1002/cssc.201601778>.
- (41) Mistry, H.; Reske, R.; Strasser, P.; Roldan Cuenya, B. Size-Dependent Reactivity of Gold-Copper Bimetallic Nanoparticles during CO<sub>2</sub> Electroreduction. *Catalysis Today* **2017**, *288*, 30–36. <https://doi.org/10.1016/j.cattod.2016.09.017>.
- (42) Jeon, H. S.; Sinev, I.; Scholten, F.; Divins, N. J.; Zegkinoglou, I.; Pielsticker, L.; Cuenya, B. R. Operando Evolution of the Structure and Oxidation State of Size-Controlled Zn Nanoparticles during CO<sub>2</sub> Electroreduction. *J. Am. Chem. Soc.* **2018**, *140* (30), 9383–9386. <https://doi.org/10.1021/jacs.8b05258>.
- (43) Bernal, M.; Bagger, A.; Scholten, F.; Sinev, I.; Bergmann, A.; Ahmadi, M.; Rossmeisl, J.; Cuenya, B. R. CO<sub>2</sub> Electroreduction on Copper-Cobalt Nanoparticles: Size and Composition Effect. *Nano Energy* **2018**, *53*, 27–36. <https://doi.org/10.1016/j.nanoen.2018.08.027>.
- (44) Loiudice, A.; Lobaccaro, P.; Kamali, E. A.; Thao, T.; Huang, B. H.; Ager, J. W.; Buonsanti, R. Tailoring Copper Nanocrystals towards C<sub>2</sub> Products in Electrochemical CO<sub>2</sub> Reduction. *Angewandte Chemie International Edition* **2016**, *55*(19), 5789–5792. <https://doi.org/10.1002/anie.201601582>.
- (45) Grosse, P.; Gao, D.; Scholten, F.; Sinev, I.; Mistry, H.; Roldan Cuenya, B. Dynamic Changes in the Structure, Chemical State and Catalytic Selectivity of Cu Nanocubes during CO<sub>2</sub> Electroreduction: Size and Support Effects. *Angewandte Chemie International Edition* **2018**, *57* (21), 6192–6197. <https://doi.org/10.1002/anie.201802083>.
- (46) Hori, Y. Electrochemical CO<sub>2</sub> Reduction on Metal Electrodes. In *Modern Aspects of Electrochemistry*; Vayenas, C. G., White, R. E., Gamboa-Aldeco, M. E., Eds.; Modern Aspects of Electrochemistry; Springer: New York, NY, 2008; pp 89–189. [https://doi.org/10.1007/978-0-387-49489-0\\_3](https://doi.org/10.1007/978-0-387-49489-0_3).
- (47) Ginger, D. S.; Zhang, H.; Mirkin, C. A. The Evolution of Dip-Pen Nanolithography. *Angewandte Chemie International Edition* **2004**, *43* (1), 30–45. <https://doi.org/10.1002/anie.200300608>.

- (48) Xia, Y.; Xiong, Y.; Lim, B.; Skrabalak, S. E. Shape-Controlled Synthesis of Metal Nanocrystals: Simple Chemistry Meets Complex Physics? *Angewandte Chemie International Edition* **2009**, *48* (1), 60–103. <https://doi.org/10.1002/anie.200802248>.
- (49) Wu, Y.; Wang, D.; Li, Y. Nanocrystals from Solutions: Catalysts. *Chem. Soc. Rev.* **2014**, *43* (7), 2112–2124. <https://doi.org/10.1039/C3CS60221D>.
- (50) Chen, P.-C.; Liu, G.; Zhou, Y.; Brown, K. A.; Chernyak, N.; Hedrick, J. L.; He, S.; Xie, Z.; Lin, Q.-Y.; Dravid, V. P.; O'Neill-Slawecki, S. A.; Mirkin, C. A. Tip-Directed Synthesis of Multimetallic Nanoparticles. *J. Am. Chem. Soc.* **2015**, *137* (28), 9167–9173. <https://doi.org/10.1021/jacs.5b05139>.
- (51) Wu, Z.-Y.; Zhu, P.; Cullen, D. A.; Hu, Y.; Yan, Q.-Q.; Shen, S.-C.; Chen, F.-Y.; Yu, H.; Shakouri, M.; Arregui-Mena, J. D.; Ziabari, A.; Paterson, A. R.; Liang, H.-W.; Wang, H. A General Synthesis of Single Atom Catalysts with Controllable Atomic and Mesoporous Structures. *Nat. Synth* **2022**, *1* (8), 658–667. <https://doi.org/10.1038/s44160-022-00129-x>.
- (52) Xia, C.; Qiu, Y.; Xia, Y.; Zhu, P.; King, G.; Zhang, X.; Wu, Z.; Kim, J. Y. (Timothy); Cullen, D. A.; Zheng, D.; Li, P.; Shakouri, M.; Heredia, E.; Cui, P.; Alshareef, H. N.; Hu, Y.; Wang, H. General Synthesis of Single-Atom Catalysts with High Metal Loading Using Graphene Quantum Dots. *Nat. Chem.* **2021**, *13* (9), 887–894. <https://doi.org/10.1038/s41557-021-00734-x>.
- (53) Liu, M.; Kong, Y.; Hu, H.; Kovács, N.; Sun, C.; Zelocualtecatl Montiel, I.; Gálvez Vázquez, M. de J.; Hou, Y.; Mirolo, M.; Martens, I.; Drnec, J.; Vesztergom, S.; Broekmann, P. The Capping Agent Is the Key: Structural Alterations of Ag NPs during CO<sub>2</sub> Electrolysis Probed in a Zero-Gap Gas-Flow Configuration. *Journal of Catalysis* **2021**, *404*, 371–382. <https://doi.org/10.1016/j.jcat.2021.10.016>.
- (54) Varela, A. S.; Ju, W.; Strasser, P. Molecular Nitrogen–Carbon Catalysts, Solid Metal Organic Framework Catalysts, and Solid Metal/Nitrogen-Doped Carbon (MNC) Catalysts for the Electrochemical CO<sub>2</sub> Reduction. *Advanced Energy Materials* **2018**, *8* (30), 1703614. <https://doi.org/10.1002/aenm.201703614>.
- (55) Lü, F.; Bao, H.; Mi, Y.; Liu, Y.; Sun, J.; Peng, X.; Qiu, Y.; Zhuo, L.; Liu, X.; Luo, J. Electrochemical CO<sub>2</sub> Reduction: From Nanoclusters to Single Atom Catalysts. *Sustainable Energy Fuels* **2020**, *4* (3), 1012–1028. <https://doi.org/10.1039/C9SE00776H>.
- (56) Schneider, J.; Jia, H.; Kobi, K.; Cabelli, D. E.; Muckerman, J. T.; Fujita, E. Nickel(II) Macrocycles: Highly Efficient Electrocatalysts for the Selective Reduction of CO<sub>2</sub> to CO. *Energy Environ. Sci.* **2012**, *5* (11), 9502–9510. <https://doi.org/10.1039/C2EE22528J>.
- (57) Varela, A. S.; Ranjbar Sahraie, N.; Steinberg, J.; Ju, W.; Oh, H.-S.; Strasser, P. Metal-Doped Nitrogenated Carbon as an Efficient Catalyst for Direct CO<sub>2</sub> Electroreduction to CO and Hydrocarbons. *Angewandte Chemie International Edition* **2015**, *54* (37), 10758–10762. <https://doi.org/10.1002/anie.201502099>.

- (58) Hossain, M. D.; Huang, Y.; Yu, T. H.; Goddard III, W. A.; Luo, Z. Reaction Mechanism and Kinetics for CO<sub>2</sub> Reduction on Nickel Single Atom Catalysts from Quantum Mechanics. *Nat Commun* **2020**, *11* (1), 2256. <https://doi.org/10.1038/s41467-020-16119-6>.
- (59) Yang, H. B.; Hung, S.-F.; Liu, S.; Yuan, K.; Miao, S.; Zhang, L.; Huang, X.; Wang, H.-Y.; Cai, W.; Chen, R.; Gao, J.; Yang, X.; Chen, W.; Huang, Y.; Chen, H. M.; Li, C. M.; Zhang, T.; Liu, B. Atomically Dispersed Ni( i ) as the Active Site for Electrochemical CO<sub>2</sub> Reduction. *Nature Energy* **2018**, *3* (2), 140–147. <https://doi.org/10.1038/s41560-017-0078-8>.
- (60) Liu, L.; Corma, A. Metal Catalysts for Heterogeneous Catalysis: From Single Atoms to Nanoclusters and Nanoparticles. *Chem. Rev.* **2018**, *118* (10), 4981–5079. <https://doi.org/10.1021/acs.chemrev.7b00776>.
- (61) Zhang, L.; Zhou, M.; Wang, A.; Zhang, T. Selective Hydrogenation over Supported Metal Catalysts: From Nanoparticles to Single Atoms. *Chem. Rev.* **2020**, *120* (2), 683–733. <https://doi.org/10.1021/acs.chemrev.9b00230>.
- (62) Peterson, A. A.; Abild-Pedersen, F.; Studt, F.; Rossmeisl, J.; Nørskov, J. K. How Copper Catalyzes the Electroreduction of Carbon Dioxide into Hydrocarbon Fuels. *Energy Environ. Sci.* **2010**, *3* (9), 1311–1315. <https://doi.org/10.1039/C0EE00071J>.
- (63) Nørskov, J. K.; Abild-Pedersen, F.; Studt, F.; Bligaard, T. Density Functional Theory in Surface Chemistry and Catalysis. *PNAS* **2011**, *108* (3), 937–943. <https://doi.org/10.1073/pnas.1006652108>.
- (64) Peterson, A. A.; Nørskov, J. K. Activity Descriptors for CO<sub>2</sub> Electroreduction to Methane on Transition-Metal Catalysts. *J. Phys. Chem. Lett.* **2012**, *3* (2), 251–258. <https://doi.org/10.1021/jz201461p>.
- (65) Kirk, C.; Chen, L. D.; Siahrostami, S.; Karamad, M.; Bajdich, M.; Voss, J.; Nørskov, J. K.; Chan, K. Theoretical Investigations of the Electrochemical Reduction of CO on Single Metal Atoms Embedded in Graphene. *ACS Cent. Sci.* **2017**, *3* (12), 1286–1293. <https://doi.org/10.1021/acscentsci.7b00442>.
- (66) Ju, W.; Bagger, A.; Hao, G.-P.; Varela, A. S.; Sinev, I.; Bon, V.; Roldan Cuenya, B.; Kaskel, S.; Rossmeisl, J.; Strasser, P. Understanding Activity and Selectivity of Metal-Nitrogen-Doped Carbon Catalysts for Electrochemical Reduction of CO<sub>2</sub>. *Nature Communications* **2017**, *8* (1), 944. <https://doi.org/10.1038/s41467-017-01035-z>.
- (67) Feng, X.; Jiang, K.; Fan, S.; Kanan, M. W. Grain-Boundary-Dependent CO<sub>2</sub> Electroreduction Activity. *J. Am. Chem. Soc.* **2015**, *137* (14), 4606–4609. <https://doi.org/10.1021/ja5130513>.
- (68) Feng, X.; Jiang, K.; Fan, S.; Kanan, M. W. A Direct Grain-Boundary-Activity Correlation for CO Electroreduction on Cu Nanoparticles. *ACS Cent. Sci.* **2016**, *2* (3), 169–174. <https://doi.org/10.1021/acscentsci.6b00022>.
- (69) Wang, Y.; Han, P.; Lv, X.; Zhang, L.; Zheng, G. Defect and Interface Engineering for Aqueous Electrocatalytic CO<sub>2</sub> Reduction. *Joule* **2018**, *2* (12), 2551–2582. <https://doi.org/10.1016/j.joule.2018.09.021>.

- (70) Mezzavilla, S.; Horch, S.; Stephens, I. E. L.; Seger, B.; Chorkendorff, I. Structure Sensitivity in the Electrocatalytic Reduction of CO<sub>2</sub> with Gold Catalysts. *Angewandte Chemie International Edition* **2019**, *58* (12), 3774–3778. <https://doi.org/10.1002/anie.201811422>.
- (71) Kang, M. P. L.; Kolb, M. J.; Calle-Vallejo, F.; Yeo, B. S. The Role of Undercoordinated Sites on Zinc Electrodes for CO<sub>2</sub> Reduction to CO. *Advanced Functional Materials* **2022**, *32* (23), 2111597. <https://doi.org/10.1002/adfm.202111597>.
- (72) Deng, W.; Zhang, P.; Seger, B.; Gong, J. Unraveling the Rate-Limiting Step of Two-Electron Transfer Electrochemical Reduction of Carbon Dioxide. *Nat Commun* **2022**, *13* (1), 803. <https://doi.org/10.1038/s41467-022-28436-z>.
- (73) Rosen, J.; Hutchings, G. S.; Lu, Q.; Rivera, S.; Zhou, Y.; Vlachos, D. G.; Jiao, F. Mechanistic Insights into the Electrochemical Reduction of CO<sub>2</sub> to CO on Nanostructured Ag Surfaces. *ACS Catal.* **2015**, *5* (7), 4293–4299. <https://doi.org/10.1021/acscatal.5b00840>.
- (74) Back, S.; Yeom, M. S.; Jung, Y. Active Sites of Au and Ag Nanoparticle Catalysts for CO<sub>2</sub> Electroreduction to CO. *ACS Catal.* **2015**, *5* (9), 5089–5096. <https://doi.org/10.1021/acscatal.5b00462>.
- (75) Sullivan, B. P.; Krist, K.; Guard, H. E. *Electrochemical and Electrocatalytic Reactions of Carbon Dioxide*; Elsevier, 1993.
- (76) Schouten, K. J. P.; Qin, Z.; Pérez Gallent, E.; Koper, M. T. M. Two Pathways for the Formation of Ethylene in CO Reduction on Single-Crystal Copper Electrodes. *J. Am. Chem. Soc.* **2012**, *134* (24), 9864–9867. <https://doi.org/10.1021/ja302668n>.
- (77) Calle-Vallejo, F.; Koper, M. T. M. Theoretical Considerations on the Electroreduction of CO to C<sub>2</sub> Species on Cu(100) Electrodes. *Angewandte Chemie International Edition* **2013**, *52* (28), 7282–7285. <https://doi.org/10.1002/anie.201301470>.
- (78) Pérez-Gallent, E.; Figueiredo, M. C.; Calle-Vallejo, F.; Koper, M. T. M. Spectroscopic Observation of a Hydrogenated CO Dimer Intermediate During CO Reduction on Cu(100) Electrodes. *Angewandte Chemie International Edition* **2017**, *56* (13), 3621–3624. <https://doi.org/10.1002/anie.201700580>.
- (79) Li, H.; Li, Y.; Koper, M. T. M.; Calle-Vallejo, F. Bond-Making and Breaking between Carbon, Nitrogen, and Oxygen in Electrocatalysis. *J. Am. Chem. Soc.* **2014**, *136* (44), 15694–15701. <https://doi.org/10.1021/ja508649p>.
- (80) Piqué, O.; Low, Q. H.; Handoko, A. D.; Yeo, B. S.; Calle-Vallejo, F. Selectivity Map for the Late Stages of CO and CO<sub>2</sub> Reduction to C<sub>2</sub> Species on Copper Electrodes. *Angewandte Chemie International Edition* **2021**, *60* (19), 10784–10790. <https://doi.org/10.1002/anie.202014060>.
- (81) Durand, W. J.; Peterson, A. A.; Studt, F.; Abild-Pedersen, F.; Nørskov, J. K. Structure Effects on the Energetics of the Electrochemical Reduction of CO<sub>2</sub> by Copper Surfaces. *Surface Science* **2011**, *605* (15), 1354–1359. <https://doi.org/10.1016/j.susc.2011.04.028>.

- (82) Verga, L. G.; Mendes, P. C. D.; Ocampo-Restrepo, V. K.; Silva, J. L. F. D. Exploring the Adsorption Site Coordination as a Strategy to Tune Copper Catalysts for CO<sub>2</sub> Electro-Reduction. *Catal. Sci. Technol.* **2022**, *12* (3), 869–879. <https://doi.org/10.1039/D1CY02010B>.
- (83) Zhao, Z.; Chen, Z.; Zhang, X.; Lu, G. Generalized Surface Coordination Number as an Activity Descriptor for CO<sub>2</sub> Reduction on Cu Surfaces. *J. Phys. Chem. C* **2016**, *120* (49), 28125–28130. <https://doi.org/10.1021/acs.jpcc.6b10155>.
- (84) Schouten, K. J. P.; Pérez Gallent, E.; Koper, M. T. M. The Influence of PH on the Reduction of CO and CO<sub>2</sub> to Hydrocarbons on Copper Electrodes. *Journal of Electroanalytical Chemistry* **2014**, *716*, 53–57. <https://doi.org/10.1016/j.jelechem.2013.08.033>.
- (85) Bagger, A.; Ju, W.; Varela, A. S.; Strasser, P.; Rossmeisl, J. Electrochemical CO<sub>2</sub> Reduction: Classifying Cu Facets. *ACS Catal.* **2019**, *9* (9), 7894–7899. <https://doi.org/10.1021/acscatal.9b01899>.
- (86) Van Hardeveld, R.; Hartog, F. The Statistics of Surface Atoms and Surface Sites on Metal Crystals. *Surface Science* **1969**, *15* (2), 189–230. [https://doi.org/10.1016/0039-6028\(69\)90148-4](https://doi.org/10.1016/0039-6028(69)90148-4).
- (87) Iyengar, P.; Huang, J.; Gregorio, G. L. D.; Gadiyar, C.; Buonsanti, R. Size Dependent Selectivity of Cu Nano-Octahedra Catalysts for the Electrochemical Reduction of CO<sub>2</sub> to CH<sub>4</sub>. *Chem. Commun.* **2019**, *55* (60), 8796–8799. <https://doi.org/10.1039/C9CC02522G>.
- (88) Mangione, G.; Huang, J.; Buonsanti, R.; Corminboeuf, C. Dual-Facet Mechanism in Copper Nanocubes for Electrochemical CO<sub>2</sub> Reduction into Ethylene. *J. Phys. Chem. Lett.* **2019**, *10* (15), 4259–4265. <https://doi.org/10.1021/acs.jpcclett.9b01471>.
- (89) Chen, J.; Wang, L. Effects of the Catalyst Dynamic Changes and Influence of the Reaction Environment on the Performance of Electrochemical CO<sub>2</sub> Reduction. *Advanced Materials* **2022**, *34* (25), 2103900. <https://doi.org/10.1002/adma.202103900>.
- (90) Popović, S.; Smiljanić, M.; Jovanović, P.; Vavra, J.; Buonsanti, R.; Hodnik, N. Stability and Degradation Mechanisms of Copper-Based Catalysts for Electrochemical CO<sub>2</sub> Reduction. *Angewandte Chemie International Edition* **2020**, *59* (35), 14736–14746. <https://doi.org/10.1002/anie.202000617>.
- (91) Huang, J.; Hörmann, N.; Oveisi, E.; Loiudice, A.; De Gregorio, G. L.; Andreussi, O.; Marzari, N.; Buonsanti, R. Potential-Induced Nanoclustering of Metallic Catalysts during Electrochemical CO<sub>2</sub> Reduction. *Nature Communications* **2018**, *9* (1), 3117. <https://doi.org/10.1038/s41467-018-05544-3>.
- (92) Magnin, Y.; Villermaux, E.; Amara, H.; Bichara, C.; Pellenq, R. J. M. Morphology Control of Metallic Nanoparticles Supported on Carbon Substrates in Catalytic Conditions. *Carbon* **2020**, *159*, 504–511. <https://doi.org/10.1016/j.carbon.2019.12.025>.

- (93) Dinh, C.-T.; Burdyny, T.; Kibria, M. G.; Seifitokaldani, A.; Gabardo, C. M.; Arquer, F. P. G. de; Kiani, A.; Edwards, J. P.; Luna, P. D.; Bushuyev, O. S.; Zou, C.; Quintero-Bermudez, R.; Pang, Y.; Sinton, D.; Sargent, E. H. CO<sub>2</sub> Electroreduction to Ethylene via Hydroxide-Mediated Copper Catalysis at an Abrupt Interface. *Science* **2018**, *360* (6390), 783–787. <https://doi.org/10.1126/science.aas9100>.
- (94) Kim, C.; Bui, J. C.; Luo, X.; Cooper, J. K.; Kusoglu, A.; Weber, A. Z.; Bell, A. T. Tailored Catalyst Microenvironments for CO<sub>2</sub> Electroreduction to Multicarbon Products on Copper Using Bilayer Ionomer Coatings. *Nat Energy* **2021**, *6* (11), 1026–1034. <https://doi.org/10.1038/s41560-021-00920-8>.
- (95) Pham, T. H. M.; Zhang, J.; Li, M.; Shen, T.-H.; Ko, Y.; Tileli, V.; Luo, W.; Züttel, A. Enhanced Electrocatalytic CO<sub>2</sub> Reduction to C<sub>2</sub>+ Products by Adjusting the Local Reaction Environment with Polymer Binders. *Advanced Energy Materials* **2022**, *12* (9), 2103663. <https://doi.org/10.1002/aenm.202103663>.
- (96) Deng, X.; Alfonso, D.; Nguyen-Phan, T.-D.; Kauffman, D. R. Resolving the Size-Dependent Transition between CO<sub>2</sub> Reduction Reaction and H<sub>2</sub> Evolution Reaction Selectivity in Sub-5 Nm Silver Nanoparticle Electrocatalysts. *ACS Catal.* **2022**, 5921–5929. <https://doi.org/10.1021/acscatal.2c00960>.
- (97) Huang, Y.; Mao, X.; Yuan, G.; Zhang, D.; Pan, B.; Deng, J.; Shi, Y.; Han, N.; Li, C.; Zhang, L.; Wang, L.; He, L.; Li, Y.; Li, Y. Size-Dependent Selectivity of Electrochemical CO<sub>2</sub> Reduction on Converted In<sub>2</sub>O<sub>3</sub> Nanocrystals. *Angewandte Chemie International Edition* **2021**, *60* (29), 15844–15848. <https://doi.org/10.1002/anie.202105256>.
- (98) Hochfilzer, D.; Sørensen, J. E.; Clark, E. L.; Scott, S. B.; Chorkendorff, I.; Kibsgaard, J. The Importance of Potential Control for Accurate Studies of Electrochemical CO Reduction. *ACS Energy Lett.* **2021**, 1879–1885. <https://doi.org/10.1021/acscenergylett.1c00496>.
- (99) Weng, Z.; Wu, Y.; Wang, M.; Jiang, J.; Yang, K.; Huo, S.; Wang, X.-F.; Ma, Q.; Brudvig, G. W.; Batista, V. S.; Liang, Y.; Feng, Z.; Wang, H. Active Sites of Copper-Complex Catalytic Materials for Electrochemical Carbon Dioxide Reduction. *Nature Communications* **2018**, *9* (1), 415. <https://doi.org/10.1038/s41467-018-02819-7>.
- (100) Kim, D.; Resasco, J.; Yu, Y.; Asiri, A. M.; Yang, P. Synergistic Geometric and Electronic Effects for Electrochemical Reduction of Carbon Dioxide Using Gold–Copper Bimetallic Nanoparticles. *Nature Communications* **2014**, *5* (1), 1–8. <https://doi.org/10.1038/ncomms5948>.
- (101) Pfeiffer, T. V.; Feng, J.; Schmidt-Ott, A. New Developments in Spark Production of Nanoparticles. *Advanced Powder Technology* **2014**, *25* (1), 56–70. <https://doi.org/10.1016/j.apt.2013.12.005>.
- (102) Wondergem, C. S.; Kromwijk, J. J. G.; Slagter, M.; Vrijburg, W. L.; Hensen, E. J. M.; Monai, M.; Vogt, C.; Weckhuysen, B. M. In Situ Shell-Isolated Nanoparticle-Enhanced Raman Spectroscopy of Nickel-Catalyzed Hydrogenation Reactions. *ChemPhysChem* **2020**, *21* (7), 625–632. <https://doi.org/10.1002/cphc.201901162>.

- (103) Becker, R.; Weber, K.; Pfeiffer, T. V.; Kranendonk, J. van; Schouten, K. J. A Scalable High-Throughput Deposition and Screening Setup Relevant to Industrial Electrocatalysis. *Catalysts* **2020**, *10* (10), 1165. <https://doi.org/10.3390/catal10101165>.
- (104) Iyengar, P.; Kolb, M. J.; Pankhurst, J.; Calle-Vallejo, F.; Buonsanti, R. Theory-Guided Enhancement of CO<sub>2</sub> Reduction to Ethanol on Ag–Cu Tandem Catalysts via Particle-Size Effects. *ACS Catal.* **2021**, *11* (21), 13330–13336. <https://doi.org/10.1021/acscatal.1c03717>.
- (105) Iyengar, P.; Kolb, M. J.; Pankhurst, J. R.; Calle-Vallejo, F.; Buonsanti, R. Elucidating the Facet-Dependent Selectivity for CO<sub>2</sub> Electroreduction to Ethanol of Cu–Ag Tandem Catalysts. *ACS Catal.* **2021**, *11* (8), 4456–4463. <https://doi.org/10.1021/acscatal.1c00420>.
- (106) Arenz, M.; Gilb, S.; Heiz, U. Chapter 1 Size Effects in the Chemistry of Small Clusters. In *The Chemical Physics of Solid Surfaces*; Woodruff, D. P., Ed.; Atomic Clusters: From Gas Phase to Deposited; Elsevier, 2007; Vol. 12, pp 1–51. [https://doi.org/10.1016/S1571-0785\(07\)12001-0](https://doi.org/10.1016/S1571-0785(07)12001-0).
- (107) Gilb, S.; Weis, P.; Furche, F.; Ahlrichs, R.; Kappes, M. M. Structures of Small Gold Cluster Cations (Au<sup>n+</sup>, N<14): Ion Mobility Measurements versus Density Functional Calculations. *J. Chem. Phys.* **2002**, *116* (10), 4094–4101. <https://doi.org/10.1063/1.1445121>.
- (108) Rao, B. K.; Jena, P. Evolution of the Electronic Structure and Properties of Neutral and Charged Aluminum Clusters: A Comprehensive Analysis. *Journal of Chemical Physics* **1999**, *111* (5), 1890–1904. <https://doi.org/10.1063/1.479458>.
- (109) Maisser, A.; Barmounis, K.; Holm, S.; Attoui, M.; Schmidt-Ott, A.; Kangasluoma, J.; Biskos, G. Characterization of Atmospheric-Pressure Spark Generated Atomic Silver and Gold Clusters by Time-of-Flight Mass Spectrometry. *Journal of Aerosol Science* **2021**, *156*, 105780. <https://doi.org/10.1016/j.jaerosci.2021.105780>.
- (110) Furche, F.; Ahlrichs, R.; Weis, P.; Jacob, C.; Gilb, S.; Bierweiler, T.; Kappes, M. M. The Structures of Small Gold Cluster Anions as Determined by a Combination of Ion Mobility Measurements and Density Functional Calculations. *J. Chem. Phys.* **2002**, *117* (15), 6982–6990. <https://doi.org/10.1063/1.1507582>.
- (111) Vajda, S.; Pellin, M. J.; Greeley, J. P.; Marshall, C. L.; Curtiss, L. A.; Ballentine, G. A.; Elam, J. W.; Catillon-Mucherie, S.; Redfern, P. C.; Mehmood, F.; Zapol, P. Subnanometre Platinum Clusters as Highly Active and Selective Catalysts for the Oxidative Dehydrogenation of Propane. *Nature Mater* **2009**, *8* (3), 213–216. <https://doi.org/10.1038/nmat2384>.
- (112) Nesselberger, M.; Roefzaad, M.; Fayçal Hamou, R.; Ulrich Biedermann, P.; Schweinberger, F. F.; Kunz, S.; Schloegl, K.; Wiberg, G. K. H.; Ashton, S.; Heiz, U.; Mayrhofer, K. J. J.; Arenz, M. The Effect of Particle Proximity on the Oxygen Reduction Rate of Size-Selected Platinum Clusters. *Nature Mater* **2013**, *12* (10), 919–924. <https://doi.org/10.1038/nmat3712>.
- (113) Palmer, R. E.; Pratontep, S.; Boyen, H.-G. Nanostructured Surfaces from Size-Selected Clusters. *Nature Mater* **2003**, *2* (7), 443–448. <https://doi.org/10.1038/nmat897>.



- (114) Sattler, K.; Mühlbach, J.; Recknagel, E. Generation of Metal Clusters Containing from 2 to 500 Atoms. *Phys. Rev. Lett.* **1980**, *45* (10), 821–824. <https://doi.org/10.1103/PhysRevLett.45.821>.
- (115) Seong, H.; Efremov, V.; Park, G.; Kim, H.; Yoo, J. S.; Lee, D. Atomically Precise Gold Nanoclusters as Model Catalysts for Identifying Active Sites for Electroreduction of CO<sub>2</sub>. *Angewandte Chemie International Edition* **2021**, *60* (26), 14563–14570. <https://doi.org/10.1002/anie.202102887>.
- (116) Karapinar, D.; Huan, N. T.; Sahraie, N. R.; Li, J.; Wakerley, D.; Touati, N.; Zanna, S.; Taverna, D.; Tizei, L. H. G.; Zitolo, A.; Jaouen, F.; Mougél, V.; Fontecave, M. Electroreduction of CO<sub>2</sub> on Single-Site Copper-Nitrogen-Doped Carbon Material: Selective Formation of Ethanol and Reversible Restructuration of the Metal Sites. *Angewandte Chemie International Edition* **2019**, *58* (42), 15098–15103. <https://doi.org/10.1002/anie.201907994>.
- (117) Xu, H.; Rebollar, D.; He, H.; Chong, L.; Liu, Y.; Liu, C.; Sun, C.-J.; Li, T.; Muntean, J. V.; Winans, R. E.; Liu, D.-J.; Xu, T. Highly Selective Electrocatalytic CO<sub>2</sub> Reduction to Ethanol by Metallic Clusters Dynamically Formed from Atomically Dispersed Copper. *Nature Energy* **2020**, *5* (8), 623–632. <https://doi.org/10.1038/s41560-020-0666-x>.
- (118) Tyo, E. C.; Vajda, S. Catalysis by Clusters with Precise Numbers of Atoms. *Nature Nanotechnology* **2015**, *10* (7), 577–588. <https://doi.org/10.1038/nnano.2015.140>.
- (119) Li, S.; Alfonso, D.; Nagarajan, A. V.; House, S. D.; Yang, J. C.; Kauffman, D. R.; Mpourmpakis, G.; Jin, R. Monopalladium Substitution in Gold Nanoclusters Enhances CO<sub>2</sub> Electroreduction Activity and Selectivity. *ACS Catal.* **2020**, *10* (20), 12011–12016. <https://doi.org/10.1021/acscatal.0c02266>.
- (120) Li, S.; Nagarajan, A. V.; Alfonso, D. R.; Sun, M.; Kauffman, D. R.; Mpourmpakis, G.; Jin, R. Boosting CO<sub>2</sub> Electrochemical Reduction with Atomically Precise Surface Modification on Gold Nanoclusters. *Angewandte Chemie International Edition* **2021**, *60* (12), 6351–6356. <https://doi.org/10.1002/anie.202016129>.
- (121) Appel, A. M.; Bercaw, J. E.; Bocarsly, A. B.; Dobbek, H.; DuBois, D. L.; Dupuis, M.; Ferry, J. G.; Fujita, E.; Hille, R.; Kenis, P. J. A.; Kerfeld, C. A.; Morris, R. H.; Peden, C. H. F.; Portis, A. R.; Ragsdale, S. W.; Rauchfuss, T. B.; Reek, J. N. H.; Seefeldt, L. C.; Thauer, R. K.; Waldrop, G. L. Frontiers, Opportunities, and Challenges in Biochemical and Chemical Catalysis of CO<sub>2</sub> Fixation. *Chem. Rev.* **2013**, *113* (8), 6621–6658. <https://doi.org/10.1021/cr300463y>.
- (122) Bonin, J.; Chaussemier, M.; Robert, M.; Routier, M. Homogeneous Photocatalytic Reduction of CO<sub>2</sub> to CO Using Iron(0) Porphyrin Catalysts: Mechanism and Intrinsic Limitations. *ChemCatChem* **2014**, *6* (11), 3200–3207. <https://doi.org/10.1002/cctc.201402515>.
- (123) Hinogami, R.; Yotsuhashi, S.; Deguchi, M.; Zenitani, Y.; Hashiba, H.; Yamada, Y. Electrochemical Reduction of Carbon Dioxide Using a Copper Rubeanate Metal Organic Framework. *ECS Electrochem. Lett.* **2012**, *1* (4), H17. <https://doi.org/10.1149/2.001204eel>.

- (124) Hod, I.; Sampson, M. D.; Deria, P.; Kubiak, C. P.; Farha, O. K.; Hupp, J. T. Fe-Porphyrin-Based Metal–Organic Framework Films as High-Surface Concentration, Heterogeneous Catalysts for Electrochemical Reduction of CO<sub>2</sub>. *ACS Catal.* **2015**, *5* (11), 6302–6309. <https://doi.org/10.1021/acscatal.5b01767>.
- (125) Kornienko, N.; Zhao, Y.; Kley, C. S.; Zhu, C.; Kim, D.; Lin, S.; Chang, C. J.; Yaghi, O. M.; Yang, P. Metal–Organic Frameworks for Electrocatalytic Reduction of Carbon Dioxide. *J. Am. Chem. Soc.* **2015**, *137* (44), 14129–14135. <https://doi.org/10.1021/jacs.5b08212>.
- (126) Dong, B.-X.; Qian, S.-L.; Bu, F.-Y.; Wu, Y.-C.; Feng, L.-G.; Teng, Y.-L.; Liu, W.-L.; Li, Z.-W. Electrochemical Reduction of CO<sub>2</sub> to CO by a Heterogeneous Catalyst of Fe–Porphyrin-Based Metal–Organic Framework. *ACS Appl. Energy Mater.* **2018**, *1* (9), 4662–4669. <https://doi.org/10.1021/acsaem.8b00797>.
- (127) Matheu, R.; Gutierrez-Puebla, E.; Monge, M. Á.; Diercks, C. S.; Kang, J.; Prévot, M. S.; Pei, X.; Hanikel, N.; Zhang, B.; Yang, P.; Yaghi, O. M. Three-Dimensional Phthalocyanine Metal–Catecholates for High Electrochemical Carbon Dioxide Reduction. *J. Am. Chem. Soc.* **2019**, *141* (43), 17081–17085. <https://doi.org/10.1021/jacs.9b09298>.
- (128) Kang, X.; Wang, B.; Hu, K.; Lyu, K.; Han, X.; Spencer, B. F.; Frogley, M. D.; Tuna, F.; McInnes, E. J. L.; Dryfe, R. A. W.; Han, B.; Yang, S.; Schröder, M. Quantitative Electro-Reduction of CO<sub>2</sub> to Liquid Fuel over Electro-Synthesized Metal–Organic Frameworks. *J. Am. Chem. Soc.* **2020**, *142* (41), 17384–17392. <https://doi.org/10.1021/jacs.0c05913>.
- (129) Meng, Z.; Luo, J.; Li, W.; Mirica, K. A. Hierarchical Tuning of the Performance of Electrochemical Carbon Dioxide Reduction Using Conductive Two-Dimensional Metallophthalocyanine Based Metal–Organic Frameworks. *J. Am. Chem. Soc.* **2020**, *142* (52), 21656–21669. <https://doi.org/10.1021/jacs.0c07041>.
- (130) Lin, S.; Diercks, C. S.; Zhang, Y.-B.; Kornienko, N.; Nichols, E. M.; Zhao, Y.; Paris, A. R.; Kim, D.; Yang, P.; Yaghi, O. M.; Chang, C. J. Covalent Organic Frameworks Comprising Cobalt Porphyrins for Catalytic CO<sub>2</sub> Reduction in Water. *Science* **2015**, *349* (6253), 1208–1213. <https://doi.org/10.1126/science.aac8343>.
- (131) Diercks, C. S.; Lin, S.; Kornienko, N.; Kapustin, E. A.; Nichols, E. M.; Zhu, C.; Zhao, Y.; Chang, C. J.; Yaghi, O. M. Reticular Electronic Tuning of Porphyrin Active Sites in Covalent Organic Frameworks for Electrocatalytic Carbon Dioxide Reduction. *J. Am. Chem. Soc.* **2018**, *140* (3), 1116–1122. <https://doi.org/10.1021/jacs.7b11940>.
- (132) Wu, Q.; Xie, R.-K.; Mao, M.-J.; Chai, G.-L.; Yi, J.-D.; Zhao, S.-S.; Huang, Y.-B.; Cao, R. Integration of Strong Electron Transporter Tetrathiafulvalene into Metalloporphyrin-Based Covalent Organic Framework for Highly Efficient Electroreduction of CO<sub>2</sub>. *ACS Energy Lett.* **2020**, *5* (3), 1005–1012. <https://doi.org/10.1021/acsenerylett.9b02756>.
- (133) Zhao, C.; Dai, X.; Yao, T.; Chen, W.; Wang, X.; Wang, J.; Yang, J.; Wei, S.; Wu, Y.; Li, Y. Ionic Exchange of Metal–Organic Frameworks to Access Single Nickel Sites for Efficient Electroreduction of CO<sub>2</sub>. *J. Am. Chem. Soc.* **2017**, *139* (24), 8078–8081. <https://doi.org/10.1021/jacs.7b02736>.

- (134) Li, X.; Bi, W.; Chen, M.; Sun, Y.; Ju, H.; Yan, W.; Zhu, J.; Wu, X.; Chu, W.; Wu, C.; Xie, Y. Exclusive Ni-N<sub>4</sub> Sites Realize Near-Unity CO Selectivity for Electrochemical CO<sub>2</sub> Reduction. *J. Am. Chem. Soc.* **2017**, *139* (42), 14889–14892. <https://doi.org/10.1021/jacs.7b09074>.
- (135) Varela, A. S.; Kroschel, M.; Leonard, N. D.; Ju, W.; Steinberg, J.; Bagger, A.; Rossmeisl, J.; Strasser, P. PH Effects on the Selectivity of the Electrocatalytic CO<sub>2</sub> Reduction on Graphene-Embedded Fe–N–C Motifs: Bridging Concepts between Molecular Homogeneous and Solid-State Heterogeneous Catalysis. *ACS Energy Lett.* **2018**, *3* (4), 812–817. <https://doi.org/10.1021/acscatal.8b00273>.
- (136) Jiang, K.; Siahrostami, S.; Zheng, T.; Hu, Y.; Hwang, S.; Stavitski, E.; Peng, Y.; Dynes, J.; Gangisetty, M.; Su, D.; Attenkofer, K.; Wang, H. Isolated Ni Single Atoms in Graphene Nanosheets for High-Performance CO<sub>2</sub> Reduction. *Energy Environ. Sci.* **2018**, *11* (4), 893–903. <https://doi.org/10.1039/C7EE03245E>.
- (137) Pan, F.; Deng, W.; Justiniano, C.; Li, Y. Identification of Champion Transition Metals Centers in Metal and Nitrogen-Codoped Carbon Catalysts for CO<sub>2</sub> Reduction. *Applied Catalysis B: Environmental* **2018**, *226*, 463–472. <https://doi.org/10.1016/j.apcatb.2018.01.001>.
- (138) Hu, X.-M.; Hval, H. H.; Bjerglund, E. T.; Dalgaard, K. J.; Madsen, M. R.; Pohl, M.-M.; Welter, E.; Lamagni, P.; Buhl, K. B.; Bremholm, M.; Beller, M.; Pedersen, S. U.; Skrydstrup, T.; Daasbjerg, K. Selective CO<sub>2</sub> Reduction to CO in Water Using Earth-Abundant Metal and Nitrogen-Doped Carbon Electrocatalysts. *ACS Catal.* **2018**, *8* (7), 6255–6264. <https://doi.org/10.1021/acscatal.8b01022>.
- (139) Gu, J.; Hsu, C.-S.; Bai, L.; Chen, H. M.; Hu, X. Atomically Dispersed Fe<sup>3+</sup> Sites Catalyze Efficient CO<sub>2</sub> Electroreduction to CO. *Science* **2019**, *364* (6445), 1091–1094. <https://doi.org/10.1126/science.aaw7515>.
- (140) Yang, H.; Wu, Y.; Li, G.; Lin, Q.; Hu, Q.; Zhang, Q.; Liu, J.; He, C. Scalable Production of Efficient Single-Atom Copper Decorated Carbon Membranes for CO<sub>2</sub> Electroreduction to Methanol. *J. Am. Chem. Soc.* **2019**, *141* (32), 12717–12723. <https://doi.org/10.1021/jacs.9b04907>.
- (141) Zhang, E.; Wang, T.; Yu, K.; Liu, J.; Chen, W.; Li, A.; Rong, H.; Lin, R.; Ji, S.; Zheng, X.; Wang, Y.; Zheng, L.; Chen, C.; Wang, D.; Zhang, J.; Li, Y. Bismuth Single Atoms Resulting from Transformation of Metal–Organic Frameworks and Their Use as Electrocatalysts for CO<sub>2</sub> Reduction. *J. Am. Chem. Soc.* **2019**, *141* (42), 16569–16573. <https://doi.org/10.1021/jacs.9b08259>.
- (142) Li, J.; Pršlja, P.; Shinagawa, T.; Martín Fernández, A. J.; Krumeich, F.; Artyushkova, K.; Atanassov, P.; Zitolo, A.; Zhou, Y.; García-Muelas, R.; López, N.; Pérez-Ramírez, J.; Jaouen, F. Volcano Trend in Electrocatalytic CO<sub>2</sub> Reduction Activity over Atomically Dispersed Metal Sites on Nitrogen-Doped Carbon. *ACS Catal.* **2019**, *9* (11), 10426–10439. <https://doi.org/10.1021/acscatal.9b02594>.

- (143) Jiao, L.; Yang, W.; Wan, G.; Zhang, R.; Zheng, X.; Zhou, H.; Yu, S.-H.; Jiang, H.-L. Single-Atom Electrocatalysts from Multivariate Metal–Organic Frameworks for Highly Selective Reduction of CO<sub>2</sub> at Low Pressures. *Angewandte Chemie* **2020**, *132* (46), 20770–20776. <https://doi.org/10.1002/ange.202008787>.
- (144) Liu, J.; Kong, X.; Zheng, L.; Guo, X.; Liu, X.; Shui, J. Rare Earth Single-Atom Catalysts for Nitrogen and Carbon Dioxide Reduction. *ACS Nano* **2020**, *14* (1), 1093–1101. <https://doi.org/10.1021/acsnano.9b08835>.
- (145) Büchele, S.; Martín, A. J.; Mitchell, S.; Krumeich, F.; Collins, S. M.; Xi, S.; Borgna, A.; Pérez-Ramírez, J. Structure Sensitivity and Evolution of Nickel-Bearing Nitrogen-Doped Carbons in the Electrochemical Reduction of CO<sub>2</sub>. *ACS Catal.* **2020**, *10* (5), 3444–3454. <https://doi.org/10.1021/acscatal.9b05333>.
- (146) Guo, J.-H.; Zhang, X.-Y.; Dao, X.-Y.; Sun, W.-Y. Nanoporous Metal–Organic Framework-Based Ellipsoidal Nanoparticles for the Catalytic Electroreduction of CO<sub>2</sub>. *ACS Appl. Nano Mater.* **2020**, *3* (3), 2625–2635. <https://doi.org/10.1021/acsanm.0c00007>.
- (147) Guan, A.; Chen, Z.; Quan, Y.; Peng, C.; Wang, Z.; Sham, T.-K.; Yang, C.; Ji, Y.; Qian, L.; Xu, X.; Zheng, G. Boosting CO<sub>2</sub> Electroreduction to CH<sub>4</sub> via Tuning Neighboring Single-Copper Sites. *ACS Energy Lett.* **2020**, *5* (4), 1044–1053. <https://doi.org/10.1021/acsenrgylett.0c00018>.
- (148) Zhao, K.; Nie, X.; Wang, H.; Chen, S.; Quan, X.; Yu, H.; Choi, W.; Zhang, G.; Kim, B.; Chen, J. G. Selective Electroreduction of CO<sub>2</sub> to Acetone by Single Copper Atoms Anchored on N-Doped Porous Carbon. *Nature Communications* **2020**, *11* (1), 2455. <https://doi.org/10.1038/s41467-020-16381-8>.
- (149) Han, L.; Song, S.; Liu, M.; Yao, S.; Liang, Z.; Cheng, H.; Ren, Z.; Liu, W.; Lin, R.; Qi, G.; Liu, X.; Wu, Q.; Luo, J.; Xin, H. L. Stable and Efficient Single-Atom Zn Catalyst for CO<sub>2</sub> Reduction to CH<sub>4</sub>. *J. Am. Chem. Soc.* **2020**, *142* (29), 12563–12567. <https://doi.org/10.1021/jacs.9b12111>.
- (150) Wang, Y.; Chen, Z.; Han, P.; Du, Y.; Gu, Z.; Xu, X.; Zheng, G. Single-Atomic Cu with Multiple Oxygen Vacancies on Ceria for Electrocatalytic CO<sub>2</sub> Reduction to CH<sub>4</sub>. *ACS Catal.* **2018**, *8* (8), 7113–7119. <https://doi.org/10.1021/acscatal.8b01014>.
- (151) Jiao, J.; Lin, R.; Liu, S.; Cheong, W.-C.; Zhang, C.; Chen, Z.; Pan, Y.; Tang, J.; Wu, K.; Hung, S.-F.; Chen, H. M.; Zheng, L.; Lu, Q.; Yang, X.; Xu, B.; Xiao, H.; Li, J.; Wang, D.; Peng, Q.; Chen, C.; Li, Y. Copper Atom–Pair Catalyst Anchored on Alloy Nanowires for Selective and Efficient Electrochemical Reduction of CO<sub>2</sub>. *Nature Chemistry* **2019**, *11* (3), 222–228. <https://doi.org/10.1038/s41557-018-0201-x>.
- (152) Li, Y.; Chen, C.; Cao, R.; Pan, Z.; He, H.; Zhou, K. Dual-Atom Ag<sub>2</sub>/Graphene Catalyst for Efficient Electroreduction of CO<sub>2</sub> to CO. *Applied Catalysis B: Environmental* **2020**, *268*, 118747. <https://doi.org/10.1016/j.apcatb.2020.118747>.

- (153) Sun, M.-J.; Gong, Z.-W.; Yi, J.-D.; Zhang, T.; Chen, X.; Cao, R. A Highly Efficient Diatomic Nickel Electrocatalyst for CO<sub>2</sub> Reduction. *Chem. Commun.* **2020**, 56 (62), 8798–8801. <https://doi.org/10.1039/D0CC03410J>.
- (154) Cheng, H.; Wu, X.; Feng, M.; Li, X.; Lei, G.; Fan, Z.; Pan, D.; Cui, F.; He, G. Atomically Dispersed Ni/Cu Dual Sites for Boosting the CO<sub>2</sub> Reduction Reaction. *ACS Catal.* **2021**, 12673–12681. <https://doi.org/10.1021/acscatal.1c02319>.
- (155) Geng, K.; He, T.; Liu, R.; Dalapati, S.; Tan, K. T.; Li, Z.; Tao, S.; Gong, Y.; Jiang, Q.; Jiang, D. Covalent Organic Frameworks: Design, Synthesis, and Functions. *Chem. Rev.* **2020**, 120 (16), 8814–8933. <https://doi.org/10.1021/acs.chemrev.9b00550>.
- (156) Zhou, H.-C.; Long, J. R.; Yaghi, O. M. Introduction to Metal-Organic Frameworks. *Chem Rev* **2012**, 112 (2), 673–674. <https://doi.org/10.1021/cr300014x>.
- (157) Ji, S.; Chen, Y.; Wang, X.; Zhang, Z.; Wang, D.; Li, Y. Chemical Synthesis of Single Atomic Site Catalysts. *Chem. Rev.* **2020**, 120(21), 11900–11955. <https://doi.org/10.1021/acs.chemrev.9b00818>.
- (158) Qu, Q.; Ji, S.; Chen, Y.; Wang, D.; Li, Y. The Atomic-Level Regulation of Single-Atom Site Catalysts for the Electrochemical CO<sub>2</sub> Reduction Reaction. *Chemical Science* **2021**, 12 (12), 4201–4215. <https://doi.org/10.1039/D0SC07040H>.
- (159) Zhu, Y.; Yang, X.; Peng, C.; Priest, C.; Mei, Y.; Wu, G. Carbon-Supported Single Metal Site Catalysts for Electrochemical CO<sub>2</sub> Reduction to CO and Beyond. *Small* **2021**, 17 (16), 2005148. <https://doi.org/10.1002/smll.202005148>.
- (160) Gao, D.; Liu, T.; Wang, G.; Bao, X. Structure Sensitivity in Single-Atom Catalysis toward CO<sub>2</sub> Electroreduction. *ACS Energy Lett.* **2021**, 6 (2), 713–727. <https://doi.org/10.1021/acscenergylett.0c02665>.
- (161) Zhang, J.; Cai, W.; Hu, F. X.; Yang, H.; Liu, B. Recent Advances in Single Atom Catalysts for the Electrochemical Carbon Dioxide Reduction Reaction. *Chem. Sci.* **2021**, 12 (20), 6800–6819. <https://doi.org/10.1039/D1SC01375K>.
- (162) Qi, K.; Chhowalla, M.; Voiry, D. Single Atom Is Not Alone: Metal-Support Interactions in Single-Atom Catalysis. *Materials Today* **2020**, 40, 173–192. <https://doi.org/10.1016/j.mattod.2020.07.002>.
- (163) Liu, J.; Cai, Y.; Song, R.; Ding, S.; Lyu, Z.; Chang, Y.-C.; Tian, H.; Zhang, X.; Du, D.; Zhu, W.; Zhou, Y.; Lin, Y. Recent Progress on Single-Atom Catalysts for CO<sub>2</sub> Electroreduction. *Materials Today* **2021**. <https://doi.org/10.1016/j.mattod.2021.02.005>.
- (164) Wang, Y.; Liu, T.; Li, Y. Why Heterogeneous Single-Atom Catalysts Preferentially Produce CO in the Electrochemical CO<sub>2</sub> Reduction Reaction. *Chem. Sci.* **2022**. <https://doi.org/10.1039/D2SC01593E>.
- (165) Vijay, S.; Ju, W.; Brückner, S.; Tsang, S.-C.; Strasser, P.; Chan, K. Unified Mechanistic Understanding of CO<sub>2</sub> Reduction to CO on Transition Metal and Single Atom Catalysts. *Nat Catal* **2021**, 4 (12), 1024–1031. <https://doi.org/10.1038/s41929-021-00705-y>.

- (166) Zhang, Z.; Xiao, J.; Chen, X.-J.; Yu, S.; Yu, L.; Si, R.; Wang, Y.; Wang, S.; Meng, X.; Wang, Y.; Tian, Z.-Q.; Deng, D. Reaction Mechanisms of Well-Defined Metal-N<sub>4</sub> Sites in Electrocatalytic CO<sub>2</sub> Reduction. *Angewandte Chemie International Edition* **2018**, *57* (50), 16339–16342. <https://doi.org/10.1002/anie.201808593>.
- (167) Bonetto, R.; Crisanti, F.; Sartorel, A. Carbon Dioxide Reduction Mediated by Iron Catalysts: Mechanism and Intermediates That Guide Selectivity. *ACS Omega* **2020**, *5* (34), 21309–21319. <https://doi.org/10.1021/acsomega.0c02786>.
- (168) Shen, J.; Kortlever, R.; Kas, R.; Birdja, Y. Y.; Diaz-Morales, O.; Kwon, Y.; Ledezma-Yanez, I.; Schouten, K. J. P.; Mul, G.; Koper, M. T. M. Electrocatalytic Reduction of Carbon Dioxide to Carbon Monoxide and Methane at an Immobilized Cobalt Protoporphyrin. *Nat Commun* **2015**, *6* (1), 8177. <https://doi.org/10.1038/ncomms9177>.
- (169) Kuhl, K. P.; Hatsukade, T.; Cave, E. R.; Abram, D. N.; Kibsgaard, J.; Jaramillo, T. F. Electrocatalytic Conversion of Carbon Dioxide to Methane and Methanol on Transition Metal Surfaces. *J. Am. Chem. Soc.* **2014**, *136* (40), 14107–14113. <https://doi.org/10.1021/ja505791r>.
- (170) Hatsukade, T.; Kuhl, K. P.; Cave, E. R.; Abram, D. N.; Feaster, J. T.; Jongerius, A. L.; Hahn, C.; Jaramillo, T. F. Carbon Dioxide Electroreduction Using a Silver–Zinc Alloy. *Energy Technology* **2017**, *5* (6), 955–961. <https://doi.org/10.1002/ente.201700087>.
- (171) Chen, D.; Chen, Z.; Lu, Z.; Tang, J.; Zhang, X.; Singh, C. V. Computational Screening of Homo and Hetero Transition Metal Dimer Catalysts for Reduction of CO<sub>2</sub> to C<sub>2</sub> Products with High Activity and Low Limiting Potential. *J. Mater. Chem. A* **2020**, *8* (40), 21241–21254. <https://doi.org/10.1039/D0TA05212D>.
- (172) Wang, X.; Chen, Z.; Zhao, X.; Yao, T.; Chen, W.; You, R.; Zhao, C.; Wu, G.; Wang, J.; Huang, W.; Yang, J.; Hong, X.; Wei, S.; Wu, Y.; Li, Y. Regulation of Coordination Number over Single Co Sites: Triggering the Efficient Electroreduction of CO<sub>2</sub>. *Angewandte Chemie International Edition* **2018**, *57* (7), 1944–1948. <https://doi.org/10.1002/anie.201712451>.
- (173) Gong, Y.-N.; Jiao, L.; Qian, Y.; Pan, C.-Y.; Zheng, L.; Cai, X.; Liu, B.; Yu, S.-H.; Jiang, H.-L. Regulating the Coordination Environment of MOF-Templated Single-Atom Nickel Electrocatalysts for Boosting CO<sub>2</sub> Reduction. *Angew Chem Int Ed Engl* **2020**, *59* (7), 2705–2709. <https://doi.org/10.1002/anie.201914977>.
- (174) Koper, M. T. M. Analysis of Electrocatalytic Reaction Schemes: Distinction between Rate-Determining and Potential-Determining Steps. *J Solid State Electrochem* **2013**, *17* (2), 339–344. <https://doi.org/10.1007/s10008-012-1918-x>.
- (175) Pedersen, J. K.; Batchelor, T. A. A.; Bagger, A.; Rossmeisl, J. High-Entropy Alloys as Catalysts for the CO<sub>2</sub> and CO Reduction Reactions. *ACS Catal.* **2020**, *10* (3), 2169–2176. <https://doi.org/10.1021/acscatal.9b04343>.

- (176) Batchelor, T. A. A.; Pedersen, J. K.; Winther, S. H.; Castelli, I. E.; Jacobsen, K. W.; Rossmeisl, J. High-Entropy Alloys as a Discovery Platform for Electrocatalysis. *Joule* **2019**, *3* (3), 834–845. <https://doi.org/10.1016/j.joule.2018.12.015>.
- (177) Wakerley, D.; Lamaison, S.; Ozanam, F.; Menguy, N.; Mercier, D.; Marcus, P.; Fontecave, M.; Mougél, V. Bio-Inspired Hydrophobicity Promotes CO<sub>2</sub> Reduction on a Cu Surface. *Nature Materials* **2019**, *18*(11), 1222–1227. <https://doi.org/10.1038/s41563-019-0445-x>.
- (178) Hara, K.; Kudo, A.; Sakata, T. Electrochemical Reduction of Carbon Dioxide under High Pressure on Various Electrodes in an Aqueous Electrolyte. *Journal of Electroanalytical Chemistry* **1995**, *391* (1), 141–147. [https://doi.org/10.1016/0022-0728\(95\)03935-A](https://doi.org/10.1016/0022-0728(95)03935-A).
- (179) Sonoyama, N.; Kirii, M.; Sakata, T. Electrochemical Reduction of CO<sub>2</sub> at Metal-Porphyrin Supported Gas Diffusion Electrodes under High Pressure CO<sub>2</sub>. *Electrochemistry Communications* **1999**, *1* (6), 213–216. [https://doi.org/10.1016/S1388-2481\(99\)00041-7](https://doi.org/10.1016/S1388-2481(99)00041-7).
- (180) Monteiro, M. C. O.; Dattila, F.; Hagedoorn, B.; García-Muelas, R.; López, N.; Koper, M. T. M. Absence of CO<sub>2</sub> Electroreduction on Copper, Gold and Silver Electrodes without Metal Cations in Solution. *Nat Catal* **2021**, *4* (8), 654–662. <https://doi.org/10.1038/s41929-021-00655-5>.
- (181) Kim, J. Y. ‘Timothy’; Zhu, P.; Chen, F.-Y.; Wu, Z.-Y.; Cullen, D. A.; Wang, H. Recovering Carbon Losses in CO<sub>2</sub> Electrolysis Using a Solid Electrolyte Reactor. *Nat Catal* **2022**, *5*(4), 288–299. <https://doi.org/10.1038/s41929-022-00763-w>.

## 2.8. Supporting Information

Half-reaction	$E^0$ [V vs. RHE]	Product and named-reactions
$2\text{H}_2\text{O} \rightarrow \text{O}_2 + 4\text{H}^+ + 4\text{e}^-$	1.23	Oxygen evolution reaction (OER)
$2\text{H}^+ + 2\text{e}^- \rightarrow \text{H}_2$	0	Hydrogen evolution reaction (HER)
$x\text{CO}_2 + n\text{H}^+ + ne^- \rightarrow \text{product} + y\text{H}_2\text{O}$		CO <sub>2</sub> reduction reaction (CO <sub>2</sub> RR)
$\text{CO}_2 + 2\text{H}^+ + 2\text{e}^- \rightarrow \text{HCOOH}$	-0.12	Formic acid
$\text{CO}_2 + 2\text{H}^+ + 2\text{e}^- \rightarrow \text{CO} + \text{H}_2\text{O}$	-0.10	Carbon monoxide
$\text{CO}_2 + 6\text{H}^+ + 6\text{e}^- \rightarrow \text{CH}_3\text{OH} + 6\text{e}^-$	0.03	Methanol
$\text{CO}_2 + 4\text{H}^+ + 4\text{e}^- \rightarrow \text{C} + 2\text{H}_2\text{O}$	0.21	Graphite
$\text{CO}_2 + 8\text{H}^+ + 8\text{e}^- \rightarrow \text{CH}_4 + \text{H}_2\text{O}$	0.17	Methane
$2\text{CO}_2 + 2\text{H}^+ + 2\text{e}^- \rightarrow (\text{COOH})_2$	-0.47	Oxalic Acid
$2\text{CO}_2 + 8\text{H}^+ + 8\text{e}^- \rightarrow \text{CH}_3\text{COOH} + 2\text{H}_2\text{O}$	0.11	Acetic Acid
$2\text{CO}_2 + 10\text{H}^+ + 10\text{e}^- \rightarrow \text{CH}_3\text{CHO} + 3\text{H}_2\text{O}$	0.06	Acetaldehyde
$2\text{CO}_2 + 12\text{H}^+ + 12\text{e}^- \rightarrow \text{C}_2\text{H}_5\text{OH} + 3\text{H}_2\text{O}$	0.09	Ethanol
$2\text{CO}_2 + 12\text{H}^+ + 12\text{e}^- \rightarrow \text{C}_2\text{H}_4 + 4\text{H}_2\text{O}$	0.08	Ethylene
$2\text{CO}_2 + 14\text{H}^+ + 14\text{e}^- \rightarrow \text{C}_2\text{H}_6 + 4\text{H}_2\text{O}$	0.14	Ethane
$3\text{CO}_2 + 16\text{H}^+ + 16\text{e}^- \rightarrow \text{C}_2\text{H}_5\text{CHO} + 5\text{H}_2\text{O}$	0.09	Propionaldehyde
$3\text{CO}_2 + 18\text{H}^+ + 18\text{e}^- \rightarrow \text{C}_3\text{H}_7\text{OH} + 5\text{H}_2\text{O}$	0.10	Propanol
$4\text{CO}_2 + 24\text{H}^+ + 24\text{e}^- \rightarrow \text{C}_4\text{H}_9\text{OH} + 7\text{H}_2\text{O}$	0.13	Butanol

**Table S1.** Table of CO<sub>2</sub>RR products, other relevant half-reactions and their equilibrium potentials.<sup>5,6,7</sup>

The equilibrium potentials of the most valued products of the CO<sub>2</sub> reduction reaction listed here comprise the cathodic side of the redox reaction and are reported versus the reversible hydrogen electrode. Therefore, by definition, the equilibrium potential of the hydrogen evolution reaction is zero. In the main text, the anodic reaction was in all cases the oxygen evolution reaction. Cell voltages (without overpotentials) can be determined from:

$$E_{cell}^0 = E_{red.}^0 - E_{ox.}^0$$



## Note S2. List of references for Figure 3 in the manuscript

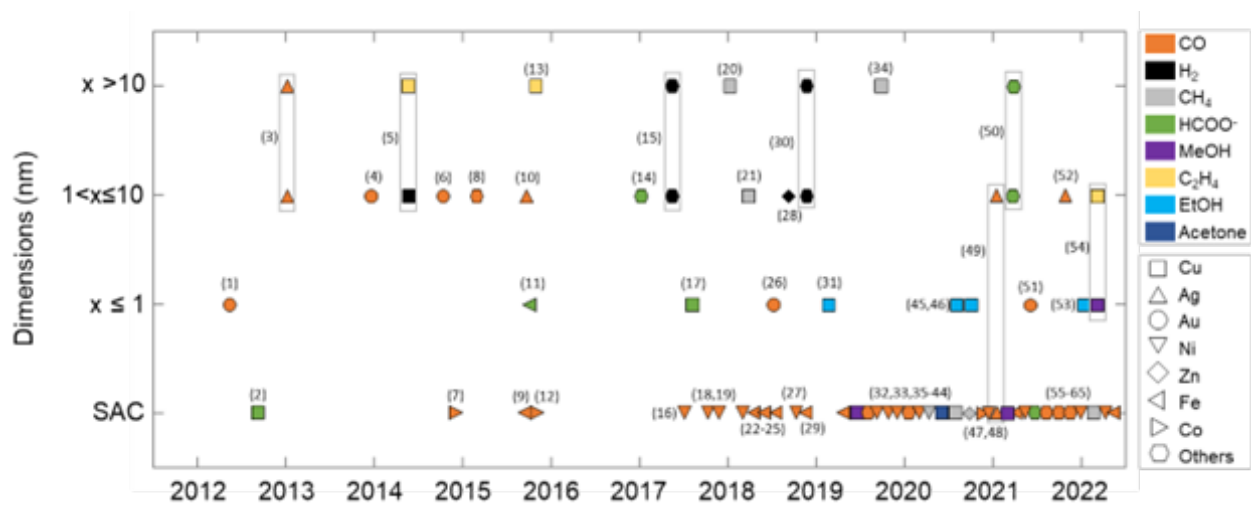


**Figure S1.** Numbers in this figure correspond to the numbered references below.

- (1) Kauffman, D. R.; Alfonso, D.; Matranga, C.; Qian, H.; Jin, R. Experimental and Computational Investigation of Au<sub>25</sub> Clusters and CO<sub>2</sub>: A Unique Interaction and Enhanced Electrocatalytic Activity. *J. Am. Chem. Soc.* **2012**, *134* (24), 10237–10243. <https://doi.org/10.1021/ja303259q>.
- (2) Hinogami, R.; Yotsuhashi, S.; Deguchi, M.; Zenitani, Y.; Hashiba, H.; Yamada, Y. Electrochemical Reduction of Carbon Dioxide Using a Copper Rubenate Metal Organic Framework. *ECS Electrochem. Lett.* **2012**, *1* (4), H17. <https://doi.org/10.1149/2.001204eel>.
- (3) Salehi-Khojin, A.; Jhong, H.-R. M.; Rosen, B. A.; Zhu, W.; Ma, S.; Kenis, P. J. A.; Masel, R. I. Nanoparticle Silver Catalysts That Show Enhanced Activity for Carbon Dioxide Electrolysis. *J. Phys. Chem. C* **2013**, *117* (4), 1627–1632. <https://doi.org/10.1021/jp310509z>.
- (4) Zhu, W.; Michalsky, R.; Metin, Ö.; Lv, H.; Guo, S.; Wright, C. J.; Sun, X.; Peterson, A. A.; Sun, S. Monodisperse Au Nanoparticles for Selective Electrocatalytic Reduction of CO<sub>2</sub> to CO. *J. Am. Chem. Soc.* **2013**, *135* (45), 16833–16836. <https://doi.org/10.1021/ja409445p>.
- (5) Reske, R.; Mistry, H.; Behafarid, F.; Roldan Cuenya, B.; Strasser, P. Particle Size Effects in the Catalytic Electroreduction of CO<sub>2</sub> on Cu Nanoparticles. *J. Am. Chem. Soc.* **2014**, *136* (19), 6978–6986. <https://doi.org/10.1021/ja500328k>.
- (6) Mistry, H.; Reske, R.; Zeng, Z.; Zhao, Z.-J.; Greeley, J.; Strasser, P.; Cuenya, B. R. Exceptional Size-Dependent Activity Enhancement in the Electroreduction of CO<sub>2</sub> over Au Nanoparticles. *J. Am. Chem. Soc.* **2014**, *136* (47), 16473–16476. <https://doi.org/10.1021/ja508879j>.
- (7) Varela, A. S.; Ranjbar Sahraie, N.; Steinberg, J.; Ju, W.; Oh, H.-S.; Strasser, P. Metal-Doped Nitrogenated Carbon as an Efficient Catalyst for Direct CO<sub>2</sub> Electroreduction to CO and Hydrocarbons. *Angew. Chem. Int. Ed.* **2015**, *54* (37), 10758–10762. <https://doi.org/10.1002/anie.201502099>.
- (8) Gao, D.; Zhou, H.; Wang, J.; Miao, S.; Yang, F.; Wang, G.; Wang, J.; Bao, X. Size-Dependent Electrocatalytic Reduction of CO<sub>2</sub> over Pd Nanoparticles. *J. Am. Chem. Soc.* **2015**, *137* (13), 4288–4291. <https://doi.org/10.1021/jacs.5b00046>.
- (9) Hod, I.; Sampson, M. D.; Deria, P.; Kubiak, C. P.; Farha, O. K.; Hupp, J. T. Fe-Porphyrin-Based Metal-Organic Framework Films as High-Surface Concentration, Heterogeneous Catalysts for Electrochemical Reduction of CO<sub>2</sub>. *ACS Catal.* **2015**, *5* (11), 6302–6309. <https://doi.org/10.1021/acscatal.5b01767>.
- (10) Kim, C.; Jeon, H. S.; Eom, T.; Jee, M. S.; Kim, H.; Friend, C. M.; Min, B. K.; Hwang, Y. J. Achieving Selective and Efficient Electrocatalytic Activity for CO<sub>2</sub> Reduction Using Immobilized Silver Nanoparticles. *J. Am. Chem. Soc.* **2015**, *137* (43), 13844–13850. <https://doi.org/10.1021/jacs.5b06568>.
- (11) Taheri, A.; Thompson, E. J.; Fettinger, J. C.; Berben, L. A. An Iron Electrocatalyst for Selective Reduction of CO<sub>2</sub> to Formate in Water: Including Thermochemical Insights. *ACS Catal.* **2015**, *5* (12), 7140–7151. <https://doi.org/10.1021/acscatal.5b01708>.
- (12) Kornienko, N.; Zhao, Y.; Kley, C. S.; Zhu, C.; Kim, D.; Lin, S.; Chang, C. J.; Yaghi, O. M.; Yang, P. Metal-Organic Frameworks for Electrocatalytic Reduction of Carbon Dioxide. *J. Am. Chem. Soc.* **2015**, *137* (44), 14129–14135. <https://doi.org/10.1021/jacs.5b08212>.

- (13) Loiudice, A.; Lobaccaro, P.; Kamali, E. A.; Thao, T.; Huang, B. H.; Ager, J. W.; Buonsanti, R. Tailoring Copper Nanocrystals towards C<sub>2</sub> Products in Electrochemical CO<sub>2</sub> Reduction. *Angew. Chem. Int. Ed.* **2016**, *55* (19), 5789–5792. <https://doi.org/10.1002/anie.201601582>.
- (14) Rahaman, M.; Dutta, A.; Broekmann, P. Size-Dependent Activity of Palladium Nanoparticles: Efficient Conversion of CO<sub>2</sub> into Formate at Low Overpotentials. *ChemSusChem* **2017**, *10*(8), 1733–1741. <https://doi.org/10.1002/cssc.201601778>.
- (15) Mistry, H.; Reske, R.; Strasser, P.; Roldan Cuenya, B. Size-Dependent Reactivity of Gold-Copper Bimetallic Nanoparticles during CO<sub>2</sub> Electroreduction. *Catal. Today* **2017**, *288*, 30–36. <https://doi.org/10.1016/j.cattod.2016.09.017>.
- (16) Zhao, C.; Dai, X.; Yao, T.; Chen, W.; Wang, X.; Wang, J.; Yang, J.; Wei, S.; Wu, Y.; Li, Y. Ionic Exchange of Metal–Organic Frameworks to Access Single Nickel Sites for Efficient Electroreduction of CO<sub>2</sub>. *J. Am. Chem. Soc.* **2017**, *139* (24), 8078–8081. <https://doi.org/10.1021/jacs.7b02736>.
- (17) Tang, Q.; Lee, Y.; Li, D.-Y.; Choi, W.; Liu, C. W.; Lee, D.; Jiang, D. Lattice-Hydride Mechanism in Electrocatalytic CO<sub>2</sub> Reduction by Structurally Precise Copper-Hydride Nanoclusters. *J. Am. Chem. Soc.* **2017**, *139* (28), 9728–9736. <https://doi.org/10.1021/jacs.7b05591>.
- (18) Ju, W.; Bagger, A.; Hao, G.-P.; Varela, A. S.; Sinev, I.; Bon, V.; Roldan Cuenya, B.; Kaskel, S.; Rossmeisl, J.; Strasser, P. Understanding Activity and Selectivity of Metal-Nitrogen-Doped Carbon Catalysts for Electrochemical Reduction of CO<sub>2</sub>. *Nat. Commun.* **2017**, *8* (1), 944. <https://doi.org/10.1038/s41467-017-01035-z>.
- (19) Li, X.; Bi, W.; Chen, M.; Sun, Y.; Ju, H.; Yan, W.; Zhu, J.; Wu, X.; Chu, W.; Wu, C.; Xie, Y. Exclusive Ni–N<sub>4</sub> Sites Realize Near-Unity CO Selectivity for Electrochemical CO<sub>2</sub> Reduction. *J. Am. Chem. Soc.* **2017**, *139* (42), 14889–14892. <https://doi.org/10.1021/jacs.7b09074>.
- (20) Grosse, P.; Gao, D.; Scholten, F.; Sinev, I.; Mistry, H.; Roldan Cuenya, B. Dynamic Changes in the Structure, Chemical State and Catalytic Selectivity of Cu Nanocubes during CO<sub>2</sub> Electroreduction: Size and Support Effects. *Angew. Chem. Int. Ed.* **2018**, *57* (21), 6192–6197. <https://doi.org/10.1002/anie.201802083>.
- (21) Weng, Z.; Wu, Y.; Wang, M.; Jiang, J.; Yang, K.; Huo, S.; Wang, X.-F.; Ma, Q.; Brudvig, G. W.; Batista, V. S.; Liang, Y.; Feng, Z.; Wang, H. Active Sites of Copper-Complex Catalytic Materials for Electrochemical Carbon Dioxide Reduction. *Nat. Commun.* **2018**, *9* (1), 415. <https://doi.org/10.1038/s41467-018-02819-7>.
- (22) Yang, H. B.; Hung, S.-F.; Liu, S.; Yuan, K.; Miao, S.; Zhang, L.; Huang, X.; Wang, H.-Y.; Cai, W.; Chen, R.; Gao, J.; Yang, X.; Chen, W.; Huang, Y.; Chen, H. M.; Li, C. M.; Zhang, T.; Liu, B. Atomically Dispersed Ni(II) as the Active Site for Electrochemical CO<sub>2</sub> Reduction. *Nat. Energy* **2018**, *3* (2), 140–147. <https://doi.org/10.1038/s41560-017-0078-8>.
- (23) Varela, A. S.; Kroschel, M.; Leonard, N. D.; Ju, W.; Steinberg, J.; Bagger, A.; Rossmeisl, J.; Strasser, P. PH Effects on the Selectivity of the Electrocatalytic CO<sub>2</sub> Reduction on Graphene-Embedded Fe–N–C Motifs: Bridging Concepts between Molecular Homogeneous and Solid-State Heterogeneous Catalysis. *ACS Energy Lett.* **2018**, *3* (4), 812–817. <https://doi.org/10.1021/acsenergylett.8b00273>.

- (24) Pan, F.; Deng, W.; Justiniano, C.; Li, Y. Identification of Champion Transition Metals Centers in Metal and Nitrogen-Codoped Carbon Catalysts for CO<sub>2</sub> Reduction. *Appl. Catal. B Environ.* **2018**, *226*, 463–472. <https://doi.org/10.1016/j.apcatb.2018.01.001>.
- (25) Dong, B.-X.; Qian, S.-L.; Bu, F.-Y.; Wu, Y.-C.; Feng, L.-G.; Teng, Y.-L.; Liu, W.-L.; Li, Z.-W. Electrochemical Reduction of CO<sub>2</sub> to CO by a Heterogeneous Catalyst of Fe–Porphyrin-Based Metal–Organic Framework. *ACS Appl. Energy Mater.* **2018**, *1* (9), 4662–4669. <https://doi.org/10.1021/acsaem.8b00797>.
- (26) Zhao, S.; Austin, N.; Li, M.; Song, Y.; House, S. D.; Bernhard, S.; Yang, J. C.; Mpourmpakis, G.; Jin, R. Influence of Atomic-Level Morphology on Catalysis: The Case of Sphere and Rod-Like Gold Nanoclusters for CO<sub>2</sub> Electroreduction. *ACS Catal.* **2018**, *8* (6), 4996–5001. <https://doi.org/10.1021/acscatal.8b00365>.
- (27) Jiang, K.; Siahrostami, S.; Zheng, T.; Hu, Y.; Hwang, S.; Stavitski, E.; Peng, Y.; Dynes, J.; Gangisetty, M.; Su, D.; Attenkofer, K.; Wang, H. Isolated Ni Single Atoms in Graphene Nanosheets for High-Performance CO<sub>2</sub> Reduction. *Energy Environ. Sci.* **2018**, *11* (4), 893–903. <https://doi.org/10.1039/C7EE03245E>.
- (28) Jeon, H. S.; Sinev, I.; Scholten, F.; Divins, N. J.; Zegkinoglou, I.; Pielsticker, L.; Cuenya, B. R. Operando Evolution of the Structure and Oxidation State of Size-Controlled Zn Nanoparticles during CO<sub>2</sub> Electroreduction. *J. Am. Chem. Soc.* **2018**, *140* (30), 9383–9386. <https://doi.org/10.1021/jacs.8b05258>.
- (29) Zhang, Z.; Xiao, J.; Chen, X.-J.; Yu, S.; Yu, L.; Si, R.; Wang, Y.; Wang, S.; Meng, X.; Wang, Y.; Tian, Z.-Q.; Deng, D. Reaction Mechanisms of Well-Defined Metal–N<sub>4</sub> Sites in Electrocatalytic CO<sub>2</sub> Reduction. *Angewandte Chemie International Edition* **2018**, *57* (50), 16339–16342. <https://doi.org/10.1002/anie.201808593>.
- (30) Bernal, M.; Bagger, A.; Scholten, F.; Sinev, I.; Bergmann, A.; Ahmadi, M.; Rossmeisl, J.; Cuenya, B. R. CO<sub>2</sub> Electroreduction on Copper-Cobalt Nanoparticles: Size and Composition Effect. *Nano Energy* **2018**, *53*, 27–36. <https://doi.org/10.1016/j.nanoen.2018.08.027>.
- (31) Karapinar, D.; Huan, N. T.; Sahraie, N. R.; Li, J.; Wakerley, D.; Touati, N.; Zanna, S.; Taverna, D.; Tizei, L. H. G.; Zitolo, A.; Jaouen, F.; Mougél, V.; Fontecave, M. Electroreduction of CO<sub>2</sub> on Single-Site Copper-Nitrogen-Doped Carbon Material: Selective Formation of Ethanol and Reversible Restructuration of the Metal Sites. *Angew. Chem. Int. Ed.* **2019**, *58* (42), 15098–15103. <https://doi.org/10.1002/anie.201907994>.
- (32) Gu, J.; Hsu, C.-S.; Bai, L.; Chen, H. M.; Hu, X. Atomically Dispersed Fe<sup>3+</sup> Sites Catalyze Efficient CO<sub>2</sub> Electroreduction to CO. *Science* **2019**, *364* (6445), 1091–1094. <https://doi.org/10.1126/science.aaw7515>.
- (33) Yang, H.; Wu, Y.; Li, G.; Lin, Q.; Hu, Q.; Zhang, Q.; Liu, J.; He, C. Scalable Production of Efficient Single-Atom Copper Decorated Carbon Membranes for CO<sub>2</sub> Electroreduction to Methanol. *J. Am. Chem. Soc.* **2019**, *141* (32), 12717–12723. <https://doi.org/10.1021/jacs.9b04907>.

- (34) Iyengar, P.; Huang, J.; Gregorio, G. L. D.; Gadiyar, C.; Buonsanti, R. Size Dependent Selectivity of Cu Nano-Octahedra Catalysts for the Electrochemical Reduction of CO<sub>2</sub> to CH<sub>4</sub>. *Chem. Commun.* **2019**, *55* (60), 8796–8799. <https://doi.org/10.1039/C9CC02522G>.
- (35) Zhang, E.; Wang, T.; Yu, K.; Liu, J.; Chen, W.; Li, A.; Rong, H.; Lin, R.; Ji, S.; Zheng, X.; Wang, Y.; Zheng, L.; Chen, C.; Wang, D.; Zhang, J.; Li, Y. Bismuth Single Atoms Resulting from Transformation of Metal–Organic Frameworks and Their Use as Electrocatalysts for CO<sub>2</sub> Reduction. *J. Am. Chem. Soc.* **2019**, *141* (42), 16569–16573. <https://doi.org/10.1021/jacs.9b08259>.
- (36) Matheu, R.; Gutierrez-Puebla, E.; Monge, M. Á.; Diercks, C. S.; Kang, J.; Prévot, M. S.; Pei, X.; Hanikel, N.; Zhang, B.; Yang, P.; Yaghi, O. M. Three-Dimensional Phthalocyanine Metal-Catecholates for High Electrochemical Carbon Dioxide Reduction. *J. Am. Chem. Soc.* **2019**, *141* (43), 17081–17085. <https://doi.org/10.1021/jacs.9b09298>.
- (37) Li, J.; Pršljaja, P.; Shinagawa, T.; Martín Fernández, A. J.; Krumeich, F.; Artyushkova, K.; Atanassov, P.; Zitolo, A.; Zhou, Y.; García-Muelas, R.; López, N.; Pérez-Ramírez, J.; Jaouen, F. Volcano Trend in Electrocatalytic CO<sub>2</sub> Reduction Activity over Atomically Dispersed Metal Sites on Nitrogen-Doped Carbon. *ACS Catal.* **2019**, *9* (11), 10426–10439. <https://doi.org/10.1021/acscatal.9b02594>.
- (38) Jiao, L.; Yang, W.; Wan, G.; Zhang, R.; Zheng, X.; Zhou, H.; Yu, S.-H.; Jiang, H.-L. Single-Atom Electrocatalysts from Multivariate Metal–Organic Frameworks for Highly Selective Reduction of CO<sub>2</sub> at Low Pressures. *Angew. Chem.* **2020**, *132* (46), 20770–20776. <https://doi.org/10.1002/ange.202008787>.
- (39) Liu, J.; Kong, X.; Zheng, L.; Guo, X.; Liu, X.; Shui, J. Rare Earth Single-Atom Catalysts for Nitrogen and Carbon Dioxide Reduction. *ACS Nano* **2020**, *14* (1), 1093–1101. <https://doi.org/10.1021/acsnano.9b08835>.
- (40) Büchele, S.; Martín, A. J.; Mitchell, S.; Krumeich, F.; Collins, S. M.; Xi, S.; Borgna, A.; Pérez-Ramírez, J. Structure Sensitivity and Evolution of Nickel-Bearing Nitrogen-Doped Carbons in the Electrochemical Reduction of CO<sub>2</sub>. *ACS Catal.* **2020**, *10* (5), 3444–3454. <https://doi.org/10.1021/acscatal.9b05333>.
- (41) Guo, J.-H.; Zhang, X.-Y.; Dao, X.-Y.; Sun, W.-Y. Nanoporous Metal–Organic Framework-Based Ellipsoidal Nanoparticles for the Catalytic Electroreduction of CO<sub>2</sub>. *ACS Appl. Nano Mater.* **2020**, *3* (3), 2625–2635. <https://doi.org/10.1021/acsnm.0c00007>.
- (42) Guan, A.; Chen, Z.; Quan, Y.; Peng, C.; Wang, Z.; Sham, T.-K.; Yang, C.; Ji, Y.; Qian, L.; Xu, X.; Zheng, G. Boosting CO<sub>2</sub> Electroreduction to CH<sub>4</sub> via Tuning Neighboring Single-Copper Sites. *ACS Energy Lett.* **2020**, *5* (4), 1044–1053. <https://doi.org/10.1021/acsenergylett.0c00018>.

- (43) Zhao, K.; Nie, X.; Wang, H.; Chen, S.; Quan, X.; Yu, H.; Choi, W.; Zhang, G.; Kim, B.; Chen, J. G. Selective Electroreduction of CO<sub>2</sub> to Acetone by Single Copper Atoms Anchored on N-Doped Porous Carbon. *Nat. Commun.* **2020**, *11* (1), 2455. <https://doi.org/10.1038/s41467-020-16381-8>.
- (44) Han, L.; Song, S.; Liu, M.; Yao, S.; Liang, Z.; Cheng, H.; Ren, Z.; Liu, W.; Lin, R.; Qi, G.; Liu, X.; Wu, Q.; Luo, J.; Xin, H. L. Stable and Efficient Single-Atom Zn Catalyst for CO<sub>2</sub> Reduction to CH<sub>4</sub>. *J. Am. Chem. Soc.* **2020**, *142* (29), 12563–12567. <https://doi.org/10.1021/jacs.9b12111>.
- (45) Xu, H.; Rebollar, D.; He, H.; Chong, L.; Liu, Y.; Liu, C.; Sun, C.-J.; Li, T.; Muntean, J. V.; Winans, R. E.; Liu, D.-J.; Xu, T. Highly Selective Electrocatalytic CO<sub>2</sub> Reduction to Ethanol by Metallic Clusters Dynamically Formed from Atomically Dispersed Copper. *Nat. Energy* **2020**, *5* (8), 623–632. <https://doi.org/10.1038/s41560-020-0666-x>.
- (46) Chen, D.; Chen, Z.; Lu, Z.; Tang, J.; Zhang, X.; Singh, C. V. Computational Screening of Homo and Hetero Transition Metal Dimer Catalysts for Reduction of CO<sub>2</sub> to C<sub>2</sub> Products with High Activity and Low Limiting Potential. *J. Mater. Chem. A* **2020**, *8* (40), 21241–21254. <https://doi.org/10.1039/D0TA05212D>.
- (47) Meng, Z.; Luo, J.; Li, W.; Mirica, K. A. Hierarchical Tuning of the Performance of Electrochemical Carbon Dioxide Reduction Using Conductive Two-Dimensional Metallophthalocyanine Based Metal–Organic Frameworks. *J. Am. Chem. Soc.* **2020**, *142* (52), 21656–21669. <https://doi.org/10.1021/jacs.0c07041>.
- (48) Sun, Q.; Ren, W.; Zhao, Y.; Zhao, C. Gram-Scale Synthesis of Single-Atom Metal–N–CNT Catalysts for Highly Efficient CO<sub>2</sub> Electroreduction. *Chem. Commun.* **2021**. <https://doi.org/10.1039/D0CC07263J>.
- (49) Zhang, N.; Zhang, X.; Tao, L.; Jiang, P.; Ye, C.; Lin, R.; Huang, Z.; Li, A.; Pang, D.; Yan, H.; Wang, Y.; Xu, P.; An, S.; Zhang, Q.; Liu, L.; Du, S.; Han, X.; Wang, D.; Li, Y. Silver Single-Atom Catalyst for Efficient Electrochemical CO<sub>2</sub> Reduction Synthesized from Thermal Transformation and Surface Reconstruction. *Angew. Chem. Int. Ed.* **2021**, anie.202014718. <https://doi.org/10.1002/anie.202014718>.
- (50) Yao, D.; Tang, C.; Vasileff, A.; Zhi, X.; Jiao, Y.; Qiao, S. Z. The Controllable Reconstruction of Bi-MOFs for Electrochemical CO<sub>2</sub> Reduction through Electrolyte and Potential Mediation. *Angew. Chem. Int. Ed.* **2021**, *60* (33), 18178–18184. <https://doi.org/10.1002/anie.202104747>.
- (51) Wan, X.-K.; Wang, J.-Q.; Wang, Q.-M. Ligand-Protected Au<sub>55</sub> with a Novel Structure and Remarkable CO<sub>2</sub> Electroreduction Performance. *Angew. Chem. Int. Ed.* **2021**, *60* (38), 20748–20753. <https://doi.org/10.1002/anie.202108207>.
- (52) Deng, X.; Alfonso, D.; Nguyen-Phan, T.-D.; Kauffman, D. R. Resolving the Size-Dependent Transition between CO<sub>2</sub> Reduction Reaction and H<sub>2</sub> Evolution Reaction Selectivity in Sub-5 Nm Silver Nanoparticle Electrocatalysts. *ACS Catal.* **2022**, 5921–5929. <https://doi.org/10.1021/acscatal.2c00960>.

- (53) Su, X.; Jiang, Z.; Zhou, J.; Liu, H.; Zhou, D.; Shang, H.; Ni, X.; Peng, Z.; Yang, F.; Chen, W.; Qi, Z.; Wang, D.; Wang, Y. Complementary Operando Spectroscopy Identification of In-Situ Generated Metastable Charge-Asymmetry  $\text{Cu}_2\text{-CuN}_3$  Clusters for  $\text{CO}_2$  Reduction to Ethanol. *Nat Commun.* **2022**, 13 (1), 1322. <https://doi.org/10.1038/s41467-022-29035-8>.
- (54) Zhang, H.; Yang, Y.; Liang, Y.; Li, J.; Zhang, A.; Zheng, H.; Geng, Z.; Li, F.; Zeng, J. Molecular Stabilization of Sub-Nanometer Cu Clusters for Selective  $\text{CO}_2$  Electromethanation. *ChemSusChem* **2022**, 15 (1), e202102010. <https://doi.org/10.1002/cssc.202102010>.
- (55) Zhao, Q.; Zhang, C.; Hu, R.; Du, Z.; Gu, J.; Cui, Y.; Chen, X.; Xu, W.; Cheng, Z.; Li, S.; Li, B.; Liu, Y.; Chen, W.; Liu, C.; Shang, J.; Song, L.; Yang, S. Selective Etching Quaternary MAX Phase toward Single Atom Copper Immobilized MXene ( $\text{Ti}_3\text{C}_2\text{Cl}_x$ ) for Efficient  $\text{CO}_2$  Electroreduction to Methanol. *ACS Nano* **2021**, 15 (3), 4927–4936. <https://doi.org/10.1021/acsnano.0c09755>.
- (56) Chen, Z.; Huang, A.; Yu, K.; Cui, T.; Zhuang, Z.; Liu, S.; Li, J.; Tu, R.; Sun, K.; Tan, X.; Zhang, J.; Liu, D.; Zhang, Y.; Jiang, P.; Pan, Y.; Chen, C.; Peng, Q.; Li, Y.  $\text{Fe}_1\text{N}_4\text{-O}_1$  Site with Axial Fe–O Coordination for Highly Selective  $\text{CO}_2$  Reduction over a Wide Potential Range. *Energy & Environ. Sci.* **2021**. <https://doi.org/10.1039/D1EE00569C>.
- (57) Jiang, H.-L.; Zhang, Y.; Jiao, L.; Yang, W.; Xie, C. Rational Fabrication of Low-Coordinate Single-Atom Ni Electrocatalysts by MOFs for Highly Selective  $\text{CO}_2$  Reduction. *Angew. Chem. In. Ed.* **2021**, anie.202016219. <https://doi.org/10.1002/anie.202016219>.
- (58) Lu, P.; Tan, X.; Zhao, H.; Xiang, Q.; Liu, K.; Zhao, X.; Yin, X.; Li, X.; Hai, X.; Xi, S.; Wee, A. T. S.; Pennycook, S. J.; Yu, X.; Yuan, M.; Wu, J.; Zhang, G.; Smith, S. C.; Yin, Z. Atomically Dispersed Indium Sites for Selective  $\text{CO}_2$  Electroreduction to Formic Acid. *ACS Nano* **2021**. <https://doi.org/10.1021/acsnano.1c00858>.
- (59) Tan, H.-Y.; Lin, S.-C.; Wang, J.; Chang, C.-J.; Haw, S.-C.; Lin, K.-H.; Tsai, L. D.; Chen, H.-C.; Chen, H. M. MOF-Templated Sulfurization of Atomically Dispersed Manganese Catalysts Facilitating Electroreduction of  $\text{CO}_2$  to CO. *ACS Appl. Mater. Interfaces* **2021**, acsami.1c10059. <https://doi.org/10.1021/ACSAMI.1C10059>.
- (60) Wang, Q.; Liu, K.; Fu, J.; Cai, C.; Li, H.; Long, Y.; Chen, S.; Liu, B.; Li, H.; Li, W.; Qiu, X.; Zhang, N.; Hu, J.; Pan, H.; Liu, M. Atomically Dispersed S-Block Magnesium Sites for Electroreduction of  $\text{CO}_2$  to CO. *Angew. Chem. In. Ed.* **2021**, 60 (48), 25241–25245. <https://doi.org/10.1002/anie.202109329>.
- (61) Wu, Y.; Chen, C.; Yan, X.; Sun, X.; Zhu, Q.; Li, P.; Li, Y.; Liu, S.; Ma, J.; Huang, Y.; Han, B. Boosting  $\text{CO}_2$  Electroreduction over a Cadmium Single-Atom Catalyst by Tuning of the Axial Coordination Structure. *Angew. Chem. In. Ed.* **2021**, 60 (38), 20803–20810. <https://doi.org/10.1002/ANIE.202105263>.

- (62) Cao, X.; Zhao, L.; Wulan, B.; Tan, D.; Chen, Q.; Ma, J.; Zhang, J. Atomic Bridging Structure of Nickel-Nitrogen-Carbon for Highly Efficient Electrocatalytic Reduction of CO<sub>2</sub>. *Angew. Chem. Int. Ed.* **2022**, 61 (6), e202113918. <https://doi.org/10.1002/anie.202113918>.
- (63) Chen, S.; Li, W.-H.; Jiang, W.; Yang, J.; Zhu, J.; Wang, L.; Ou, H.; Zhuang, Z.; Chen, M.; Sun, X.; Wang, D.; Li, Y. MOF Encapsulating N-Heterocyclic Carbene-Ligated Copper Single-Atom Site Catalyst towards Efficient Methane Electrosynthesis. *Angew. Chem. Int. Ed.* n/a (n/a). <https://doi.org/10.1002/anie.202114450>.
- (64) Li, Y.; Adli, N. M.; Shan, W.; Wang, M.; Zachman, M. J.; Hwang, S.; Tabassum, H.; Karakalos, S.; Feng, Z.; Wang, G.; Li, Y. C.; Wu, G. Atomically Dispersed Single Ni Site Catalysts for High-Efficiency CO<sub>2</sub> Electroreduction at Industrial-Level Current Densities. *Energy Environ. Sci.* **2022**, 15 (5), 2108–2119. <https://doi.org/10.1039/D2EE00318J>.
- (65) Wang, Y.; Park, B. J.; Paidi, V. K.; Huang, R.; Lee, Y.; Noh, K.-J.; Lee, K.-S.; Han, J. W. Precisely Constructing Orbital Coupling-Modulated Dual-Atom Fe Pair Sites for Synergistic CO<sub>2</sub> Electroreduction. *ACS Energy Lett.* **2022**, 7 (2), 640–649. <https://doi.org/10.1021/acsenergylett.1c02446>.



## Note S3. Geometrical model: cube, octahedra, truncated octahedra

### S3.1. Geometrical model of the cube

In order to determine the relative contribution of the facet, edge- and corner sites as well as the bulk atoms to the total number of atoms a particle consist of, we first defined the particles mass, which for a cube is given by:

$$m_{cube} = \rho \cdot l_{edge-length}^3$$

With  $\rho$  the density of the bulk and  $l_{edge-length}$  the particle edge-length. This then, allows to determine the number of atoms based on the mass via:

$$Atoms_{mass} = \frac{m_{cube} \cdot N_A}{MW}$$

in which  $N_A$  is Avogadro's number and MW the molecular weight. Alternatively, one can calculate the total number of atoms based on the volume and the volume of the unit cell:

$$Atoms_{volume} = \frac{l_{edge-length}^3 \cdot n_{atoms}}{l_{unit\ cell}^3}$$

With  $n_{atoms}$  the number of atoms in the unit cell and the lattice constant (FCC). The number of atoms calculated based on the mass and the volume match for the first two significant digits. Since it is uncertain if the bulk density is a reliable quantity on the nanoscale, we have opted to use the volumetric atom number instead.

To determine the number of surface atoms, we first defined a subsurface, which comprises the  $V_{cube}$  but with one monolayer of atoms subtracted (see Figure S1 for a spherical representative schematic):

$$V_{subsurface} = (l_{edge-length} - 4r_{covalent})^3$$

in which  $r_{\text{covalent}}$  is the metal-metal bond length. In here the constraint is applied that and that only a complete monolayer can be removed at a time. The number of surface atoms then becomes:

$$Atoms_{\text{surface}} = \frac{(V_{\text{Cube}} - V_{\text{subsurface}}) \cdot n_{\text{atoms}}}{l_{\text{unit cell}}^3}$$

With

$$Atoms_{\text{bulk}} = Atoms_{\text{volume}} - Atoms_{\text{surface}} = Atoms_{\text{subsurface}}$$

Since a cube consists of 6 equal faces, the number of (100) facet atoms become:

$$Atoms_{\{100\}} = \frac{6 \cdot (l_{\text{edge-length}} - 4r_{\text{covalent}}) \cdot r_{\text{covalent}} \cdot n_{\text{atoms}}}{l_{\text{unit cell}}^3}$$

And as the number of corners remain constant i.e. 8, the number of edge sites becomes:

$$Atoms_{\text{Edge}} = Atoms_{\text{surface}} - Atoms_{\{100\}} - Atoms_{\text{corners}}$$

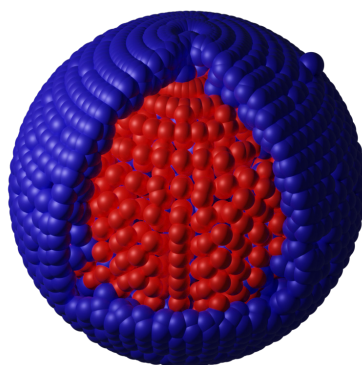


**Figure S2.** Ball model describing the subsurface approach to the determination of the number of surface atoms. The surface atoms in the geometrical model, here depicted in blue, consist of a single monolayer.

### S3.2. Geometrical model of the Octahedra.

In order to determine the relative contribution of the facet, edge- and corner sites as well as the bulk atoms to the total number of atoms a particle consist of, we first defined the particles mass, which for a cube is given by:

$$Atoms_{volume} = \frac{8\sqrt{2} \cdot l_{edge-length}^3 \cdot n_{atoms}}{l_{unit\ cell}^3}$$

and

$$Atoms_{subsurface} = \frac{8\sqrt{2}(l_{edge-length} - 2r_{covalent})^3 \cdot n_{atoms}}{l_{unit\ cell}^3}$$

and

$$Atoms_{(111)} = \frac{3\sqrt{3} \cdot (l_{edge-length} - 2r_{covalent})^2 \cdot r_{covalent} \cdot n_{atoms}}{2 \cdot l_{unit\ cell}^3}$$

and

$$Atoms_{(100)} = \frac{(l_{edge-length} - 2r_{covalent})^2 \cdot r_{covalent} \cdot n_{atoms}}{l_{unit\ cell}^3}$$

### S3.3. Geometrical model of the Truncated Octahedra

The geometrical model of the truncated octahedra was derived following the same logic as for the cube. We will, therefore, only list the changes respective of the geometry.

$$Atoms_{volume} = \frac{8\sqrt{2} \cdot l_{edge-length}^3 \cdot n_{atoms}}{l_{unit\ cell}^3}$$

and

$$Atoms_{subsurface} = \frac{8\sqrt{2}(l_{edge-length} - 2r_{covalent})^3 \cdot n_{atoms}}{l_{unit\ cell}^3}$$

and

$$Atoms_{(111)} = \frac{3\sqrt{3} \cdot (l_{edge-length} - 2r_{covalent})^2 \cdot r_{covalent} \cdot n_{atoms}}{2 \cdot l_{unit\ cell}^3}$$

and

$$Atoms_{(100)} = \frac{(l_{edge-length} - 2r_{covalent})^2 \cdot r_{covalent} \cdot n_{atoms}}{l_{unit\ cell}^3}$$

Chapter 3

# Research Objectives

### 3.1. Objectives of the Thesis

Based on the comprehensive critical review of experimental data on the CO<sub>2</sub>RR on metal catalysts spanning well-over three decades as discussed in Chapter 2,<sup>1</sup> and in particular from Figure 7 (reprinted here for reasons of clarity), it can be concluded that for the production of C<sub>2+</sub> products and especially liquid fuels, the sole practical catalyst to consider is Cu. All other pure elements produce mostly H<sub>2</sub>, CO, CH<sub>4</sub> or HCOO<sup>-</sup>. As the aim of the thesis is to improve upon electrocatalyst design for enhanced selectivity towards liquid fuels, we narrow our scope of potential catalyst candidates to Cu-based species. This brings us to the second observation. In the size regime >10 nm, the facet dominated regime, barely any

Cu alloys have been reported (i.e. others, mostly limited to Cu-Au and Cu-Pd). This means that the facet effect, in combination with the electronic effect upon the alloying of Cu with other components, is poorly understood. Therefore,

Objective 1:

Produce catalysts of Cu-X alloys that are facet controlled to study the effect of the facet in combination with the electronic effect of alloying in the CO<sub>2</sub>RR with the aim to enhance the selectivity towards liquid fuels.

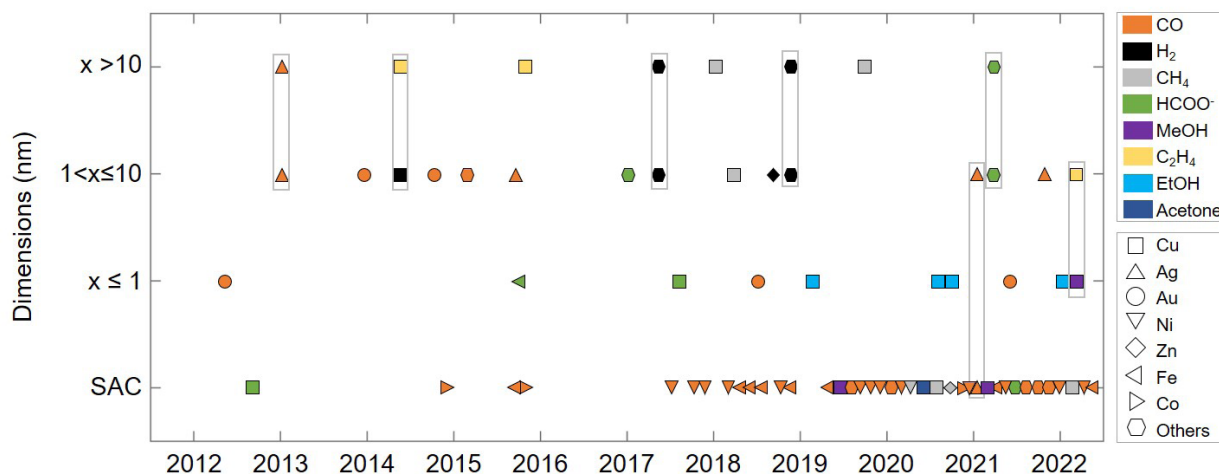


Figure 7. The most common products of CO<sub>2</sub>RR for typical metal catalysts in different size regimes: single-crystal and facet dominated nanoparticle (>10 nm), ultra-small particle (1<x≤10 nm), cluster (≤1 nm), and SAC. The metal utilized to obtain the results is indicated by shape, and the product is indicated by color. The ‘others’ series includes Cu alloys and other metals. Each point represents a published study, where studies covering different size regimes are included in the gray box. For a list of the publications, see Note S2 of the Supporting Information. Note that publications in Figure 7 have been selected for their investigation of metal catalysts of different sizes using the same synthesis technique. Further, to highlight the differing performance of metal catalysts versus their SAC counterparts, we have included a selection of those as well.

Cu-X candidate selection, was then inspired by computational efforts of collaborators of this work, e.g. Figure 22.<sup>2</sup>

Especially, the bimetallic Cu-Ag system is of interest due to the fact that A) it has a promising high predicted selectivity of CO<sub>2</sub>RR over HER (Figure 22b, abscissa) as well as a promising high activities predicted for CORR, i.e., C-C coupling (Figure 22b, ordinate) in comparison to pure Cu and B) no facet controlled Cu-Ag system in this size regime has been reported due to the

immiscibility of Cu and Ag making it an extremely challenging system to produce.<sup>3</sup> Therefore, Objective 1 was narrowed further,

Objective 1.1:

Produce catalysts of Cu-X (with X = at least Ag) alloys that are facet controlled to study the effect of the facet in combination with the electronic effect of alloying in the CO<sub>2</sub>RR with the aim to enhance the selectivity towards liquid fuels.

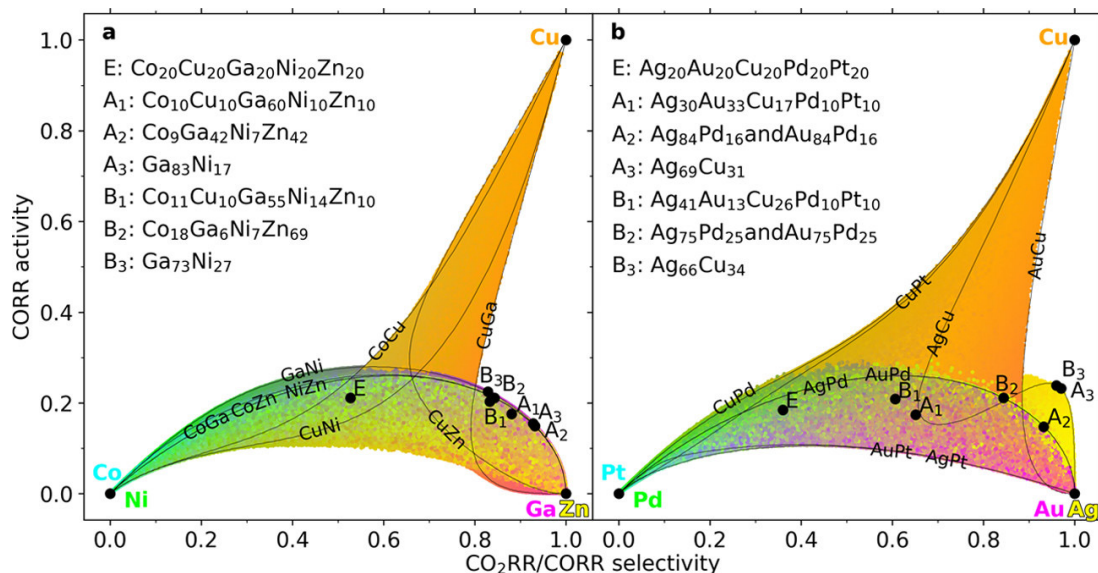


**Figure 22.** Selectivity vs activity plots of Cu based alloys of up to five components as based on predicted values via a supervised machine algorithm trained with adsorption energies of key intermediates, H\* and CO\*. Reprinted with permission from ref. <sup>2</sup>

From the fact that no procedure exists that offers insight in the composition distribution of multimetallic nanoparticles with ensemble representative statistics as current state of the art either offers ensemble averages, i.e. via inductively coupled plasma mass spectrometry or optical emission spectroscopy, X-ray diffraction, X-ray absorption spectroscopy etc., or the composition of a single particle via means of electron microscopy or diffraction, an information gap emerges: knowledge of the composition on the nanoscale, cannot be extrapolated to the bulk. Therefore,

Objective 2:

Develop a methodology to determine the composition distribution of multimetallic nanoparticles at the single particle level of detection but with ensemble representative statistics to correlate nanoscale characteristics (such as composition fluctuations) to bulk phenomena such as catalysis.

Following the comprehensive review and in particular Figure 7,<sup>1</sup> another conclusion can be drawn. In the size regime <1 nm, a disproportionately large degree of high liquid

fuel selectivity has been reported on Cu cluster catalysts and with a limited number of systems investigated. Further, strong correlation with the product selectivity and the cluster atomicity (number of atoms bonded) has been observed. Further, no bimetallic Cu-based cluster system has been reported to date. Finally, the effect of the support has not yet been fully deconvoluted from other effects in cluster electrocatalysis and remains unknown. Therefore, finally,

Objective 3:

Develop a synthesis process to produce Cu-X (with X = at least Ag) clusters functionalized on various carbonaceous supports to study the effect of cluster atomicity, composition and support effect in the CO<sub>2</sub>RR with the aim to enhance the selectivity towards liquid fuels.



## 3.2. Overview of the research work

Based on the previous objectives outlined, a brief overview of the research work in the present thesis is provided. First, a discussion on the newly developed methodology to determine ensemble representative composition distributions of multimetallic nanoparticles based on single-particle inductively coupled plasma mass spectrometry will follow in Chapter 4.<sup>4</sup> Thereafter, the low-temperature non-equilibrium synthesis developed presently to produce multimetallic facet-controlled nanoparticle alloys, which were used as model electrocatalyst in CO<sub>2</sub>RR towards liquid fuels will be discussed in Chapter 5. And finally, the developed synthesis procedure to produce Cu-Ag clusters, which were used to electrocatalytically convert CO<sub>2</sub> to acetaldehyde, will be discussed in Chapter 6.

### 3.3. References

- (1) Koolen, C. D.; Luo, W.; Züttel, A. From Single Crystal to Single Atom Catalysts: Structural Factors Influencing the Performance of Metal Catalysts for CO<sub>2</sub> Electroreduction. *ACS Catal.* **2022**, 948–973. <https://doi.org/10.1021/acscatal.2c03842>.
- (2) Pedersen, J. K.; Batchelor, T. A. A.; Bagger, A.; Rossmeisl, J. High-Entropy Alloys as Catalysts for the CO<sub>2</sub> and CO Reduction Reactions. *ACS Catal.* **2020**, 10 (3), 2169–2176. <https://doi.org/10.1021/acscatal.9b04343>.
- (3) Ozoliņš, V.; Wolverton, C.; Zunger, A. Cu-Au, Ag-Au, Cu-Ag, and Ni-Au Intermetallics: First-Principles Study of Temperature-Composition Phase Diagrams and Structures. *Phys. Rev. B* **1998**, 57 (11), 6427–6443. <https://doi.org/10.1103/PhysRevB.57.6427>.
- (4) Koolen, C. D.; Torrent, L.; Agarwal, A.; Meili-Borovinskaya, O.; Gasilova, N.; Li, M.; Luo, W.; Züttel, A. High-Throughput Sizing, Counting, and Elemental Analysis of Anisotropic Multimetallic Nanoparticles with Single-Particle Inductively Coupled Plasma Mass Spectrometry. *ACS Nano* **2022**. <https://doi.org/10.1021/acsnano.2c01840>.

## Chapter 4

# High-throughput sizing, counting and elemental analysis of anisotropic multimetallic nanoparticles with single-particle inductively-coupled plasma mass spectrometry

**Post print version:** this section has been published as a full-length article in *ACS Nano*, 2022, 16, 8, 11968-11978

DOI: 10.021/acsnano.2c01840

Edit: caption numbers of figures, tables, and equations were edited to match the thesis **chapter number**.

**Permission to reproduce:** reproduced with permission from the publisher.

**Cedric David Koolen<sup>a,b</sup>, Laura Torrentc, Ayush Agarwalc,<sup>d</sup>, Olga Meili-Borovinskayae, Natalia Gasilovaf, Mo Li<sup>a,b</sup>, Wen Luog\*, Andreas Züttela,<sup>b</sup>**

<sup>a</sup>Laboratory of Materials for Renewable Energy (LMER), Institute of Chemical Sciences and Engineering (ISIC), Basic Science Faculty (SB), École polytechnique fédérale de Lausanne (EPFL) Valais/Wallis, Energypolis, Sion, 1951, Switzerland.

<sup>b</sup>Empa Materials Science & Technology, Dübendorf, 8600, Switzerland.

<sup>c</sup>Bioenergy and Catalysis Laboratory (LBK), Energy and Environment Research Division (ENE), Paul Scherrer Institute (PSI), Villigen, 5232, Switzerland.

<sup>d</sup>School of Architecture, Civil and Environmental Engineering (ENAC IIE GR-LUD), École Polytechnique Fédérale de Lausanne (EPFL), Lausanne, 1035, Switzerland

<sup>e</sup>TOFWERK AG, Thun, 3645, Switzerland.

<sup>f</sup>Mass Spectrometry and Elemental Analysis Platform (MSEAP), Institute of Chemical Sciences and Engineering (ISIC), Basic Science Faculty (SB), École Polytechnique Fédérale de Lausanne (EPFL) Valais/Wallis, Energypolis, Sion, 1951, Switzerland.

<sup>g</sup>School of Environmental and Chemical Engineering, Shanghai University, Shanghai, 200444, China.

\*Corresponding author: wenluo@shu.edu.cn

## Abstract

Nanoparticles (NPs) have wide applications in physical and chemical processes, and their individual properties (e.g., shape, size, and composition) and ensemble properties (e.g., distribution and homogeneity) can significantly affect the performance. However, the extrapolation of information from a single particle to the ensemble remains a challenge due to the lack of suitable techniques. Herein, we report a high-throughput single-particle inductively-coupled plasma mass spectrometry (SP-ICP-MS) based protocol to simultaneously determine the size, count, and elemental make-up of several thousands of (an)isotropic NPs independent of composition, size, shape, and dispersing medium with atomistic precision in a matter of minutes. By introducing highly diluted nebulized aqueous dispersions of NPs directly into the plasma torch of an ICP-MS instrument, individual NPs are atomized and ionized, resulting in ion plumes that can be registered by the mass analyzer (typically quadrupole, sector-field, or time-of-flight tube). Our proposed protocol includes a phase transfer step for NPs synthesized in organic media, which are otherwise incompatible with ICP-MS instruments, and a modeling tool that extends the measurement of particle morphologies beyond spherical to include cubes, truncated octahedra, and tetrahedra, exemplified by anisotropic Cu NPs. Finally, we demonstrate the versatility of our method by studying the doping of bulk-dilute (<1 at. %) CuAg nanosurface alloys as well as the ease with which ensemble composition distributions of multimetallic NPs (i.e., CuPd and CuPdAg) can be obtained providing different insights in the chemistry of nanomaterials. We believe our combined protocol could deepen the understanding of macroscopic phenomena involving nanoscale structures by bringing about a statistics renaissance in research areas including, amongst others, materials science, materials chemistry, (nano)physics, (nano)photonics, catalysis, and electrochemistry.

## Keywords

Nanoparticle, Single-particle ICP-MS, multimetallic, size, shape, composition, protocol

## 4.1. Introduction

The size and composition of nanoparticles (NPs) have shown to play an important role in a variety of physical and chemical processes, including light-matter interactions, magnetism, catalysis, etc.<sup>1,2,3,4,5,6</sup> To determine structure-property relations for such phenomena, the size and composition of the NP must be accurately and precisely described. Advancements in electron tomography using aberration-corrected microscopes have allowed for an exact 3D description of NPs with each individual atom accounted for.<sup>7</sup> However, at least eight orders of magnitude separate a single particle from its bulk powder. Therefore, the sample space that can reasonably be attained with high resolution electron microscopes (EM) is too low for statistically sound extrapolation to the bulk. An information gap immerses.<sup>8,9</sup>

More crudely but with better statistics, NPs can be sized through the production of low resolution EM images and subsequent automated edge-length analysis.<sup>10,11</sup> Several commercial and open-source image processing software exist that can be of aid herein.<sup>12,13,8</sup>

However, exact determination of atomicity using such approaches is impossible as the resolution required lies outside the information limit. Further, the success of automated sizing is often frustrated by tedious sample preparation steps and the large quantities of micrographs needed for reasonable statistics.<sup>8,9</sup> In the present study, we propose the use of a methodology complementary to EM that allows to determine atomicity, composition, size, and number concentration of inorganic NP dispersions independent of element and shape with ensemble-representative statistics in a single experiment, based on single-particle inductively-coupled plasma mass spectrometry (SP-ICP-MS).<sup>14,15,16,17,18</sup>

ICP-MS is routinely used to determine the concentration of elements in their ionic form. In the framework of nanomaterials, this entails the digestion of particulate matter using strong acids such as concentrated nitric acid ( $\text{HNO}_3$ ), hydrochloric acid (HCl), or aqua regia yielding dissolved ionic solutions of the respective materials. The MS determines the ion intensities of a

defined mass to charge ratio for each of the analytes and correlates it to the absolute concentration based on the external calibration curve prepared using standard solutions of the analytes at known concentrations.<sup>19</sup> Such an approach allows for the determination of average elemental make-up, synthesis yields, dispersion concentrations etc., but is insensitive to the homogeneity of the ensemble. For

an ICP-MS instrument with a quadrupole mass analyzer, an intensity reading is acquired every defined time interval, known as dwell time or integration time, and averaged over the total acquisition time. Instead, in single-particle-ICP-MS, undigested NP dispersions are nebulized and introduced to the plasma torch directly, after which the individual particles become desolvated, vaporized, atomized and ionized, and arrive at the mass analyzer

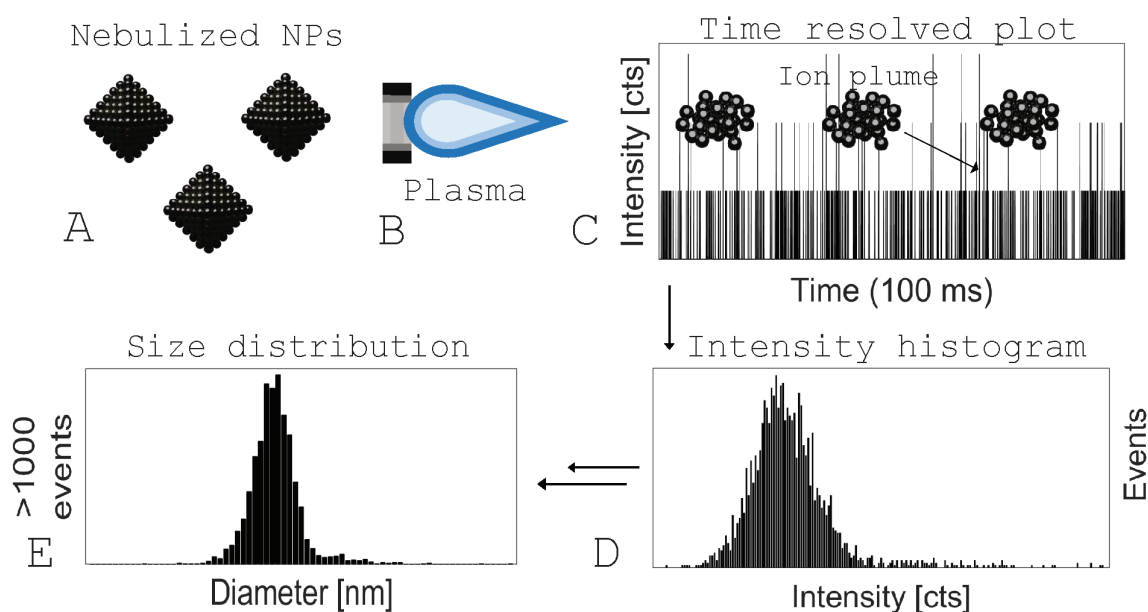



**Figure 23.** Schematic diagram of the general approach for obtaining size distribution of NP dispersions using SP-ICP-MS. (A) Nebulized NPs formed after nebulization of the sample dispersions. (B) Plasma torch of the ICP-MS instrument used for the desolvation, vaporization, atomization, and ionization of the particles present in the aerosol. (C) SP-ICP-MS raw data containing both background signal (e.g., dissolved ions) and particle events (ion plumes). A snapshot of 100 ms is depicted for representation. (D) Histogram of the raw data obtained via a sorting algorithm after background subtraction equating the intensity to the number of observations (events). (E) Final solution of SP-ICP-MS data processing pipeline, e.g., size distributions.

as discrete ion packages, or ion plumes, retaining the information of the elemental make-up of each individual particle (**Figures 23A, B**).<sup>20</sup> Intensity spikes above the background herald the arrival of an ion plume or particle event at the detector. This is distinctively different from dissolved ion intensities, or background signal, which remain constant. To distinguish between these discrete particle events and the dissolved ions, dwell times much shorter than in conventional ICP-MS are needed ( $\mu\text{s}$  to  $\text{ms}$ ). Each individual acquisition of the intensity read-out is then plotted against the acquisition time representing the SP-ICP-MS raw data (**Figure 23C**). A series of steps (**Figure 23D**) have to be executed before raw SP-ICP-MS data can be transformed into a meaningful data-set such as a NP size distribution (**Figure 23E**).<sup>14,16</sup>

Traditionally, SP-ICP-MS has been used to determine particle number concentrations and size distributions of undefined, crude dispersions relevant to environmental research, health and/or food sciences, limited to metal oxides and noble metals such as Au, Ag, and Pt.<sup>15,17,20,21,22,23,24,25,26</sup>

Recently, some more complex analytes (e.g., TiNbCN and AuAg) have been studied as well albeit of undefined morphology or isotropic in nature.<sup>27, 28</sup> Moreover, due to the incompatibility of ICP-MS with organic solvents, samples analyzed are produced or dispersible in water alone. Herein, we show the capabilities of SP-ICP-MS to determine the size, count and composition of transition metal (an)isotropic (multi) metallic NPs of well-defined size and shape, including but not limited to spheres, cubes, truncated octahedra and tetrahedra, synthesized in organic media using our in-house developed syntheses procedure (**Figure 24**). We further demonstrate that the high sensitivity of the quadrupole mass analyzer allows to quantify the atomicity of bulk-dilute (<1 at. %) anisotropic CuAg nanosurface alloys (NSA), corroborated with X-ray photoelectron spectroscopy (XPS), offering a roadmap for the study of NP doping with reliable statistics using SP-ICP-MS. Finally, by extending upon our in-house developed syntheses, we produce CuPd and CuPdAg cubic multimetallic NPs and use a time-of-flight (TOF) ICP-MS to show



that the composition of NP ensembles can be studied with ease. We further verify these results with scanning transmission electron microscopy energy dispersive X-ray spectroscopy (STEM-EDX). We aim at providing a method to the reader to quantify (an)isotropic inorganic NP dispersions complementary to EM. We believe that this method can also be applied to a variety of materials, including semiconductors (e.g., CdSe, CsPbBr<sub>3</sub>, InP, etc.), upconversion nanocrystals (e.g., NaYF<sub>4</sub>, NaGdF<sub>4</sub>, NaLuF<sub>4</sub>, etc.), metal oxide (e.g., Al<sub>2</sub>O<sub>3</sub>, TiO<sub>2</sub>, ZnO<sub>2</sub>

etc.), metal organic frameworks (e.g., ZIF-8, HKUST-1, UiO-66, etc.) and finally, metals and alloys (e.g., Mn, Co, Ni etc.). Therefore, a complete description of the instrument calibration and data processing pipeline is provided in the following section.



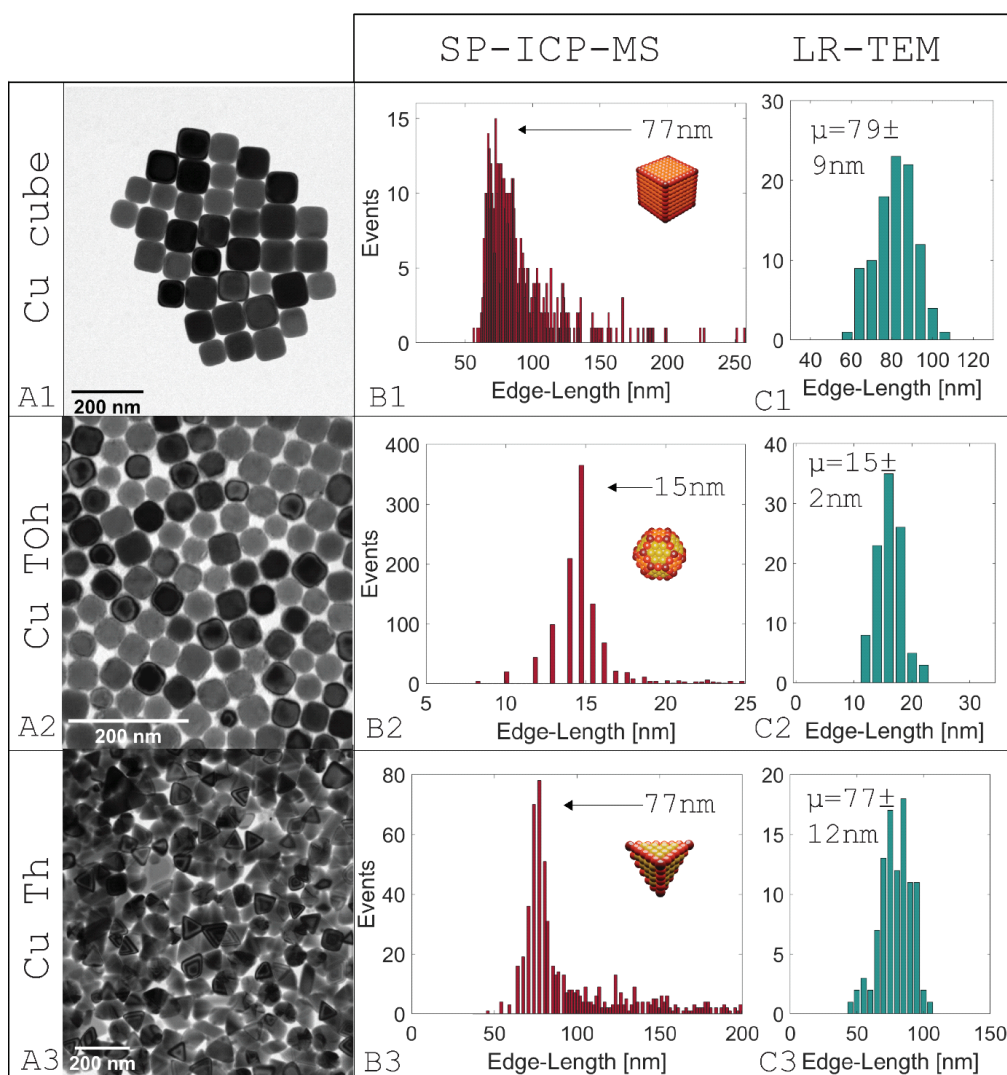


**Figure 24.** (A1-A3) Low resolution transmission electron microscopy (LR-TEM) micrographs of cubic (C), truncated octahedral (TOh), and tetrahedral (Th) Cu NPs synthesized using a phosphine-derivative mediated wet-chemical procedure. (B1-B3) Size distributions of the C-, TOh- and Th-Cu NPs obtained using SP-ICP-MS. The particle most frequently observed has an edge-length of: 77, 15 and 77 nm, respectively. Edge-length is defined as the center-to-center distance between two corner atoms of a particle (depicted in deep red in the ball models in the inset). The total number of particles observed in a single experiment was as high as 1100 for a measurement of 100 s duration with a dwell time of 50  $\mu$ s. Excellent agreement exists between the SP-ICP-MS and LR-TEM (C1-C3) measurements. Aggregates in the sample that are missed by the LR-TEM can be observed (events at the far end of the distributions in (B1-B3), giving a more complete picture of the ensemble. (C1-C3) Size distributions of 100 C-, TOh- and Th-Cu NPs using particle counting of LR-TEM micrographs.

## 4.2. Instrument calibration and data processing

As described in the introduction, SP-ICP-MS raw data consist of a signal intensity as a function of time (**Figure 25A**). This includes a background/dissolved analyte signal and particle events evidenced by intensity spikes above the background. In order to extract all particle events, background subtraction has to be performed, which is achieved mathematically and iteratively (see **Methods**). All extracted particle events are then grouped and sorted based on their respective intensity values and reported as events-versus-intensity histograms (**Figure 25B**).<sup>29</sup> The total number of events is a direct measure of the number of particles that have reached the detector, which can be converted into a number concentration using Eq. 1:

$$N = \frac{f}{tQ\eta_t} \quad (1)$$

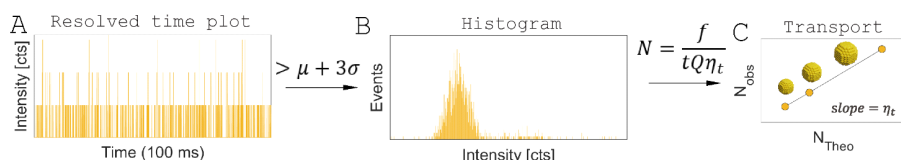
in which  $N$  is the NP number concentration ( $\text{mL}^{-1}$ ),  $f$  the total number of events,  $t$  the total acquisition time (min), and  $Q$  the sample flow rate ( $\text{mL min}^{-1}$ ), which can be estimated from the mass change of an arbitrary volume of water consumed by the instrument as a function of time. The dimensionless quantity  $\eta_t$ , known as the transport efficiency, is introduced to account for the fraction of particles originally introduced that can actually be detected and is generally  $<10\%$ .<sup>14,16</sup> This is due to losses associated with the generation of the aerosol, which is instrument and size dependent.<sup>30</sup> Therefore, sets of known particle size and concentration are introduced and their observed number concentrations are determined (**Figure 25C**). Calibration can then be performed using Eq. 2:

$$N_{obs} = \frac{f}{Qt} = \eta_t N_{Theo} \quad (2)$$

in which  $N_{obs}$  is the observed particle number concentration and  $N_{Theo}$  the theoretical particle number concentration. Alternatively, calibration can also be performed based on the particle size but requires an additional external calibration step.<sup>14,16</sup> Often used calibrants are monodisperse isotropic Ag and Au NPs, which can be purchased from various sources and of which the latter is used presently (see **Methods, Figure S1** and **S2**). In theory, any set of

well-defined, monodisperse particles with known characteristics can be used for the calibration. Ideally, one would use standard dispersions of the same element as well as the same matrix as the analyte. However, commercial availability is limited. Therefore, we are working on sets of synthesized NP calibrants to match our analyte and determine its effect, if any, which is the subject of a later work.

### Instrument calibration



### Data processing

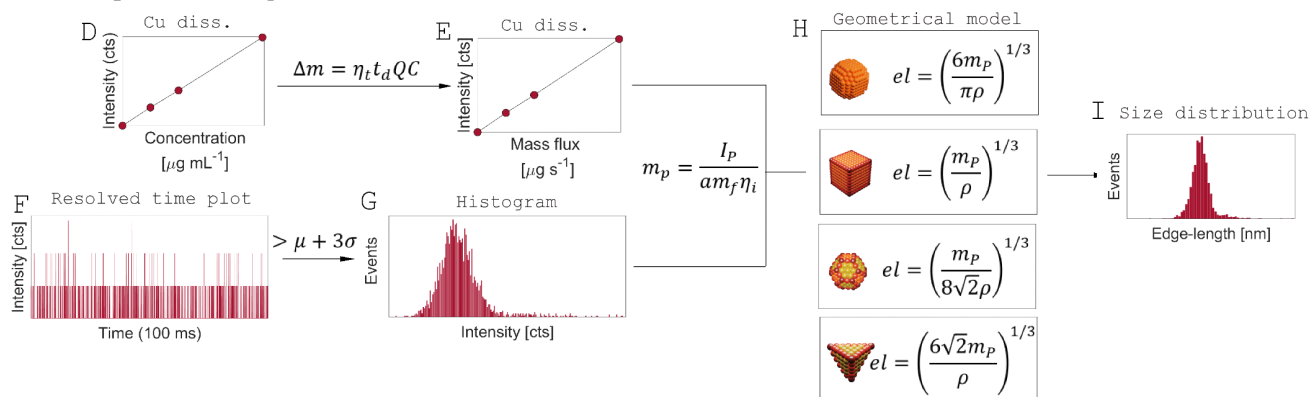


**Figure 25.** (A) Time resolved plot of the SP-ICP-MS raw data of a calibrant (yellow). Only 100 ms is depicted for clarity. (B) Intensity-versus-events histogram of a calibrant (yellow). (C) Transport efficiency ( $\eta_t$ ) calibration curve of particle dispersions of known size and number concentration (in the present study Au NP (see **Methods, Figure S1** and **S2**)). (D) Dissolved standard solutions calibration curve (Cu in the present study). (E) Converted  $\mu\text{g s}^{-1}$  calibration curve of the dissolved ion standards (Cu in the present study). (F) Time resolved plot of the SP-ICP-MS raw data of an analyte (red). (G) Intensity-versus-events histogram of an analyte (red). A snapshot of 100 ms is depicted for representation. (H) Various geometrical models to extract dimensional parameters such as edge-length including but not limited to spheres, cubes, truncated octahedra and tetrahedra. (I) Final solution of the SP-ICP-MS data processing pipeline representing a NP size distribution.

With the instrument calibrated and  $\eta_t$  obtained, one could directly measure the number concentration of a given unknown NP dispersion. However, in order to determine the mass of the particles counted, another calibration is required. As mentioned before, in ICP-MS, the dissolved analyte concentration of an unknown solution is determined by comparing its average intensity to the intensity measured of solutions of known concentrations. However, SP-ICP-MS intensities are detected at discrete intervals. Therefore, to relate such a discrete intensity to an ion plume mass, the average concentration of the calibration curve ( $\mu\text{g mL}^{-1}$ ; **Figure 25D**) needs to be converted into the amount of material detected at any given dwell time ( $\mu\text{g s}^{-1}$ ; **Figure 25E**). This can be achieved according to Eq. 3:

$$\Delta m = \eta_t t_d QC \quad (3)$$

in which  $t_d$  is the dwell time (or integration time) and  $C$  the dissolved ion concentration. The slope of the converted calibration curve ( $a$ ) then relates the intensity of the ion plume ( $I_p$ ) to the particle mass ( $m_p$ ) through Eq. 4:

$$m_p = \frac{I_p}{am_f \eta_i} \quad (4)$$

in which  $\eta_i$  is the ionization efficiency, the dimensionless parameter that allows for a correction factor for materials that ionize poorly. Partial ionization is strongly mass dependent both relative and absolute, and has been determined for Au to occur for particles  $>150$  nm.<sup>20,31</sup> Further, partial ionization may also play a role for metal oxides for their generally high boiling points.<sup>20,31</sup> As the materials investigated in this study (i.e., Cu, CuAg, CuPd, and CuPdAg NPs) have lower melting points and ionization potentials than Au and are smaller than 150 nm in size, it is reasonable to assume an ionization efficiency of 100%.

Another parameter  $m_f$ , the mass fraction, or the contribution of the element analyzed to the total particle mass, is introduced for modelling purposes. For example, only metal species in metal oxides can be detected by ICP-MS and this can be accounted for by a corresponding  $m_f$  value.

With the particle mass in hand, the events per intensity histogram of the analyte can be converted into a size distribution of a specific particle geometry by using a dimensional descriptor such as the edge-lengths ( $el$ ). This includes but is not limited to spheres (Eq. 5), cubes (Eq. 6), truncated octahedra (Eq. 7), and tetrahedra (Eq. 8):

where  $\rho$  is the density.

$$el_{Sph} = \left( \frac{6m_p}{\pi\rho} \right)^{\frac{1}{3}} \quad (5)$$

$$el_{Cu} = \left( \frac{m_p}{\rho} \right)^{\frac{1}{3}} \quad (6)$$

$$el_{TOh} = \left( \frac{m_p}{8\sqrt{2}\rho} \right)^{\frac{1}{3}} \quad (7)$$

$$el_{Th} = \left( \frac{6\sqrt{2}m_p}{\rho} \right)^{\frac{1}{3}} \quad (8)$$

## 4.3. Results and Discussion

### 4.3.1. NP concentration optimization

In order to have the most accurate measurement, it is adamant that each particle event can be distinguished from the background. If the ionic contribution to the signal is too high (e.g., a residual from the synthesis), NPs having intensities similar or below that of the dissolved analyte cannot be identified by the algorithm. However, since the intensity of each particle is fixed and the intensity of the dissolved analyte is concentration dependent, sample dilution can help detect the smaller particles in the ensemble as well (for particles above the limit of detection (LOD)).<sup>32,33</sup> To evaluate the effect of NP concentration on the results, in **Figure 26**, a suspension of 15 nm TOH-Cu NPs at a concentration of  $10^5 \text{ mL}^{-1}$  was analyzed by SP-ICP-MS as well as their 3- and 6-fold dilutions. The measured most frequent size was: 29 nm (**Figure 26A, Table S1**), 23 nm (**Figure 26B, Table S1**) and 15 nm (**Figure 26C, Table S1**), respectively. The latter one portrays the complete distribution whereas for the former two only a portion of the ensemble can be observed. This shows the dissolved analyte concentration cap. Above it, the background signal is too

high to extract the full distribution. Diluting further, on the other hand, will result in progressively lower numbers of events as less and less intervals will contain a particle event. Of course, this could be off-set by extending the measurement time but this is rather impractical: for every additional second measured, with  $t_d = 50 \mu\text{s}$ ,  $2 \times 10^4$  data points are added to the data file. Therefore, there exists an optimized dissolved analyte to particle concentration that yields good statistics with the least amount of data, but excludes the loss of information due to a too high ionic background. For the Cu NPs reported here and using the instrument settings as outlined in the **Methods** section, this optimal concentration lies between 10,000-20,000  $\text{mL}^{-1}$ . However, this value can vary strongly between particles of different elements and depends on both the chemical nature of the NPs, their size, the instrument and its corresponding settings and finally the synthesis procedure used (e.g., for Au NPs of 30-100 nm used presently this value is  $\sim 50,000 \text{ mL}^{-1}$  for  $t_d = 50 \mu\text{s}$  on a quadrupole based ICP-MS instrument).<sup>34,29</sup> Preparing dilution series as

in **Figure 26** can be of tremendous value to calibrate a measurement when optimal number concentrations are unknown. It is worth noting the difference in events between **Figure 26A, 4B** and **4C**. When the dissolved analyte concentration is too high, only the tail of the distribution can be extracted resulting in a low number of events. Once the ionic background intensity

falls below that of the smallest particle of the ensemble, the total number of events goes up by at least an order of magnitude. This change in NP events can be used as a handle to find the optimal concentration.

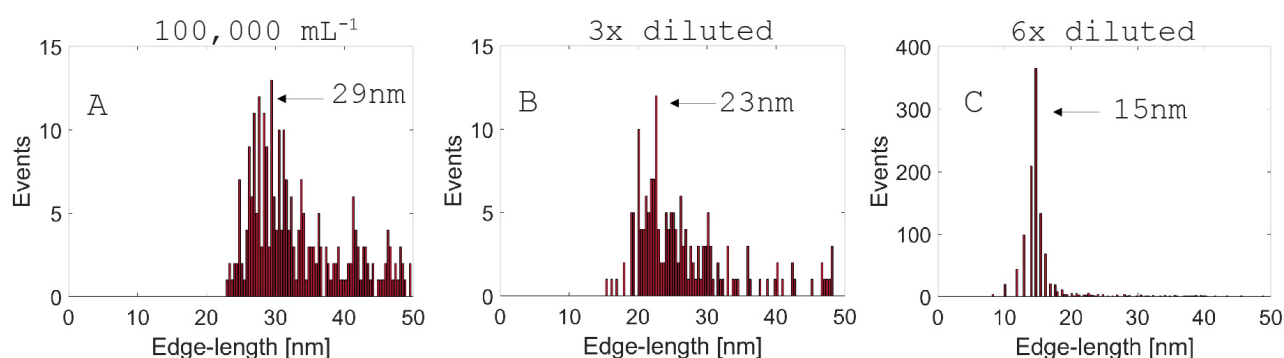


**Figure 26.** Size distributions of a dilution series of TOh-Cu NPs. (A) NP number concentration (N):  $10^5$  mL<sup>-1</sup>, (B) NP number concentration (N):  $1/3 \times 10^5$  mL<sup>-1</sup>, (C) NP number concentration (N):  $1/6 \times 10^5$  mL<sup>-1</sup>. Shift of the average size, thus mass, to lower values, upon dilution highlights the significant effect of the dissolved analyte concentration on data quality. If the dissolved analyte concentration is too high, ion plumes derived from initial particles of intensities close to the dissolved analyte cannot be distinguished from the background. Optimization and calibration of N is instrumental to correct distribution determination. This feature perseveres even with an independent instrument calibration used (**Figure S3**). The gain in the number of events is evidence that all particle events can be extracted.

### 4.3.2. Reliability of the method

To determine the reliability of the technique to provide reproducible size distributions (as it is still one of the main means to show ensemble (in)homogeneity),<sup>10,11</sup> we prepared two dilution series of the same NPs (TOh-Cu, **Figures 26A-C** and **S3A1-C1**) but used independent standards for the instrument calibration of  $\eta_t$  (**Figures S1** and **S2**). By using the same mass  $s^{-1}$  calibration curve for both dilution series (**Figure S4**), we ensured that any changes to the size distribution that originated from inaccuracy in the determination of the  $\eta_t$ , which is expected to introduce the largest error,<sup>14</sup> are taken into account. When the particle concentration reaches its optimal value, a perfect match in the particle mass is obtained with the edge-length of the TOh-Cu NPs determined at 15 nm in both cases, independently of calibrant used (**Figures 26C** and **S3C1**). With a well-calibrated instrument, precise and accurate size distributions can be obtained reproducibly, independent of particle size and shape (for particles above the LOD) as equally agreeing results could be obtained for the Th-Cu NPs (**Figures S3A2-C3** and **S4**).

We further investigated the accuracy and precision of SP-ICP-MS to determine NP number concentrations as they are of interest to study colloidal stability, nanoparticle sintering and catalytically active surface area estimation, amongst others.<sup>35,36,37,38</sup> We prepared six independent dilutions of C-, TOh-, and Th-Cu NPs, based on a three-fold dilution series, and measured the particle concentrations (**Table S2**). With an uncertainty of the measurement of only 4% (estimated through error propagation of the dilution series based on manufacturer reported uncertainties at 2%, **Table S2.2**), SP-ICP-MS allows for number concentration determinations with high precision. Further, it reveals a consistently lower particle concentration (~10%) than estimated based on LR-TEM particle counting. This is most likely a result of aggregates in the sample, however.



### 4.3.3. Applications

Beside the size and the particle number concentration, SP-ICP-MS can be used to quantify different elements within a particle ensemble.<sup>40</sup> Due to the short dwell times needed for SP-ICP-MS, TOF mass analyzers are required to obtain a full elemental spectrum in a single dwell/integration time.<sup>18,20,41,42</sup> Very recently, a SP-ICP-MS method has been established to simultaneously measure two elements by extending the signal duration through the introduction of a collision cell.<sup>28</sup> This limits the LOD, however. Alternatively, one may perform sequential spectral analysis.<sup>20</sup> Using a galvanic exchange reaction, we were able to synthesize anisotropic CuAg NSAs (C-CuAg, **Figure 27A1, A2** and TOH- and Th-CuAg **Figure S5**). With the Ag and Cu distributions obtained via SP-ICP-MS, followed by a subsequent subsurface based modelling step, we were able to determine the ensemble average surface composition of our anisotropic particles (**Figure 27C1-C2**). We deduce that 0.59 monolayer of Ag has been deposited in the case of the C-CuAg NSA. Further, we show that Ag at. % is normally distributed around

the mean (max. Ag 9 at. %, **Figure 27C2**). Our method offers the same information as for dopant distributions that have been studied for bulk materials, e.g., n-type semiconductors.<sup>43,44,45</sup> We further confirmed these results with the good agreement of those obtained from XPS by comparing the estimated penetration-depth to the inelastic mean free path information depth (error <5%, **Figure S6** and **Table S3**).<sup>46</sup>

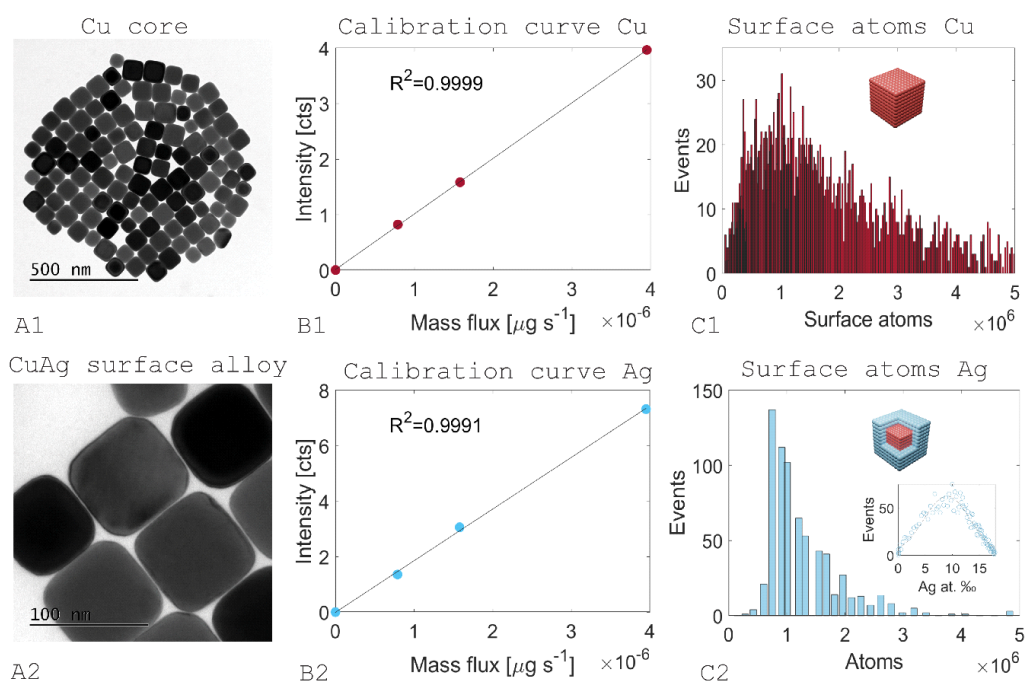


**Figure 27.** SP-ICP-MS as a method to characterize anisotropic NSAs.<sup>39</sup> The C-Cu NPs synthesized in the present study were coated with an ultrathin shell of Ag using a galvanic exchange reaction (see **Methods**). (A1-A2) LR-TEM micrograph of the Cu cubic core and the CuAg cubic NSA, respectively. (B1-B2) Cu and Ag mass flux calibration curve used to convert the intensity measured to the mass of the particle. (C1) Using a subsurface model (**Note S2**), the Cu particle mass distribution obtained with SP-ICP-MS can be converted into an ensemble distribution of surface atoms. (C2) Distribution of Ag atoms obtained via SP-ICP-MS. By taking the ensemble average, we deduce that 0.59 monolayer of Ag has been deposited. Inset shows the normally distributed doping concentration of Ag by superimposing the Cu and Ag spectra, respectively.

While sequential analysis suffices for simple bimetallic samples, experiment and data treatment quickly becomes tedious for more complex systems (e.g., high-entropy alloys<sup>47</sup>). Further, data treatment requires assumptions and preexisting knowledge of the sample, e.g., that each particle contains all elements. Therefore, we further extended upon our galvanic replacement reaction to produce next to C-CuAg NSAs, C-CuPd and C-CuPdAg anisotropic multimetallic NPs to show the capabilities of TOF mass analyzers to determine the elemental make-up of every *single* particle simultaneously and its advantage over quadrupole mass analyzers for, e.g., doping studies (**Figure 27**). As a benchmark, we first sized C-Cu NPs using SP-ICP-TOFMS to determine the reliability of the method and alternative calibration procedure using monodisperse microdroplets of element solutions, which showed an excellent match with LR-TEM (**Figure S7**). Further, we confirmed the normal distribution of Ag in the C-CuAg NSA (**Figure 28C1**) and determined that in the case of CuPd, a positive skew followed with an order larger Pd content (**Figure 28C2**). We invoke differences in standard reduction potentials of both metals to explain the difference in reactivity (+0.7996 and +0.915 V for Ag(I) and Pd(II), respectively). We could verify the presence of Ag and Pd in the respective bimetallic systems using STEM-EDX, which showed a core-shell like morphology for C-CuPd NPs, corroborating

the higher average Pd content determined with SP-ICP-TOFMS (**Figure 28B1-B2**). Moreover, by reintroducing C-CuAg NSAs in the Pd-precursor reaction mixture, we were able to synthesize C-CuPdAg NPs as well (**Figure 28A3-C3**). Interestingly, it could be deduced that Ag had corroded instead of the expected Cu alone (+0.52 V, **Figure S8**). This can be explained by the more facile etching of Ag in the presence of Cl<sup>-</sup> ions. Further scrutiny of the SP-ICP-TOFMS data pointed towards the presence of bimetallic AgPd NPs in the ensemble as well albeit of low occurrence. After reexamination of the sample with STEM-EDX, these particles could eventually be observed likewise (**Figure S9**). Finally, we show that using SP-ICP-TOFMS it is possible to distinguish bimetallic physical mixtures (CuAg + CuPd) from multimetallic NPs, which would not have been possible using a quadrupole mass analyzer (**Figure S10**). With the TOF instrument used presently, any ion within the range of 7-175 *m/z* can be observed simultaneously (**Table S4**).<sup>48</sup> This includes most of the elements of the periodic table. However, not all elements can be observed with equal sensitivity. For a list of elements that can be quantified with SP-ICP-TOFMS and their reported LODs if any, we direct the reader to the SI (**Table S5**).

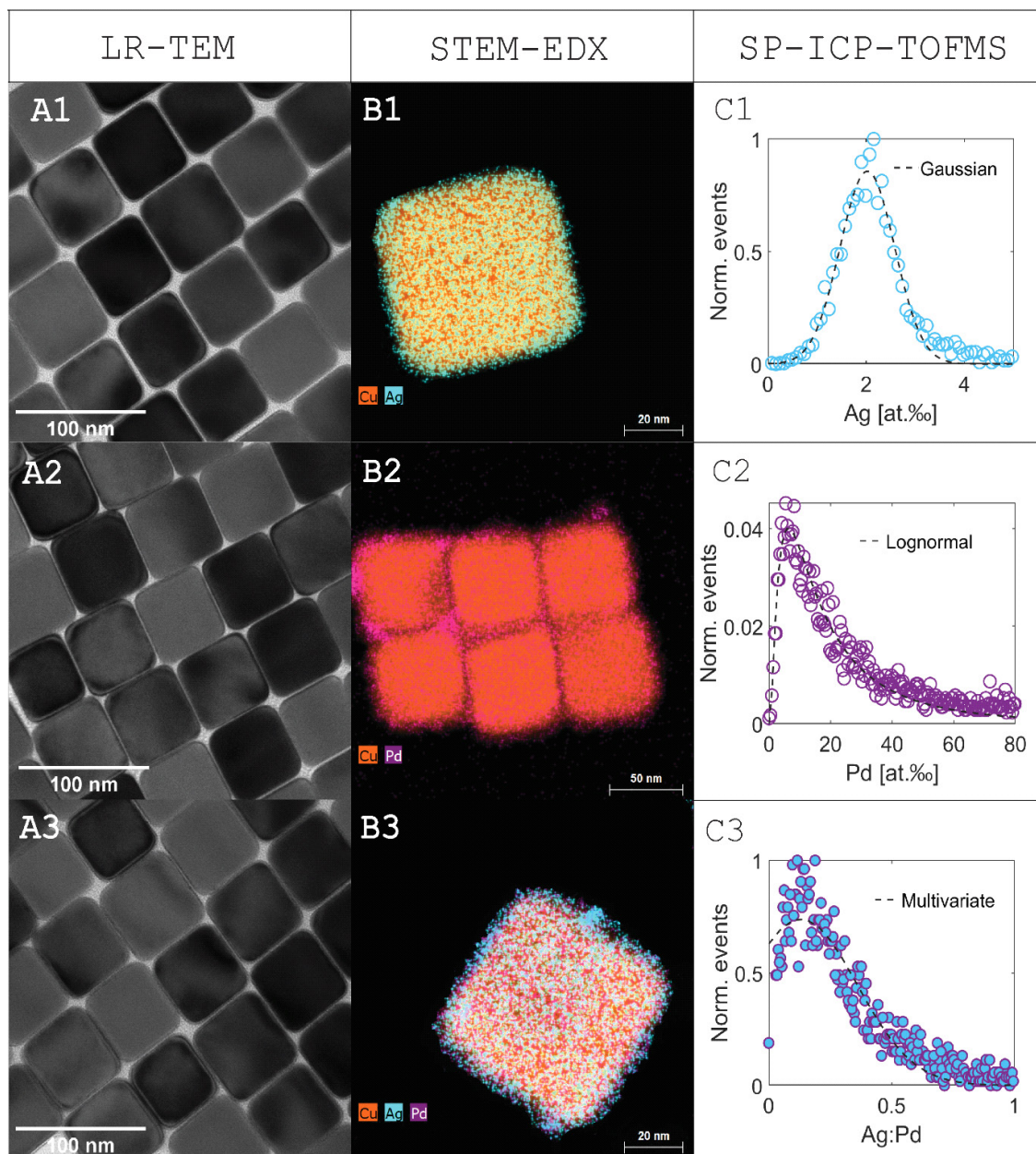


**Figure 28.** (A1-A3) TEM micrographs of the C-CuAg, C-CuPd, and C-CuPdAg multimetallic NPs, respectively. (B1-B3) STEM-EDX elemental maps of C-CuAg, C-CuPd, and C-CuPdAg NPs. (C1-C3) Normalized composition distributions of C-CuAg, C-CuPd, and C-CuPdAg multimetallic NPs obtained with a TOF mass analyzer. The C-CuAg and C-CuPdAg distributions were normalized by the number of events. The C-CuPd distribution was normalized so that the probability density function integral equaled to one. (C1) The C-CuAg distribution shows that Ag is normally distributed around the mean, corroborating the results obtained using the quadrupole (Gaussian fit:  $R^2 = 0.9723$ , see **Note S4**). The maximum lies at  $\sim 2.2$  Ag at. %, a four-fold reduction with respect to the SP-ICP-MS determined composition distribution (**Figure 5C2**), which can be explained by the higher number concentration at a fixed mass loading (see **Figure S7** and **S11**). (C2) The C-CuPd is lognormally distribution evidenced by the positive skew ( $R^2 = 0.9816$ , see **Note S4**). (C3) The C-CuPdAg distribution shows against a normal distribution ( $R^2 = 0.9467$ , see **Note S4**).

## 4.4. Conclusion

The high-throughput, element discriminative, dispersing media indiscriminate, size and shape independent NP dispersion quantification and characterization protocol, based on SP-ICP-MS, is a powerful tool that may help to bring about a statistics renaissance in the nanomaterial's science world. With this approach, nanoscale structures relevant to bulk phenomena can be quantified and characterized with ease and with ensemble-representative reliability. With four shapes of NPs (Au spheres and Cu

cubes, truncated octahedra and tetrahedra) and three Cu-based surface-alloy NPs (CuAg, CuPd and CuPdAg) as successful examples, we believe that the protocol can be applied to more complex structures and other inorganic nanomaterials in the future. We hope this method finds use in, amongst others, materials science, materials chemistry, (nano)physics, (nano)photonics, catalysis and electrochemistry.

## 4.5. Methods

### 4.5.1. Chemicals

The following chemicals and solvents were acquired from Sigma-Aldrich: copper bromide 99.99% (CuBr), palladium chloride 99% (PdCl<sub>2</sub>), nitric acid 70% (HNO<sub>3</sub>), trioctylphosphine oxide 99% (TOPO), trioctylphosphine 99% (TOP), oleyl amine 70% (OLAM), polyvinylpyrrolidone (PVP, MW ~55,000), dichloromethane (DCM), and dimethyl formamide (DMF). Anhydrous

ethanol 95% was purchased from ACROS organics (EtOH) and anhydrous toluene (99.8%) from Alfa Aesar. Silver nitrate 99.9995% was obtained from Puratrem (AgNO<sub>3</sub>). All chemicals were used as received without any further purification. All aqueous solutions were prepared with di-ionized (DI) water with a resistivity of 18.2 MΩ cm<sup>-1</sup>.

## 4.5.2. Synthesis of anisotropic copper crystals

Cu NPs of three different morphologies were synthesized using a reflux set-up under inert conditions. For the C-Cu synthesis, adapted from Guo et al and Lojudice et al,<sup>49,50</sup> 0.45904 g CuBr and 1.78 mL TOP stored in a glove box, were mixed with 9 mL of degassed OLAM and sonicated for 10 min to form a transparent, pale yellow solution. Meanwhile, 50 mL of OLAM (70 %) were added to a 250 mL three-necked flask and degassed under vacuum. The flask was purged with N<sub>2</sub> after the bubble formation has stopped. Using a clean syringe, the reaction mixture was then quickly added to the flask. The mixture was heated to 80 °C using a heating mantle and kept at that temperature for 30 min while using a low vacuum to dry the solution. The yellow transparent reaction mixture was purged with N<sub>2</sub> and the temperature was quickly increased to 270 °C and kept for 1 hour. At 270 °C, the reaction mixture turned red, indicating nucleation. After the solution had cooled to room temperature, the reaction mixture was transferred to the glove box and washed with toluene using centrifugation (7,500 rpm for 5 min). The C-Cu pellet was

redispersed in 5 mL of toluene. For TOh-Cu, the reaction was carried out at 260 °C instead, all other conditions were kept the same. For the Th-Cu, 0.23908 g CuBr and 3.12417 g dry TOPO were dissolved in 5 mL degassed OLAM using ultrasonication (10 min), yielding a pale-yellow translucent solution. This was then quickly added to 34 mL OLAM in a three-necked flask under inert atmosphere using a syringe. Then, the temperature was raised to 80 °C under vacuum, kept for 30 min, and raised further to 180 °C to cause boiling. The pale-yellow solution turned to a deep gold color. At this point, a N<sub>2</sub> purge was applied and the temperature was further raised to 260 °C upon which the solution turned translucent black, indicating nucleation. The reaction was continued for 1 h to yield a purple dispersion, which was then washed using toluene.

### 4.5.3. Synthesis of multimetallic NPs

The synthesis of the multimetallic NPs was inspired by the protocol from Lee et al.<sup>51</sup> 4 mg of NPs dispersed in toluene were added to a 10 mL glass vial to which 3.5 mL of degassed OLAM were carefully added, without disturbing the NP film. Additionally, 0.5 mg of dry AgNO<sub>3</sub> or PdCl<sub>2</sub> were added to 1.5 mL of degassed OLAM and heated at 50 or 80 °C using an oil bath until dissolved. AgNO<sub>3</sub> or PdCl<sub>2</sub> in OLAM was then carefully added to the reaction vial, which was then

allowed to react at 80 °C for 60 s with C-Cu and TOh-Cu, or 50 °C for 300 s with Th-Cu, after which the reaction was quenched with toluene. This yielded the Th- and TOh-CuAg and C-CuAg/Pd. For the synthesis of C-CuPdAg, 4 mg of C-CuAg rather than C-Cu NPs were used instead. All other parameters were kept the same. The coated crystals were washed with toluene and stored in a glovebox.

### 4.5.4. Preparation of aqueous dispersions

100 µL of the (multi)metallic anisotropic nanoparticle dispersions at concentrations of 2-20 mg mL<sup>-1</sup> were ligand exchanged by washing with DMF (1 mL, 5,000 rpm and 2 min) in three-fold and dispersed in 100 µL DMF using the protocol of Johnson et al.<sup>52</sup> An aliquot equivalent of 100,000 mL<sup>-1</sup> over a 3-step dilution series was added to deionized water, which was used for sampling.<sup>53,54</sup>

## 4.5.5. Characterization

**Electron microscopy (EM).** LR-TEM images were acquired with a FEI Tecnai Basic Spirit operated at 120 kV in bright field mode. The microscope was equipped with a Gatan charge-coupled device (CCD) camera and Digital Micrograph for imaging. Samples were drop-casted on ultrathin 400 mesh carbon film Au grids from Ted Pella Inc., which were washed with ethanol before and after drop-casting. Size distributions were obtained through edge-length analysis using the FIJI ImageJ software package of at least 100 unique particles. Scanning transmission electron microscopy high-angle annular dark-field (STEM-HAADF) micrographs and EDX elemental maps were obtained using a FEI Tecnai Osiris operated at 200 kV. The high-resolution TEM is outfitted with a X-FEG field emission gun reaching a brightness of  $1.8 \times 10^9 \text{ A cm}^{-2} \text{ srad}$  at 200 kV and when operated in scanning mode optimized for EDX, has a probe size of 1.0 nm with a current of 1 nA. The silicon drift Super-X EDX detectors in combination with the Bruker Esprit imaging software were used to acquire and analyze the EDX elemental maps.

**X-ray photoelectron spectroscopy (XPS).** XPS was performed with a Kratos Axis Supra system, using a monochromated Al  $K_{\alpha}$  (1486.61 eV) X-ray source at a nominal power of 225 W. The samples were drop-casted on gold foil in a  $N_2$  glovebox and transferred for measurement without exposure to air. No charge compensation was required and the binding energies (BEs) were referenced to Au  $4f_{7/2}$  at 83.95 eV. A pass energy of 20 eV was used for acquiring all core-level and Auger electron spectra.

**Inductively coupled plasma - optical emission spectroscopy (ICP-OES).** The concentration of the NP solution was determined with an Agilent 5110 ICP-OES with a VistaChip II CCD camera. The NPs were digested overnight in 2%  $HNO_3$  and filtered with 0.4  $\mu\text{m}$  pore size Ultrapore nylon filters. The calibration curves were obtained through the preparation of a dilution series of elemental standards obtained from Sigma Aldrich.



**Inductively-coupled plasma mass spectrometry (ICP-MS).** Particle sizing, counting and elemental analysis of the C-, TOh- and Th-Cu NPs as well as C-, TOh- and Th-CuAg NSAs was achieved with a NexION 350D ICP-MS instrument from PerkinElmer operated in continuous data acquisition mode. An icpTOF instrument of TOFWERK AG, Thun, Switzerland equipped with an orthogonal-acceleration TOF mass analyzer was used to size C-Cu and determine the composition of C-CuAg, C-CuPd, and C-CuPdAg NPs. For a comparison of the operating conditions of both ICP-MS instruments see **Table S6**. Particles were extracted from the raw data using both commercial software from Perkin Elmer (Syngistix) and TOFWERK AG (TofPilot) as well as via an in-house developed MATLAB script (see **Table S7**). In the case of Syngistix and our MATLAB script, data processing, e.g., particle event extraction, was achieved by averaging over all intensities (counts) and determining the standard deviation ( $\sigma$ ). A particle event is defined as any intensity  $3\sigma$  above the average of all intensity counts (raw data).<sup>30,55</sup> This is done iteratively. After

the first set of particle events has been collected, which are all the intensities (counts) above the determined threshold, the average and the  $\sigma$  of the new data-set (remaining intensity counts) is determined and the process is repeated until no signal  $>\text{average} + 3\sigma$  remains. TofPilot performs iterative signal/background separation every 1000 data points instead.<sup>56,57</sup> This allows for corrections in fluctuations of the dissolved signal. The average and  $\sigma$  are determined for each data subset with the threshold of a particle event defined as  $>\text{average} + (3.29\sigma) + 2.72$  reducing false positives. Alternative methods to reduce false positives exist as well, which may offer better results under certain conditions.<sup>58,59</sup> Calibration of the transport efficiency ( $\eta_t$ ) of the NexION 350D ICP-MS instrument was achieved in parallel with Au NPs standards of 61, 78 and 98 nm purchased from NanoComposix as well as 30, 50 and 80 nm purchased from PerkinElmer at number concentration of  $\sim 50,000 \text{ mL}^{-1}$  (**Figures S1 and S2, Table S8**). After Au NPs standards introduction, the instrument was rinsed with 1% HCl for 30 s and 2%  $\text{HNO}_3$  after

Cu, CuAg, CuPd and CuPdAg NP sampling. After rinsing with acid, i.e., before sample introduction, the sampler was rinsed with DI water. Dissolved metal calibration curves were obtained from elemental standards purchased from Sigma Aldrich. For the icpTOF instrument, calibration was achieved using an online droplet calibration method with a microdroplet generator described by Hendriks et al.<sup>54</sup> Monodisperse microdroplets of Cu, Pd, and Ag were used as calibrants and introduced into the NP aerosol flow in calibration run. Construction of the composition distributions was achieved in-house (see **Note S2**). The most abundant mass was used in all cases but inspected for false positives using all other isotopes and their

respective LODs (See **Table S9** and **S10** for the LODs of the quadrupole and time-of-flight based methods respectively). For complex media, or highly concentrated salts such as phosphate buffered saline (PBS), matrix effects, such as spectral overlap and intensity changes, may significantly affect sizing and or composition determination accuracy.<sup>53,54</sup> Since in the present study only aqueous dispersions were used, matrix effects were of lesser concern. Further, the calibration method used in this work ensures that the analyte and calibrant experience the same plasma conditions, thus allowing for matrix-independent mass quantification.

## 4.6. References

- (1) Liz-Marzán, L. M. Tailoring Surface Plasmons through the Morphology and Assembly of Metal Nanoparticles. *Langmuir* **2006**, *22*, 32–41.
- (2) Xia, Y.; Xiong, Y.; Lim, B.; Skrabalak, S. E. Shape-Controlled Synthesis of Metal Nanocrystals: Simple Chemistry Meets Complex Physics? *Angew. Chem. Int. Ed.* **2009**, *48*, 60–103.
- (3) Jones, M. R.; Osberg, K. D.; Macfarlane, R. J.; Langille, M. R.; Mirkin, C. A. Templated Techniques for the Synthesis and Assembly of Plasmonic Nanostructures. *Chem. Rev.* **2011**, *111*, 3736–3827.
- (4) Chen, G.; Qiu, H.; Prasad, P. N.; Chen, X. Upconversion Nanoparticles: Design, Nanochemistry, and Applications in Theranostics. *Chem. Rev.* **2014**, *114*, 5161–5214.
- (5) Kleijn, S. E. F.; Lai, S. C. S.; Koper, M. T. M.; Unwin, P. R. Electrochemistry of Nanoparticles. *Angew. Chem. Int. Ed.* **2014**, *53*, 3558–3586.
- (6) Liu, L.; Corma, A. Metal Catalysts for Heterogeneous Catalysis: From Single Atoms to Nanoclusters and Nanoparticles. *Chem. Rev.* **2018**, *118*, 4981–5079.
- (7) Van Aert, S.; Batenburg, K. J.; Rossell, M. D.; Erni, R.; Van Tendeloo, G. Three-Dimensional Atomic Imaging of Crystalline Nanoparticles. *Nature* **2011**, *470*, 374–377.
- (8) Laramy, C. R.; Brown, K. A.; O'Brien, M. N.; Mirkin, Chad. A. High-Throughput, Algorithmic Determination of Nanoparticle Structure from Electron Microscopy Images. *ACS Nano* **2015**, *9*, 12488–12495.
- (9) Lee, B.; Yoon, S.; Lee, J. W.; Kim, Y.; Chang, J.; Yun, J.; Ro, J. C.; Lee, J.-S.; Lee, J. H. Statistical Characterization of the Morphologies of Nanoparticles through Machine Learning Based Electron Microscopy Image Analysis. *ACS Nano* **2020**, *14*, 17125–17133.
- (10) Chen, C.; Kang, Y.; Huo, Z.; Zhu, Z.; Huang, W.; Xin, H. L.; Snyder, J. D.; Li, D.; Herron, J. A.; Mavrikakis, M.; Chi, M.; More, K. L.; Li, Y.; Markovic, N. M.; Somorjai, G. A.; Yang, P.; Stamenkovic, V. R. Highly Crystalline Multimetallic Nanoframes with Three-Dimensional Electrocatalytic Surfaces. *Science* **2014**, *343*, 1339–1343.
- (11) Choukroun, D.; Pacquets, L.; Li, C.; Hoekx, S.; Arnouts, S.; Baert, K.; Hauffman, T.; Bals, S.; Breugelmanns, T. Mapping Composition–Selectivity Relationships of Supported Sub-10 Nm Cu–Ag Nanocrystals for High-Rate CO<sub>2</sub> Electroreduction. *ACS Nano* **2021**, *15*, 14858–14872.
- (12) *Particle Analysis*. ImageJ Wiki. <https://imagej.github.io/imaging/particle-analysis> (accessed 2021-09-21).
- (13) Mondini, S.; Ferretti, A. M.; Puglisi, A.; Ponti, A. PEBBLES and PEBBLEJUGGLER: Software for Accurate, Unbiased, and Fast Measurement and Analysis of Nanoparticle Morphology from Transmission Electron Microscopy (TEM) Micrographs. *Nanoscale* **2012**, *4*, 5356–5372.

- (14) Pace, H. E.; Rogers, N. J.; Jarolimek, C.; Coleman, V. A.; Higgins, C. P.; Ranville, J. F. Determining Transport Efficiency for the Purpose of Counting and Sizing Nanoparticles via Single Particle Inductively Coupled Plasma Mass Spectrometry. *Anal. Chem.* **2011**, *83*, 9361–9369.
- (15) Laborda, F.; Jiménez-Lamana, J.; Bolea, E.; Castillo, J. R. Selective Identification, Characterization and Determination of Dissolved Silver(I) and Silver Nanoparticles Based on Single Particle Detection by Inductively Coupled Plasma Mass Spectrometry. *J. Anal. At. Spectrom.* **2011**, *26*, 1362–1371.
- (16) Pace, H. E.; Rogers, N. J.; Jarolimek, C.; Coleman, V. A.; Higgins, C. P.; Ranville, J. F. Correction to Determining Transport Efficiency for the Purpose of Counting and Sizing Nanoparticles via Single Particle Inductively Coupled Plasma Mass Spectrometry. *Anal. Chem.* **2012**, *84*, 4633–4633.
- (17) Mitrano, D. M.; Leshner, E. K.; Bednar, A.; Monserud, J.; Higgins, C. P.; Ranville, J. F. Detecting Nanoparticulate Silver Using Single-Particle Inductively Coupled Plasma–Mass Spectrometry. *Environ. Toxicol. Chem.* **2012**, *31*, 115–121.
- (18) Borovinskaya, O.; Hattendorf, B.; Tanner, M.; Gschwind, S.; Günther, D. A Prototype of a New Inductively Coupled Plasma Time-of-Flight Mass Spectrometer Providing Temporally Resolved, Multi-Element Detection of Short Signals Generated by Single Particles and Droplets. *J. Anal. At. Spectrom.* **2013**, *28*, 226–233.
- (19) Vogl, J. Calibration Strategies and Quality Assurance. In *Inductively Coupled Plasma Mass Spectrometry Handbook*; S.M. Nelms (Ed.), Blackwell Publishing, Oxford UK, 2005; pp 147–181.
- (20) Mozhayeva, D.; Engelhard, C. A Critical Review of Single Particle Inductively Coupled Plasma Mass Spectrometry – A Step towards an Ideal Method for Nanomaterial Characterization. *J. Anal. At. Spectrom.* **2020**, *35*, 1740–1783.
- (21) Mitrano, D. M.; Barber, A.; Bednar, A.; Westerhoff, P.; Higgins, C. P.; Ranville, J. F. Silver Nanoparticle Characterization Using Single Particle ICP-MS (SP-ICP-MS) and Asymmetrical Flow Field Flow Fractionation ICP-MS (AF4-ICP-MS). *J. Anal. At. Spectrom.* **2012**, *27*, 1131–1142.
- (22) Liu, J.; Murphy, K. E.; MacCuspie, R. I.; Winchester, M. R. Capabilities of Single Particle Inductively Coupled Plasma Mass Spectrometry for the Size Measurement of Nanoparticles: A Case Study on Gold Nanoparticles. *Anal. Chem.* **2014**, *86*, 3405–3414.
- (23) Laborda, F.; Bolea, E.; Jiménez-Lamana, J. Single Particle Inductively Coupled Plasma Mass Spectrometry for the Analysis of Inorganic Engineered Nanoparticles in Environmental Samples. *Trends Environ. Anal. Chem.* **2016**, *9*, 15–23.
- (24) Hendriks, L.; Gundlach-Graham, A.; Günther, D. Analysis of Inorganic Nanoparticles by Single-Particle Inductively Coupled Plasma Time-of-Flight Mass Spectrometry. *Chim. Int. J. Chem.* **2018**, *72*, 221–226.

- (25) Hadioui, M.; Knapp, G.; Azimzada, A.; Jreije, I.; Frechette-Viens, L.; Wilkinson, K. J. Lowering the Size Detection Limits of Ag and TiO<sub>2</sub> Nanoparticles by Single Particle ICP-MS. *Anal. Chem.* **2019**, *91*, 13275–13284.
- (26) Folens, K.; Van Acker, T.; Bolea-Fernandez, E.; Cornelis, G.; Vanhaecke, F.; Du Laing, G.; Rauch, S. Identification of Platinum Nanoparticles in Road Dust Leachate by Single Particle Inductively Coupled Plasma-Mass Spectrometry. *Sci. Total Environ.* **2018**, *615*, 849–856.
- (27) Hegetschweiler, A.; Borovinskaya, O.; Staudt, T.; Kraus, T. Single-Particle Mass Spectrometry of Titanium and Niobium Carbonitride Precipitates in Steels. *Anal. Chem.* **2019**, *91*, 943–950.
- (28) Donahue, N. D.; Kanapilly, S.; Stephan, C.; Marlin, M. C.; Francek, E. R.; Haddad, M.; Guthridge, J.; Wilhelm, S. Quantifying Chemical Composition and Reaction Kinetics of Individual Colloidally Dispersed Nanoparticles. *Nano Lett.* **2022**, *22*, 294–301.
- (29) Strengel, I.; Engelhard, C. Single Particle Inductively Coupled Plasma Mass Spectrometry: Investigating Nonlinear Response Observed in Pulse Counting Mode and Extending the Linear Dynamic Range by Compensating for Dead Time Related Count Losses on a Microsecond Timescale. *J. Anal. At. Spectrom.* **2020**, *35*, 84–99.
- (30) Degueldre, C.; Favarger, P.-Y.; Wold, S. Gold Colloid Analysis by Inductively Coupled Plasma-Mass Spectrometry in a Single Particle Mode. *Anal. Chim. Acta* **2006**, *555*, 263–268.
- (31) Ho, K.-S.; Lui, K.-O.; Lee, K.-H.; Chan, W.-T. Considerations of Particle Vaporization and Analyte Diffusion in Single-Particle Inductively Coupled Plasma-Mass Spectrometry. *Spectrochim. Acta Part B At. Spectrosc.* **2013**, *89*, 30–39.
- (32) Laborda, F.; Gimenez-Ingalaturre, A. C.; Bolea, E.; Castillo, J. R. About Detectability and Limits of Detection in Single Particle Inductively Coupled Plasma Mass Spectrometry. *Spectrochim. Acta Part B At. Spectrosc.* **2020**, *169*, 105883.
- (33) Lee, S.; Bi, X.; Reed, R. B.; Ranville, J. F.; Herckes, P.; Westerhoff, P. Nanoparticle Size Detection Limits by Single Particle ICP-MS for 40 Elements. *Environ. Sci. Technol.* **2014**, *48*, 10291–10300.
- (34) Shaw, P.; Donard, A. Nano-Particle Analysis Using Dwell Times between 10 Ms and 70 Ms with an Upper Counting Limit of Greater than  $3 \times 10^7$  Cps and a Gold Nanoparticle Detection Limit of Less than 10 Nm Diameter. *J. Anal. At. Spectrom.* **2016**, *31*, 1234–1242.
- (35) Reske, R.; Mistry, H.; Behafarid, F.; Roldan Cuenya, B.; Strasser, P. Particle Size Effects in the Catalytic Electroreduction of CO<sub>2</sub> on Cu Nanoparticles. *J. Am. Chem. Soc.* **2014**, *136*, 6978–6986.
- (36) Donahue, N. D.; Francek, E. R.; Kiyotake, E.; Thomas, E. E.; Yang, W.; Wang, L.; Detamore, M. S.; Wilhelm, S. Assessing Nanoparticle Colloidal Stability with Single-Particle Inductively Coupled Plasma Mass Spectrometry (SP-ICP-MS). *Anal. Bioanal. Chem.* **2020**, *412*, 5205–5216.

- (37) Hou, Y.; Kovács, N.; Xu, H.; Sun, C.; Erni, R.; Gálvez-Vázquez, M. de J.; Rieder, A.; Hu, H.; Kong, Y.; Liu, M.; Wiley, B. J.; Veszteg, S.; Broekmann, P. Limitations of Identical Location SEM as a Method of Degradation Studies on Surfactant Capped Nanoparticle Electrocatalysts. *J. Catal.* **2021**, *394*, 58–66.
- (38) Holišová, V.; Urban, M.; Konvičková, Z.; Kolenčík, M.; Mančík, P.; Slabotinský, J.; Kratošová, G.; Plachá, D. Colloidal Stability of Phytosynthesised Gold Nanoparticles and Their Catalytic Effects for Nerve Agent Degradation. *Sci. Rep.* **2021**, *11*, 4071.
- (39) Arena, D. A.; Bartynski, R. A.; Hulbert, S. L. The Electronic Structure of Ag/Cu(100) and Pd/Cu(100) Surface Alloys Studied by Auger-Photoelectron Coincidence Spectroscopy. In *Many-Particle Spectroscopy of Atoms, Molecules, Clusters, and Surfaces*; Berakdar, J., Kirschner, J., Eds.; Springer US: Boston, MA, 2001; pp 471–480.
- (40) Merrifield, R. C.; Stephan, C.; Lead, J. R. Single-Particle Inductively Coupled Plasma Mass Spectroscopy Analysis of Size and Number Concentration in Mixtures of Monometallic and Bimetallic (Core-Shell) Nanoparticles. *Talanta* **2017**, *162*, 130–134.
- (41) Praetorius, A.; Gundlach-Graham, A.; Goldberg, E.; Fabienke, W.; Navratilova, J.; Gondikas, A.; Kaegi, R.; Günther, D.; Hofmann, T.; Kammer, F. von der. Single-Particle Multi-Element Fingerprinting (SpMEF) Using Inductively-Coupled Plasma Time-of-Flight Mass Spectrometry (ICP-TOFMS) to Identify Engineered Nanoparticles against the Elevated Natural Background in Soils. *Environ. Sci. Nano* **2017**, *4*, 307–314.
- (42) Naasz, S.; Weigel, S.; Borovinskaya, O.; Serva, A.; Cascio, C.; Undas, A. K.; Simeone, F. C.; Marvin, H. J. P.; Peters, R. J. B. Multi-Element Analysis of Single Nanoparticles by ICP-MS Using Quadrupole and Time-of-Flight Technologies. *J. Anal. At. Spectrom.* **2018**, *33*, 835–845.
- (43) Ratuszek, M.; Zakrzewski, Z.; Majewski, J. Characteristics of Thermally Diffused Transit Areas of Single-Mode Telecommunication Fibers. *J. Light. Technol.* **2009**, *27*, 3050–3056.
- (44) Demoulin, R.; Roussel, M.; Duguay, S.; Muller, D.; Mathiot, D.; Pareige, P.; Talbot, E. Atomic-Scale Characterization of N-Doped Si Nanocrystals Embedded in SiO<sub>2</sub> by Atom Probe Tomography. *J. Phys. Chem. C* **2019**, *123*, 7381–7389.
- (45) Perego, M.; Caruso, F.; Seguíni, G.; Arduca, E.; Mantovan, R.; Sparnacci, K.; Laus, M. Doping of Silicon by Phosphorus End-Terminated Polymers: Drive-in and Activation of Dopants. *J. Mater. Chem. C* **2020**, *8*, 10229–10237.
- (46) Hill, J. M.; Royce, D. G.; Fadley, C. S.; Wagner, L. F.; Grunthaler, F. J. Properties of Oxidized Silicon as Determined by Angular-Dependent X-Ray Photoelectron Spectroscopy. *Chem. Phys. Lett.* **1976**, *44*, 225–231.
- (47) Löffler, T.; Savan, A.; Garzón-Manjón, A.; Meischein, M.; Scheu, C.; Ludwig, A.; Schuhmann, W. Toward a Paradigm Shift in Electrocatalysis Using Complex Solid Solution Nanoparticles. *ACS Energy Lett.* **2019**, *4*, 1206–1214.
- (48) Hendriks, L.; Gundlach-Graham, A.; Hattendorf, B.; Günther, D. Characterization of a New ICP-TOFMS Instrument with Continuous and Discrete Introduction of Solutions. *J. Anal. At. Spectrom.* **2017**, *32*, 548–561.

- (49) Guo, H.; Chen, Y.; Cortie, M. B.; Liu, X.; Xie, Q.; Wang, X.; Peng, D.-L. Shape-Selective Formation of Monodisperse Copper Nanospheres and Nanocubes via Disproportionation Reaction Route and Their Optical Properties. *J. Phys. Chem. C* **2014**, *118*, 9801–9808.
- (50) Loiudice, A.; Lobaccaro, P.; Kamali, E. A.; Thao, T.; Huang, B. H.; Ager, J. W.; Buonsanti, R. Tailoring Copper Nanocrystals towards C<sub>2</sub> Products in Electrochemical CO<sub>2</sub> Reduction. *Angew. Chem. Int. Ed.* **2016**, *55*, 5789–5792.
- (51) Lee, C.; Kim, N. R.; Koo, J.; Lee, Y. J.; Lee, H. M. Cu-Ag Core-Shell Nanoparticles with Enhanced Oxidation Stability for Printed Electronics. *Nanotechnology* **2015**, *26*, 455601.
- (52) Johnson, N. J. J.; Sangeetha, N. M.; Boyer, J.-C.; Veggel, F. C. J. M. van. Facile Ligand-Exchange with Polyvinylpyrrolidone and Subsequent Silica Coating of Hydrophobic Upconverting  $\beta$ -NaYF<sub>4</sub>:Yb<sup>3+</sup>/Er<sup>3+</sup> Nanoparticles. *Nanoscale* **2010**, *2*, 771–777.
- (53) Tan, S. H.; Horlick, G. Matrix-Effect Observations in Inductively Coupled Plasma Mass Spectrometry. *J. Anal. At. Spectrom.* **1987**, *2*, 745–763.
- (54) Hendriks, L.; Ramkorun-Schmidt, B.; Gundlach-Graham, A.; Koch, J.; Grass, R. N.; Jakubowski, N.; Günther, D. Single-Particle ICP-MS with Online Microdroplet Calibration: Toward Matrix Independent Nanoparticle Sizing. *J. Anal. At. Spectrom.* **2019**, *34*, 716–728.
- (55) Degueldre, C.; Favarger, P.-Y.; Rossé, R.; Wold, S. Uranium Colloid Analysis by Single Particle Inductively Coupled Plasma-Mass Spectrometry. *Talanta* **2006**, *68*, 623–628.
- (56) Gschwind, S.; Flamigni, L.; Koch, J.; Borovinskaya, O.; Groh, S.; Niemax, K.; Günther, D. Capabilities of Inductively Coupled Plasma Mass Spectrometry for the Detection of Nanoparticles Carried by Monodisperse Microdroplets. *J. Anal. At. Spectrom.* **2011**, *26*, 1166–1174.
- (57) Ramkorun-Schmidt, B.; Pergantis, S. A.; Esteban-Fernández, D.; Jakubowski, N.; Günther, D. Investigation of a Combined Microdroplet Generator and Pneumatic Nebulization System for Quantitative Determination of Metal-Containing Nanoparticles Using ICPMS. *Anal. Chem.* **2015**, *87*, 8687–8694.
- (58) Tuoriniemi, J.; Cornelis, G.; Hassellöv, M. A New Peak Recognition Algorithm for Detection of Ultra-Small Nanoparticles by Single Particle ICP-MS Using Rapid Time Resolved Data Acquisition on a Sector-Field Mass Spectrometer. *J. Anal. At. Spectrom.* **2015**, *30*, 1723–1729.
- (59) Laborda, F.; Gimenez-Ingalaturre, A. C.; Bolea, E.; Castillo, J. R. Single Particle Inductively Coupled Plasma Mass Spectrometry as Screening Tool for Detection of Particles. *Spectrochim. Acta Part B At. Spectrosc.* **2019**, *159*, 105654.

## 4.7. Supporting Information

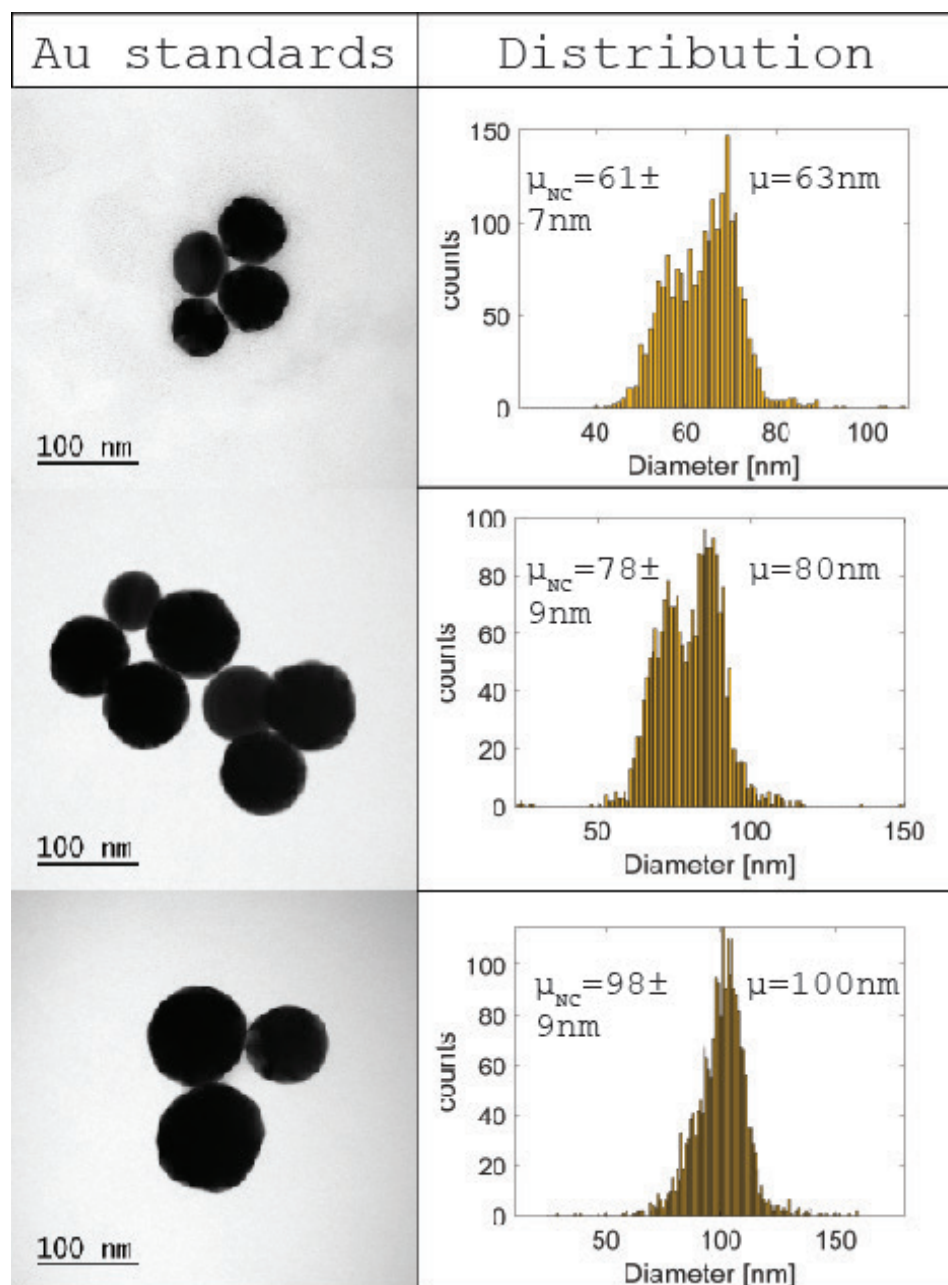


**Figure S1.** NanoComposix Au standard particle suspensions. The experimental mean ( $\mu$ ) obtained via SP-ICP-MS matches the certified mean ( $\mu_{NC}$ ) in all instances within error of measurement. Particle concentration was 50,000 mL<sup>-1</sup>.



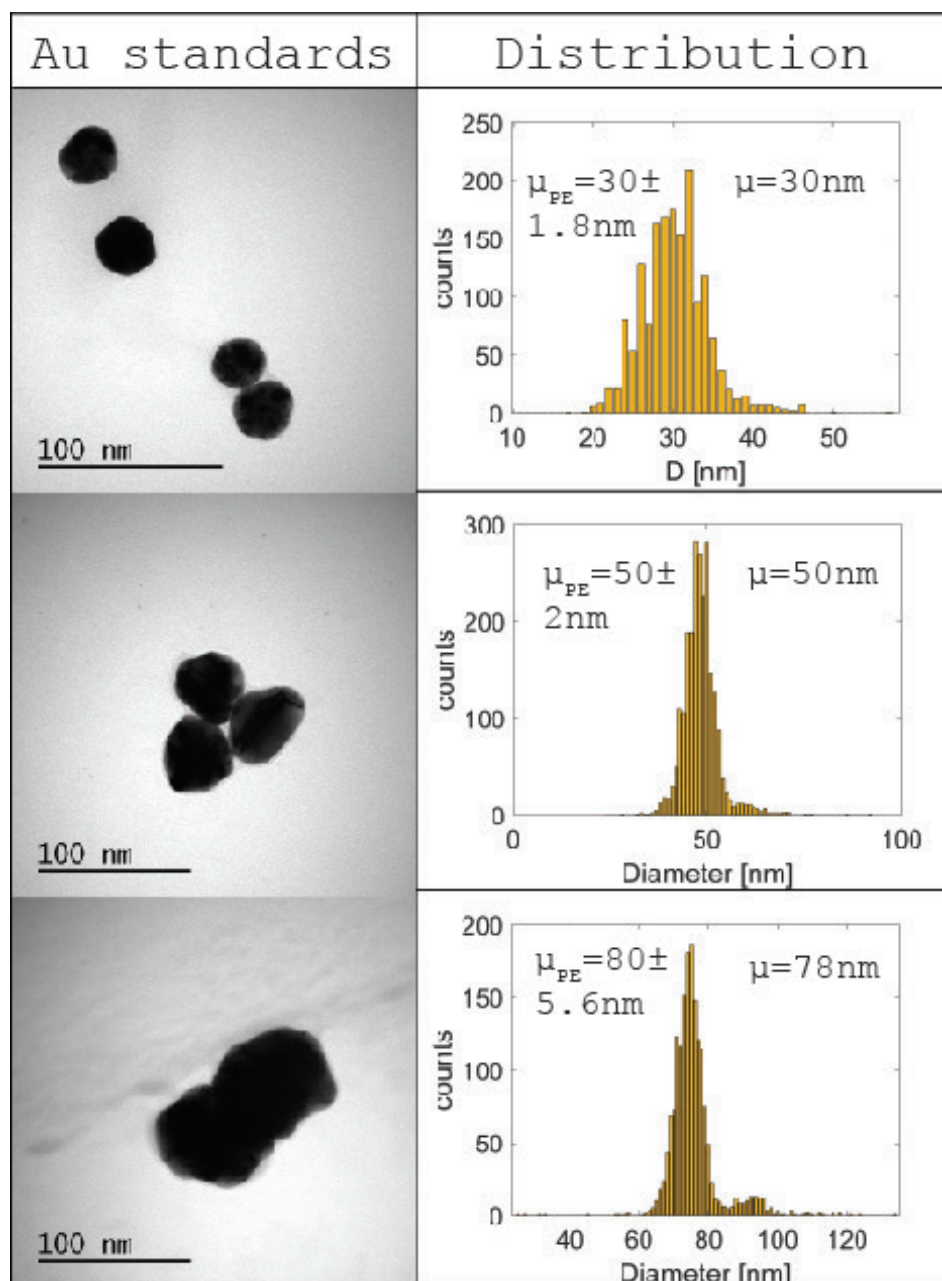


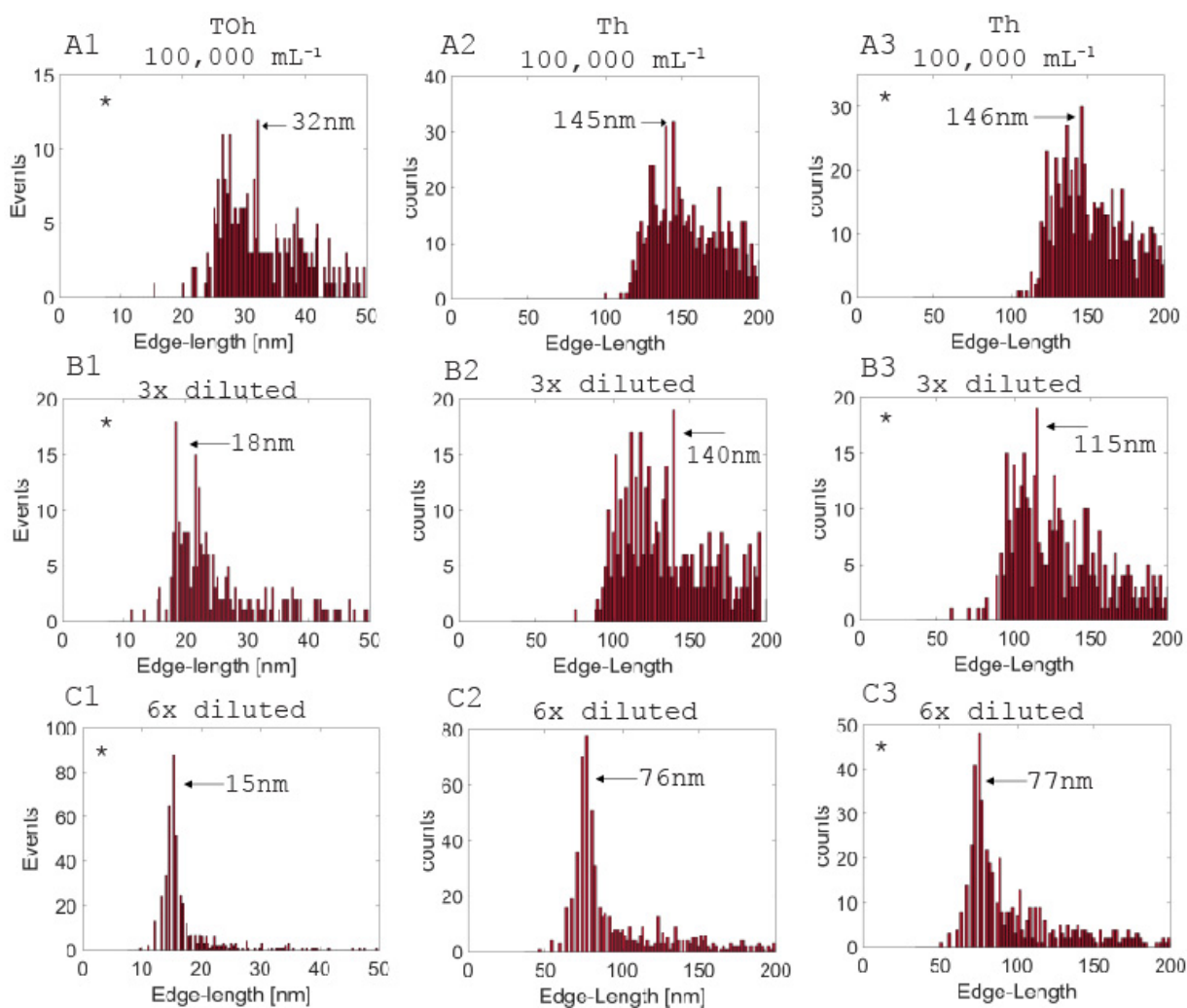
**Figure S2.** PerkinElmer Au standard particle suspensions. The experimental mean ( $\mu$ ) obtained via SP-ICP-MS matches the certified mean ( $\mu_{NC}$ ) in all instances within error of measurement. Particle concentration was 50,000  $\text{mL}^{-1}$ .

TOh	Particle concentration (NPs mL <sup>-1</sup> )	Most frequent size (nm)	Particle size mean (nm)	Dissolved. Concentration (µg L <sup>-1</sup> )	η <sub>t</sub> (%)	R <sup>2</sup>
Stock	100000	32.3	42	3.1	3.46	0.9997
3×	33333	18.3	30.6	0.94	3.46	0.9997
6×	16667	15.4	19.3	0.35	3.46	0.9997

TOh_2	Particle concentration (NPs mL <sup>-1</sup> )	Most frequent size (nm)	Particle size mean (nm)	Dissolved Concentration (µg L <sup>-1</sup> )	η <sub>t</sub> (%)	R <sup>2</sup>
Stock	100000	29.4	41.8	3.1	4.11	0.9997
3×	33333	22.6	32.4	0.90	4.11	0.9997
6×	16667	14.7	16.33	0.31	4.11	0.9997

**Table S1.** Results of the TOh-Cu NP suspension of 10<sup>5</sup> mL<sup>-1</sup> (15 ±2 nm) and its dilution series. Particle extraction achieved with Syngistix. Geometrical fitting performed in-house.



**Figure S3.** Dilution series of TOh and Th-Cu NPs using calibrants from **Figure S1** and **S2**. A1-A3) NP number concentration ( $N$ ):  $10^5 \text{ mL}^{-1}$ , B1-B3) NP number concentration ( $N$ ):  $1/3 \times 10^5 \text{ mL}^{-1}$ , C1-C3) NP number concentration ( $N$ ):  $1/6 \times 10^5 \text{ mL}^{-1}$ . A1-C1) dilution series of TOh Cu NPs complementary to **Figure 4** in the main text. A2-C3) dilution series of Th Cu NPs. Expected size based on LR-TEM particle counting was  $77 \pm 12 \text{ nm}$ . Difference in total number of events between the six-fold diluted measurements with calibrants **Figure S1** and **S2** for the TOh in the main text and for the Th arrive from particle aggregation.

## Note S1. Considerations of the distribution of the dilution series.

**Figure S3** shows that with both calibrants we achieve the same results at appropriate dilution. We have not used the average of all 6 NP standards (**Figure S1** and **S2**) as we explicitly wanted to determine if we could quantify correctly with different standards. Further, the coefficient of variability for the 61, 78 and 98 nm Au spheres measured with SP-ICP-MS for instance (12%, 13% and 11%) matches the manufacturers well (11%, 12% and 9%, respectively). Nevertheless, as seen in **Table S1**, the change to the transport efficiency (~15%) between both sets is actually reflected in the assigned mass. In example, the most frequently observed particle had about a ~13% lower mass when determined with the particle set in **Figure S2** than when obtained with those in **Figure S1**. However, this translates only to a difference in edge-length of 0.7 nm (~5%). Therefore, we conclude that within the error of measurement, correct sizing can be achieved independently of the calibrant used.

We would like to point out the difference in events between the particles observed in the 30-40 nm range (<10, **Figure 4** and

**Figure S3A1-B1**) and the smaller particles that can only be observed upon sufficient dilution (>100, **Figure 4** and **Figure S3C1**). Some of the 30-40 nm particles are actually still present in the final distribution. However, due to their low number of events, their contribution is easily overlooked due to different y-axis scale. Nevertheless, their frequency actually goes down when the dilution factor is increased. We explain that with the following. We argue, namely, that with a high ionic background, the smaller particles are not only 'invisible', observable particle size also shift to higher values. The reason for this is that it becomes harder and harder for the algorithm to correctly assign particle events when the ionic background is high. As a result, the degree of false positives increases. This leads to two sorts of artifacts. The creation of false particles and the addition of background signal to real particle events. The latter, in which mass is added to existing particles, explains the decrease in frequency upon reduction of the background signal.

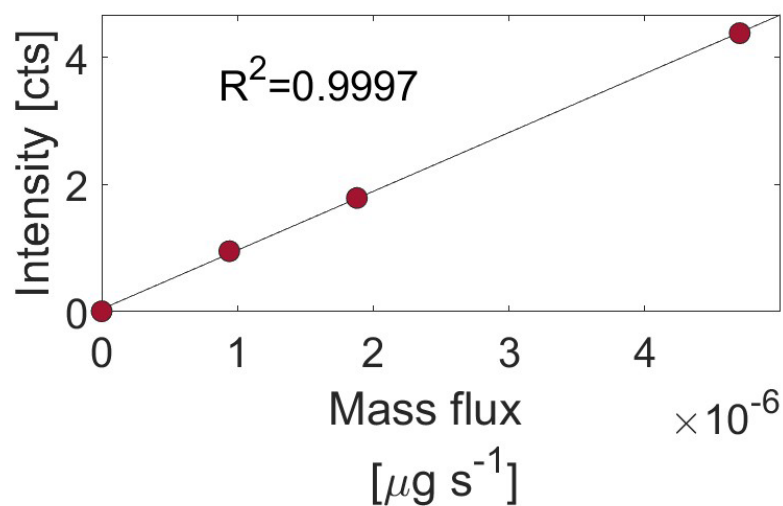


**Figure S4.** Cu dissolved standard calibration curve.

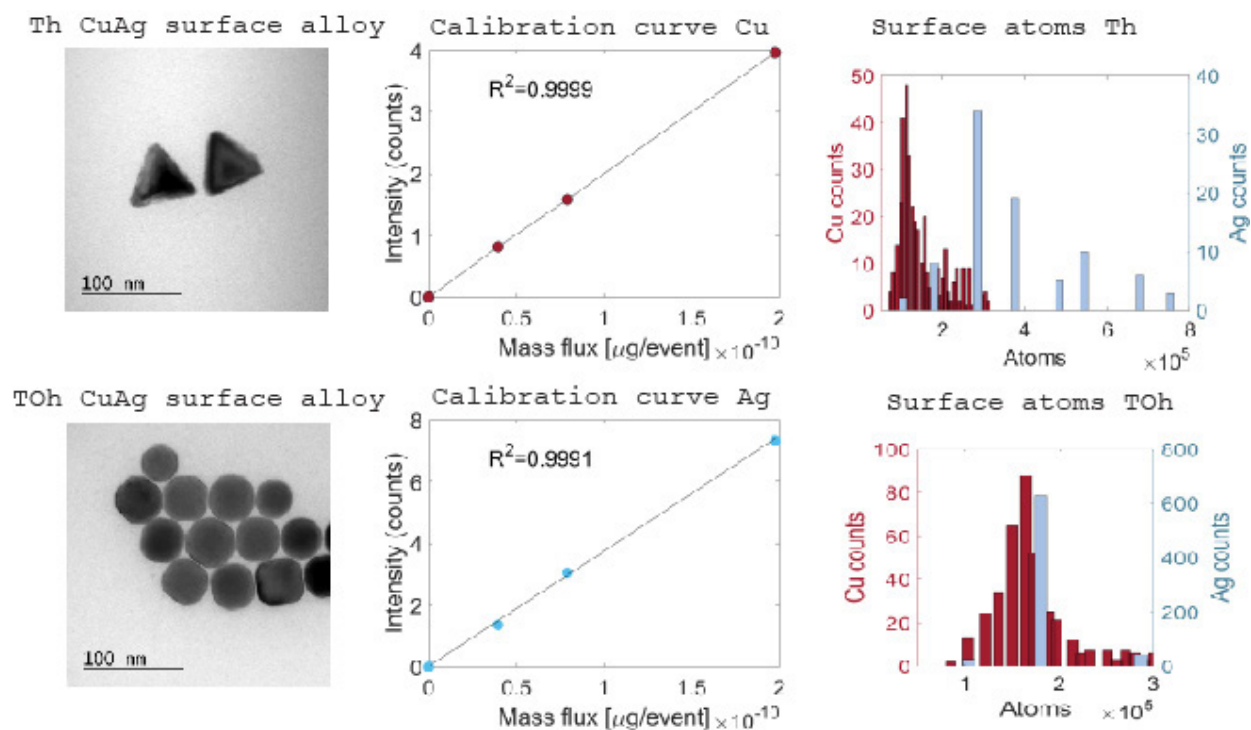


**Figure S5.** Surface atom compositions of Th- and TOh-CuAg NSA as determined by SP-ICP-MS.

Theoretical particle concentration [NPs mL <sup>-1</sup> ]	Measured particle concentration [mL <sup>-1</sup> ]	particle	Measured particle concentration [mL <sup>-1</sup> ]	particle
16,667	14,197 ± 562	Calibrated micropipette	15,027 ± 3964	Uncalibrated micropipette
<b>Nanoparticle concentration [mL<sup>-1</sup>]</b>				
	19889*		13170	14102
<b>calibration 1</b>				
Nanoparticle concentration [mL <sup>-1</sup> ]	14771		14342	14603
<b>calibration 2</b>				

**Table S2.1.** Measured particle concentration based on calibrated pipettes. \*Outlier.

Particle concentration [mL <sup>-1</sup> ]	~10 <sup>13</sup>	~10 <sup>14</sup>	~10 <sup>7</sup>	~10 <sup>5</sup>
Volume pipetted (μL)	20	20	200	-
Manufacturer uncertainty	σ <sub>a</sub> = 1%	σ <sub>b</sub> = 1%	σ <sub>c</sub> = 0.8%	σ <sub>x</sub> = 2%

**Table S2.2.** Overall uncertainty determined through error propagation of each dilution step in 3-fold dilution series.

$$\sigma_x = \sqrt{(\sigma_a^2 + \sigma_b^2 + \sigma_c^2)}$$

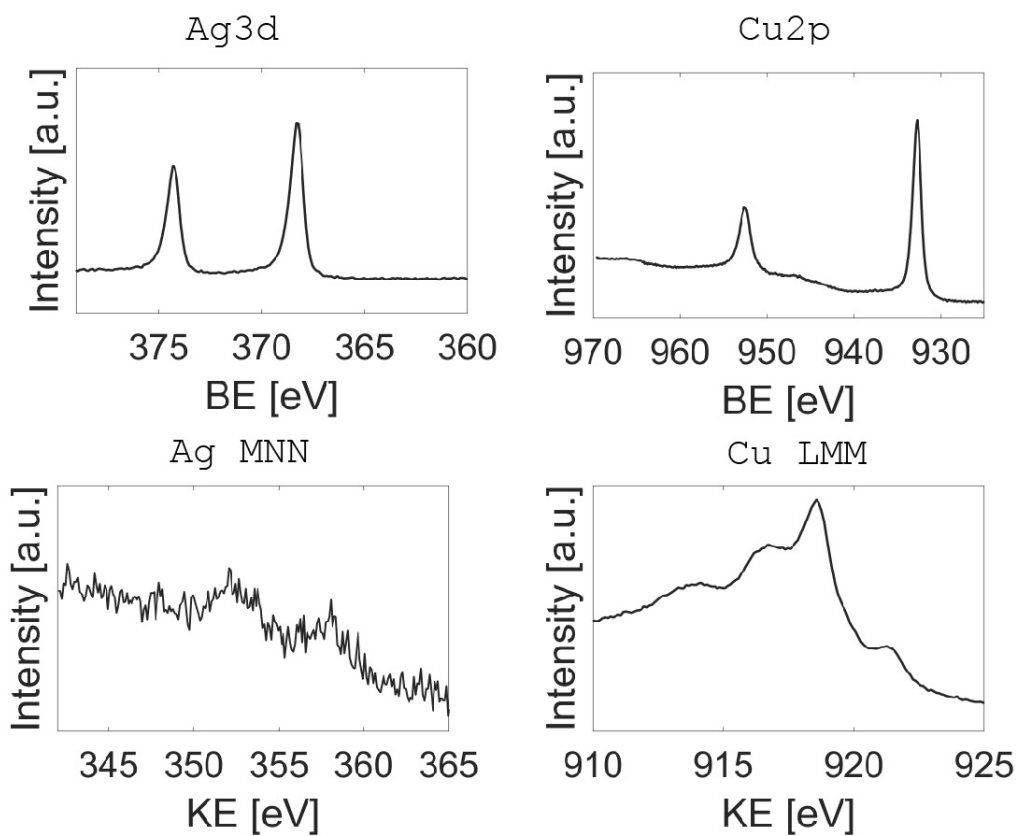


**Figure S6.** XPS and Auger spectra of C-CuAg NSA.

	KE [eV]	IMFP/Å	$\lambda/\text{Å}$
Ag 3d <sub>5/2</sub>	1118.5	16.03	48.09
Cu 2p <sub>3/2</sub>	554	10.09	30.27
Cu LMM	916.7	14.47	43.41
Subsurface model	-	-	31.36
(CuAg <sub>0.09</sub> )			

**Table S3.** Comparison penetration depths determined via IMPF method and modelled penetration depth based on normalized surface composition C-CuAg NSA as determined with XPS and SP-ICP-MS data.

## Note S2. Penetration depth and overlay thickness calculation XPS

The inelastic mean free path (IMFP) of the photoelectrons is calculated using the QUASES-IMFP-TPP2M Ver. 3.0 software.<sup>1</sup> And the information depth is three times of the IMFP.

The thickness of the Ag overlayer is calculated using the method developed by Hill et al using Eq. 11.<sup>2</sup>

$$t = -\lambda \cos\theta \ln \left( 1 + \frac{\left(\frac{I_o}{S_o}\right)}{\left(\frac{I_s}{S_s}\right)} \right) \quad (11)$$

where  $t$  is the overlayer thickness,  $\lambda$  is the attenuation length of the photoelectrons in the overlayer (obtained from the NIST electron effective-attenuation-length database<sup>3</sup>,  $\vartheta$  is the emission angle ( $58.2^\circ$  in this work),  $I_o$  and  $I_s$  are the peak intensities of the overlayer and the substrate, respectively, and  $S_o$  and  $S_s$  are their relative sensitivity factors. The thickness of the overlayer was determined at 0.25 ML of Ag assuming planar geometry, which is almost half of the thickness determined by SP-ICP-MS assuming cubic geometry.

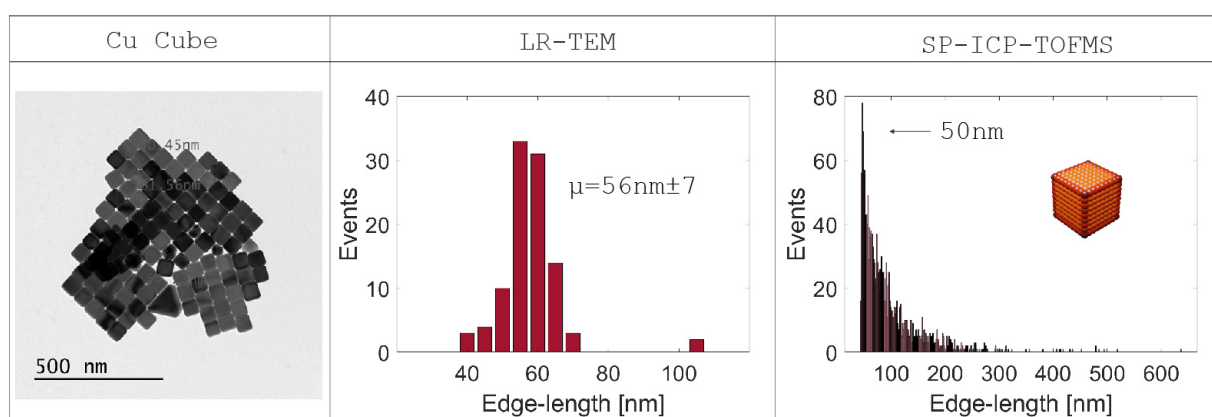


**Figure S7.** To ensure the reliability of the SP-ICP-TOFMS method, bare C-Cu NPs were introduced to the instrument and sized. An excellent match exists between the low resolution TEM particle counting and SP-ICP-TOFMS size distributions.



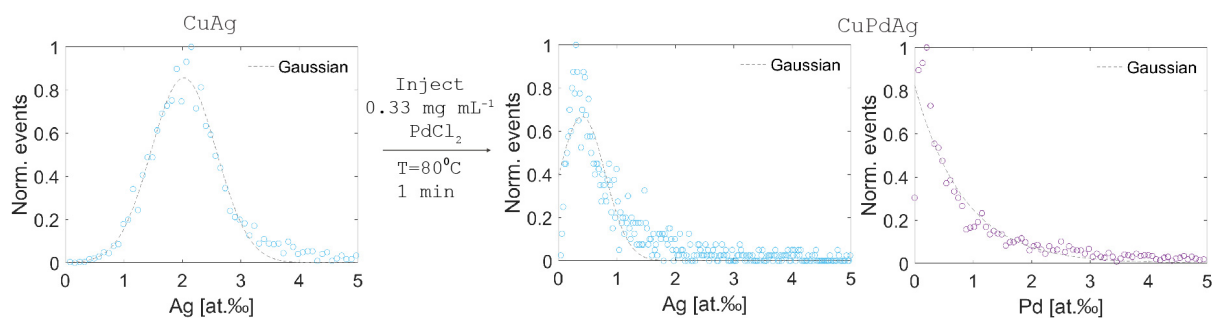


**Figure S8.** Conversion of C-CuAg NSA into C-CuPdAg NSA. Based on the Ag distribution upon introduction of the PdCl<sub>2</sub> precursor, and the subsequent shift of the maximum to lower Ag compositions, it can be deduced that Ag is being corroded more strongly than Cu. Based on the standard reduction potentials of the metals involved alone (Cu(II) + 2e<sup>-</sup> → Cu: +0.337 V, Cu(I) + e<sup>-</sup> → Cu: +0.52 V, Ag(I) + e<sup>-</sup> → Ag: +0.7996 V, Pd(II) + 2e<sup>-</sup> → Pd: +0.915V), the reverse would be expected. However, the presence of Cl<sup>-</sup> ions greatly suppresses Ag's resistance towards oxidation (AgCl + e<sup>-</sup> → Ag + Cl<sup>-</sup>: +0.22233 V vs PdCl<sub>6</sub><sup>4-</sup> + 2e<sup>-</sup> → Pd + 6 Cl<sup>-</sup>: +0.615 V).

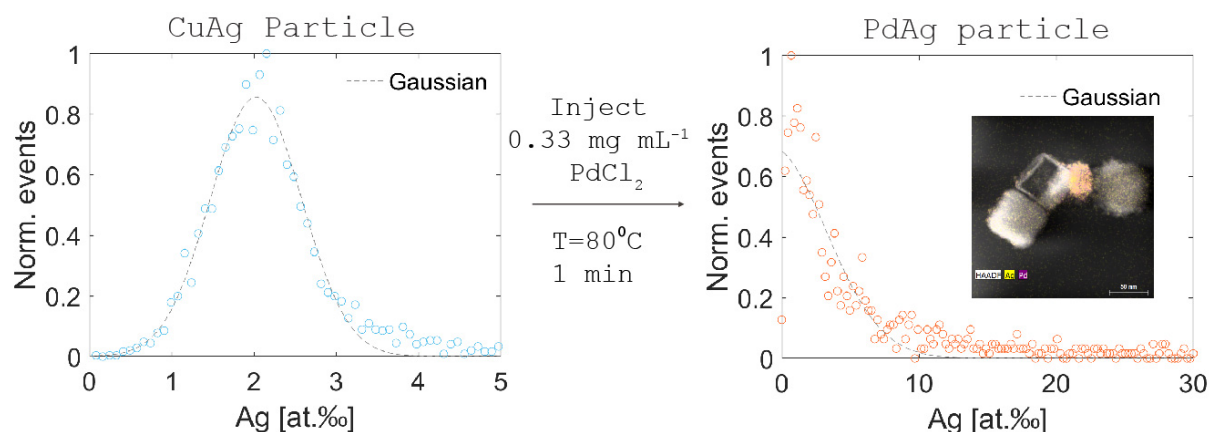


**Figure S9.** Other than the presence of C-CuPdAg NPs as determined with the SP-ICP-TOFMS, particles consisting solely of PdAg were detected as well. This could be confirmed with STEM-HAADF and STEM-EDX (see inset). This can be explained invoking a co-reduction mechanism in which the dissolving Ag is reduced together with unreacted Pd precursor. Alternatively, AgCl is poorly soluble and might precipitate out of solution possibly adhering to Pd NPs formed through homogeneous nucleation or unreacted PdCl<sub>2</sub> precursor.

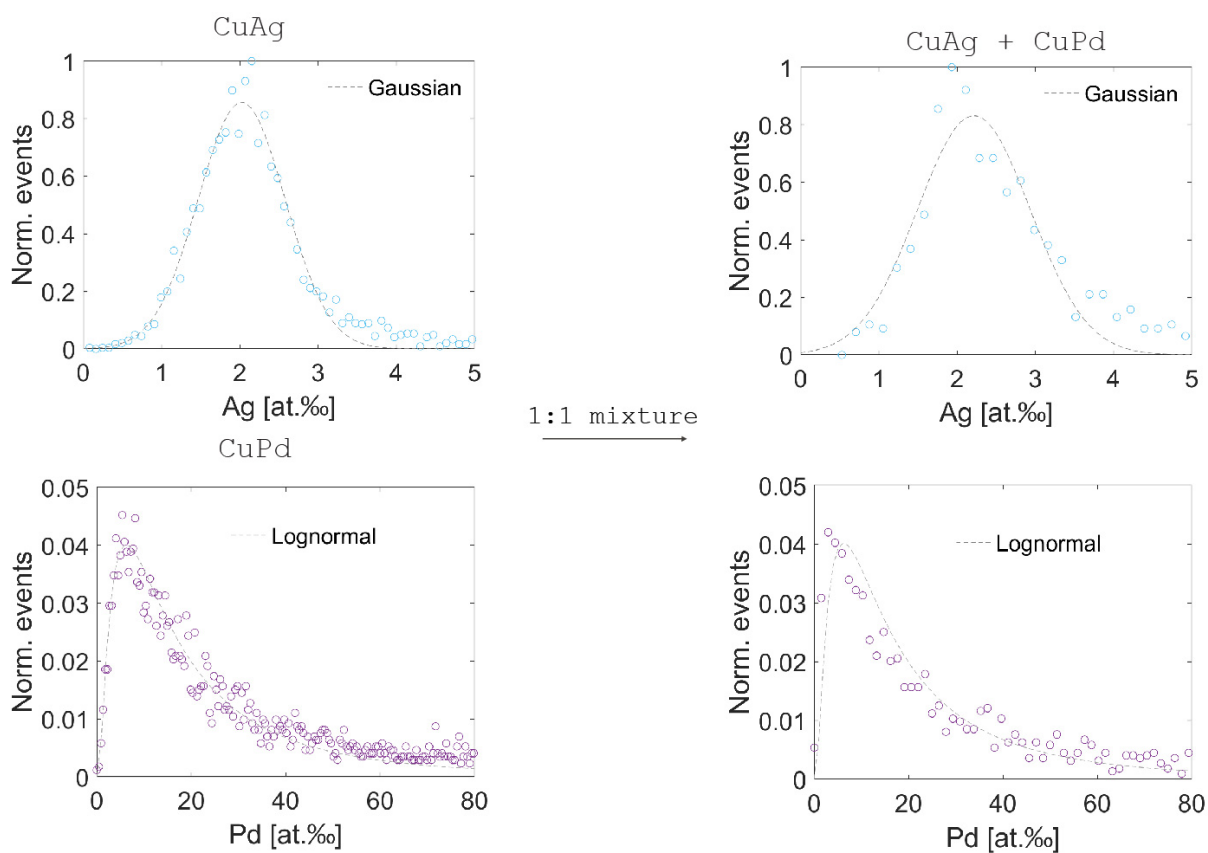


**Figure S10.** Normalized composition distributions of C-CuAg and C-CuPd NPs as compared to those obtained by analyzing a physical mixture of both. C-CuAg was normalized using the maximum value. C-CuPd was normalized such that the probability density function integral equaled to 1. The same distribution could be obtained by sequential as well as simultaneous measurements. <10 counts of PdAg NPs were observed in the physical mixture, which is most likely an artifact stemming from intensity spill-over effects. With well over 1000 particles counted, the significance of this result is minimal. This clearly shows the superiority of the TOF mass analyzer to study multimetallic NP systems over the quadrupole-based process as events containing either element from single elements cannot be distinguished.

	Quadrupole	Time-of-flight
Acronym	ICP-QMS	ICP-TOFMS
Separation mechanism	DC/RF stability	Ion velocity
Manufacturer	PerkinElmer	TOFWERK AG
Simultaneous acquisition range	None	14-275 m/z, 7-175 m/z
Concentration limit of detection	0.01 [pg g <sup>-1</sup> ]	0.1-100 [pg g <sup>-1</sup> ]
Sensitivity	10 <sup>9</sup> [cps ppm <sup>-1</sup> ]	6x10 <sup>7</sup> [cps ppm <sup>-1</sup> ]
Linear dynamic range (Au)	At least 30-100 [nm]	30-250 [nm]
Limit of detection (Au)	13-20 [nm] <sup>4,a</sup>	18 [nm] <sup>5,b</sup>
Cost	low	high
Isotope ratio precision	<0.1% <sup>6</sup>	<0.023% <sup>6</sup>

<sup>a</sup>Limit of detection as determined using the  $3\sigma+\mu$  method. <sup>b</sup> Limit of detection as determined using the Poisson ( $3.27\sigma+\mu+2.72$ ) method.

**Table S4.** A comparison of the general specifications of the quadruple ICP-MS and ICP-TOFMS used in the present study.

The periodic table is color-coded as follows:
 

- Green:** Elements for which a limit of detection using SP-ICP-TOFMS has been reported. These include: Mg, Al, Si, P, S, Cl, Ar, Ga, Ge, As, Se, Br, Kr, Zr, Nb, Mo, Tc, Ru, Rh, Pd, Ag, Cd, In, Sn, Sb, Te, I, Xe, Hf, Ta, W, Re, Os, Ir, Pt, Au, Hg, Tl, Pb, Bi, Po, At, Rn, U, Np, Pu, Am, Cm, Bk, Cf, Es, Fm, Md, No, Lr.
- Blue:** Elements for which the technique is sensitive and could be reported. These include: Li, Be, B, C, N, O, F, Ne, Na, K, Ca, Sc, Ti, V, Cr, Mn, Fe, Co, Ni, Cu, Zn, Ga, Ge, As, Se, Br, Kr, Rb, Sr, Y, Zr, Nb, Mo, Tc, Ru, Rh, Pd, Ag, Cd, In, Sn, Sb, Te, I, Xe, Cs, Ba, La, Hf, Ta, W, Re, Os, Ir, Pt, Au, Hg, Tl, Pb, Bi, Po, At, Rn, Fr, Ra, Ac, Rf, Db, Sg, Bh, Hs, Mt, Ds, Rg, Cn, Nh, Fl, Mc, Lv, Ts, Og, Ce, Pr, Nd, Pm, Sm, Eu, Gd, Tb, Dy, Ho, Er, Tm, Yb, Lu, Th, Pa, U, Np, Pu, Am, Cm, Bk, Cf, Es, Fm, Md, No, Lr.
- Yellow:** Elements that cannot be detected with SP-ICP-TOFMS. These include: H, He, Li, Be, B, C, N, O, F, Ne, Na, Mg, Al, Si, P, S, Cl, Ar, K, Ca, Sc, Ti, V, Cr, Mn, Fe, Co, Ni, Cu, Zn, Ga, Ge, As, Se, Br, Kr, Rb, Sr, Y, Zr, Nb, Mo, Tc, Ru, Rh, Pd, Ag, Cd, In, Sn, Sb, Te, I, Xe, Cs, Ba, La, Hf, Ta, W, Re, Os, Ir, Pt, Au, Hg, Tl, Pb, Bi, Po, At, Rn, Fr, Ra, Ac, Rf, Db, Sg, Bh, Hs, Mt, Ds, Rg, Cn, Nh, Fl, Mc, Lv, Ts, Og, Ce, Pr, Nd, Pm, Sm, Eu, Gd, Tb, Dy, Ho, Er, Tm, Yb, Lu, Th, Pa, U, Np, Pu, Am, Cm, Bk, Cf, Es, Fm, Md, No, Lr.

**Table S5.** Periodic table of elements. In green elements of which a limit of detection using SP-ICP-TOFMS has been reported, in blue those elements for which the technique is sensitive and could be reported and in yellow those elements that cannot be detected with SP-ICP-TOFMS.<sup>6,7</sup> Size detection limits extracted from Hendriks et al. are converted from the absolute mass LODs using the bulk density and assuming spherical geometry.<sup>6</sup> LODs were determined using the Poisson equation. Montañó et al did not report the background extraction method used but also made use of a TOFWERK AG instrument. Only 30 out of 90 possible elements have been reported to our knowledge.

## Note S3. Goodness of the fit of the SP-ICP-TOFMS composition distributions.

Fitting was achieved using the curve fitting application of MATLAB.

### CuPd Pd At.% Lognormal distribution fit

General model:

$$f(x) = \frac{1}{(b*x*((2*\pi)^{(1/2)}))} * \exp(-((\log(x)-a)^2)/(2*b^2))$$

Coefficients (with 95% confidence bounds):

$$a = 3.126 (3.093, 3.158)$$

$$b = 1.28 (1.25, 1.31)$$

Goodness of fit:

SSE: 9.082e-05

R-square: 0.9816

Adjusted R-square: 0.9814

RMSE: 0.0008326

### CuAg At.% Gaussian fit

val =

$$b1 = 2.132 (2.125, 2.14)$$

$$c1 = 0.7254 (0.715, 0.7358)$$

General model Gauss1:

$$\text{val}(x) = a1 * \exp(-((x-b1)/c1)^2)$$

Coefficients (with 95% confidence bounds):

$$a1 = 0.8563 (0.8474, 0.8652)$$

$$b1 = 2.024 (2.017, 2.031)$$

$$c1 = 0.7866 (0.7772, 0.796)$$

Goodness of fit:

R-square: 0.9986

Adjusted R-square: 0.9986

RMSE: 0.0034

### CuAg Ag% Cu65Ag109

General model Gauss1:

$$f(x) = a1 * \exp(-((x-b1)/c1)^2)$$

Coefficients (with 95% confidence bounds):

$$a1 = 0.7647 (0.7553, 0.7742)$$

RMSE: 0.05944

### CuAgPd Pd At.%

Goodness of fit:

SSE: 0.4776

R-square: 0.9723

Adjusted R-square: 0.9722

RMSE: 0.02189

**CuAgPd Ag At.%**

General model Gauss1:

$$f(x) = a1 * \exp(-((x-b1)/c1)^2)$$

Coefficients (with 95% confidence bounds):

a1 = 0.6685 (0.6421, 0.6949)

b1 = 0.407 (0.3819, 0.4322)

c1 = 0.5564 (0.5182, 0.5947)

b1 = 0.1308 (0.1273, 0.1344)

c1 = 0.323 (0.3187, 0.3272)

General model Gauss1:

$$f(x) = a1 * \exp(-((x-b1)/c1)^2)$$

Coefficients (with 95% confidence bounds):

a1 = 4.225e+293 (-Inf, Inf)

b1 = -1130 (-4.448e+04, 4.221e+04)

c1 = 43.47 (-789.3, 876.3)

Goodness of fit:

SSE: 0.5869

R-square: 0.8852

Adjusted R-square: 0.8852

RMSE: 0.007662

**CuAgPd Ag/Pd At.%**

Adjusted R-square: 0.8595

RMSE: 0.01819

**CuAg+CuPd Ag at.%**

Goodness of fit:

SSE: 1.756

R-square: 0.8627

Adjusted R-square: 0.8621

Goodness of fit:

SSE: 5384

R-square: 0.9467

Adjusted R-square: 0.9466

RMSE: 0.7341

**CuAgPd AgPd At.%**

General model Gauss1:

$$f(x) = a1 * \exp(-((x-b1)/c1)^2)$$

Coefficients (with 95% confidence bounds):

$$a1 = 0.6988 (0.6647, 0.7328)$$

$$b1 = -0.83 (-1.326, -0.3335)$$

$$c1 = 5.713 (5.339, 6.087)$$

General model Gauss1:

$$f(x) = a1 * \exp(-((x-b1)/c1)^2)$$

Coefficients (with 95% confidence bounds):

$$a1 = 39.27 (39.06, 39.48)$$

General model Gauss1:

$$f(x) = a1 * \exp(-((x-b1)/c1)^2)$$

Coefficients (with 95% confidence bounds):

$$a1 = 0.8312 (0.795, 0.8675)$$

$$b1 = 2.214 (2.178, 2.251)$$

$$c1 = 1.022 (0.9698, 1.074)$$

Goodness of fit:

SSE: 0.3166

R-square: 0.9346

Adjusted R-square: 0.9339

RMSE: 0.040

Goodness of fit:

SSE: 0.992

R-square: 0.8596

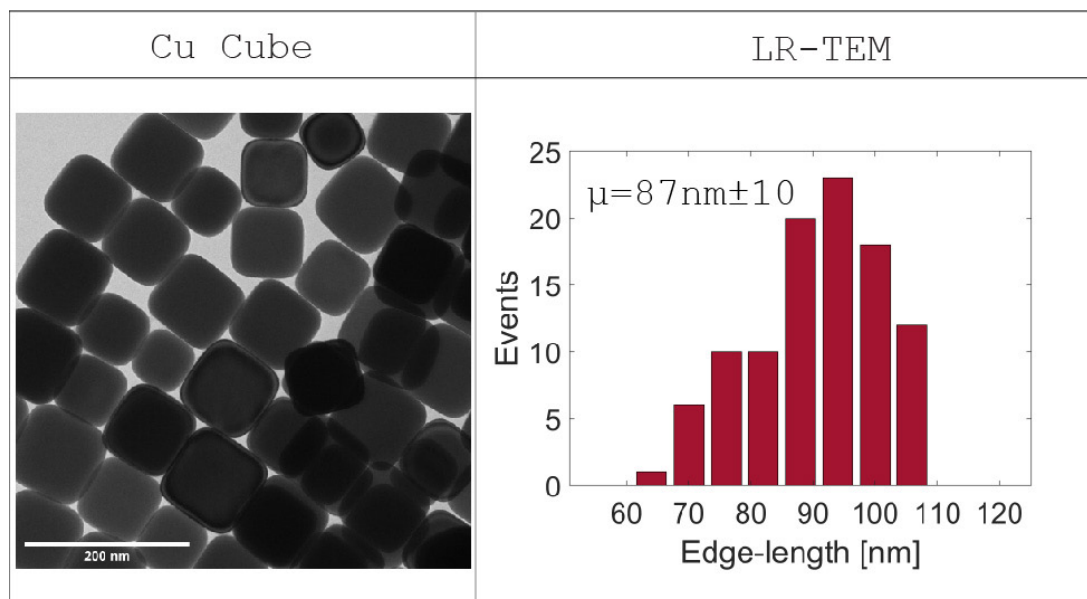


**Figure S11.** Particle size distribution of the C-Cu core used to synthesize the CuAg NSA quantified using the quadrupole. Larger average particle size (87 vs 56 nm) results in ~4-fold smaller particle number concentration at the same mass loading as for the C-Cu used to produce the C-CuAg, C-CuPd and C-CuPdAg NSAs analyzed with the TOF mass analyzer.

Poisson	[63Cu] <sup>+</sup> (cts)	[65Cu] <sup>+</sup> (cts)	[105Pd] <sup>+</sup> (cts)	[106Pd] <sup>+</sup> (cts)	[107Ag] <sup>+</sup> (cts)	[109Ag] <sup>+</sup> (cts)
SD BKG signal (cts)	4.9	3.2	0.17	0.18	0.18	0.18
LOD (Poisson) (cts)	20	13	3.3	3.3	3.3	3.3
Sensitivity (cts/fg)	38.8	19.7	37.8	47.2	107	105
LOD (fg)	0.488	0.663	0.0866	0.0701	0.0310	0.0317
LOD (g)	4.88E-16	6.64E-16	8.66E-17	7.01E-17	3.10E-17	3.17E-17
Density of a pure metal (g/cm <sup>3</sup> )	8.96	8.96	12.023	12.023	10.49	10.49
LOD Metal particle volume (cm <sup>3</sup> )	5.44E-17	7.41E-17	7.20E-18	5.83E-18	2.96E-18	3.02E-18
LOD Metal particle diameter (nm)	47.0	52.1	24.0	22.3	17.8	17.9
3*SD	[63Cu] <sup>+</sup>	[65Cu] <sup>+</sup>	[105Pd] <sup>+</sup>	[106Pd] <sup>+</sup>	[107Ag] <sup>+</sup>	[109Ag] <sup>+</sup>

**Table S6.** Optimized operational conditions used for the NexION 350D and icpTOF ICP-MS instruments used in the present study.

TOh	Particle concentration (NPs mL <sup>-1</sup> )	Most frequent size (nm)	Particle size mean (nm)	Dissolved. Concentration (μg L <sup>-1</sup> )	η <sub>t</sub> (%)	R <sup>2</sup>
Stock	100000	20.0	36.4	3.1	3.46	0.9997
3x	33333	15.1	28.5	0.94	3.46	0.9997
6x	16667	13.3	18.3	0.35	3.46	0.9997

TOh_2	Particle concentration (NPs mL <sup>-1</sup> )	Most frequent size (nm)	Particle size mean (nm)	Dissolved Concentration (μg L <sup>-1</sup> )	η <sub>t</sub> (%)	R <sup>2</sup>
Stock	100000	18.8	34.9	3.1	4.11	0.9997
3x	33333	15.8	25.7	0.90	4.11	0.9997
6x	16667	13.5	19.6	0.31	4.11	0.9997

**Table S7.** Results of the TOh-Cu NP suspension of 10<sup>5</sup> NPs mL<sup>-1</sup> (15 nm) and its dilution series. Complete raw data processing achieved using our in-house developed MATLAB script.

Name	Manufacturer	Ligand	Diameter (TEM)
30 nm Spherical Nanoparticles	Gold Nanopartz	Carboxylic acid	30±2 nm
50 nm Spherical Nanoparticles	Gold Nanopartz	Carboxylic acid	50±2 nm
60 nm Gold Nanospheres	NanoComposix	Citrate	61±7 nm
80 nm Spherical Nanoparticles	Gold Nanopartz	Carboxylic acid	50±6 nm
80 nm Gold Nanospheres	NanoComposix	Citrate	78±9 nm
100 nm Gold Nanospheres	NanoComposix	Citrate	98±9 nm

**Table S8.** Detailed specifications of the Au NPs purchased from NanoComposix and PerkinElmer (Nanopartz) of **Figure S1** and **S2**, respectively.



	Truncated Octahedra [ <sup>63</sup> Cu] <sup>+</sup> (cts)	Tetrahedra [ <sup>63</sup> Cu] <sup>+</sup> (cts)
Threshold ( $\mu+3\sigma$ ) [cts]	1.4	3.1
Sensitivity (cts/fg)	92.6	92.6
LOD (fg)	0.015	0.033
LOD (g)	1.49E-17	3.33E-17
Density of a pure metal (g/cm <sup>3</sup> )	8.96	8.96
LOD Metal particle volume (cm <sup>3</sup> )	1.67E-17	3.71E-18
LOD Metal particle Edge-length (nm)	10.6	15.2

**Table S9.** Limit of detections for the TOh- and Th-Cu NPs based on their edge-length as defined in **Figure 1** in the main text determined via the  $3\sigma$  background subtraction method.

Poisson	[63Cu]+ (cts)	[65Cu]+ (cts)	[105Pd]+ (cts)	[106Pd]+ (cts)	[107Ag]+ (cts)	[109Ag]+ (cts)
SD BKG signal (cts)	4.9	3.2	0.17	0.18	0.18	0.18
LOD (Poisson) (cts)	20	13	3.3	3.3	3.3	3.3
Sensitivity (cts/fg)	<b>38.8</b>	<b>19.7</b>	<b>37.8</b>	<b>47.2</b>	<b>107</b>	<b>105</b>
LOD (fg)	0.488	0.663	0.0866	0.0701	0.0310	0.0317
LOD (g)	4.88E-16	6.64E-16	8.66E-17	7.01E-17	3.10E-17	3.17E-17
Density of a pure metal (g/cm <sup>3</sup> )	8.96	8.96	12.023	12.023	10.49	10.49
LOD Metal particle volume (cm <sup>3</sup> )	5.44E-17	7.41E-17	7.20E-18	5.83E-18	2.96E-18	3.02E-18
LOD Metal particle diameter (nm)	47.0	52.1	24.0	22.3	17.8	17.9

3*SD	[63Cu]+ (cts)	[65Cu]+ (cts)	[105Pd]+ (cts)	[106Pd]+ (cts)	[107Ag]+ (cts)	[109Ag]+ (cts)
SD BKG signal (cts)	4.9	3.2	0.17	0.18	0.18	0.18
LOD 3*SD (cts)	15	9.5	0.50	0.54	0.55	0.55
Sensitivity (cts/fg)	38.8	19.7	37.8	47.2	107	105
LOD (fg)	0.381	0.479	0.0133	0.0114	0.00517	0.00526
LOD (g)	3.81E-16	4.79E-16	1.33E-17	1.14E-17	5.17E-18	5.261E-18
Density of a pure metal (g/cm <sup>3</sup> )	8.96	8.96	12.023	12.023	10.49	10.49
LOD Metal particle volume (cm <sup>3</sup> )	4.25E-17	5.35E-17	1.10E-18	9.47E-19	4.93E-19	5.01E-19
LOD Metal particle diameter (nm)	43.3	46.8	12.8	12.2	9.80	9.86

**Table S10.** Limit of detections for the C-CuPdAg NPs assuming spherical geometry comparing the Poisson and 3 $\sigma$  background subtraction methods.

## Note S4. Background determination via Syngistix software/ MATLAB script.

Syngistix and our MATLAB script uses the  $\mu+3\sigma$  method to determine the threshold iteratively ( $Th(i)$ ). This means that all intensities  $\leq$  the  $\mu+3\sigma$  ( $Th(1)$ ) of the entire data set are collected and stored in a new data set. Then, the  $\mu+3\sigma$  is determined again of the new data set ( $Th(2)$ ) and the previous procedure repeated until the threshold converges ( $Th(N-1)=Th(N)$ ). The final threshold is then used to do peak identification. The ionic background signal is then the average intensity of all intensity values  $\leq$  that threshold. Figure S13 shows the background determination process reported in the PerkinElmer US patent on which the Syngistix software is built.

Although we acknowledge the importance of reducing false positives, we would like to stress that reducing false positives by increasing the threshold not necessarily results in the desired outcome as it is highly dependent on particle size. Laborda et al showed that for Au NPs of 100 nm, the compromise between overestimation of the critical value (threshold) and the reduction of false positives is optimal for the  $\mu+5\sigma$  case.<sup>8</sup> However, this optimum is size dependent. For smaller particles, overestimation is obviously more problematic than for large

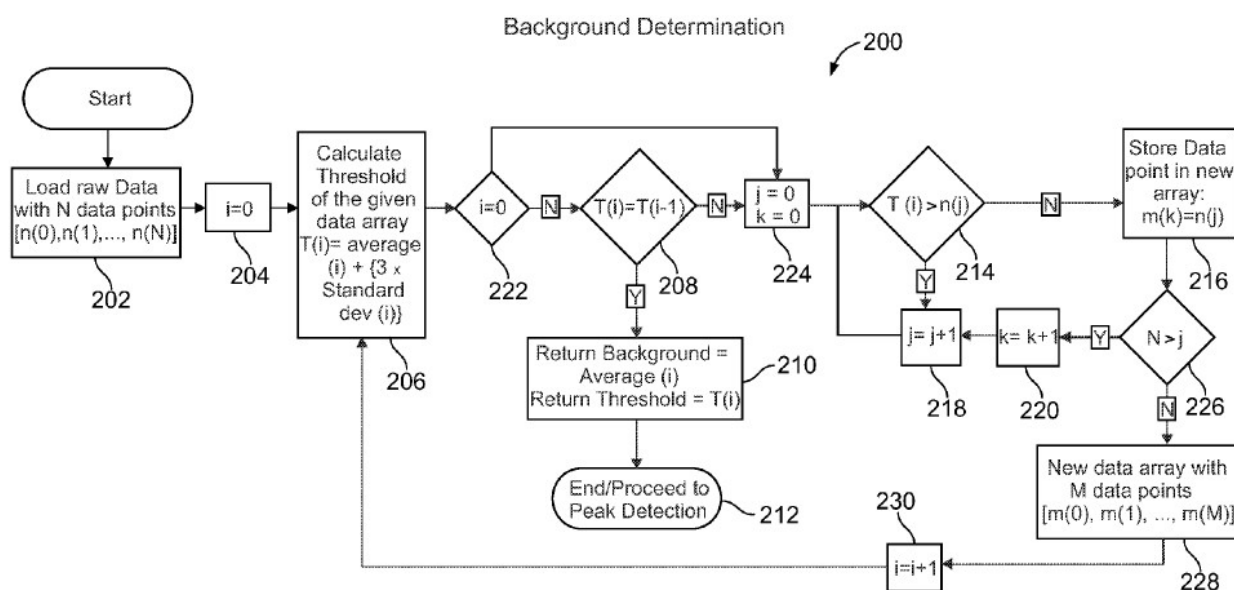


**Figure S12.** The background determination process. (US20150235833A1 Single Particle Data Treatment)

particles. This suggests that this optimum actually shifts with particle size. Indeed, when we change the threshold criteria to  $\mu+5\sigma$  in our MATLAB script, the number concentration of the TOh (**Figure 4**) is  $<2000 \text{ mL}^{-1}$  and the average size to 37 nm (from  $\sim 18000 \text{ mL}^{-1}$  and  $\sim 18 \text{ nm}$ ). We have effectively raised the threshold so much that the smallest particles are no longer visible (similar to the effect of having a high ionic background).

An alternative approach to reduce false positives is to add additional criteria to the peak determination process other than

having an intensity above a predetermined threshold. For instance, having the condition that a signal can only be considered a peak as it has a certain number of consecutive values higher than the threshold. Syngistix makes use of such an approach as well as do we in our MATLAB script (**Figure S14**). However, the details on this are subject to a later study. Be advised that for instruments with long minimum dwell times such false positives reduction methods cannot be used as each dwell is assumed to either contain a complete particle or not.

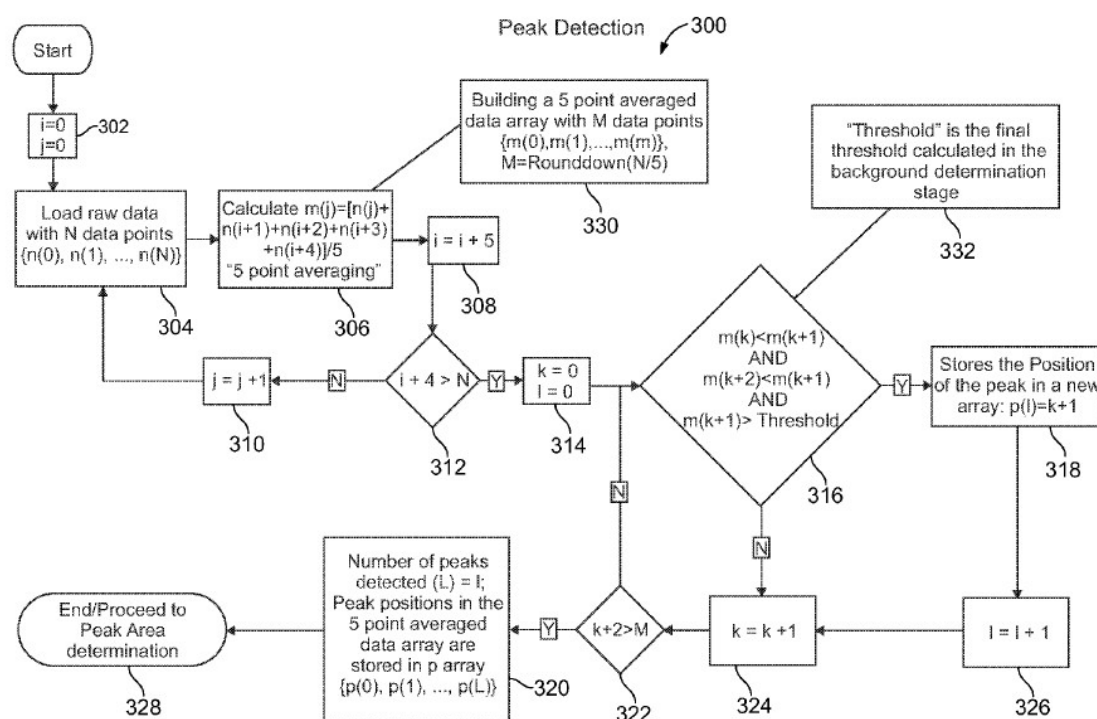


**Figure S13.** The peak detection process. (US20150235833A1 Single Particle Data Treatment).

## S5. References

- (1) Tanuma, S.; Powell, C. J.; Penn, D. R. Calculation of electron inelastic mean free paths (IMFPs) VII. Reliability of the TPP-2M IMFP predictive equation. *Surf. Interface Anal.* **2003**, *35*, 268–275.
- (2) Hill, J. M.; Royce, D. G.; Fadley, C. S.; Wagner, L. F.; Grunthaner, F. J. Properties of Oxidized Silicon as Determined by Angular-Dependent X-Ray Photoelectron Spectroscopy. *Chem. Phys. Lett.* **1976**, *44*, 225–231
- (3) Powell, C. J.; Jablonski, A. The NIST Electron Effective-Attenuation-Length Database. *J. Surf. Anal.* **2002**, *9*, 322–325.
- (4) Lee, S.; Bi, X.; Reed, R. B.; Ranville, J. F.; Herckes, P.; Westerhoff, P. Nanoparticle Size Detection Limits by Single Particle ICP-MS for 40 Elements. *Environ. Sci. Technol.* **2014**, *48*, 10291–10300.
- (5) Naasz, S.; Weigel, S.; Borovinskaya, O.; Serva, A.; Cascio, C.; Undas, A. K.; Simeone, F. C.; Marvin, H. J. P.; Peters, R. J. B. Multi-Element Analysis of Single Nanoparticles by ICP-MS Using Quadrupole and Time-of-Flight Technologies. *J. Anal. At. Spectrom.* **2018**, *33*, 835–845.
- (6) Hendriks, L.; Gundlach-Graham, A.; Hattendorf, B.; Günther, D. Characterization of a New ICP-TOFMS Instrument with Continuous and Discrete Introduction of Solutions. *J. Anal. At. Spectrom.* **2017**, *32*, 548–561.
- (7) Montaña, M. D.; Cuss, C. W.; Holliday, H. M.; Javed, M. B.; Shotyk, W.; Sobocinski, K. L.; Hofmann, T.; Kammer, F. von der; Ranville, J. F. Exploring Nanogeochemical Environments: New Insights from Single Particle ICP-TOFMS and AF4-ICPMS. *ACS Earth Space Chem.* **2022**, *6* (4), 943–952.
- (8) Laborda, F.; Bolea, E.; Jiménez-Lamana, J. Single Particle Inductively Coupled Plasma Mass Spectrometry: A Powerful Tool for Nanoanalysis. *Anal. Chem.* **2014**, *86*, 2270–2278.



## Chapter 5

# Low-temperature non-equilibrium synthesis of anisotropic multimetallic nanosurface alloys for the electrochemical CO<sub>2</sub> reduction reaction

**Preprint version:** this section has been accepted as a full-length article in *Nature Synthesis*.

**Edit:** caption numbers of figures, tables, and equations were edited to match the thesis chapter number.

**Cedric David KOOLEN<sup>a,b</sup>, Emad OVEISI<sup>c</sup>, Jie ZHANG<sup>d</sup>, Mo LI<sup>a,b</sup>, Jack K. PEDERSEN<sup>e</sup>, Jan ROSSMEISL<sup>e</sup>, Wen LUO<sup>f\*</sup>, Andreas ZUETTEL<sup>a,b</sup>**

<sup>a</sup>Laboratory of Materials for Renewable Energy (LMER), Institute of Chemical Sciences and Engineering (ISIC), Basic Science Faculty (SB), École polytechnique fédérale de Lausanne (EPFL) Valais/Wallis, Energypolis, Sion, 1951, Switzerland.

<sup>b</sup>Empa Materials Science & Technology, Dübendorf, 8600, Switzerland.

<sup>c</sup>Interdisciplinary Centre for Electron Microscopy (CIME), École Polytechnique Fédérale de Lausanne (EPFL), CH-1015 Lausanne, Switzerland.

<sup>d</sup>Department of Chemistry, Faculty of Science, National University of Singapore (NUS), 119077 Singapore, Singapore

<sup>e</sup>Center for High Entropy Alloy Catalysis (CHEAC), Department of Chemistry, University of Copenhagen, 2100 København Ø, Denmark

<sup>f</sup>School of Environmental and Chemical Engineering, Shanghai University, Shanghai, 200444, China.

\*Corresponding author: wenluo@shu.edu.cn

## Abstract

Multimetallic nanoparticles are of interest as functional materials for their highly tunable properties. However, synthesizing congruent mixtures of immiscible components is limited to high-temperature procedures followed by rapid quenching which lack size and shape control. Here, we report a low-temperature ( $\leq 80$  °C) non-equilibrium synthesis of nanosurface alloys (NSAs) with tunable size, shape and composition regardless of miscibility. We show the generality of our method by producing both bulk miscible and immiscible monodisperse anisotropic Cu-based NSAs of up to three components. We demonstrate our synthesis as a screening platform to investigate the effects of crystal facet and elemental composition by testing tetrahedral, cubic and truncated-octahedral NSAs as catalysts in the electroreduction of CO<sub>2</sub>. Finally, we resort to machine-learning to predict and synthesize both multicarbon-product selective and phase stable Cu-Ag-Pd compositions. This combination of non-equilibrium synthesis and theory-guided candidate selection is expected to accelerate test-learn-repeat cycles of structure-performance optimization schemes.



## 5.1. Introduction

Multimetallic nanoparticles are becoming increasingly important in fields such as heterogeneous-, electro- and photocatalysis.<sup>1,2,3,4,5,6,7</sup> Multimetallic systems allow for advanced active site tunability beyond size, support and facet effects to include electronic and geometric effects likewise. In combination with advanced simulations to predict the most active and selective candidates,<sup>8</sup> theory-guided catalyst selection may greatly speed up test-learn-repeat cycles in catalyst performance optimization. To harvest the potential of such approaches, a homogeneous mixture of relevant elements in the material is required. Generally, however, production of multimetallic nanomaterials has been limited to various forms of heterostructures due to the often-large miscibility gaps that exist for various metal systems whenever conventional routes are used yielding thermodynamic, phase-segregated products.<sup>9</sup> This limits the added value of a multicomponent system in reaction optimization to concurrent catalysis, e.g. tandem schemes.<sup>10</sup>

Recently, various non-equilibrium methods

have been established that allow for the mixing of the elemental constituents at the nanoscale such as spark ablation, carbo-thermal shock synthesis and laser deposition and offer, thereby, electronic and geometric tuning of the active site.<sup>11,12,13,14,15</sup> Unfortunately, these techniques require extremely harsh conditions ( $\Delta T > 900$  °C) with subsequent quenching to yield the non-equilibrium states rendering the possibility to control the exposed crystal facet improbable. As it has been shown that crystal facets play an important role in controlling reaction pathways,<sup>16</sup> allowing for mixing of various elements at the nanoscale congruent with shape control would offer tremendous insight in the fundamentals of various multimetallic catalyzed processes. One such example is the electrochemical reduction of CO<sub>2</sub> (CO<sub>2</sub>RR) in which convoluted facet and electronic effects induced by elemental mixing have been shown. For instance, for single crystals and nanoparticles (NPs) of Cu, facet dependence has been determined, e.g., Cu(111) surfaces produce CH<sub>4</sub>, Cu(110) shows selectivity for oxygenates and

Cu(100) produces  $C_2H_4$ .<sup>17,18,19,20</sup> Instead, upon the introduction of Ag adatoms in Cu(100) single crystals, the selectivity switches towards oxygenates instead.<sup>21,22</sup> Further, three-component Cu based systems such as Ag-Ru-Cu have recently been reported as the state-of-the-art in the conversion of CO towards n-propanol.<sup>23</sup>

With the opportunities of combined phase and facet control in mind, we revisited a well-known colloidal synthesis known as the galvanic replacement reaction generally yielding thermodynamic products,<sup>24</sup> but enforced kinetic trapping of non-equilibrium structures by introducing a kinetic barrier, thereby obtaining nanosurface alloys (NSAs) in which congruent mixing of multiple components is achieved in a shell surrounding a pure core (**Figure 29**). We used the Cu-Ag system as proof-of-concept to overcome immiscibility for its positive heat of mixing at nearly any composition.<sup>25</sup> Generally, syntheses of Cu-Ag yield phase-segregated materials such as core-shell, core-cluster, crescent and nanodimers,<sup>26,27,28,29</sup> and with a few exceptions alloys, but lack size and shape control.<sup>21,30,31</sup> We show that with our simple yet elegant low temperature seeded-

growth, thin film-based colloidal method, anisotropic {e.g. tetrahedral (Th), cubic (C) and truncated octahedral (TOh)} non-equilibrium multimetallic nanocrystals can be synthesized independent of size and shape, with tunable (surface) composition. We further extend our bimetallic library to include other components with a higher reduction potential than the seed, as evidenced in our Cu-M system with M = Pd, Au and Ag-Pd, to show the generalizability of our synthetic methodology towards other anisotropic NSAs.

We screen our Cu-Ag NSA library in  $CO_2RR$ , of which bulk and morphologically undefined alloyed materials have shown strong selectivity towards multicarbon products ( $C_{2+}$ ).<sup>21,30</sup> As such, we investigate the effect of the facet in this system. We find that both Cu-Ag(100) and Cu-Ag(111)/Cu-Ag(100) faceted C- and TOh-NSA show a high faradaic efficiency (FE) of ~58% towards  $C_{2+}$  products but that the interfacially truncated particles show strong selectivity towards liquid fuels (~62%), including acetate, acetaldehyde, ethanol and n-propanol. We confirm expected surface segregating tendencies of the Cu-Ag system<sup>32</sup> by various ex-situ electron

microscopy techniques and correlate it to the observed dynamic changes in the product distributions. We then demonstrate that the phase stability can be improved by introducing a ternary miscible element (Pd) into the Cu-Ag system. Further, using a supervised machine-learning approach,  $\text{Cu}_{79}\text{Ag}_{16}\text{Pd}_5$  was predicted to show high  $\text{C}_{2+}$  selectivity and phase stability, which was synthesized and its predicted performance

qualitatively met with experiment. With our seeded-growth synthesis platform, we offer unprecedented control over the facet of multimetallic non-equilibrium structures as catalysts for energy applications.

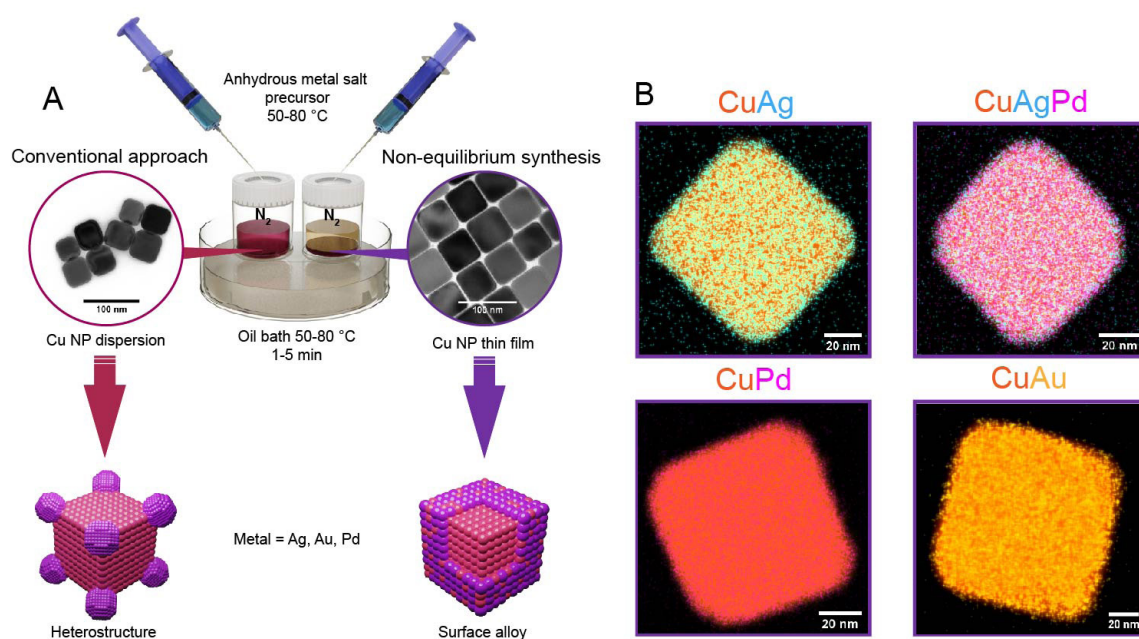


**Figure 29.** (A) Schematic illustration of the conventional and non-equilibrium galvanic replacement reaction, where phase-separated heterostructures and homogeneous surface alloys were formed, respectively. (B) STEM-EDXS elemental maps of cubic Cu-Ag, Cu-Ag-Pd, Cu-Pd and Cu-Au NSAs prepared by using the non-equilibrium method showing the random nature of the added component(s) and increased intensity at the particle edges.<sup>33</sup>

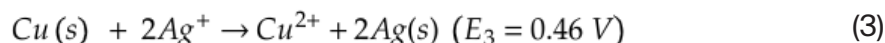
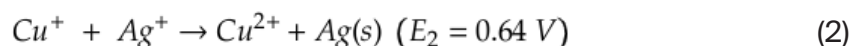
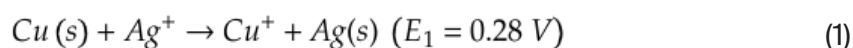
## 5.2. Results and Discussion

### 5.2.1. Low-temperature non-equilibrium synthesis of Cu-Ag anisotropic nanosurface alloys

A typical Cu-Ag galvanic replacement reaction comprised of two steps: (1) a colloidal wet-chemical synthesis to produce anisotropic Cu nanocrystals (NCs), and (2) a subsequent galvanic exchange of Cu with Ag salt. This two-step synthesis was specifically selected to have freedom of choice in seed shape. In the first step, Th-, C-, TOh-Cu NCs were synthesized as reported previously with a colloid synthesis method (**Figure S1**).<sup>33</sup> In the second step, we differentiate between a conventional galvanic replacement reaction and a non-equilibrium one. For the conventional galvanic exchange reaction, Cu crystals are well dispersed in the solution. Thus the reaction is thermodynamically controlled, where the rapid exchange rates and the positive heat of mixing of Cu seeds and Ag ions lead to the formation of individual Ag domains at the particle surfaces, preferentially at the corners and edges.<sup>26,27,28</sup> For details on the thermodynamics and kinetics of the synthesis see **Figure S3** and **Note S1** of the Supporting Information. Instead, for the non-equilibrium synthesis,

anisotropic seeds are kept undisturbed at the bottom of the vial and homogeneously-distributed Ag atoms are incorporated in the Cu lattice as the kinetic product. **Figure 1A** gives an overview of the conventional and non-equilibrium synthesis. **Figure 1B** shows the randomly-distributed solute in the Cu-based NSAs. **Figure 2** shows the extended characterization of the non-equilibrium synthesis for anisotropic Cu-Ag NSAs. Further details on the non-equilibrium synthesis can be found in **Figure S4**, and **Note S1** of the Supporting Information. For a detailed description of the protocol see **Materials and Methods**, and for a scaled-up version of the non-equilibrium synthesis, see **Figure S5**.

The key to the successful synthesis of NSAs is to precisely control the reaction kinetics by limiting the mass transport of the reactants. Take the Cu-Ag system as an example, reaction (1)-(3) can take place spontaneously during the galvanic replacement reaction.



If the replacement process proceeds through reaction (1), each Cu atom is exchanged by exactly one Ag atom. However, if reaction (2) directly follows reaction (1), or Cu is twice oxidized in a single step via reaction (3), two Ag atoms are exchanged per Cu atom. Consequently, reaction (2) and (3) require two Ag<sup>+</sup> ions for the reaction to occur, i.e., a high local concentration of Ag<sup>+</sup>, whereas reaction (1) can occur at any given concentration. Therefore, through confining the Cu seeds in a thin-film and restricting the diffusion of Ag<sup>+</sup> ions to the depletion zone, the non-equilibrium synthesis ensures the predominant occurrence of reaction (1), and ultimately leads to the formation of kinetic phase Cu-Ag NSAs, rather than thermodynamically favorable phase-separated products. This mechanism is supported by the kinetic study shown in **Figure S6**, where the nonequilibrium synthesis shows a much lower reaction rate compared to the conventional synthesis at equal bulk electrolyte concentration. Further, we show that by accelerating reaction (2) (i.e., introducing additional Cu<sup>+</sup> ions in the reaction mixture), the kinetic product can be converted into the thermodynamic heterostructure (**Figure**

**S7**), demonstrating again the importance in controlling the reaction kinetics.

The morphology of anisotropic Cu-Ag-NSAs with different shapes was studied with transmission electron microscopy in bright-field mode (BF-TEM, **Figure 30A-C**). The well-defined tetrahedral, cubic, and truncated octahedral structure indicate that the original Cu NCs structures are well preserved during Ag deposition. A homogeneous distribution of Ag at the surface of the Cu NCs was confirmed by energy dispersive X-ray spectroscopy (EDXS) in scanning transmission electron microscopy (STEM) (**Figure 30D-F**). Further, we probed the valence band spectra of the as-prepared NSAs by X-ray photoemission spectroscopy (XPS) to verify whether an alloy or separated phases have formed, as previous studies have shown that charge transfers from Cu to Ag occurs upon alloying.<sup>34,35</sup> It

is shown that the point-of-gravity of the Cu-Ag NSA valence bands shift towards the Fermi level, indicating charge-transfer, corroborating the surface alloy nature (**Figure 30J**, see **Materials and Methods** for details).<sup>36</sup>

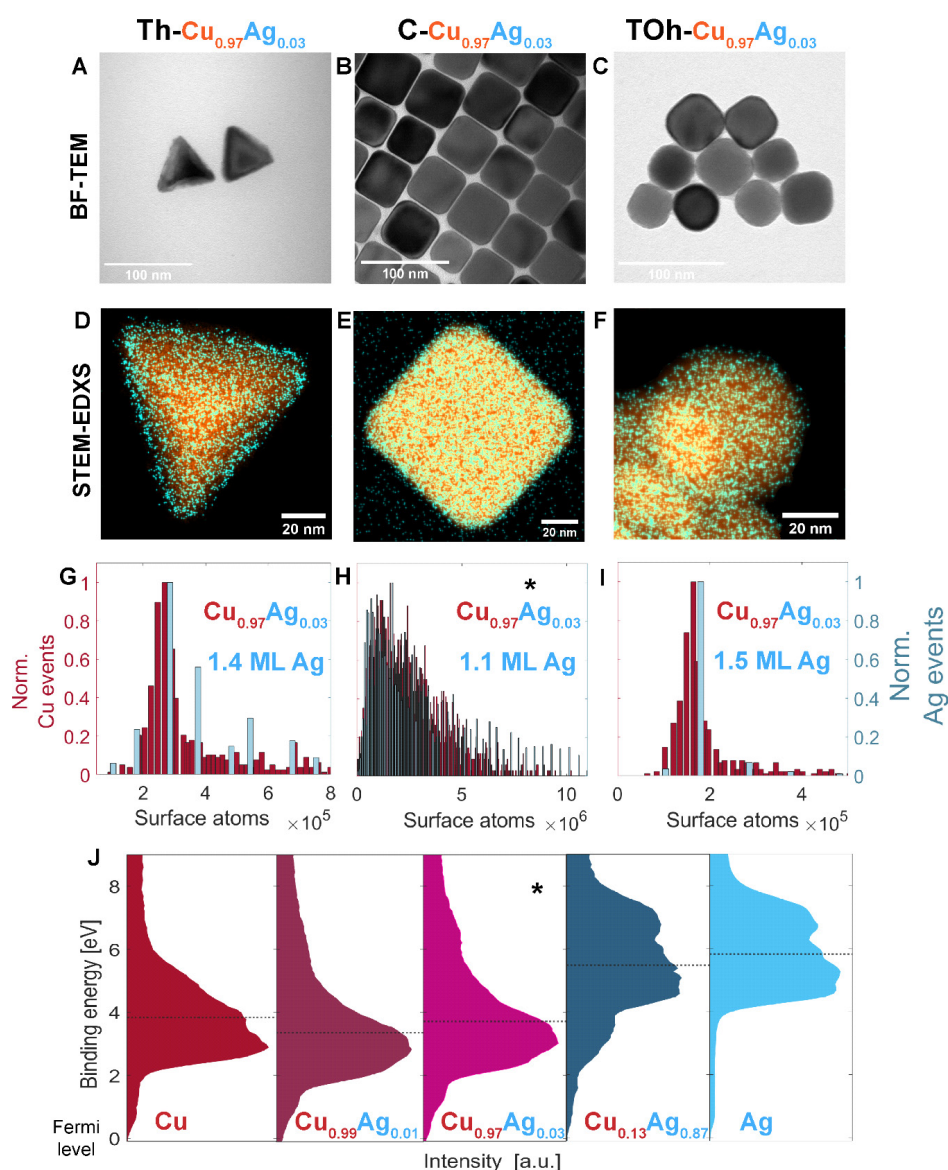


**Figure 30.** Characterization of the anisotropic Cu-Ag NSAs obtained via the non-equilibrium synthesis. Inductively coupled plasma optical emission spectroscopy (ICP-OES) determined particle bulk composition provided in the title. (A-C) BF-TEM images of C-, Th- and TOh-Cu-Ag NSAs. (D-F) STEM-EDXS elemental maps of C-, Th- and TOh-Cu-Ag NSAs with Cu in orange and Ag in turquoise showing normally distributed Ag and increased intensity at the particle edges. (G-I) Distribution of the number of atoms in the surface for  $N$  single particles of the C-, Th- and TOh-Cu-Ag NSAs as determined with single particle-inductively coupled plasma mass spectrometry (SP-ICP-MS) with  $N > 500$ , with an equivalent of 1.4, 1.1 and 1.5 ML of Ag deposited, respectively. (J) Valence band spectra of pure Cu and Ag references and three C-Cu-Ag particles synthesized at different reaction times using the non-equilibrium synthesis (1, 5 min and 2 hrs). The point-of-gravity of the valence band construed exactly half the area-under-the-curve of the spectra (denoted by the dotted line), which was determined by numerically integrating the spectra with fixed bounds at 0 and 9 eV, respectively. The shift of the valence band towards the Fermi level as compared to pure Cu confirms the random alloy nature of the C-Cu<sub>0.99</sub>Ag<sub>0.01</sub> and C-Cu<sub>0.97</sub>Ag<sub>0.03</sub> NSAs as charge-transfer occurs from Cu to Ag. Instead, for a phase-segregated material (C-Cu<sub>0.13</sub>Ag<sub>0.87</sub>), the valence band spectrum is a linear combination of the Cu and Ag reference spectra showing no charge-transfer. The asterisk (\*) in (J) indicates the valence band spectra of the same ensemble of particles indicated in (H).

We further applied the previously developed single particle-inductively coupled plasma mass spectrometry (SP-ICP-MS) method to probe the ensemble representative composition distribution.<sup>33</sup> This method allows for the determination of the complete elemental makeup of individual NPs with ensemble representative statistics, and by further geometrical modelling, surface compositions can be extracted from the obtained elemental distributions. Independent of the facet, a nearly 1:1 ratio between the number of atoms of the outermost Cu monolayer (ML) and the total number of Ag atoms present in the particles was determined, further corroborating the limit of the presence of Ag to the outermost layers of the Th-, C- and TOh-Cu-Ag NSAs (**Figure 30G-I**). We determine that an equivalent of 1.1-1.5 MLs of Ag have been deposited (as based on the 1<sup>st</sup> Cu ML, see **Figure S8**, **Table S2** and **Note S2**). Further, by determining the surface composition with XPS ( $\text{Cu}_{0.91}\text{Ag}_{0.09}$ ), we estimate a diffusion of Ag into the Cu lattice of up to 11 MLs in the C- $\text{Cu}_{0.97}\text{Ag}_{0.03}$  NSA (**Figure S9** and **Table S3**).

To determine the absolute penetration depth of the Ag atoms, we designed a microtomy based experiment<sup>37</sup> in which

the top and bottom face of C-Cu-Ag NSA was removed with a diamond knife (see **Figure S10**). This resulted in a 2D particle consisting of a Cu-Ag random alloy outer ring surrounding a pure Cu core (**Figure 31**). Atomic resolution imaging and EDXS performed on an aberration-corrected STEM<sup>38</sup> reveal that Ag is only present in the first 6 MLs of the NSA (**Figure 31B-D**). A refit of the SP-ICP-MS surface atom distribution using the revealed Ag penetration depth, puts the average surface composition at 21.3 at.% Ag (**Note S2**). Interestingly, the measured composition surpasses the bulk solid solubility of Ag in Cu at room temperature by at least two orders of magnitude, stressing the importance of this work.<sup>39</sup> We further show that by controlling the reaction time of the non-equilibrium synthesis, the surface composition of the Cu-Ag NSA can be tuned (**Figure 30J** and **Table S3**). Finally, we studied the thermal stability of our metastable NSA using in situ TEM at identical location of the specimen (**Figure S11**). The results show that C-Cu-Ag NSA remained stable until 200 °C, ~25 °C higher than that reported for  $\text{Ag}_{0.60}\text{Cu}_{0.40}$  solid solution thin films.<sup>40</sup>

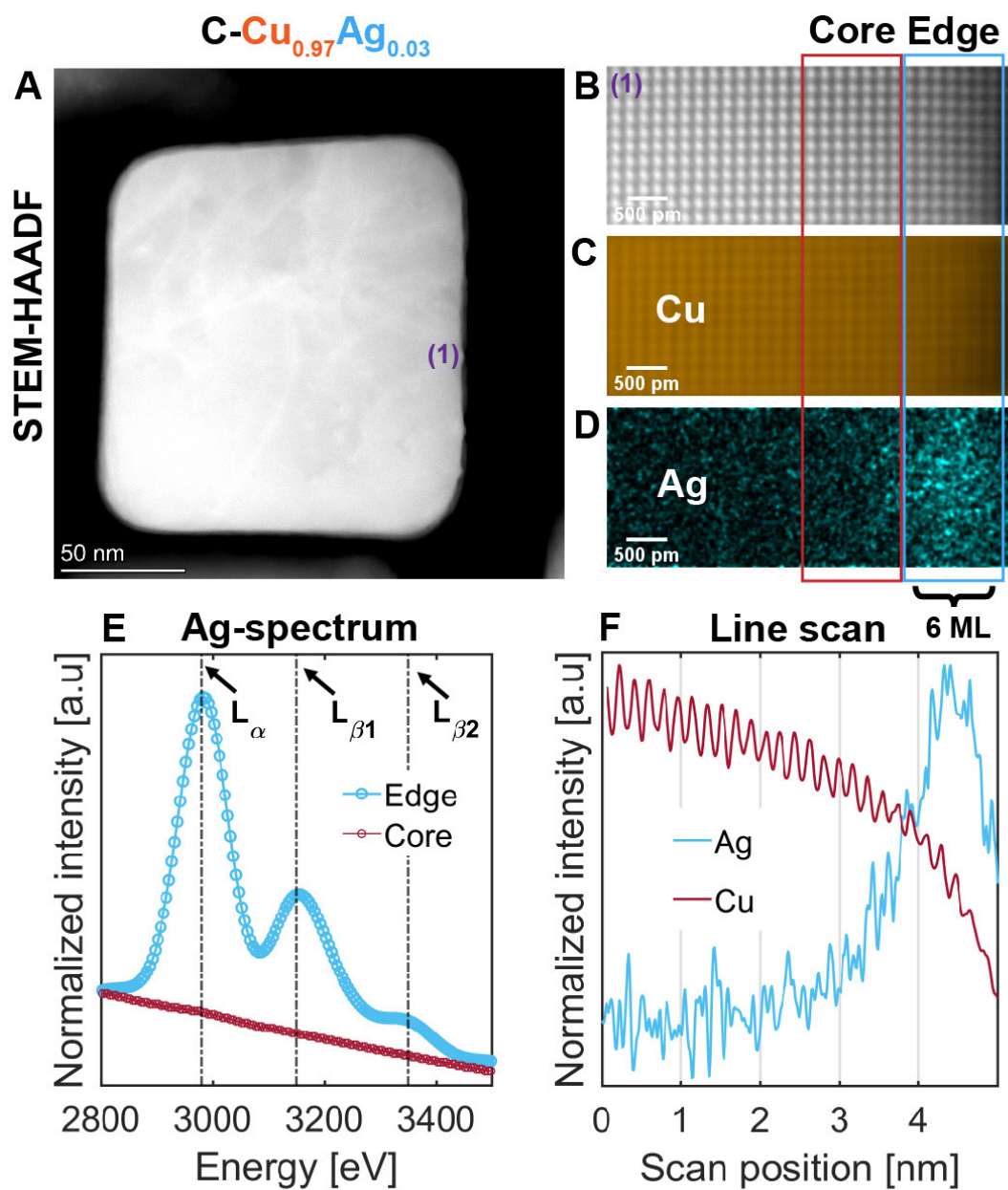


**Figure 31.** Determination of the penetration depth of Ag on the C-Cu<sub>0.97</sub>Ag<sub>0.03</sub> NSA. (A) High-resolution STEM-HAADF image of a 40 nm slice of a Cu-Ag NSA NP embedded in an epoxy resin. (B) Atomic resolution HAADF image of the Cu-Ag NSA edge. (C, D) Cu and Ag EDXS elemental maps of (B). (E) EDX spectra of the core and edge regions of the Cu-Ag NSA (indicated in B-D) showing the presence of the characteristic Ag  $L_{\alpha}$  and  $L_{\beta}$  EDXS peaks at edge regions only, corresponding to the first 6 MLs of the particle. (F) Line scan of intensity over the image in (B).



As the low-temperature non-equilibrium synthesis is based on the galvanic replacement reaction, it should be applicable to different systems as long as there is an appropriate overall cell potential.<sup>24</sup> With this in mind, Cu-Au, Cu-Pd and Cu-Pd-Ag were successfully synthesized using the same reaction parameters as those for Cu-Ag (see **Materials and Methods, Figure 29, Figure S12, and Figure S13**). We would like to emphasize that for a seed with a lower standard reduction potential than Cu, a wider range of exchangeable metals should be possible. Nonetheless, larger potential differences could result in a substantial increase in the reaction

rate, potentially compromising the control over the structure. Therefore, the overall cell potentials investigated in this study (+280 mV to +410 mV for Cu-Ag and Cu-Au systems, respectively) represent a safe range for synthesizing NSAs.<sup>41</sup> Finally, we propose that our synthesis methodology can be extended to produce multicomponent systems beyond three-elements such as high-entropy NSAs by sequentially pairing metals of progressively increasing overall cell potentials.

## 5.2.2. Facet dependent selectivity of Cu-Ag nanosurface alloys in CO<sub>2</sub>RR

We further tested our anisotropic Cu-Ag system in the CO<sub>2</sub>RR to demonstrate the low-temperature non-equilibrium synthesis as a screening platform for anisotropic alloyed multimetallic electrocatalysts (**Figure 32**). We first benchmarked our system by testing the C-, Th-, TOh-Cu single element NCs at a constant potential (-1.1 V vs RHE) in 0.1 M KHCO<sub>3</sub> in an H-cell (**Figure 32A**). Indeed, we could confirm that our faceted Cu seeds followed the same general trend as found in the literature: C-Cu(100) NCs are mostly ethylene selective (FE of 31%),<sup>18,42</sup> Th-Cu(111) is mostly methane selective (29%),<sup>43</sup> and TOh-Cu(100)/Cu(111) shows a slightly higher selectivity towards liquid fuels such as acetate and ethanol etc. (14%).<sup>44</sup> Then, to test if any Ag introduced using the galvanic replacement reaction was catalytically active, we synthesized Ag-Cu NPs as control samples and tested their CO<sub>2</sub>RR activity (**Figure S14**). By extending the reaction time and increasing the Ag<sup>+</sup> concentration in the non-equilibrium synthesis, near-to-complete conversion of the anisotropic Cu NCs to isotropic Ag NPs was achieved (> 96 at.% Ag, see **Materials and Methods** for details, **Figure S14A-D**). It is shown that CO is the majority product (FE

> 59%) independently of the shape of the seed (**Figure S14D**), confirming the activity of the introduced Ag, which is a well-known CO evolving catalyst.<sup>45</sup>

With the pure NCs benchmarked and the Ag activity confirmed, we turn to the investigation of the facet effect in bimetallic Cu-Ag alloys. To deconvolute facet from composition effects, we tested specifically those Cu-Ag NSA of equal composition in the CO<sub>2</sub>RR (C-, Th, and TOh-Cu<sub>0.97</sub>Ag<sub>0.03</sub>, **Figure 32B**). Independent of the facet, a selectivity shift from C<sub>1</sub> products to C<sub>2+</sub> could be noted upon the introduction of Ag with the starkest shift for the Th-Cu-Ag NSA (C<sub>2+</sub> FE from 15% to 40%, **Figure 32C**). Further, a significant amount of acetaldehyde could be detected in the catholyte (FE >9%, **Figure 32C-D**, **Table S4**, **Figure S15**), which is absent for the pure Cu samples.<sup>46</sup> Further, the selectivity towards ethanol improved as well, whereas the FE towards ethylene increased only marginally (**Figure 32C-D**). Therefore, we conclude that Ag adatoms in Cu surfaces favor the C<sub>2+</sub> (especially oxygenate products) over the C<sub>1</sub> products, which is in agreement with the results reported by Clark et al. for Cu-Ag(100) bulk single-crystal surface alloys.<sup>21</sup>

Notably, the TOh-Cu-Ag NSA showed the strongest gains in selectivity towards liquid fuels with acetaldehyde, ethanol and n-propanol approaching double digits (9%, 16% and 9%, respectively, **Table S4**). To our knowledge, no Cu-Ag-based NP system exists that surpasses, at comparably low overpotential in the H-cell, the 35% overall FE towards  $C_{2+}$  liquid fuels.

We attribute the remarkable general trend favoring  $C_{2+}$  liquid fuels (acetate, acetaldehyde, ethanol and n-propanol) over ethylene upon the introduction of Ag in both Cu(111) and Cu(100) faceted crystals to the electronic tuning of the active site, which is distinctly different from tandem-based catalysts.<sup>47,48,49</sup> The electronic nature of the surface determines the binding strength of key intermediates and can thereby greatly influence the selectivity.<sup>50</sup> For transition metals, the binding strength is dictated by the interaction of their d-band with an adsorbate. The closer the d-band center lies to the Fermi level, the stronger the adsorbate binding.<sup>51</sup> Stronger binding of \*CO as compared to pure Cu due to charge transfer-effects enhances the C-C coupling rate and thus the selectivity for  $C_{2+}$  products for Cu-Ag surface alloys (**Figure 30J** and

**Figure S16**). This also explains the larger enhancement factor of  $C_{2+}/C_1$  for Cu-Ag(111) vs Cu-Ag(100) surfaces: the charge-transfer for Th-Cu<sub>0.97</sub>Ag<sub>0.03</sub> and C-Cu<sub>0.97</sub>Ag<sub>0.03</sub> is 100 and 90 meV, respectively. The reason for the more pronounced production of liquid fuels over ethylene is two-fold. First, the shift of the valence band originates from charge-transfer from Cu to Ag and charge-depleted Cu has been shown to favor  $C_{2+}$  products,<sup>29,35</sup> and especially oxygenates.<sup>52</sup> Second, the weak hydrogen adsorption strength of Ag results in lower \*H coverage.<sup>8</sup> As a result, further hydrogenation is limited, steering the selectivity towards oxygen containing products. This is in agreement with observations for tandem Cu-Ag catalysts<sup>53</sup>, and bulk surface alloys<sup>21,22</sup>.

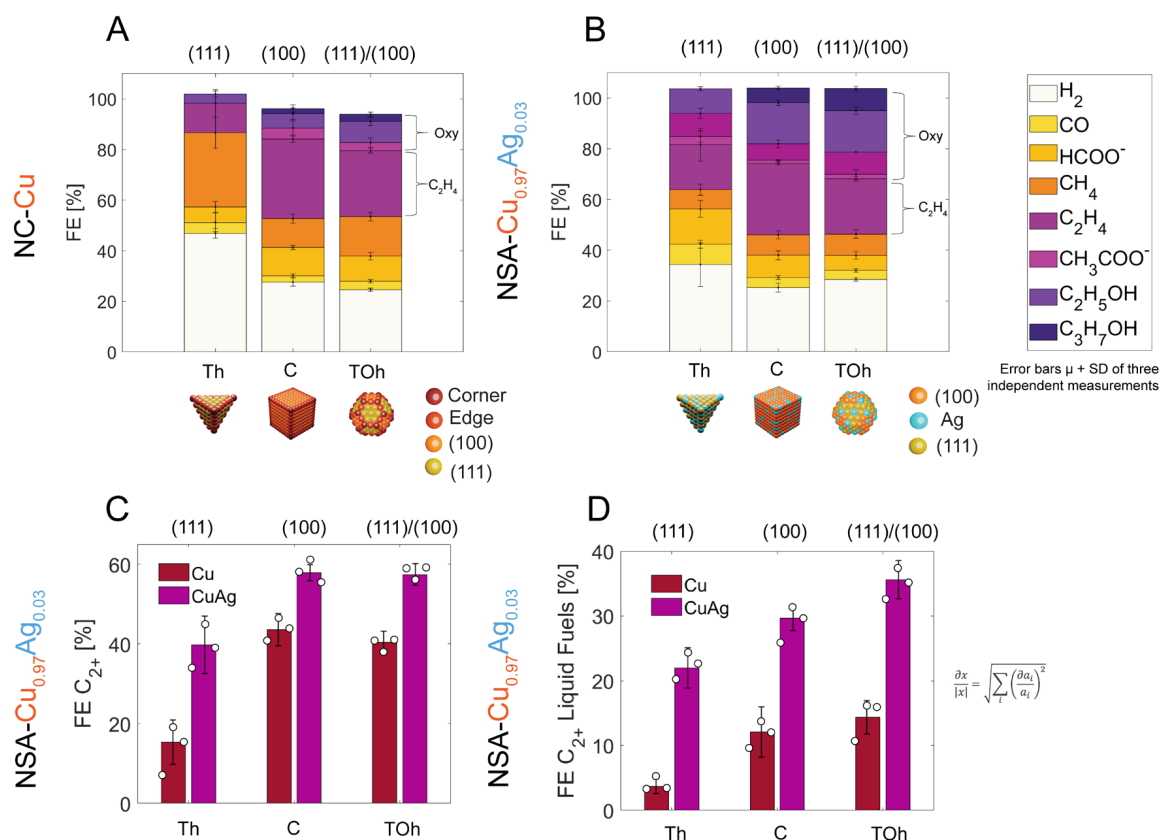


**Figure 32.** Electrocatalytic screening of the as-synthesized (an)isotropic Cu-Ag NPs, error bars represent the standard deviation of three independent measurements. Ball models in the title indicate the geometrical description of the anisotropic particles consisting of Cu(100) facets in orange, Cu(111) facets in yellow, edge sites in red and corner sites in red brown. Ag is indicated in turquoise. (A) Product distribution of the C- Th- and TOh-Cu NCs. (B) Product distribution of the anisotropic Th-Cu<sub>0.97</sub>Ag<sub>0.03</sub>, C-Cu<sub>0.97</sub>Ag<sub>0.03</sub> and TOh-Cu<sub>0.97</sub>Ag<sub>0.03</sub> NSA. (C) C<sub>2+</sub> selectivity as a function of facet and composition. (D) C<sub>2+</sub> liquid fuel selectivity as a function of facet and composition. The interface between Cu-Ag(111) and Cu-Ag(100) offers evidently the best C<sub>2+</sub> liquid fuel producing active site(s).

### 5.2.3. Phase-segregation induced selectivity shift

The strong surface segregating tendencies of the Cu-Ag bimetallic system could significantly influence the selectivity,<sup>32</sup> thus we deem this of utmost importance to evaluate the stability of our surface alloys. We subjected our best performing catalyst (TOh-Cu-Ag NSA) to a stability test at -1.1 V vs RHE and collected aliquots of the catholyte at 10 min intervals to determine the liquid product FEs during operation (**Figure S17**). As expected, the selectivity towards liquid fuels started to wane as soon as the reaction started. Therefore, we further investigated the product distribution in the initial stages of the reaction for all three NSAs (**Figure 5**). For each anisotropic Cu-Ag NSA (Th-, C-, and TOh-Cu<sub>0.97</sub>Ag<sub>0.03</sub>), a decreasing FE for liquid fuels could be observed with the fastest decay observed for the TOh-Cu<sub>0.97</sub>Ag<sub>0.03</sub> (from 35% to 25% in a matter of minutes). This was accompanied by an increase in FE of H<sub>2</sub>. Also, the geometrical partial current densities pointed towards a decaying liquid fuel activity accompanied by an increase in the H<sub>2</sub> evolution reaction (HER, **Figure S18**).

To confirm phase-segregation as the culprit for the loss in selectivity, we analyzed the spent catalyst using TEM (**Figure 33C1-3**).

Strong contrasted extrusions at the particle surface could be discerned for the Th-, C- and TOh-Cu-Ag NSA after CO<sub>2</sub>RR, which were absent in the pristine samples (**Figure 33B1-3**). The presence of extrusions at the particle surfaces of the spent catalysts could be confirmed with scanning electron microscopy (SEM), while the extrusion for the control C-Ag<sub>0.97</sub>Cu<sub>0.03</sub> NPs, which lacked the tendency of phase separation, can be excluded (**Figure S19** and **S20**). We assign these extrusions to the mobile Ag phase. Since phase-segregation results in Ag domain formation predominantly at the most undercoordinated sites, i.e., edges and corners (**Figure S10**), which are most selective for C-C coupling and especially the production of oxygenates,<sup>43,48</sup> we argue that phase-segregation blocks those active sites explaining the progressive loss of liquid fuels selectivity over time. We, therefore, stress the importance of monitoring all products of the CO<sub>2</sub>RR and the sample at least *ex situ* when testing metastable catalysts. Fast adsorbate-induced changes to the surface chemistry may otherwise cloud interpretations of the intrinsic activity.

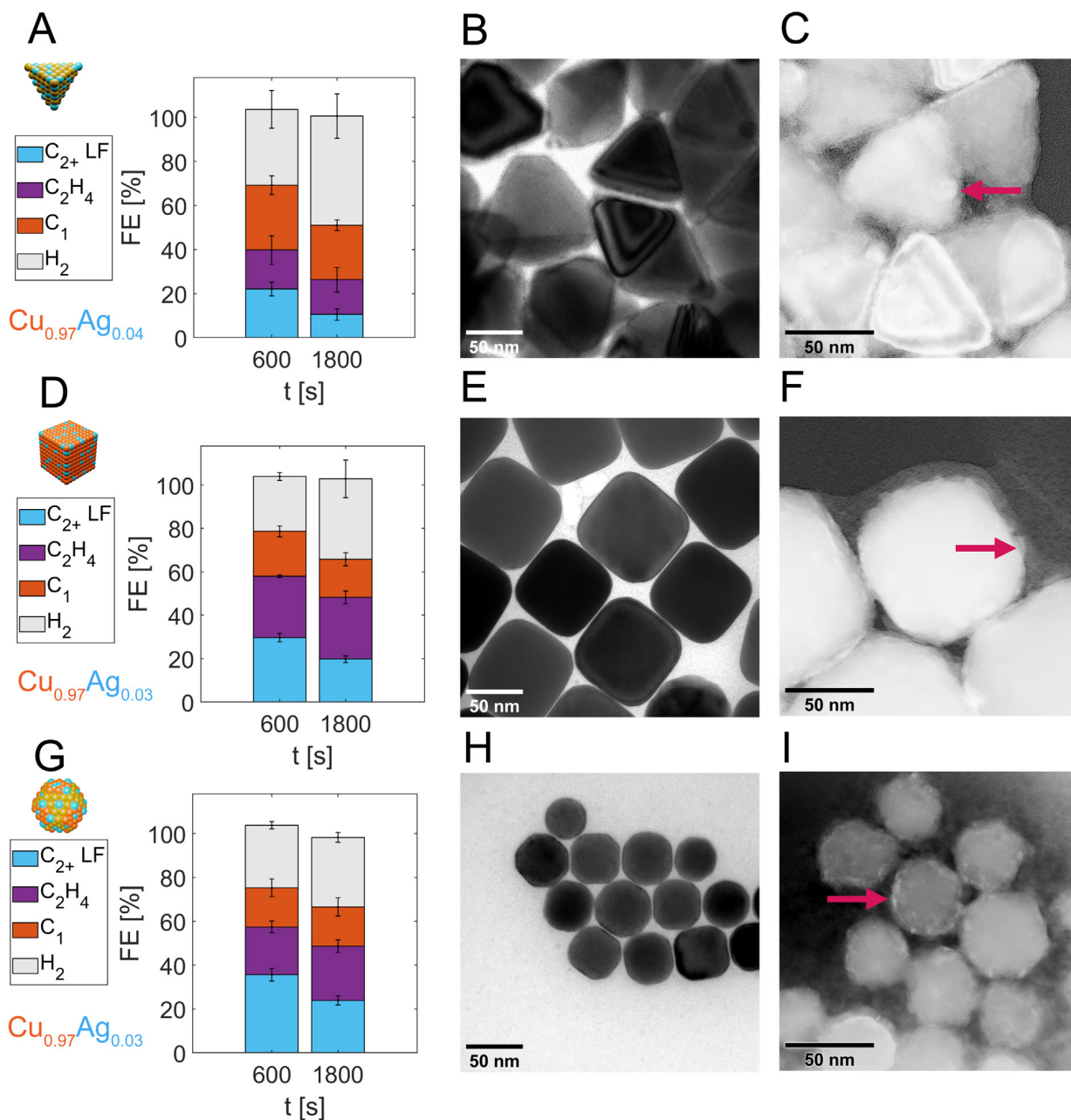


**Figure 33.** (A, D, G) Time evolution of the product distributions of the Th-,C- and TOh-Cu-Ag NSA at -1.1 V vs RHE in CO<sub>2</sub> saturated 0.1 M KHCO<sub>3</sub>. C<sub>1</sub> products including HCOO<sup>-</sup>, CO and CH<sub>4</sub> are depicted in orange. C<sub>2+</sub> liquid fuels products including CH<sub>3</sub>COO<sup>-</sup>, CH<sub>3</sub>CHO, CH<sub>3</sub>CH<sub>2</sub>OH, C<sub>3</sub>H<sub>7</sub>OH are depicted in blue. C<sub>2</sub>H<sub>4</sub> is depicted in purple and H<sub>2</sub> in grey. Error bars indicate the standard deviation of three-independent measurements (**Table S5**). Liquid products are collected under operation from a gas-tight H-cell using a clean syringe. (B, E, H) BF-TEM images of the pristine anisotropic Cu-Ag NSAs. (C, F, I) Negatives of BF-TEM images of the electrocatalysts after 30 min of CO<sub>2</sub>RR offered as a visual-aid to observe the extrusions with higher contrast at the particle surfaces (indicated with arrows) assigned to the Ag phase. Note that the alternating bright/dark areas in the BF-TEM images are the result of thickness-fringes.

#### 5.2.4. Theory-guided Cu-Ag-Pd catalyst selection for stable C<sub>2+</sub> liquid fuel electrosynthesis

Based on the wide applicability of our low-temperature non-equilibrium synthesis, we set out to improve the stability of the metastable Cu-Ag NSA using metals that are miscible with Cu. Limited only by the difference in standard reduction potentials of the metals and the solubility of the salt in the reaction medium, a range of candidates (e.g., Rh, Pt, Pd, and Au) can be selected.<sup>54</sup> Interestingly, our previous investigations of the Cu-Ag-Pd system showed that Ag could be selectively exchanged for Pd whereas Cu remained untouched by choosing the right metal salt precursor.<sup>33</sup> This offered the opportunity to systematically tune the Ag:Pd ratio without changing the bulk Cu content and determine its effect on the performance and phase-stability. Notably, Pd has a strong tendency in reducing H<sub>2</sub>O to H<sub>2</sub>,<sup>55</sup> Therefore, a delicate balance exists between HER/CO<sub>2</sub>RR upon the introduction of the ternary element.

Using a supervised machine-learning algorithm reported previously<sup>8</sup> but trained with a ternary Cu-Ag-Pd data set of density functional theory (DFT) simulated \*CO and \*H adsorption energies, compositions with high CO reduction reaction (CORR) selectivity (i.e., selectivity towards CH<sub>4</sub> and C<sub>2+</sub> products) and low H<sub>2</sub> selectivity could be predicted and selected (**Figure 34A**). CORR selectivity is here predicted as the proportion of surface sites on disordered face-centered cubic (111) surfaces with stronger \*CO adsorption than on the reference Cu(111) surface. Selectivity for reducing CO<sub>2</sub> and subsequently CO (i.e., by suppressing H<sub>2</sub> formation) is predicted as the proportion of sites with weaker \*H adsorption than on Cu(111). Prediction of adsorption energies was achieved on arbitrary surface sites using a linear regressor (**Figure S21, Table S6**). In **Figure 34A**, each data point represents a predicted CO<sub>2</sub>RR/CORR selectivity for a specific

composition of the ternary alloy. With the low-temperature non-equilibrium synthesis, such NSAs could then be synthesized and tested in CO<sub>2</sub>RR (**Figure 34B**). Computation predicted good C<sub>2+</sub> selectivity for Ag:Pd of 1:3 whereas the inverse would suffer from H<sub>2</sub> production. Indeed, extended liquid fuel production could be observed for the Cu<sub>79</sub>Ag<sub>16</sub>Pd<sub>5</sub> system whereas the higher Pd content particle (16 at.%) switched dramatically to HER (**Figure 34C**). The

good agreement between the predicted and the experimentally determined CO<sub>2</sub>RR and CORR selectivity observed confirms the validity of the machine-learning based approach in predicting selectivity relations in alloy systems.

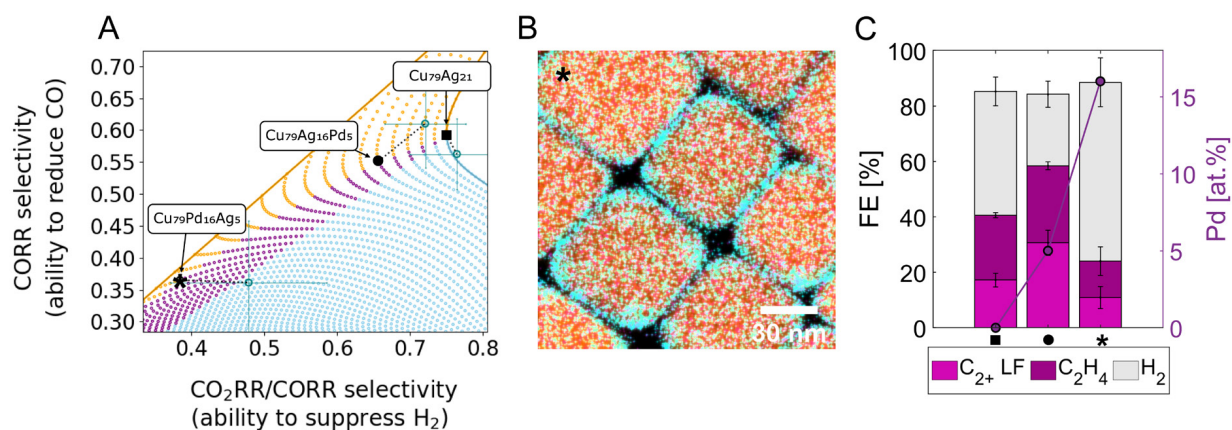


**Figure 34.** Theory-guided optimization of the ternary alloy for extended phase-stability. (A) Activity-selectivity plot of CO<sub>2</sub>RR/CORR of the ternary alloy system. Orange colored dots indicate compositions with  $\geq 74$  at.% Cu, light blue and purple colored with  $< 74$  at.% Cu and  $> 13$  at.% Ag and Pd, respectively. Black symbols (circle, star and square) denote the predicted values from the machine learning-based algorithm. Blue symbols and error bars indicate molar yields as calculated from experimental data in (C) and **Table S7** and **S8**. (B) STEM-EDXS elemental map of as-synthesized C-Cu-Ag-Pd NSA with Ag:Pd equals 1:3. (C) Time averaged FEs of C<sub>2+</sub>, liquid fuels, C<sub>2</sub>H<sub>4</sub> and H<sub>2</sub> of the C-Cu<sub>79</sub>Ag<sub>21</sub>, C-Cu<sub>79</sub>Ag<sub>16</sub>Pd<sub>5</sub> and C-Cu<sub>79</sub>Pd<sub>16</sub>Ag<sub>5</sub> NSAs, respectively. Electrochemical test was performed for 30 min at -1.1 V vs. RHE in 0.1 M KHCO<sub>3</sub>. Square, circle and star insets reflect matching composition in (A)-(C). Error bars indicate the standard deviation of three independent measurements.



## 5.3. Conclusion

Multicomponent congruently mixed nanoparticles are well underway in playing a dominant role in the energy research field. To fully harvest the catalytic potential of such systems, not only do miscibility gaps need to be overcome with advanced syntheses, it must be achieved with shape control to deconvolute the effect of the facet from that of the composition. We show with our generalizable low-temperature non-equilibrium seeded-growth method that this is now possible as evidenced by the production of anisotropic (cubic, tetrahedral, and truncated octahedral, etc.) multimetallic nanosurface alloys (Cu, Ag, Pd, and Au, etc.) of up to three components.

Further, to show the applicability of our synthesis products in electrochemical screening, we tested our shape-controlled Cu-Ag nanoparticles in the CO<sub>2</sub>RR and showed improved selectivity towards C<sub>2+</sub> liquid fuels compared with their monoelemental counterparts. Finally, guided by machine learning, we synthesized Cu-Ag-Pd NSAs with high C<sub>2+</sub> selectivity and phase stability. With a large number of multimetallic compositions and systems accessible as well as the added facet control, we expect our low-temperature non-equilibrium synthesis to be of great advantage for researchers seeking nanomaterials of specific spatial atomic arrangements.

## 5.4. Materials and Methods

### 5.4.1. Chemicals

The following chemicals and solvents were acquired from Sigma-Aldrich: copper bromide 99.99% (CuBr), palladium chloride 99% (PdCl<sub>2</sub>), gold chloride (AuCl<sub>3</sub>), nitric acid 70% (HNO<sub>3</sub>), trioctylphosphine oxide 99% (TOPO), trioctylphosphine 99% (TOP) and oleyl amine 70% (OAm). Anhydrous ethanol

95% was purchased from ACROS organics (EtOH) and anhydrous toluene (99.8%) from Alfa Aesar. Lastly, silver nitrate (AgNO<sub>3</sub>) 99.9995% was obtained from Puratrem. All chemicals were used as received without any further purification.

### 5.4.2. Non-equilibrium synthesis

The low-temperature non-equilibrium synthesis is inspired by the protocol from Lee et al.<sup>27</sup> Typically, 4 mg of anisotropic Cu NPs synthesized using a Schlenk-line (**Figure S1**) dispersed in a minimal amount of anhydrous toluene (19 mg/mL based on ICP-OES) were added to a 10 mL glass vial in the glove box creating a NP thin film, to which 3.5 mL of degassed OAm were added carefully without disturbing the film (non-equilibrium synthesis). Further, 0.5 mg of dry AgNO<sub>3</sub> were added to 1.5 mL of degassed OAm and dissolved at 50 °C using an oil bath to prevent homogeneous nucleation (Cu:Ag equals 21:1, **Figure S21**). Then, using a clean syringe, the Ag salt precursor solution were dropwise added to the reaction vial. For the C-Cu-Ag NSAs, the reaction mixture was then allowed to

react at 80 °C for 1 or 5 min. For the TOh-Cu-Ag for 5 min at 80 °C and for the Th-Cu-Ag 1 min at 50 °C. For the isotropic Ag-Cu NPs the Cu:Ag ratio was increased to 1:3 and the reaction time extended to 24 hrs to ensure near-to-complete exchange (**Figure S12**). In each case, the reaction was quenched with an excess of anhydrous toluene and washed with the same solvent. Substitution of the AgNO<sub>3</sub> with AuCl<sub>3</sub> or PdCl<sub>2</sub> and increasing the dissolution temperature to 80 °C but keeping all other conditions the same obtained the C-Cu-Au and C-Cu-Pd MMNPs. By reintroducing C-Cu-Ag NSAs and reacting with a Pd salt precursor solution, C-Cu-Pd-Ag MMNPs could be obtained as well. For details on the conventional synthesis, see SI **Note S1**.

### 5.4.3. Annealing experiments

A monolayer of C-Cu-Ag NSAs was deposited on thermally resistant  $\text{Si}_3\text{N}_4$  grids purchased from Ted Pella Inc. and placed in a MILA-5000 rapid thermal annealer. After flushing the gas tight system with  $\text{N}_2$  for 30 min. The temperature was increased to 100 °C with ramp of 50 °C·s<sup>-1</sup> and kept at that temperature for 30 min after which the reaction was quenched by flushing again with  $\text{N}_2$ . After the reaction, the wetting

behavior of the NSA was investigated using TEM imaging performed on identical sample locations. The experiment was further repeated for 200 °C, 300 °C and 400 °C and the wetting behavior observed. After the final annealing experiment, STEM-EDXS (on identical locations) was performed to confirm the mobility of the Ag phase.

### 5.4.4. Cathode preparation

Belt-shaped pieces of Toray TGP-60r carbon paper were cut out with a geometrical surface area of 0.5 cm<sup>2</sup>, to which 0.8 mg·cm<sup>-2</sup> worth of the anisotropic Cu NCs, Cu-Ag, Cu-Ag-Pd NSAs or isotropic Ag-Cu NPs dispersed in toluene were added using drop casting in the glovebox. Finally, 20 μL of 0.83 wt% Nafion dispersed in *iso*-propanol were added as binder.

## 5.4.5. Characterization

**Electron microscopy (EM).** SEM images were acquired using a Thermo Scientific Teneo. TEM images were acquired with a FEI Tecnai Basic Spirit operated at 120 kV in bright field mode. The microscope was equipped with a Gatan charge-coupled device (CCD) camera and Digital Micrograph for imaging. Samples were drop-casted on Au grids (400 mesh) from Ted Pella Inc. with ultrathin carbon film, which were washed with ethanol before and after drop-casting. Ni based grids were used for Au containing samples. Scanning transmission electron microscopy high-angle annular dark-field (STEM-HAADF) micrographs and EDXS elemental maps were obtained on a Thermo Scientific Tecnai-Osiris operated at 200 kV. This instrument is outfitted with a high brightness Schottky X-FEG. This microscope is equipped with a high brightness Schottky X-FEG gun, a Super-X EDX system comprising of four silicon drift detectors. Atomic resolution scanning transmission electron microscope images were acquired in the high-angle annular dark-field (HAADF-STEM) condition on an aberration-corrected (double Cs-corrected)

Thermo Scientific Titan-Themis 60-300 operated at 200 kV and using a beam current of 200 pA. The Super-X EDX system and Velox acquisition software were used to acquire and analyze the EDXS elemental maps. To study the penetration depth of the Ag inside the particle, some samples were embedded in the G2 resin and sliced to 40 nm thick slices by ultramicrotomy using a Leica EM FC7 machine (equipped with a Diatome cryo-knife 35° angle) at room temperature and with a cutting speed of 0.2 mm s<sup>-1</sup>. Ultramicrotomed slices were deposited on an ultra-thin carbon support grid for imaging and EDXS.

**X-ray photoelectron spectroscopy (XPS).** XPS was performed on a Kratos Axis Supra system (analysis chamber base pressure  $1 \times 10^{-9}$  mbar), using a monochromated Al K<sub>α</sub> (1486.61 eV) X-ray source at a nominal power of 225 W. A pass energy of 20 eV was used for acquiring all core-level and Auger electron spectra, as well as the X-ray excited valence band spectra. The binding energies (BEs) were referenced to Au 4f<sub>7/2</sub> at 83.95 eV. The samples were drop-casted on a gold foil in a N<sub>2</sub> glovebox and transferred

for measurement without exposure to air. No charge compensation was required as the samples were conductive.

***Inductively coupled plasma - optical emission spectroscopy (ICP-OES).*** The concentration of the digested NP solutions was determined with an Agilent 5110 ICP-OES with a VistaChip II CCD camera. The NPs were digested overnight in 2% HNO<sub>3</sub> and filtered with 400 μm pore size Ultrapore nylon filters. The calibration curves were obtained through the preparation of a dilution series of elemental standards obtained from Sigma Aldrich.

***Inductively-coupled plasma mass spectrometry (ICP-MS).*** Elemental analysis of the Th-, C- and TOh-Cu-Ag NSAs

was achieved with a NexION 350D ICP-MS instrument from PerkinElmer operated in continuous data acquisition mode. Calibration of the transport efficiency ( $\eta_t$ ) was achieved with Au NPs standards 30, 50 and 80 nm purchased from PerkinElmer at a NP number concentration of ~50,000 NPs mL<sup>-1</sup>.

## 5.4.6. Density Functional Theory Simulations

126 atop \*CO and 160 face-centered cubic (fcc) threefold hollow \*H adsorption energies were simulated on fcc (111) surfaces of randomly generated, periodically repeated surface slabs sized 3x3x5 atoms with 10 Å of vacuum above and below the slab. The lattice constants were set to the average of the constituent elements in the top layer.<sup>55</sup> Simulations were performed in the GPAW code<sup>56,57</sup> version 22.1.0 and the atomic simulation environment (ASE)<sup>58</sup> version 3.22.1 for atomic manipulations. Energies were computed using the RPBE exchange-correlation functional<sup>59</sup> using a plane wave basis set with an energy cutoff of 400 eV. The Brillouin zone was sampled on a 4x4x1 uniform Monkhorst-Pack grid of k-points, and atoms were relaxed to a force below 0.075 eV/Å. Atomic structures have been made freely available at [nano.ku.dk/english/research/theoretical-electrocatalysis/katlabdb/co2-reduction-on-ag-cu-pd/](http://nano.ku.dk/english/research/theoretical-electrocatalysis/katlabdb/co2-reduction-on-ag-cu-pd/).

## 5.5. References

1. Cui, C., Gan, L., Heggen, M., Rudi, S. & Strasser, P. Compositional segregation in shaped Pt alloy nanoparticles and their structural behaviour during electrocatalysis. *Nat. Mater.* **12**, 765–771 (2013).
2. Niu, Z. *et al.* Anisotropic phase segregation and migration of Pt in nanocrystals en route to nanoframe catalysts. *Nat. Mater.* **15**, 1188–1194 (2016).
3. Taccardi, N. *et al.* Gallium-rich Pd–Ga phases as supported liquid metal catalysts. *Nat. Chem.* **9**, 862–867 (2017).
4. Zhou, L. *et al.* Quantifying hot carrier and thermal contributions in plasmonic photocatalysis. *Science* **362**, 69–72 (2018).
5. Batchelor, T. A. A. *et al.* High-Entropy Alloys as a Discovery Platform for Electrocatalysis. *Joule* **3**, 834–845 (2019).
6. Zhang, X. *et al.* Reversible loss of core-shell structure for Ni–Au bimetallic nanoparticles during CO<sub>2</sub> hydrogenation. *Nat. Catal.* **3**, 411–417 (2020).
7. Xing, F., Nakaya, Y., Yasumura, S., Shimizu, K. & Furukawa, S. Ternary platinum–cobalt–indium nanoalloy on ceria as a highly efficient catalyst for the oxidative dehydrogenation of propane using CO<sub>2</sub>. *Nat. Catal.* **5**, 55–65 (2022).
8. Pedersen, J. K., Batchelor, T. A. A., Bagger, A. & Rossmeisl, J. High-Entropy Alloys as Catalysts for the CO<sub>2</sub> and CO Reduction Reactions. *ACS Catal.* **10**, 2169–2176 (2020).
9. Sankar, M. *et al.* Designing bimetallic catalysts for a green and sustainable future. *Chem. Soc. Rev.* **41**, 8099–8139 (2012).
10. Xie, C., Niu, Z., Kim, D., Li, M. & Yang, P. Surface and Interface Control in Nanoparticle Catalysis. *Chem. Rev.* **120**, 1184–1249 (2020).
11. Tabrizi, N. S., Xu, Q., van der Pers, N. M. & Schmidt-Ott, A. Generation of mixed metallic nanoparticles from immiscible metals by spark discharge. *J. Nanoparticle Res.* **12**, 247–259 (2010).
12. Kane, K. A., Reber, A. C., Khanna, S. N. & Bertino, M. F. Laser synthesized nanoparticle alloys of metals with bulk miscibility gaps. *Prog. Nat. Sci. Mater. Int.* **28**, 456–463 (2018).
13. Feng, J., Ramlawi, N., Biskos, G. & Schmidt-Ott, A. Internally mixed nanoparticles from oscillatory spark ablation between electrodes of different materials. *Aerosol Sci. Technol.* **52**, 505–514 (2018).
14. Yao, Y. *et al.* Carbothermal shock synthesis of high-entropy-alloy nanoparticles. *Science* **359**, 1489–1494 (2018).
15. Yang, C. *et al.* Overcoming immiscibility toward bimetallic catalyst library. *Sci. Adv.* **6**, eaaz6844 (2020).
16. Guntern, Y. T. *et al.* Colloidal Nanocrystals as Electrocatalysts with Tunable Activity and Selectivity. *ACS Catal.* **11**, 1248–1295 (2021).

17. Hori, Y., Takahashi, I., Koga, O. & Hoshi, N. Selective Formation of C<sub>2</sub> Compounds from Electrochemical Reduction of CO<sub>2</sub> at a Series of Copper Single Crystal Electrodes. *J. Phys. Chem. B* **106**, 15–17 (2002).
18. Loiudice, A. *et al.* Tailoring Copper Nanocrystals towards C<sub>2</sub> Products in Electrochemical CO<sub>2</sub> Reduction. *Angew. Chem. Int. Ed.* **55**, 5789–5792 (2016).
19. Iyengar, P., Huang, J., Gregorio, G. L. D., Gadiyar, C. & Buonsanti, R. Size dependent selectivity of Cu nano-octahedra catalysts for the electrochemical reduction of CO<sub>2</sub> to CH<sub>4</sub>. *Chem. Commun.* **55**, 8796–8799 (2019).
20. Schouten, K. J. P., Pérez Gallent, E. & Koper, M. T. M. Structure Sensitivity of the Electrochemical Reduction of Carbon Monoxide on Copper Single Crystals. *ACS Catal.* **3**, 1292–1295 (2013).
21. Clark, E. L., Hahn, C., Jaramillo, T. F. & Bell, A. T. Electrochemical CO<sub>2</sub> Reduction over Compressively Strained CuAg Surface Alloys with Enhanced Multi-Carbon Oxygenate Selectivity. *J. Am. Chem. Soc.* **139**, 15848–15857 (2017).
22. Higgins, D. *et al.* Guiding Electrochemical Carbon Dioxide Reduction toward Carbonyls Using Copper Silver Thin Films with Interphase Miscibility. *ACS Energy Lett.* **3**, 2947–2955 (2018).
23. Wang, X. *et al.* Efficient electrosynthesis of n-propanol from carbon monoxide using a Ag–Ru–Cu catalyst. *Nat. Energy* **7**, 170–176 (2022).
24. Xia, X., Wang, Y., Ruditskiy, A. & Xia, Y. 25th Anniversary Article: Galvanic Replacement: A Simple and Versatile Route to Hollow Nanostructures with Tunable and Well-Controlled Properties. *Adv. Mater.* **25**, 6313–6333 (2013).
25. Subramanian, P. R. & Perepezko, J. H. The ag-cu (silver-copper) system. *J. Phase Equilibria* **14**, 62–75 (1993).
26. Kim, N. R., Shin, K., Jung, I., Shim, M. & Lee, H. M. Ag–Cu Bimetallic Nanoparticles with Enhanced Resistance to Oxidation: A Combined Experimental and Theoretical Study. *J. Phys. Chem. C* **118**, 26324–26331 (2014).
27. Lee, C., Kim, N. R., Koo, J., Lee, Y. J. & Lee, H. M. Cu–Ag core–shell nanoparticles with enhanced oxidation stability for printed electronics. *Nanotechnology* **26**, 455601 (2015).
28. Osowiecki, W. T. *et al.* Tailoring Morphology of Cu–Ag Nanocrescents and Core–Shell Nanocrystals Guided by a Thermodynamic Model. *J. Am. Chem. Soc.* **140**, 8569–8577 (2018).
29. Huang, J., Mensi, M., Oveisi, E., Mantella, V. & Buonsanti, R. Structural Sensitivities in Bimetallic Catalysts for Electrochemical CO<sub>2</sub> Reduction Revealed by Ag–Cu Nanodimers. *J. Am. Chem. Soc.* **141**, 2490–2499 (2019).
30. Hoang, T. T. H. *et al.* Nanoporous Copper–Silver Alloys by Additive-Controlled Electrodeposition for the Selective Electroreduction of CO<sub>2</sub> to Ethylene and Ethanol. *J. Am. Chem. Soc.* **140**, 5791–5797 (2018).



31. Dettelbach, K. E. *et al.* Kinetic phases of Ag–Cu alloy films are accessible through photodeposition. *J. Mater. Chem. A* **7**, 711–715 (2019).
32. Ruban, A. V., Skriver, H. L. & Nørskov, J. K. Surface segregation energies in transition-metal alloys. *Phys. Rev. B* **59**, 15990–16000 (1999).
33. Koolen, C. D. *et al.* High-Throughput Sizing, Counting, and Elemental Analysis of Anisotropic Multimetallic Nanoparticles with Single-Particle Inductively Coupled Plasma Mass Spectrometry. *ACS Nano* (2022) doi:10.1021/acsnano.2c01840.
34. Sprunger, P. T., Lægsgaard, E. & Besenbacher, F. Growth of Ag on Cu(100) studied by STM: From surface alloying to Ag superstructures. *Phys. Rev. B* **54**, 8163–8171 (1996).
35. *Many-Particle Spectroscopy of Atoms, Molecules, Clusters, and Surfaces.* (Springer US, 2001). doi:10.1007/978-1-4615-1311-7.
36. Kim, D., Resasco, J., Yu, Y., Asiri, A. M. & Yang, P. Synergistic geometric and electronic effects for electrochemical reduction of carbon dioxide using gold–copper bimetallic nanoparticles. *Nat. Commun.* **5**, 1–8 (2014).
37. Sun, D. T. *et al.* Rapid, Selective Heavy Metal Removal from Water by a Metal–Organic Framework/Polydopamine Composite. *ACS Cent. Sci.* **4**, 349–356 (2018).
38. Bencan, A. *et al.* Atomic scale symmetry and polar nanoclusters in the paraelectric phase of ferroelectric materials. *Nat. Commun.* **12**, 3509 (2021).
39. Anderko, M. H. and K. *Constitution of binary alloys, SECOND EDITION.* (McGraw Hill Book Company, 1958).
40. Tsaur, B. Y., Lau, S. S. & Mayer, J. W. Continuous series of metastable Ag–Cu solid solutions formed by ion-beam mixing. *Appl. Phys. Lett.* **36**, 823–826 (1980).
41. Hori, Y., Takahashi, I., Koga, O. & Hoshi, N. Selective Formation of C2 Compounds from Electrochemical Reduction of CO<sub>2</sub> at a Series of Copper Single Crystal Electrodes. *J. Phys. Chem. B* **106**, 15–17 (2002).
42. Hori, Y., Takahashi, I., Koga, O. & Hoshi, N. Electrochemical reduction of carbon dioxide at various series of copper single crystal electrodes. *J. Mol. Catal. Chem.* **199**, 39–47 (2003).
43. Wu, Z.-Z. *et al.* Identification of Cu(100)/Cu(111) Interfaces as Superior Active Sites for CO Dimerization During CO<sub>2</sub> Electroreduction. *J. Am. Chem. Soc.* **144**, 259–269 (2022).
44. Salehi-Khojin, A. *et al.* Nanoparticle Silver Catalysts That Show Enhanced Activity for Carbon Dioxide Electrolysis. *J. Phys. Chem. C* **117**, 1627–1632 (2013).
45. Wang, L. *et al.* Selective reduction of CO to acetaldehyde with CuAg electrocatalysts. *Proc. Natl. Acad. Sci.* **117**, 12572–12575 (2020).
46. Progress and Perspectives of Electrochemical CO<sub>2</sub> Reduction on Copper in Aqueous Electrolyte | Chemical Reviews. <https://pubs.acs.org/doi/10.1021/acs.chemrev.8b00705>.

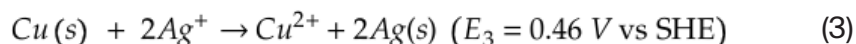
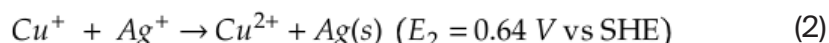
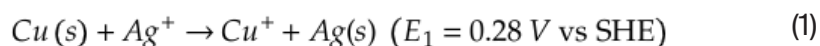
47. Iyengar, P., Kolb, M. J., Pankhurst, J. R., Calle-Vallejo, F. & Buonsanti, R. Elucidating the Facet-Dependent Selectivity for CO<sub>2</sub> Electroreduction to Ethanol of Cu–Ag Tandem Catalysts. *ACS Catal.* **11**, 4456–4463 (2021).
48. Iyengar, P., Kolb, M. J., Pankhurst, J., Calle-Vallejo, F. & Buonsanti, R. Theory-Guided Enhancement of CO<sub>2</sub> Reduction to Ethanol on Ag–Cu Tandem Catalysts via Particle-Size Effects. *ACS Catal.* **11**, 13330–13336 (2021).
49. Yu, J. *et al.* Recent Progresses in Electrochemical Carbon Dioxide Reduction on Copper-Based Catalysts toward Multicarbon Products. *Adv. Funct. Mater.* **31**, 2102151 (2021).
50. Nørskov, J. K., Bligaard, T., Rossmeisl, J. & Christensen, C. H. Towards the computational design of solid catalysts. *Nat. Chem.* **1**, 37–46 (2009).
51. Zhou, Y. *et al.* Dopant-induced electron localization drives CO<sub>2</sub> reduction to C<sub>2</sub> hydrocarbons. *Nat. Chem.* **10**, 974–980 (2018).
52. Lum, Y. & Ager, J. W. Sequential catalysis controls selectivity in electrochemical CO<sub>2</sub> reduction on Cu. *Energy Environ. Sci.* **11**, 2935–2944 (2018).
53. Subramanian, P. R. & Laughlin, D. E. Cu-Pd (Copper-Palladium). *J. Phase Equilibria* **12**, 231–243 (1991).
54. Bagger, A., Ju, W., Varela, A. S., Strasser, P. & Rossmeisl, J. Electrochemical CO<sub>2</sub> Reduction: A Classification Problem. *ChemPhysChem* **18**, 3266–3273 (2017).
55. Clausen, C. M., Pedersen, J. K., Batchelor, T. A. A. & Rossmeisl, J. Lattice distortion releasing local surface strain on high-entropy alloys. *Nano Res.* **15**, 4775–4779 (2022).
56. Mortensen, J. J., Hansen, L. B. & Jacobsen, K. W. Real-space grid implementation of the projector augmented wave method. *Phys. Rev. B* **71**, 035109 (2005).
57. Enkovaara, J. *et al.* Electronic structure calculations with GPAW: a real-space implementation of the projector augmented-wave method. *J. Phys. Condens. Matter* **22**, 253202 (2010).
58. Larsen, A. H. *et al.* The atomic simulation environment—a Python library for working with atoms. *J. Phys. Condens. Matter* **29**, 273002 (2017).
59. Hammer, B., Hansen, L. B. & Nørskov, J. K. Improved adsorption energetics within density-functional theory using revised Perdew-Burke-Ernzerhof functionals. *Phys. Rev. B* **59**, 7413–7421 (1999).

## 5.6. Supporting Information

Note S1. Thermodynamic and kinetic considerations of the conventional and non-equilibrium synthesis.

In order to understand the reaction kinetics of the Cu-Ag non-equilibrium system, we will begin to describe the thermodynamics of the conventional approach in which the seeds (in our case anisotropic Cu NPs,

**Figure S1**) are fully dispersed in the reaction medium. In its simplest form, three redox reaction can take place in the Cu-Ag system:



For all three reactions the overall cell potential is positive and, following the Nernst equation, the change in Gibbs free energy negative. Therefore, each reaction can take place spontaneously. The thermodynamic driving force follows the series (3)>(2)>(1). Since reaction (2) is dependent on reaction (1), only reaction (1) and (3) can take place in the initial stages of the reaction. From a thermodynamic standpoint, reaction (3) should dominate the overall galvanic replacement. However, since this reaction requires the participation of two Ag<sup>+</sup> ions, a significant kinetic barrier

exists and, therefore, the oxidation of Cu to Cu<sup>+</sup> dominates for low relative Ag salt concentrations. Interestingly, the further oxidation of Cu<sup>+</sup> to Cu<sup>2+</sup> and simultaneous reduction of Ag<sup>+</sup> to Ag(s) is strongly energetically favorable (~62 kJ/mol). Therefore, upon the formation of Cu<sup>+</sup> ions and given that enough Ag<sup>+</sup> ions are present for the reaction to proceed, the exchange should actually accelerate upon the occurrence of reaction (1). Further, with increasing Ag salt concentration, direct oxidation of Cu to Cu<sup>2+</sup> becomes more and more likely resulting in simultaneous

deposition of two Ag atoms per exchange reaction. Both effects, the acceleration of the reaction upon  $\text{Cu}^+$  formation as well as the 2:1 Ag:Cu stoichiometry in the two-electron oxidation, suggest a strong galvanic tendency towards the progressive

local deposition of Ag over its homogeneous distribution throughout the particle surface.

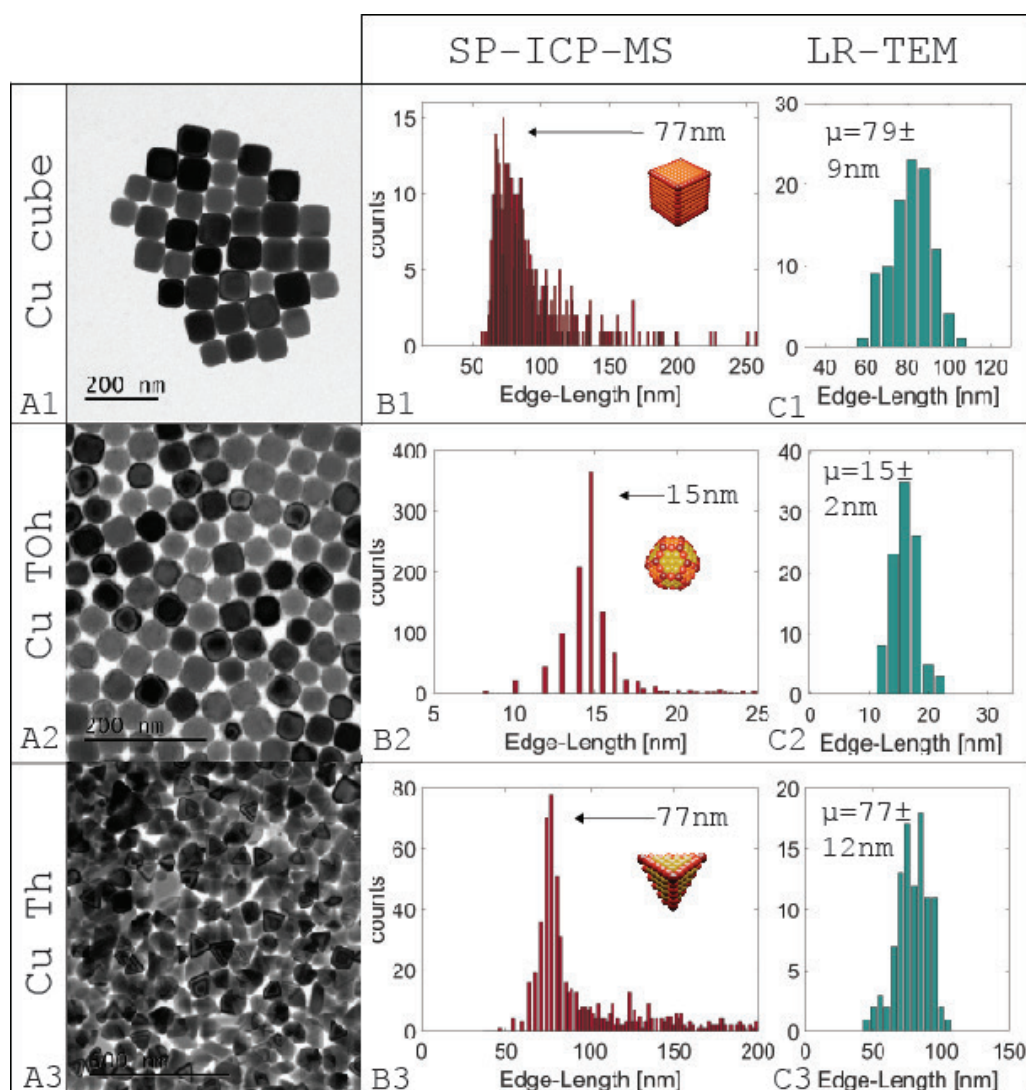


**Figure S1.** Synthesis of the anisotropic Cu seeds according to the protocol published in Ref. <sup>1</sup>. SP-ICP-MS measurements with up to 1100 particles counted show matching edge-lengths, i.e., the corner-to-corner distance, determined using the geometrical fitting in **Note 8** (and as indicated by the deep-red colored atoms in the ball models), with bright-field TEM micrograph particle counting ensuring ensemble size and shape homogeneity. Figure reprinted with permission from Ref. <sup>1</sup>

Let us now consider a cubic Cu NP (fcc) consisting of six faces, 12 edges and eight vertices (**Figure S2**). The coordination number for atoms of given spatial configuration is respectively eight, five and three. Therefore, the oxidizability (the ease at which a Cu atom oxidizes) becomes more energetically favorable for corners, followed by edges and finally facets due to the increased surface energy of undercoordinated surface species. Therefore, a preferentiality should exist for the galvanic exchange to take place at the particle edges and corners over the

faces. Beyond the coordination number, the higher degree of freedom by which an  $\text{Ag}^+$  ion may approach the Cu lattice at the edges and corners further suggest exchange to preferentially take place at the low coordination number atoms. Following the previous thermodynamic and kinetic considerations, and considering the positive interfacial energy of Cu-Ag surfaces<sup>2</sup>, we conclude that the formation of phase-segregated domains at the particle edges and or corners construes the thermodynamic product.

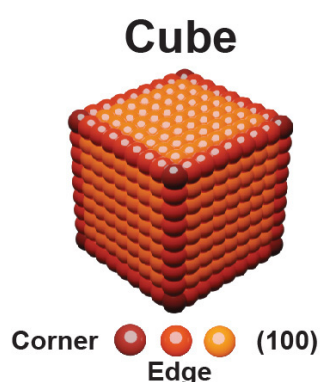


**Figure S2.** Ball model of the Cu cube with in brown red the corner atoms, red the edge atoms and orange the (100) facets.

Indeed, when the  $\text{AgNO}_3$  is fixed at  $\sim 0.6$  mM, and the Cu NPs are fully dispersed in the reaction mixture, heterostructures can be observed independently of the reaction time with strong preferential growth for edges/corners (**Figure S3A-C**). Further, the average domain size increases with the reaction time indicating that growth of individual domains is favored over the nucleation of a new domain, which agrees with Gibbs free energy consideration. The

phase-segregated nature of the bimetallic anisotropic Cu-Ag NPs and the preferential domain growth at particle edges and corners is further confirmed by STEM-EDX spectroscopy (**Figure S3D**). It is interesting to note that already after 5 min of reaction, a green color in the reaction mixture could be observed indicating the presence of  $\text{Cu}^{2+}$  ions.

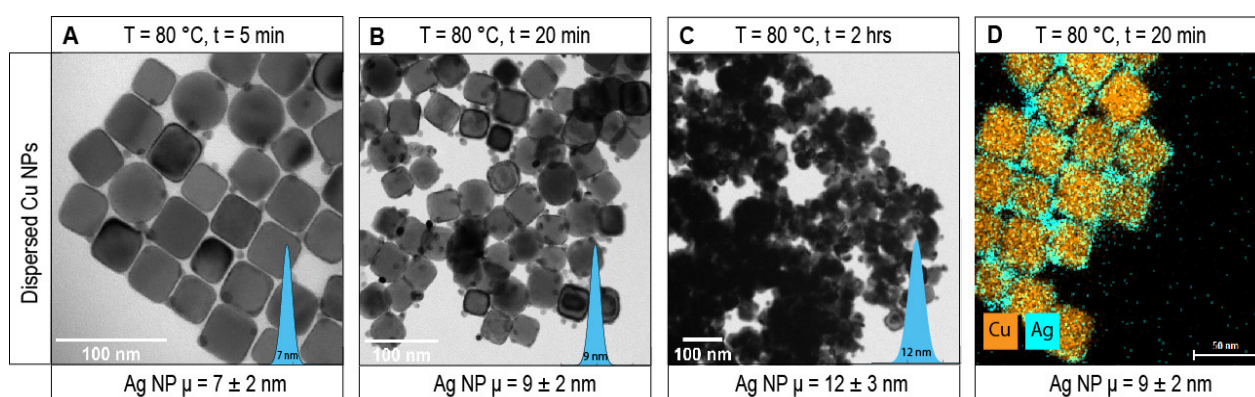


**Figure S3.** Conventional galvanic exchange reaction of C-Cu NPs (4 mg) using a 0.333 mg/mL  $\text{AgNO}_3$  in OAm precursor solution (final  $\text{AgNO}_3$  concentration  $\sim 0.6$  mM, Cu:Ag 21:1) prepared by dissolving the Ag salt at 50 °C. (**A-C**) Phase-segregated Ag domains grow with increased reaction time (blue inset shows the gaussian fit of the size distribution of 100 unique particles counted with the mean shifting to the right with increasing reaction time). (**D**) STEM-EDXS elemental map shows Ag domains (turquoise) preferentially situated at particle edges and corners.

As we can explain the reaction behavior of the thermodynamic product, we now know that in order to obtain kinetic control, it is required to suppress reaction (2) and (3). In this way, exchange may only occur in equimolar ratios. Other than the undercoordinated sites, no facet atom shows any preferentiality towards exchange, and as such, replacement becomes a random event. While it might be possible to achieve this by reducing the bulk Ag salt concentration further, a much more elegant approach would be to reduce the local Ag salt concentration as in that way, the complete composition range of the Cu-Ag system could still be probed. As mentioned in the main text, this was achieved by means of a thin film reaction and independently of the reaction time and at equally high Ag:Cu ratios, the formation of heterostructures could be excluded (**Figure S4**). After 20 min at 80 °C and high relative Ag loading, a distinct contrast difference can be noticed at the particle edges associated with the stronger diffracting Ag phase absent for the random NSA in the main text produced at low relative Ag loading (**Figure S4B**, **Figure S4A** and **Figure 2**). This is likewise reflected in the three-fold higher bulk Ag composition (9 at.% Ag). When looking at the STEM-EDXS elemental map of this system, it is clear that while some particles have

retained a homogeneous Ag distribution, others are partially overgrown by Ag (**Figure S4E**). This is in excellent agreement with observation for Ag sputtered bulk Cu(100) surfaces.<sup>3</sup> Upon extension of the Ag surface composition, beyond a certain coverage, strain built up in the lattice cannot sustain additional Ag adatoms, and island formation ensues. This is practically the highest Ag loading we could achieve in which the cubic shape was retained. If we extend the reaction further (two hours), deformation ensured matching the observation in the conventional synthesis (**Figure S4C**, **Figure S3C**). Finally, by enlarging the Ag to Cu ratio and further extension of the reaction time (24 hrs) a near-complete-exchange (Ag content >97%) could be achieved as well where spherical hollow structures ensured typical of the galvanic replacement reaction (**Figure S4D**).<sup>4</sup> Deposition of inert Ag at the particle edges in combination with a continuous stream of Cu ions originating from the center of the particles can explain its morphology. Modulation of the Ag<sup>+</sup> flux provides exquisite control over the Cu-Ag system.

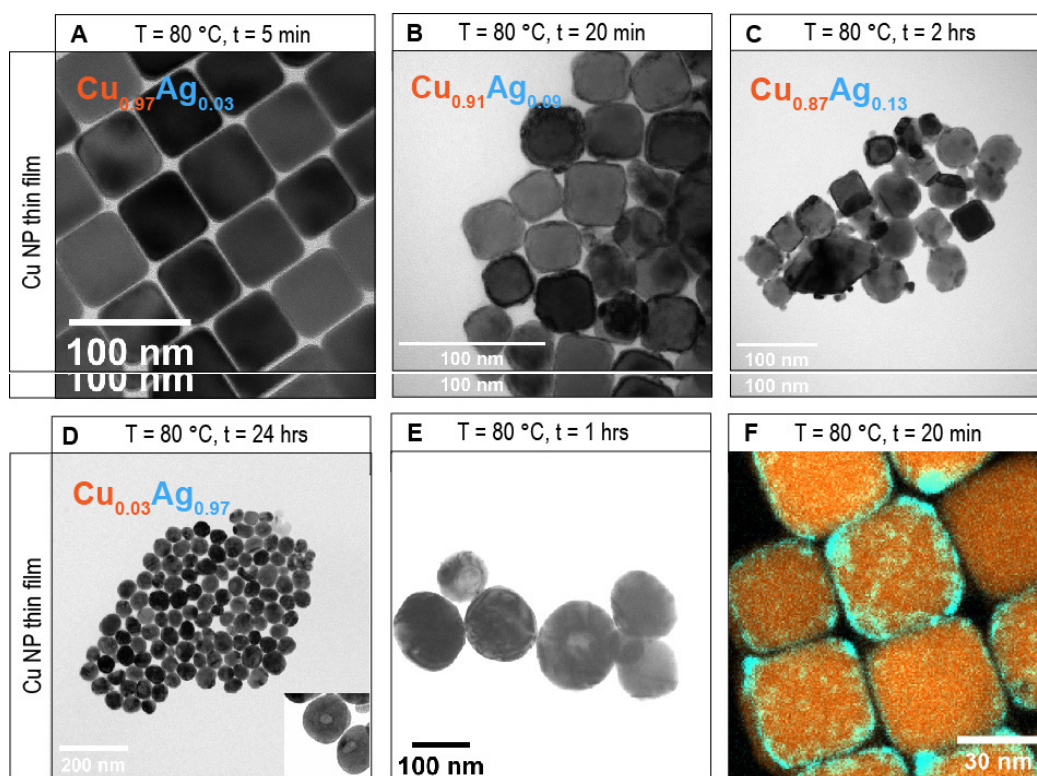


**Figure 4.** Non-equilibrium synthesis with C-Cu NP seeds. (A-C) Time evolution of the non-equilibrium synthesis where a C-Cu NPs thin film (4 mg) was exposed to a  $\sim 0.6$  mM  $\text{AgNO}_3$  in OAm precursor solution (Cu:Ag 21:1) and reacted for 5, 20 min and 2 hrs at 80 °C. (D) The non-equilibrium synthesis at high Ag:Cu ratio (3:1) for 24 hrs. The inset of the near-to-complete exchanged particle shows a hollow structure typical of the galvanic replacement reaction.<sup>4</sup> (E) The accelerated non-equilibrium synthesis at further increased Ag:Cu ratio (8:1) shows the same morphology as in (D) already after 1 hrs. TEM image depicted at high contrast and high brightness show the hollow nature. (F) STEM-EDXS elemental map of the 20 min reacted C-Cu-Ag NSA shows a homogeneous distribution of the Ag elements with patches of Ag observable for some particles. Limiting the Ag:Cu ratio and reaction time is adamant to ensure the formation of a random alloy for all particles.



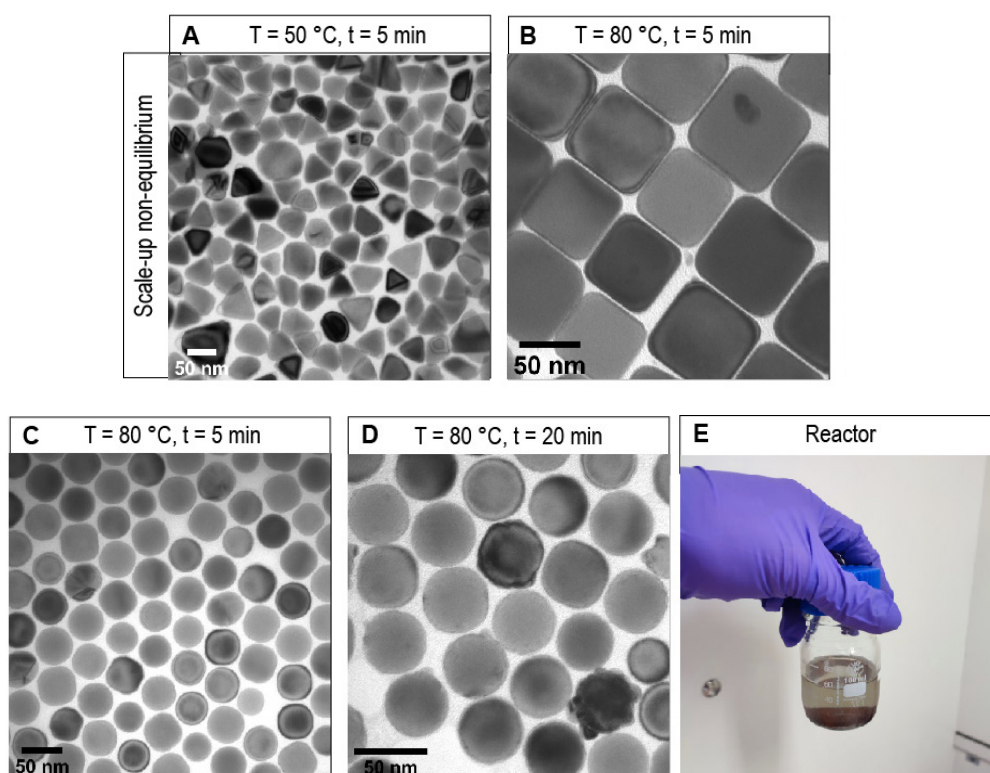


**Figure S5.** Overview of the 12.5-fold scaled-up non-equilibrium synthesis reaction. (A-D) TEM images of the synthesis products. (A) Tetrahedral Cu-Ag NSAs, (B) Cubic Cu-Ag NSAs, (C) Spherical Cu-Ag NSAs, (D) Spherical Cu-Ag NSAs with 4-fold higher Ag content, (E) Up-scaled reaction.

Reaction	E [V]	$\Delta G$ [kJ mol <sup>-1</sup> ]	$K_{\text{eq}}$
1	0.28	-26.98	9.82E+03
2	0.64	-61.81	1.40E+09
3	0.46	-89.27	1.62E+13

**Table S1.** Thermodynamics of the redox reactions of Cu and Ag indicated in the above and in the main text.  $\Delta G = -nFE$ , with  $n$  the number of electrons transferred,  $E$  the cell voltage, and  $F$  Faraday's constant.  $\Delta G = RT \ln K$  with  $R$  the gas constant,  $T$  the temperature and  $K$  the equilibrium constant.

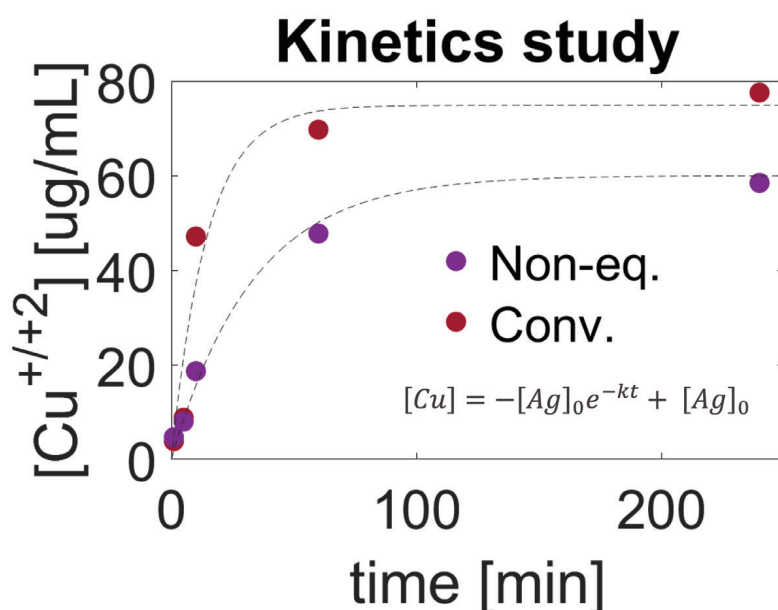


**Figure S6.** Kinetic study of the galvanic exchange rate of the conventional and the non-equilibrium synthesis in red and purple, respectively. The Cu concentration in the electrolyte was monitored using ICP-OES. Dashed-curves indicate the fitted curves according to the equation in the inset, conveying the first order rate law in which  $[Ag]_0$  denotes the  $Ag^+$  concentration at  $t=0$ ,  $t$  the time in minutes, and  $k$  the rate constant. The Cu concentration is first order dependent on the concentration of the reactant  $AgNO_3$  for both the conventional and the non-equilibrium synthesis, with  $R^2 = 0.916$  and  $0.989$  and  $k = 0.068$  and  $0.030$   $[min^{-1}]$ , respectively. The goodness of the fit excludes reaction 3 (which is second order to the concentration of Ag) from the non-equilibrium reaction. The factor 2.3 larger rate for the conventional reaction stems from a minor contribution of reaction 2 and 3 to the overall rate. Even though reaction 2 is second order dependent on both  $Cu^+$  and  $Ag^+$ , the much lower thermodynamic equilibrium constant of reaction 1 vs reaction 2 ( $9.8 \cdot 10^3$  vs  $1.4 \cdot 10^9$ , respectively, see **Table S1**) suggests reaction 1 is rate limiting and the overall rate should therefore be dominated by reaction 1 and be first order as well.

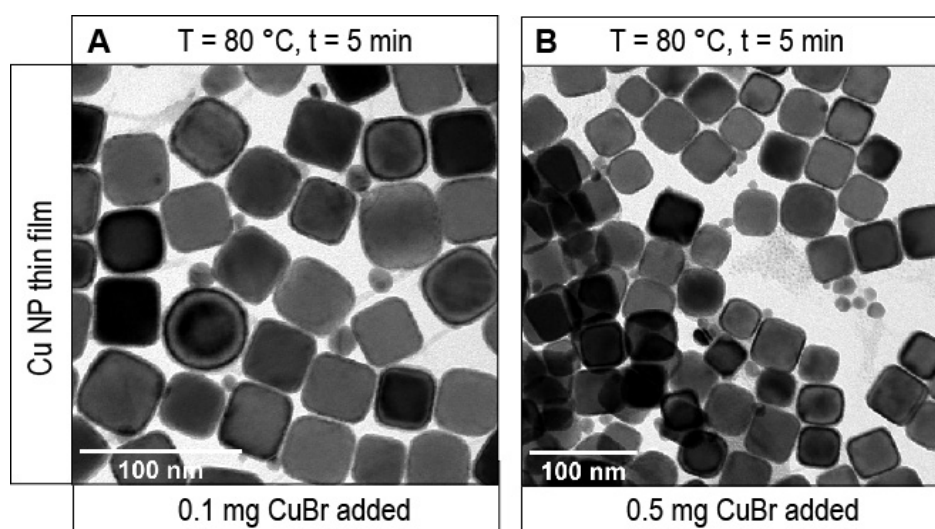


**Figure S7.** (A) BF-TEM image of the non-equilibrium synthesis of C-Cu NP in the presence of  $0.14$  mM  $Cu^+$  ions yielding a phase-segregated material with individual Ag domains. (B) BF-TEM image of the on-equilibrium synthesis of C-Cu NP in the presence of  $0.7$  mM  $Cu^+$  ions resulting in homogeneous nucleation of Ag NPs.

## Note S2. Determination of the surface composition of anisotropic CuAg NSAs.

In order to determine the Ag overlayer and surface composition of the NSAs, fitting of the Cu-Ag elemental distributions is required. First, the Cu atom distribution was converted in a surface atom distribution by using a geometrical model (**Appendix S5**). For this, an outermost shell of Cu atoms was defined of the anisotropic particles consisting of the 1<sup>st</sup> and up to the 6<sup>th</sup> monolayer (ML). Both Cu (1<sup>st</sup> and 6<sup>th</sup> ML) and Ag distributions for C-, Th- and TOh-CuAg

NSA were fitted with a lognormal distribution (**Figure S5**). Further, the probability density functions were normalized to account for the difference in events. Finally, the area under the curve was determined by numerical integration of the probability density function and evaluation at a relevant interval. The surface composition is then defined as the ratio of Ag area: Cu area.

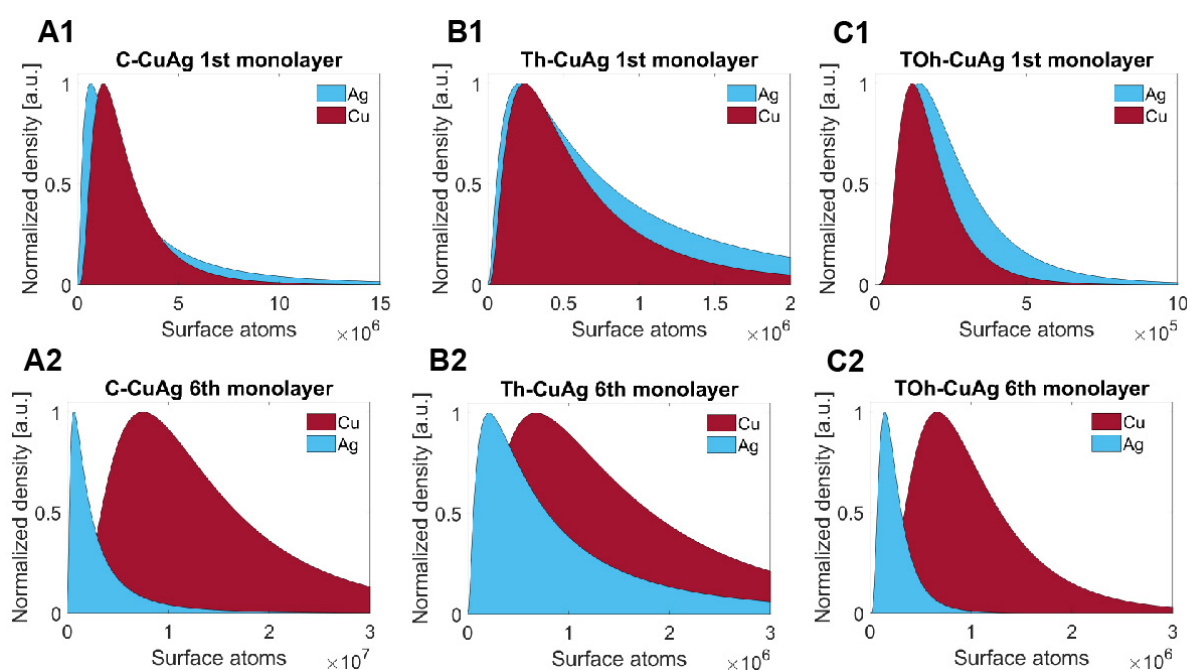


**Figure S8.** Determination of the Ag overlayer and surface composition of anisotropic Cu-Ag NSA. (A1, A2) C-Cu-Ag NSA fitted elemental distributions based on the 1<sup>st</sup> and 6<sup>th</sup> ML of Cu. (B1,B2) Th-CuAg NSA fitted elemental distributions based on the 1<sup>st</sup> and 6<sup>th</sup> ML of Cu. (C1,C2) TOh-Cu-Ag NSA fitted elemental distributions based on the 1<sup>st</sup> and 6<sup>th</sup> ML of Cu.

	Ag overlayer (1 <sup>st</sup> ML)	Surface composition (6 <sup>th</sup> ML)
C-Cu <sub>0.97</sub> Ag <sub>0.03</sub> NSA	1.15 ML	Cu <sub>78.7</sub> Ag <sub>21.3</sub>
Th-Cu <sub>0.97</sub> Ag <sub>0.03</sub> NSA	1.43 ML	Cu <sub>44.3</sub> Ag <sub>55.7</sub>
TOh-Cu <sub>0.97</sub> Ag <sub>0.03</sub> NSA	1.46 ML	Cu <sub>64.0</sub> Ag <sub>26.0</sub>

**Table S2.** Ag overlayer and surface composition of the Cu-Ag NSAs extracted from the fitting.

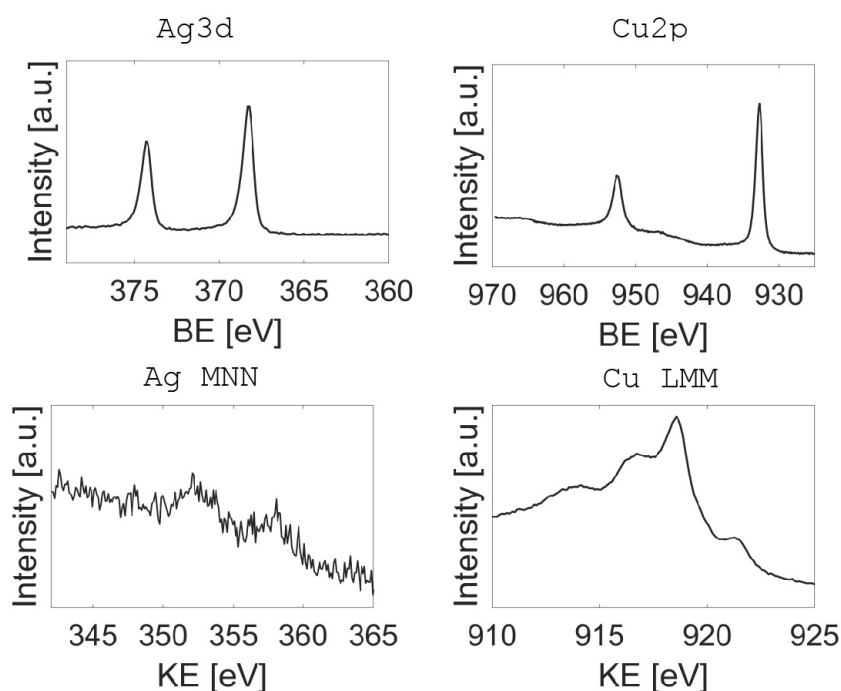


**Figure S9.** Example of XPS and Auger spectra of the C-Cu-Ag NSAs (C-Cu<sub>0.97</sub>Ag<sub>0.03</sub>) used to determine the surface composition and depth of information in **Table S1**.

	Reaction time	Surface composition	Number of Ag atoms	Number of Cu atoms at Xth ML	Ag/Cu
C-Cu <sub>0.97</sub> Ag <sub>0.03</sub> NSA	5 min	Cu <sub>0.91</sub> Ag <sub>0.09</sub>	677,441	(11 <sup>th</sup> ) 7,644,848	0.09
C-Cu <sub>0.99</sub> Ag <sub>0.01</sub> NSA	1 min	Cu <sub>0.95</sub> Ag <sub>0.05</sub>	752,647	(22 <sup>nd</sup> ) 14,356,096	0.05

**Table S3.** Calculation of the penetration depth of Ag adatoms in the C-Cu-Ag NSA as based on XPS surface composition extracted from, e.g., **Figure S7** and the absolute number of Ag atoms of the most frequent peak in the Ag distribution of the C-Cu-Ag NSA obtained via SP-ICP-MS. A C-Cu NP of 100 nm was chosen as reference.

To determine the surface composition of the NSAs. It is mandatory to know the penetration depth of the Ag atoms into the Cu lattice, as through SP-ICP-MS only the absolute number of Ag atoms in the particle is known, not its internal distribution. For this we devised a microtomy based experiment in which C-Cu-Ag NSA were embedded in an epoxy resin, vacuum degassed, cured at 80 °C and sliced using a microtome at

40 nm thickness. Micron sized slices of 40 nm thick were then deposited on a Cu TEM grid with ultrathin carbon support. STEM imaging and EDXS were performed on Thermo Scientific Tecnai-Osiris and Titan-Themis microscopes, with the latter (aberration-corrected STEM) being used to determine the penetration depth of Ag (see **Figure 3** in the main text).

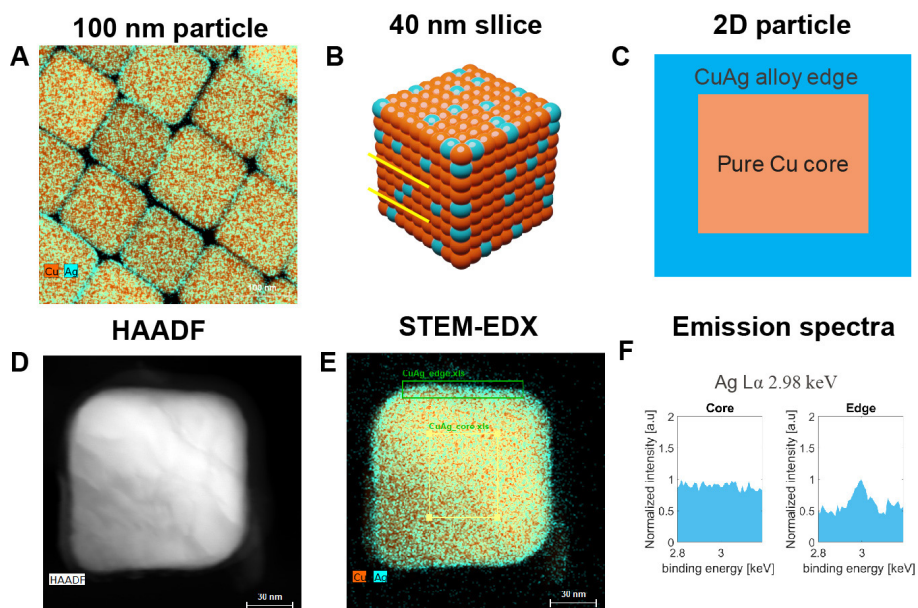


**Figure S10.** (A) EDXS elemental map of the C-Cu<sub>0.97</sub>Ag<sub>0.03</sub> NSA. Proposed microtome slice of the embedded particle cutting of the top and bottom face of the NP. The particle was embedded in a resin and sliced to a thickness of 40 nm using ultramicrotomy. (C) Schematic representation of the sliced composite NP. (D) STEM-HAADF image of a 40 nm microtomed slice and (E) corresponding EDXS elemental map of Cu and Ag. (F) Absence and presence of the characteristic Ag L<sub>α</sub> peak in the EDX spectra from core and edge.

### Note S3. Identical location TEM imaging of dewetting behavior of C-CuAg NSA.

Since we argue our surface alloys are a kinetic product, a small perturbation of the system may result in phase-segregation. To test this, we submitted the 20 min reacted C-Cu-Ag NSA (**Figure S9A**) to a step-wise temperature increase from room temperature to 400 °C under inert conditions (excluding contributions from oxidation) and observed the wetting behavior using identical location TEM (see **Materials and Methods** for details). TEM images acquired on identical locations showed that

already after 30 min at 300 °C, de-wetting of a stronger contrasting phase presented (most likely Ag, **Figure S9B**). Upon further raising of the temperature (400 °C), various particles fused (**Figure S9C**). By means of STEM-HAADF coupled with EDXS, we could confirm the segregating phase to consist of Ag (**Figure S9E-F**). The lower surface energy of Ag in comparison to Cu further corroborates Ag as the mobile phase.<sup>5</sup>

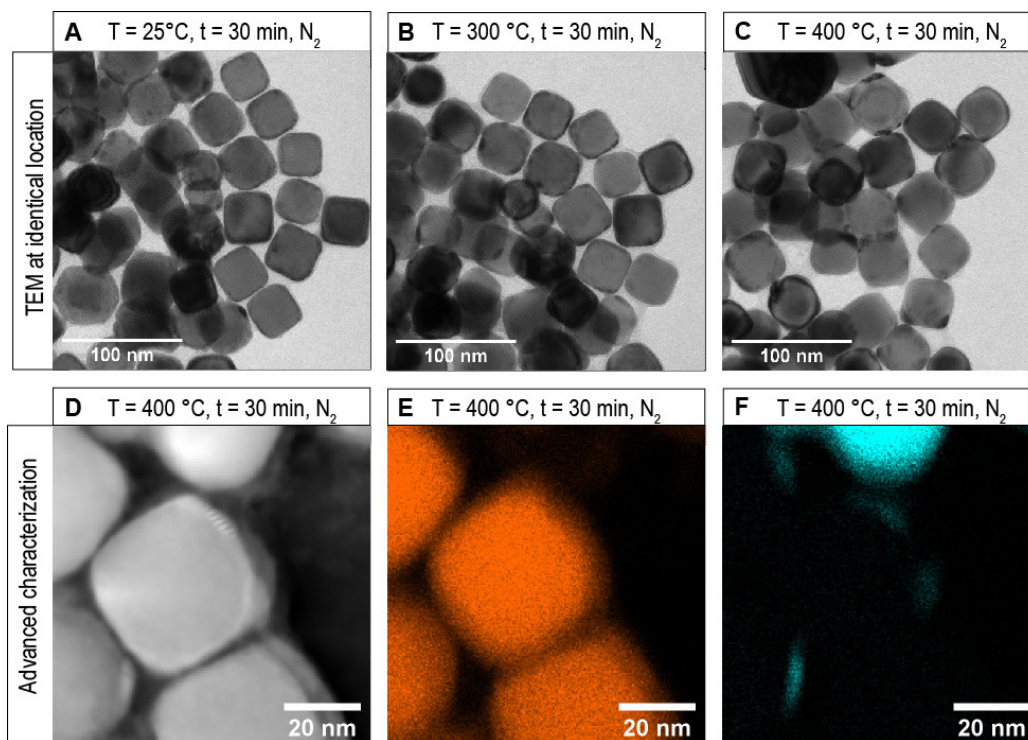


**Figure S11.** (A-C) TEM images of the C-Cu<sub>0.91</sub>Ag<sub>0.09</sub> NSA synthesized using a non-equilibrium synthesis as a function of temperature in an annealing experiment under inter conditions. (D) STEM-HAADF image showing the de-wetted nature of the particles with an Ag-rich region at the particle edge. (E-F) STEM-EDXS elemental map of Cu (in orange) and Ag (in turquoise) corroborating the phase-segregated nature of the thermally treated particles.

Finally, we devised a control experiment to corroborate our hypothesis that a low local Ag<sup>+</sup> concentration could explain the formation of our surface alloy. By artificially introducing Cu<sup>+</sup> ions in the non-equilibrium synthesis, offering a second route other than the galvanic replacement of the seed for the reduction of Ag<sup>+</sup>, we could convert the NSA into a phase-segregated material with individual Ag domains similar to the

thermodynamic product formed using the conventional synthesis (**Figure S10A**). Further, by enhancing the Cu<sup>+</sup> concentration five-fold, complete phase-separation could be induced as homogeneous nucleation of Ag particles followed corroborating the strong thermodynamic driving force of reaction (2) provided earlier (**Figure S10B**).

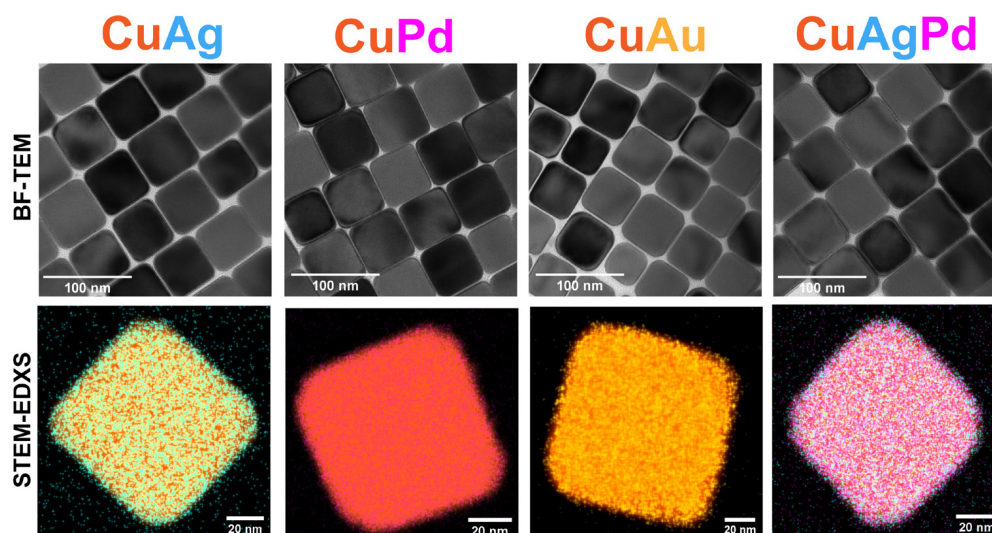


**Figure S12.** Cu-Ag, Cu-Pd, Cu-Au and Cu-Ag-Pd anisotropic multimetallic NSAs synthesized using the non-equilibrium synthesis.

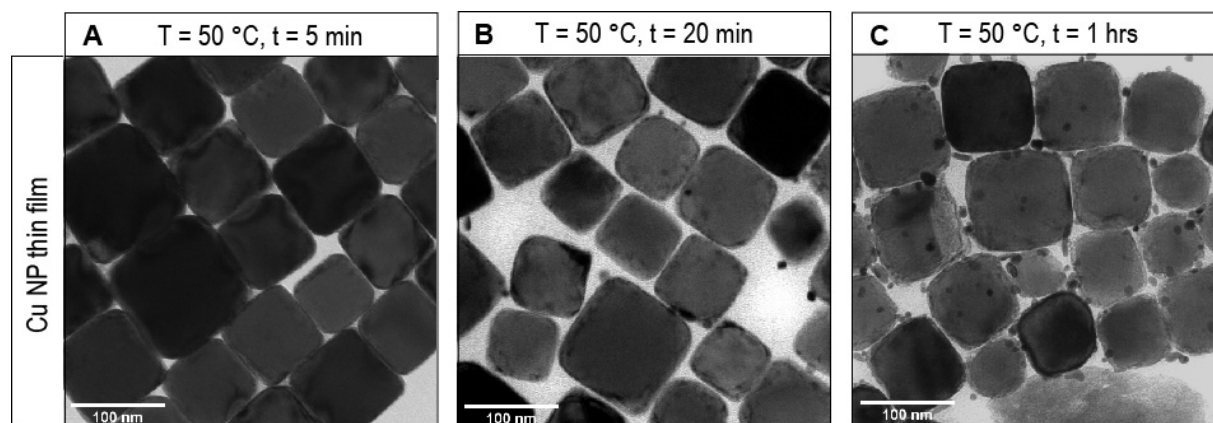


**Figure S13.** BF-TEM images of a morphology study as a function of reaction time of the Cu-Au system synthesized using the non-equilibrium synthesis.

## Note S4. Evaluation of the electrochemical performance in the CO<sub>2</sub>RR

### S4.1. Electrochemical measurements

The CO<sub>2</sub>RR performance of Cu-Ag NSAs were evaluated in a commercial gas-tight H-cell from Gaoss Union using constant potential mode controlled by a potentiostat (Autolab PGSTAT302N). All measurements were carried out in 0.1 M KHCO<sub>3</sub>, which fungated as both catholyte and electrolyte (25 mL per chamber). Chambers were kept separate by means of a cation exchange (i.e., Nafion) membrane. Prior to electrochemical testing, the electrolyte was saturated with CO<sub>2</sub> by bubbling at 25 mL·min<sup>-1</sup> for at least 15 min. Also, during any measurement, CO<sub>2</sub> was bubbled through the catholyte continuously to ensure sufficient CO<sub>2</sub> supply during the measurement. A Pt wire was used as counter electrode for the oxygen reduction

reaction. An Ag/AgCl electrode was used as reference. All measurements were carried out at -1.1 V vs RHE. The value of the potential versus Ag/AgCl was converted to the scale of the reversible hydrogen electrode (RHE) using the equation:  $E \text{ (versus RHE)} = E \text{ (versus Ag/AgCl (3 M KCl))} + 0.21 \text{ V} + 0.059 \cdot \text{pH}$ . The potential was mathematically compensated for the ohmic resistance that was determined by the electrochemical impedance spectroscopy (EIS). The FEs and currents were repeatedly measured on three individual electrodes for each material evaluated.

### S4.2. Collection of the liquid products

Collection of the liquid products was done at specific time intervals (i.e., 10 min) by means of a clean syringe operated through a septum as to minimize the introduction of

O<sub>2</sub> into the catholyte chamber and disturb the CO<sub>2</sub> to HCO<sub>3</sub><sup>-</sup> equilibrium. Aliquots of 800 μL were collected in all cases.



### S4.3. Quantification of the gas products

Gas products were analysed online (10 min interval) using a gas chromatography (GC, SRI Instrument 8610C) with the auto-sampling loop (1 mL) connected to CO<sub>2</sub> off-gas of the H-cell catholyte chamber. H<sub>2</sub> was

analysed using thermal conductive detector (TCD) and CO, CH<sub>4</sub>, and C<sub>2</sub>H<sub>4</sub> were analysed using flame ionization detector (FID) with a methanizer.

### S4.4 Quantification of the liquid products using NMR

Quantification of the liquid products was achieved according to a previously reported method.<sup>6</sup> In brief, the liquid products of all electrodes were quantified using nuclear magnetic resonance (NMR, Bruker 400 MHz AVIII HD). **Figure S15** shows a typical 1D <sup>1</sup>H NMR spectrum obtained for a standard solution containing typical liquid products from the CO<sub>2</sub>RR and the internal standards (phenol and DMSO) as indicated by the arrows. The peak area ratio of a given product to that of the internal standard, as

obtained by peak fitting using MestReNova software, was used to determine the concentration of the products. Identical NMR acquisition parameters were used for all measurements. In addition, the water peak was suppressed using the solvent suppression function. The acquisition time of d1 was 5 s and the number of scans was 260. Products with peaks with chemical shifts than larger water (> 5 ppm) were quantified using phenol, all others with DMSO.

### S4.5 Calculation of the faradaic efficiency

The faradaic efficiency (FE) was calculated for gas and liquid products, using  $FE = \frac{nFC_iV}{jRT}$  and  $FE = \frac{nFC_iV}{Q}$ , respectively, where  $n$  is the number of transferred electrons to produce one molecule of product  $i$ ,  $F$  is the faradaic constant,  $C_i$  is the concentration of the product as determined by GC or NMR,  $v$  is the flow rate of CO<sub>2</sub>,  $P$  and  $T$  are the pressure (101325 Pa) and temperature (22

°C) of the gas sampled by the GC sample loop, respectively,  $j$  is the total current when sampling,  $R$  is the gas constant,  $V$  is the volume of the electrolyte, and  $Q$  is the total charge transferred to produce the target product. FEs of the liquid products were quantified taking the change in volume of the electrolyte upon aliquot collection into account.

Note S5. Supporting figures, tables and miscellaneous for the performance testing in the CO<sub>2</sub>RR

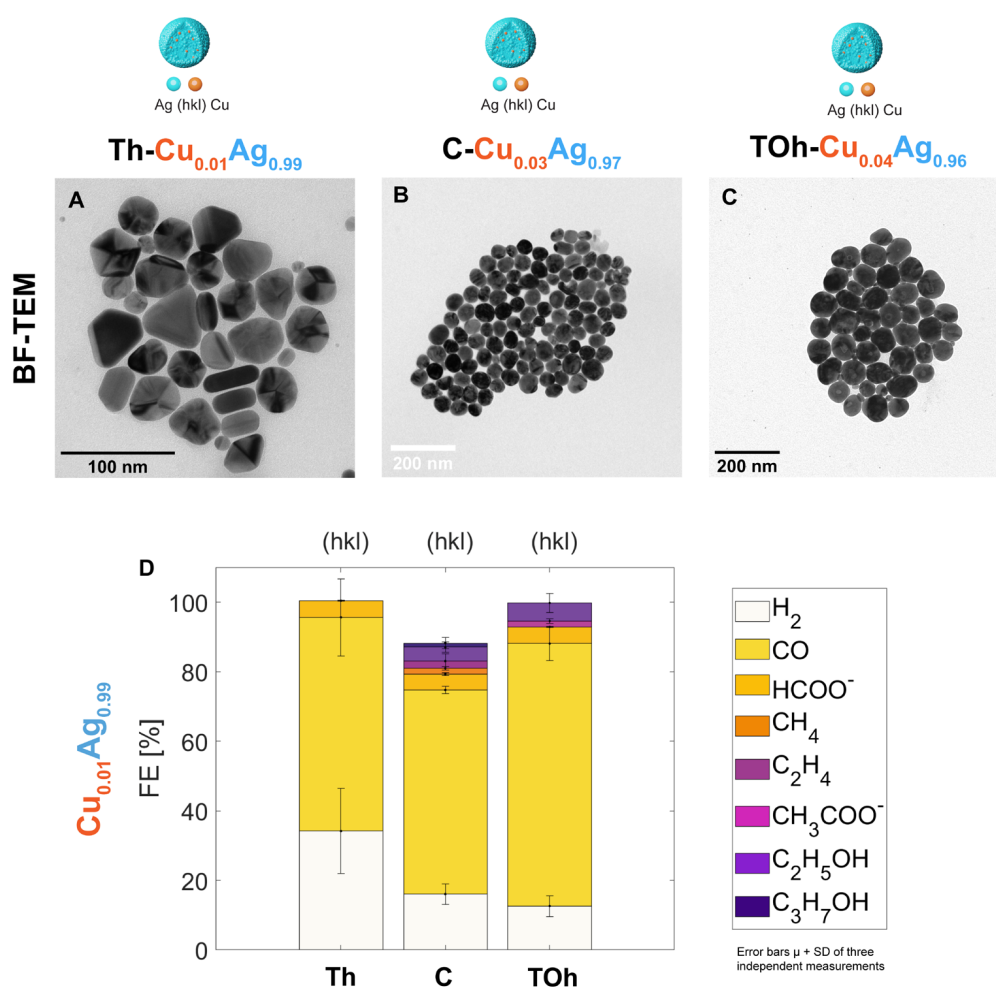


**Figure S14.** Near-to-complete-conversion of anisotropic Cu NCs in isotropic Ag NPs using the galvanic replacement reaction used as control experiment to confirm the catalytically active nature of galvanically deposited Ag. (A-C) Brightfield TEM images in which Th-, C- and TOh-Cu NCs thin films (4 mg) were exposed to a ~38 mM AgNO<sub>3</sub> in OAm precursor solution (Cu:Ag 1:3) and reacted for 24 hrs at 50, 80 and 80 °C, respectively. Ball model denotes the isotropic/undefined shape of the Ag NPs produced with the extended non-equilibrium synthesis. Bulk composition provided in the title as determined by ICP-OES. (D) Electrocatalytic screening of the as-synthesized isotropic Cu-Ag NPs, error bars represent the standard deviation of three independent measurements Control experiment showing the CO evolving nature of >95 at.% Ag NPs produced with the non-equilibrium synthesis confirming the activity of galvanically deposited Ag.

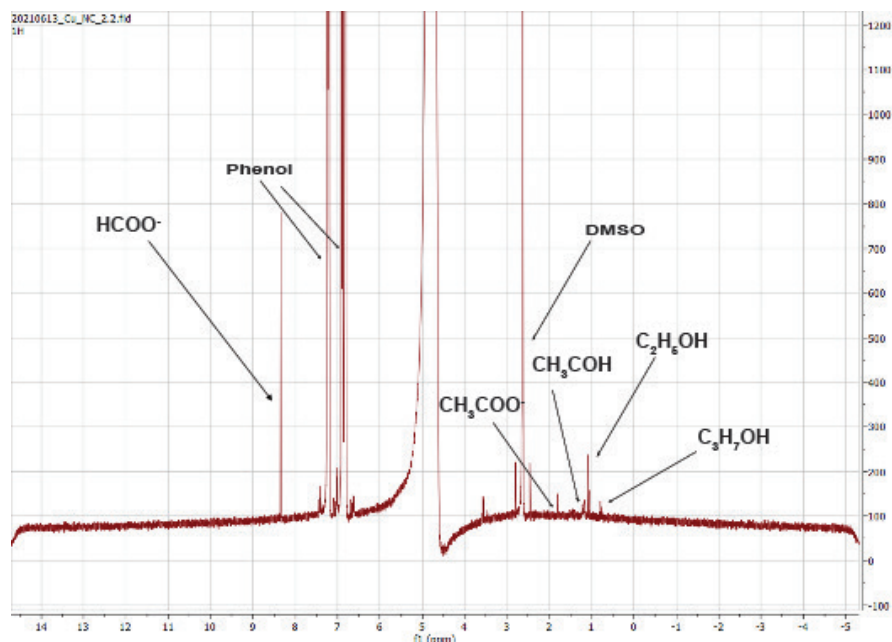


**Figure S15.** Representative NMR spectra obtained for a given electrolyte aliquot. Spectra obtained by averaging over at least 260 individual scans for signal-to-noise enhancement.

	H <sub>2</sub>	CO	HCOO <sup>-</sup>	CH <sub>4</sub>	C <sub>2</sub> H <sub>4</sub>	CH <sub>3</sub> COO <sup>-</sup>	CH <sub>3</sub> CHO	C <sub>2</sub> H <sub>5</sub> OH	C <sub>3</sub> H <sub>7</sub> OH
<b>Th-Cu NCs</b>	46.87	4.31	6.10	29.35	11.59	0.00	0.00	3.72	0.00
$\sigma$	1.95	3.73	2.19	6.12	5.45	0.00	0.00	1.13	0.00
<b>C-Cu NCs</b>	27.61	2.50	11.19	11.36	31.44	4.40	0.00	5.65	2.05
$\sigma$	1.66	0.72	0.86	1.75	1.24	2.83	0.00	2.24	1.46
<b>TOh-Cu NCs</b>	24.57	3.40	9.88	15.62	26.11	3.15	0.00	8.32	2.89
$\sigma$	0.65	0.67	1.45	1.65	0.95	1.87	0.00	1.57	0.82
<b>Th-Cu-Ag NSA</b>	34.34	8.05	13.85	7.59	17.78	3.18	9.12	9.71	0.00
$\sigma$	8.60	1.57	3.25	2.26	6.48	2.28	1.97	0.78	0.00
<b>C-Cu-Ag NSA</b>	25.26	3.98	8.73	8.03	28.22	1.21	6.52	16.13	5.81
$\sigma$	1.81	0.80	1.81	1.55	0.60	0.19	1.45	0.93	0.84
<b>TOh-Cu-Ag NSA</b>	28.53	3.52	5.82	8.46	21.80	1.74	8.81	16.29	8.76
$\sigma$	0.65	0.67	1.45	1.65	0.95	1.87	1.44	1.57	0.82
<b>Th-Ag-Cu NP</b>	34.17	61.48	4.77	0.00	0.00	0.00	0.00	0.00	0.00
$\sigma$	12.25	11.08	0.10	0.00	0.00	0.00	0.00	0.00	0.00
<b>C-Ag-Cu NP</b>	16.05	58.72	4.56	1.69	2.04	0.00	0.00	4.00	1.15
$\sigma$	2.97	1.03	0.41	0.51	2.11	0.00	0.00	1.46	1.63
<b>TOh-Ag-Cu NP</b>	12.62	75.49	4.77	0.00	0.00	1.70	0.00	5.19	0.00
$\sigma$	3.00	4.90	0.10	0.00	0.00	0.68	0.00	2.76	0.00

**Table S4.** FEs of the gaseous and liquid products of the CO<sub>2</sub>RR measured based on GC and NMR (see **Note S4**)<sup>6</sup> after 10 min at -1.1 V vs RHE in 0.1 M KHCO<sub>3</sub>. The electrolyte was saturated with CO<sub>2</sub> by bubbling at 25 ml·min<sup>-1</sup> for at least 15 min before starting the reaction and was continued during the reaction. Reported FEs are the average of three independent measurements reported with their associated standard deviations ( $\sigma$ ) corresponding to the error bars in **Figure 4** in the main text.

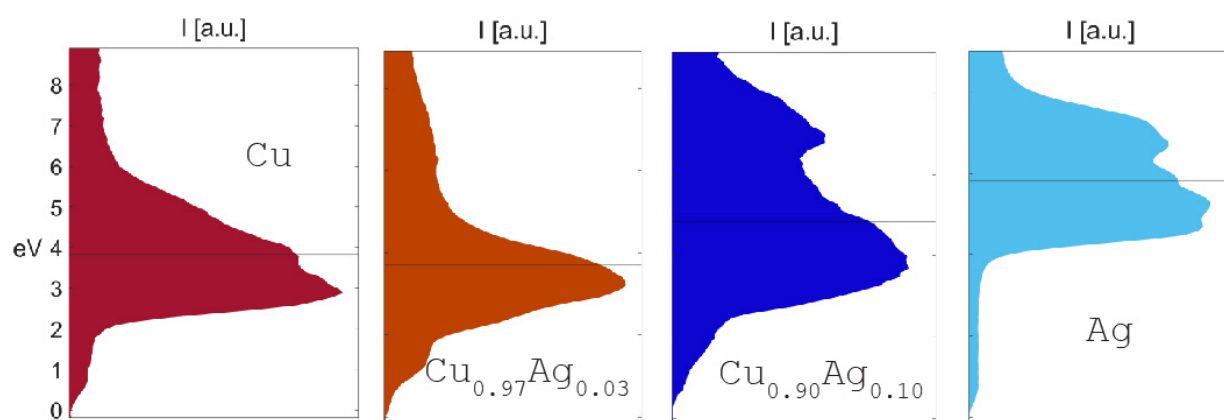


**Figure S16.** XPS valence band spectra of the as synthesized Th-Cu-Ag NSAs and pure Cu and Ag references. A Th-Cu NP thin film (4 mg) was exposed to a  $\sim 0.6$  mM  $\text{AgNO}_3$  in OAm precursor solution (Cu:Ag 21:1) and reacted for 1 and 5 min at  $50^\circ\text{C}$ , respectively. Solid black line indicates the point-of-gravity of the valence band as determined by numerical integration with the upper bound fixed at 9 eV indicating a shift towards the Fermi level for the 1 min reacted NSA corroborating its random alloy nature.

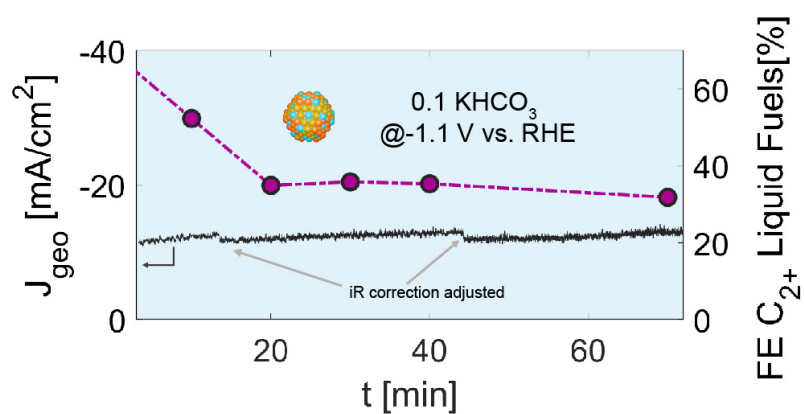


**Figure S17.** Stability test of the TOh-Cu<sub>0.97</sub>Ag<sub>0.03</sub> in CO<sub>2</sub> saturated 0.1 M KHCO<sub>3</sub> with respect to the C<sub>2+</sub> liquid fuels. Increasing current density can be assigned to the enhancement in HER.

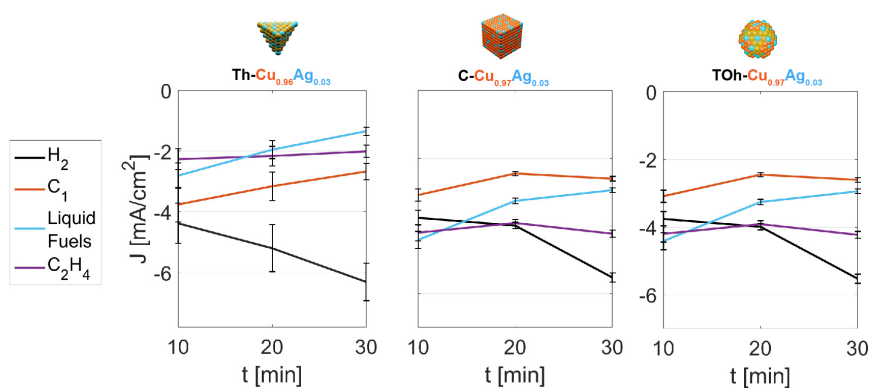


**Figure S18.** Evolution of the geometrical partial current densities of the anisotropic Cu-Ag NSAs upon applied potential (-1.1 V vs RHE) in CO<sub>2</sub> saturated 0.1 M KHCO<sub>3</sub>.

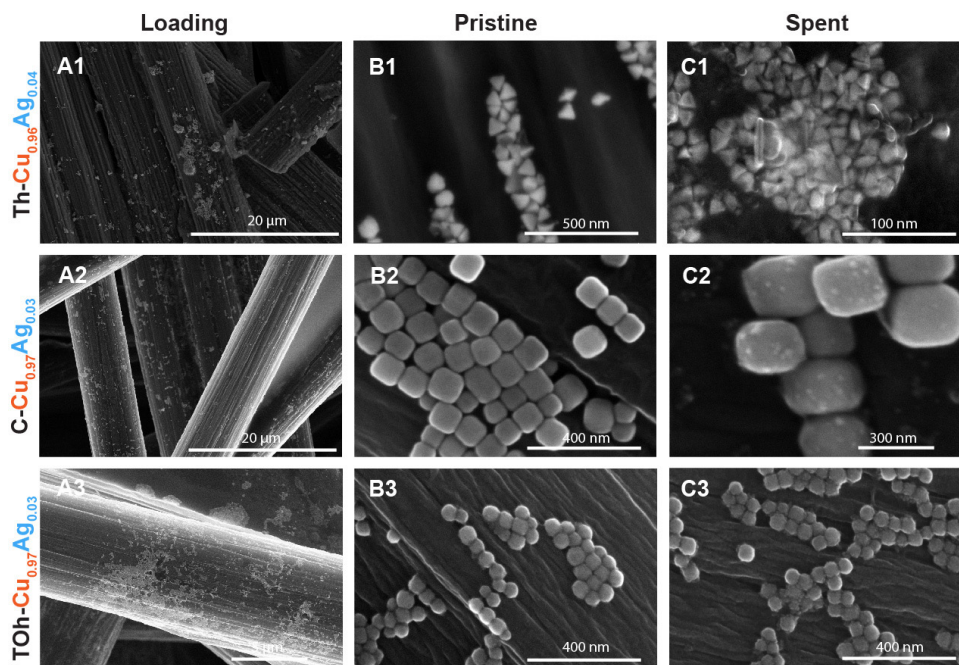


**Figure S19.** (A1-A3) SEM images showing the as synthesized Th-, C- and TOh-Cu-Ag NSAs on carbon paper support ( $1.0 \text{ mg}\cdot\text{cm}^{-2}$ ) indicating good coverage of the NCs. (B1-B3) SEM images of the as-deposited Th-, C- and TOh-Cu-Ag NSAs on carbon paper support showing the pristine, smooth nature of the NC surfaces. (C1-C3) SEM images of the Th-, C- and TOh-Cu-Ag NSAs after 30 min of  $\text{CO}_2\text{RR}$  showing a roughened surface and extrusions at the particle surface indicating phase segregation.

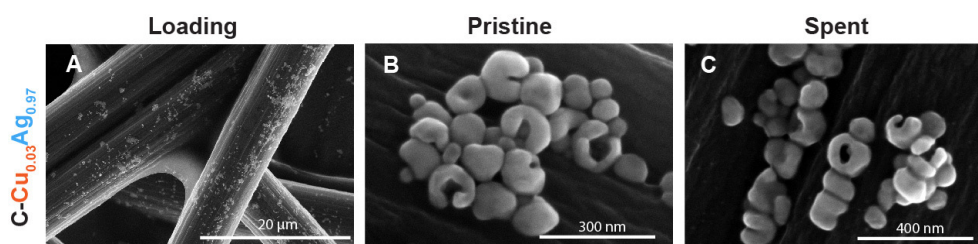


**Figure S20.** (A) SEM images of the loading studies of the drop-casted near-to-complete converted C-Cu-Ag on carbon paper support ( $1.0 \text{ mg}\cdot\text{cm}^{-2}$ ) showing a good coverage of the NCs. (B) SEM image of the as-deposited near-to-complete exchanged Cu-Ag NPs. (C) SEM image of the near-to-complete exchanged Cu-Ag NPs after 30 min of  $\text{CO}_2\text{RR}$  not showing any extrusions.

	H <sub>2</sub>	CO	HCOO <sup>-</sup>	CH <sub>4</sub>	C <sub>2</sub> H <sub>4</sub>	CH <sub>3</sub> CO O <sup>-</sup>	CH <sub>3</sub> CH O	C <sub>2</sub> H <sub>5</sub> OH	C <sub>3</sub> H <sub>7</sub> OH
Th-Cu- Ag NSA 10 min	34.34	8.05	13.85	7.59	17.78	3.18	9.12	9.71	0.00
$\sigma$	8.60	1.57	3.25	2.26	6.48	2.28	1.97	0.78	0.00
Th-Cu- Ag NSA 20 min	40.79	7.08	11.56	6.12	16.94	1.79	5.78	7.74	0.00
$\sigma$	9.12	1.30	2.34	1.85	4.17	1.16	0.80	1.29	0.00
Th-Cu- Ag NSA 30 min	49.50	6.72	9.26	4.97	15.77	0.39	2.44	5.77	1.93
$\sigma$	10.09	0.98	1.43	1.73	5.64	0.17	1.05	1.81	1.61
C - C u - Ag NSA 10 min	25.26	3.98	8.73	8.03	28.22	1.21	6.52	16.13	5.81
$\sigma$	1.81	0.80	1.81	1.55	0.60	0.19	1.45	0.93	0.84
C - C u - Ag NSA 20 min	26.82	3.57	7.40	5.49	26.30	0.98	3.74	12.90	4.29
$\sigma$	4.23	0.47	1.64	1.47	4.04	0.21	0.77	0.37	0.75
C - C u - Ag NSA 30 min	37.14	3.37	9.05	5.09	28.42	1.02	3.78	10.93	4.04
$\sigma$	8.65	0.18	0.48	1.52	2.98	0.18	0.68	1.11	0.85
TOh- Cu - Ag NSA 10 min	28.53	3.52	5.82	8.46	21.80	1.74	8.81	16.29	8.76
$\sigma$	1.75	0.23	0.76	3.93	2.66	0.47	1.44	1.90	1.41
TOh- Cu - Ag NSA 20 min	29.12	3.49	7.24	7.91	25.43	1.42	5.10	12.20	6.01
$\sigma$	0.85	0.28	1.89	3.96	2.83	0.15	1.07	1.38	0.08
TOh- Cu - Ag NSA 30 min	31.70	3.20	7.43	7.25	24.74	1.17	4.82	12.37	5.53
$\sigma$	2.17	0.32	1.49	3.84	2.83	0.19	1.79	0.44	1.04

**Table S5.** FEs of the gaseous and liquid products of the CO<sub>2</sub>RR measured with GC and NMR (see section S2)<sup>6</sup> after 10, 20 and 30 min at -1.1 V vs RHE in 0.1 M KHCO<sub>3</sub>. The electrolyte was saturated with CO<sub>2</sub> by bubbling at 25 ml·min<sup>-1</sup> for at least 15 min before starting the reaction and was continued during the reaction. Reported FEs are the average of three independent measurements reported with their associated standard deviations ( $\sigma$ ) corresponding to the error bars in **Figure 5** in the main text.

## Note S6. Supporting tables theory-guided experiment

Atomic structures from the density functional theory simulations as well as scripts necessary for reproducing the analysis have been made freely available at <https://nano.ku.dk/english/research/theoretical-electrocatalysis/katlabdb/co2-reduction-on-ag-cu-pd/>.

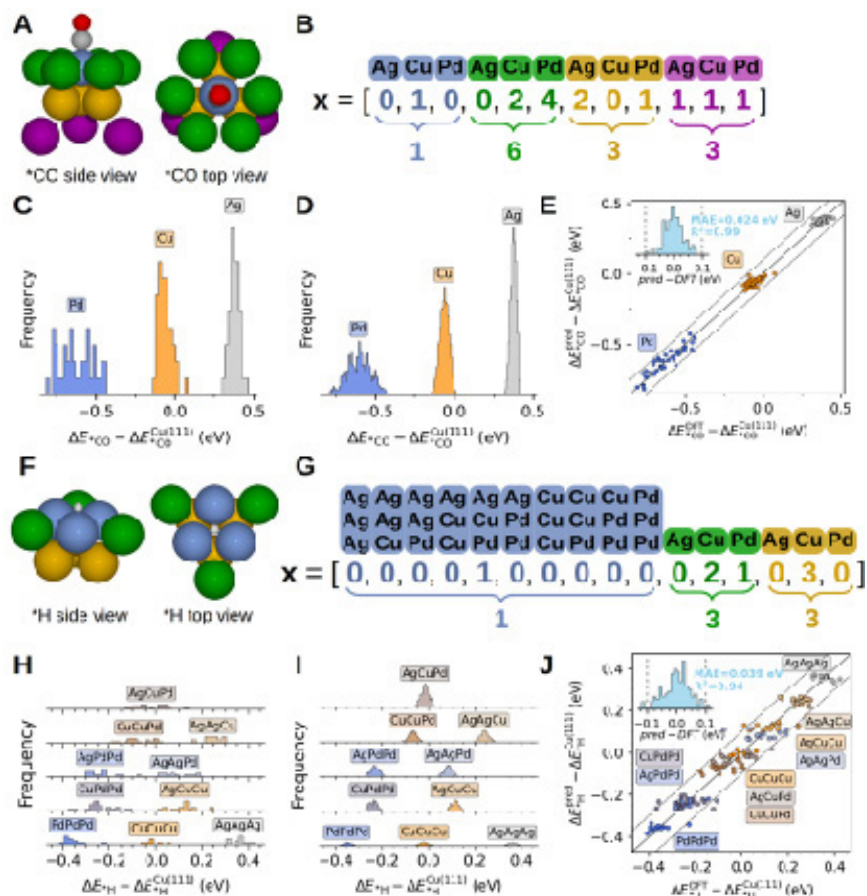


**Figure S21.** Overview of the machine learning model used to simulate \*CO and \*H adsorption energies on fcc(111) surface sites with arbitrary neighbors. (A) Structure used to account for neighboring atoms for atop \*CO adsorption including adsorption ensemble atoms (blue), surface atoms (green), subsurface atoms (orange), and 3<sup>rd</sup> layer atoms (magenta). (B) Example of features used as input for learning the adsorption energy where the constituent elements are counted in groups corresponding to the colors in (A). The numbers in each group must sum to the number of atoms of that group. (C) Distribution of the 126 DFT simulated \*CO adsorption energies used for training the linear model. The colors correspond to the adsorbing element. (D) Predicted distribution of \*CO adsorption energies using the linear model. (E) Parity plot illustrating the performance of the \*CO linear model on the training set. (F) Structure used to account for neighboring atoms for fcc hollow \*H adsorption with color coding as in (A). (G) Example of features used for \*H adsorption. Same as for (B), except that the adsorption ensemble atoms are one-hot encoded. (H) Distribution of the 160 DFT simulated \*H adsorption energies used for training. The colors correspond to the adsorbing fcc hollow site ensembles. (I) Predicted distribution of \*H adsorption energies using the model. (J) Parity plot illustrating the performance of the \*H linear model on the training set.



*CO adsorption				
Adsorption ensemble		Ag	Cu	Pd
<b>Intercept</b>		0.405785	-0.042545	-0.819863
<b>Surface element</b>	Ag	0	0.010471	0.013992
	Cu	-0.002754	0	0.011118
	Pd	0.002621	0.010323	0
<b>Subsurface element</b>	Ag	0	-0.013674	0.057961
	Cu	-0.001988	0	0.102745
	Pd	-0.007844	-0.034921	0
<b>3<sup>rd</sup> layer element</b>	Ag	0	-0.008940	0.003461
	Cu	-0.002469	0	0.001129
	Pd	-0.019618	-0.004030	0
*H adsorption				
<b>Adsorption ensemble</b>	AgAgAg	0.360826		
	AgAgCu	0.241141		
	AgAgPd	0.085678		
	AgCuCu	0.113763		
	AgCuPd	-0.015389		
	AgPdPd	-0.230785		
	CuCuCu	-0.020279		
	CuCuPd	-0.067306		
	CuPdPd	-0.238576		
	PdPdPd	-0.349699		
	<b>Surface element</b>	Ag	-0.001216	
Cu		-0.002959		
Pd		0.004175		
<b>Subsurface element</b>	Ag	0.000729		
	Cu	0.011141		
	Pd	-0.011870		

**Table S6.** Linear parameters for predicting adsorption energy distributions relative to Cu(111). All values have units of eV.

	$H_2$ , Liquid Fuels	$C_2H_4$	
	2		
<b>C-Cu<sub>79</sub>Ag<sub>21</sub> NSA 10 min</b>	44.7	23.3	17.2
<b><math>\sigma</math></b>	5.18	0.93	2.50
<b>C-Cu<sub>79</sub>Ag<sub>16</sub>Pd<sub>5</sub> NSA 10 min</b>	25.8	27.7	30.7
<b><math>\sigma</math></b>	4.71	1.42	4.51
<b>C-Cu<sub>79</sub>Pd<sub>16</sub>Ag<sub>5</sub> NSA 30 min</b>	64.4	13.1	10.9
<b><math>\sigma</math></b>	13.1	5.18	3.96

**Table S7.** FEs of CORR and HER products obtained with GC and NMR (see **Note S2**)<sup>6</sup> averaged over 30 min at -1.1 V vs RHE in 0.1 M KHCO<sub>3</sub>. The electrolyte was saturated with CO<sub>2</sub> by bubbling at 25 ml·min<sup>-1</sup> for at least 15 min before starting the reaction and was continued during the reaction. Reported FEs are the average of three independent measurements reported with their associated standard deviations ( $\sigma$ ) corresponding to the error bars in **Figure 6C** in the main text.

	CO <sub>2</sub> RR products	CORR products
<b>C-Cu<sub>79</sub>Ag<sub>21</sub> NSA molar yield</b>	0.76	0.56
<b>Yield error</b>	0.064	0.052
<b>C-Cu<sub>79</sub>Ag<sub>16</sub>Pd<sub>5</sub> NSA molar yield</b>	0.72	0.61
<b>Yield error</b>	0.055	0.069
<b>C-Cu<sub>79</sub>Pd<sub>16</sub>Ag<sub>5</sub> NSA molar yield</b>	0.48	0.36
<b>Yield error</b>	0.11	0.097

**Table S8.** Molar yields of CO<sub>2</sub>RR and CORR products, which correspond to the molar rate of a product divided by the sum of the molar rates of all products as based on the FEs reported in **Table S7** and total current densities of C-Cu<sub>79</sub>Ag<sub>21</sub>, C-Cu<sub>79</sub>Ag<sub>16</sub>Pd<sub>5</sub> and C-Cu<sub>79</sub>Pd<sub>16</sub>Ag<sub>5</sub> (14.9, 15.0 and 28 mA cm<sup>-2</sup>, respectively). Error propagation of the standard deviations in **Table S7** and the molar yields offer the data points and error bars in **Figure 6A** in the main text.

## Note S7. Supporting figures, tables and miscellaneous for Materials and Methods

The galvanic exchange reaction was performed in OAm for its ability to act both as solvent and surfactant and particularly for its ability to form complexes with metal ions to facilitate the exchange.<sup>8,9</sup> However, OAm can also fungate as reducing agent and due to the positive interfacial energy between

Cu and Ag, it is important to exclude the latter's homogenous nucleation. Therefore, we fixed the dissolution temperature of the precursor at 50 °C as above it, homogenous nucleation could not be excluded (**Figure S22**).

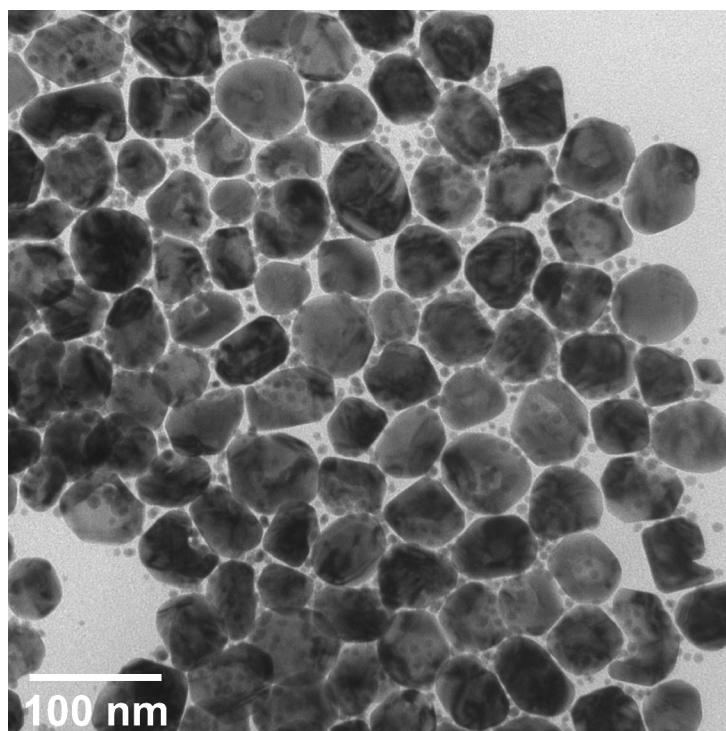


**Figure S22.** TEM image depicting the conventional galvanic exchange reaction (2 hrs 80 °C) of C-Cu NPs (500 µg) using a 0.667 mg/mL AgNO<sub>3</sub> in OAm precursor solution prepared by dissolving the Ag salt at 80 °C instead of 50 °C. Homogenous nucleation of Ag NPs can be observed in combination with galvanic exchange reaction.

## S8. References.

- (1) Koolen, C. D.; Torrent, L.; Agarwal, A.; Meili-Borovinskaya, O.; Gasilova, N.; Li, M.; Luo, W.; Züttel, A. High-Throughput Sizing, Counting, and Elemental Analysis of Anisotropic Multimetallic Nanoparticles with Single-Particle Inductively Coupled Plasma Mass Spectrometry. *ACS Nano* **2022**. <https://doi.org/10.1021/acsnano.2c01840>.
- (2) Ozoliņš, V.; Wolverton, C.; Zunger, A. Cu-Au, Ag-Au, Cu-Ag, and Ni-Au Intermetallics: First-Principles Study of Temperature-Composition Phase Diagrams and Structures. *Phys. Rev. B* **1998**, *57* (11), 6427–6443. <https://doi.org/10.1103/PhysRevB.57.6427>.
- (3) Sprunger, P. T.; Lægsgaard, E.; Besenbacher, F. Growth of Ag on Cu(100) Studied by STM: From Surface Alloying to Ag Superstructures. *Phys. Rev. B* **1996**, *54* (11), 8163–8171. <https://doi.org/10.1103/PhysRevB.54.8163>.
- (4) Xia, X.; Wang, Y.; Ruditskiy, A.; Xia, Y. 25th Anniversary Article: Galvanic Replacement: A Simple and Versatile Route to Hollow Nanostructures with Tunable and Well-Controlled Properties. *Adv. Mater.* **2013**, *25* (44), 6313–6333. <https://doi.org/10.1002/adma.201302820>.
- (5) Zhevnenko, S. N.; Khairullin, A. K. Surface Energy and Grain Boundary Diffusion in Ag(Cu) Solid Solutions. *Mater. Lett.* **2019**, *248*, 127–129. <https://doi.org/10.1016/j.matlet.2019.04.021>.
- (6) Zhang, J.; Luo, W.; Züttel, A. Crossover of Liquid Products from Electrochemical CO<sub>2</sub> Reduction through Gas Diffusion Electrode and Anion Exchange Membrane. *J. Catal.* **2020**, *385*, 140–145. <https://doi.org/10.1016/j.jcat.2020.03.013>.
- (7) Lu, X.; Tuan, H.-Y.; Chen, J.; Li, Z.-Y.; Korgel, B. A.; Xia, Y. Mechanistic Studies on the Galvanic Replacement Reaction between Multiply Twinned Particles of Ag and H<sub>2</sub>AuCl<sub>4</sub> in an Organic Medium. *J. Am. Chem. Soc.* **2007**, *129* (6), 1733–1742. <https://doi.org/10.1021/ja067800f>.
- (8) Mourdikoudis, S.; Liz-Marzán, L. M. Oleylamine in Nanoparticle Synthesis. *Chem. Mater.* **2013**, *25* (9), 1465–1476. <https://doi.org/10.1021/cm4000476>.
- (9) Tanuma, S.; Powell, C. J.; Penn, D. R. Calculation of electron inelastic mean free paths (IMFPs) VII. Reliability of the TPP-2M IMFP predictive equation. *Surf. Interface Anal.* **2003**, *35* (3), 268–275. <https://doi.org/10.1002/sia.1526>.
- (10) Hill, J. M.; Royce, D. G.; Fadley, C. S.; Wagner, L. F.; Grunthaner, F. J. Properties of Oxidized Silicon as Determined by Angular-Dependent X-Ray Photoelectron Spectroscopy. *Chem. Phys. Lett.* **1976**, *44* (2), 225–231. [https://doi.org/10.1016/0009-2614\(76\)80496-4](https://doi.org/10.1016/0009-2614(76)80496-4).
- (11) Powell, C. J.; Jablonski, A. The NIST Electron Effective-Attenuation-Length Database. *J. Surf. Anal.* **2002**, *9* (3), 322–325. <https://doi.org/10.1384/jsa.9.322>.

## Chapter 6

# Scalable synthesis of Cu(Ag) oxide clusters for the highly selective electrochemical conversion of CO<sub>2</sub> to acetaldehyde

**Preprint version:** submission of this section has been delayed to enable incorporation of in situ data XAS studies to be collected at the SuperXAS beamline of the Swiss Light Source of the Paul Scherrer Institute in March 2023.

**Edit:** caption numbers of figures, tables, and equations were edited to match the thesis chapter number.

**Cedric David KOOLEN<sup>a,b\*</sup>, Bernardus ZIJLSTRA<sup>c</sup>, Maximilian WINZELY<sup>d</sup>, Jie ZHANG<sup>e</sup>, Tobias PFEIFFER<sup>c</sup>, Wilbert VRIJBURG<sup>c</sup>, Mo LI<sup>a,b</sup>, Bart BOSHUIZEN<sup>f</sup>, Ayush AGARWAL<sup>g,h</sup>, Youngdon KO<sup>a,b</sup>, Yunting WANG<sup>a,b</sup>, Liping ZHONG<sup>a,b</sup>, Juan HERRANZ SALANER<sup>d</sup>, Olga SAFONOVA<sup>d</sup>, Andreas SCHMIDT-OTT<sup>c,f</sup>, Wen LUO<sup>i\*</sup>, Andreas ZUETTEL<sup>a,b</sup>**

<sup>a</sup>Laboratory of Materials for Renewable Energy (LMER), Institute of Chemical Sciences and Engineering (ISIC), Basic Science Faculty (SB), École polytechnique fédérale de Lausanne (EPFL) Valais/Wallis, Energypolis, Sion, Switzerland

<sup>b</sup>Empa Materials Science & Technology, Dübendorf, Switzerland

<sup>c</sup>VSPARTICLE B.V., Delft, the Netherlands.

<sup>d</sup>Paul Scherrer Institute, CH-5232 Villigen, Switzerland

<sup>e</sup>National University of Singapore, Singapore, Singapore

<sup>f</sup>Faculty of Applied Sciences Technical University of Delft, Delft, the Netherlands.

<sup>g</sup>Bioenergy and Catalysis Laboratory (LBK), Energy and Environment Research Division (ENE), Paul Scherrer Institute (PSI), Villigen, 5232, Switzerland.

<sup>h</sup>School of Architecture, Civil and Environmental Engineering (ENAC IIE GR-LUD), École Polytechnique Fédérale de Lausanne (EPFL), Lausanne, 1035, Switzerland

<sup>i</sup>School of Environmental and Chemical Engineering, Shanghai University, Shanghai, 200090, China.

\*Corresponding author: [cedric.koolen@epfl.ch](mailto:cedric.koolen@epfl.ch); [wenluo@shu.edu.cn](mailto:wenluo@shu.edu.cn)

## Abstract

The electrochemical conversion of CO<sub>2</sub> to the base chemical acetaldehyde offers a sustainable and green alternative to the Wacker process. However, current electrocatalyst cannot compete due to their limited selectivity for acetaldehyde resulting in low energy efficiencies. Here, we report a series of Cu(-Ag) oxide cluster catalysts (~ 1 nm) immobilized on various hetero-atom doped carbonaceous supports produced via spark ablation of Cu (and Ag) electrodes, that achieve an acetaldehyde selectivity as high as 92% a mere 560 meV from the equilibrium potential. Further, the catalyst demonstrated reusability as it retained performance over 30 hrs during a stress test which included repeated start-stop cycles (3x). EXAFS and XANES post catalysis showed that the initial oxide clusters had completely reduced under cathodic potential and had retained its metallic nature even after air exposure explaining its recyclability.

## 6.1. Main

The electrification of the chemical industry is needed for a complete and unambiguous energy transition.<sup>1</sup> Many processes depend heavily on the petrochemical industry, which are neither green nor energy efficient. One such process is the well-known homogeneously catalyzed production of the base chemical acetaldehyde, used in the production of drugs, dyes, and fragrances.<sup>2</sup> Commercialized under the name of the Wacker process, the PdII catalyzed oxidation of ethylene to acetaldehyde supplies the vast majority of the global acetaldehyde market worth well over 1.2B USD.<sup>3,4,5</sup> This process not only uses a cracking product, ethylene, it requires large amounts of hydrochloric acid to achieve required conversions.<sup>4,5</sup> Although reliable, overcoming the limitations of this resource and energy intensive process is needed for a sustainable supply in the long term. Attempts have been made to heterogeneously convert ethylene to acetaldehyde using Pd-Cu zeolite catalysts fixing the acid sites on the support significantly reducing the environmental toll of the process.<sup>6</sup> However, such methods

still rely on the petrochemically sourced ethylene and selectivity's are not yet at par. Here we propose a fully green, carbon neutral process instead to selectively produce acetaldehyde electrochemically using CO<sub>2</sub> as a resource.

The electrochemical CO<sub>2</sub> reduction reaction (CO<sub>2</sub>RR) is a promising technology of industrial relevance that kills two birds with one stone: 1) it has the ability to significantly reduce our CO<sub>2</sub> footprint by fixating it in useful products and 2) it tackles the intermittence problem associated with renewable energy as it offers to store energy long-term in chemical bonds.<sup>7</sup> However, it comes with significant challenges.<sup>8</sup> In particular, the more valuable products that require carbon-carbon coupling such as ethanol, ethylene and acetaldehyde can only be produced on Cu.<sup>9</sup> Moreover, polycrystalline Cu catalyzes the reaction of no less than 16 individual products resulting in low selectivity's for specific products and thus large energy losses.<sup>10</sup> Previous works have shown that on bulk Cu specific active sites have activities for specific products, i.e. Cu(111) surfaces

produce majority CH<sub>4</sub>, Cu(100) majority ethylene and Cu(110) majority oxygenates including ethanol.<sup>11,12,13,14</sup> Further, defects, steps, kinks- and edge-sites have also shown preferentiality towards specific pathways.<sup>15,16,17</sup> Therefore, tremendous efforts have gone out to engineer Cu electrodes to expose those facets, defects and or sites to produce specific products with unitary selectivity's.<sup>18,19,20,21,22</sup> Also, attempts have been made to mix in other elements in the form of homogeneous Cu alloys and change the catalyst electronic nature.<sup>23,24,25,26</sup> Unfortunately, for any of these attempts, selectivity's >50% have seldomly been reported.<sup>20,26</sup>

Recently, Cu clusters <2 nm have been proposed as an opportunity to improve the

definition of the catalyst active site<sup>27</sup> and has successfully enhanced the selectivity towards ethanol to industrial relevance (>90%).<sup>28,29,30</sup> Here, we report a scalable synthesis of Cu(Ag) oxide clusters <2 nm with 92% selectivity for the acetaldehyde and only 560 meV from the equilibrium potential. Further, by excluding the effect of support,<sup>28,29,30</sup> we show that cluster atomicity is key in differentiating between pathways. This offers a new catalyst design strategy for the selective electrosynthesis of base chemicals.



## 6.2. Catalyst synthesis and characterization

The catalyst synthesis is depicted in **Figure 35**. In brief, a power source is applied to two hollow metal electrodes (Cu-Cu or Cu-Ag) in between a gap through which a carrier gas (Ar) is flowed (**Figure 35A**). Upon the breakdown of the potential, the gas is briefly ionized ( $\sim\mu\text{s}$ ) and becomes conductive creating a plasma pulse producing temperatures  $>20,000\text{ K}$  (similar to the workings of a spark plug).<sup>31</sup> By controlling the gas flow rate, repetition frequency, and energy per spark, the electrode ablation rate can be controlled producing an aerosol of clusters of well-defined size and composition.<sup>32,33</sup> However, the high degree of undercoordination of the cluster produced makes them extremely susceptible to agglomeration. Therefore, a selection of heteroatom doped carbonaceous supports with strong cluster-support interaction, i.e.,

graphene oxide and N-doped carbon black nanoparticles (GO-, NCB-NPs) synthesized in-house at  $>1\text{ g}$  scale,<sup>34,35</sup> were used for successful immobilization. Finally, cathodes were fashioned from a commercial gas diffusion layer (GDL) air brushed with an optimized loading of carbonaceous support, and used as filters to collect the clusters from the aerosol stream (**Figure 35B**). For information regarding the synthesis of the catalyst supports, see **Note S1** and **Figure S1** of the Supporting Information. For details on the cluster production see **Note S2** and **Figure S2-S4**. For details on the cluster immobilization see **Note S3-S4** and **Figure S5-S11**. For details on the cathode production process see **Note S4** and **Figure S12-S15**.

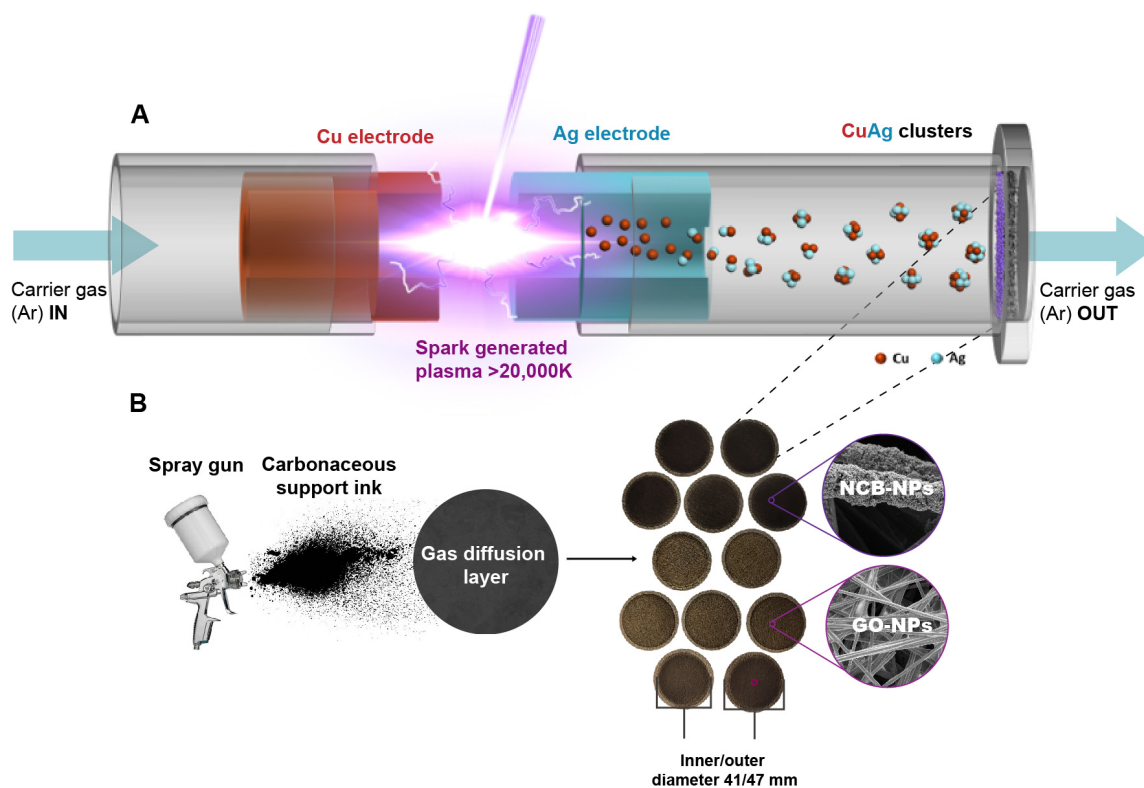


**Figure 35.** Schematic of the spark ablation (A) and immobilization (B) of Cu(-Ag) oxide clusters on heteroatom doped carbonaceous support GDL composites.

Four ~0.1wt% metal catalysts were produced and denoted Cu(-Ag)-GO (graphene oxide) and Cu(-Ag)-NCB (N-doped carbon black). We investigated the size of the clusters produced in the aerosol with a differential mobility analyzer (DMA) and the state of the immobilized clusters using scanning transmission electron microscopy high-angle annular darkfield (STEM-HAADF) imaging (**Figure 36**, **Figure S5-S9**). The average Cu and Cu-Ag cluster size of 1.6 and 1.5 nm measured with the DMA (**Figure S3-S4**) was confirmed with STEM-

HAADF with the FWHM of Cu, respectively, Cu-Ag clusters of  $1.5 \pm 0.5$  and  $1.4 \pm 0.3$  nm (**Figure 36A-B**, **S6** and **S8**). Interestingly, when N-edge functionalized graphene and multiwalled carbon nanotubes were used as supports, cluster agglomeration was observed (**Figure S7** and **S9**). The strength of the cluster-support interaction was not a measure of the support work function (**Figure S10**). Instead, both the crystallinity and absence of specific ligation sites explained the difference (**Figure S11-S12**). STEM-energy dispersive X-ray

spectroscopy (EDXS) was used to confirm the Cu, respective, Cu-Ag nature of the STEM-HAADF identified clusters (**Figure 36C-D**) and to determine the average composition of the bimetallic clusters at  $\text{Cu}_{84}\text{Ag}_{16}$  (at. %), which was later confirmed with X-ray photoemission spectroscopy (XPS, **Figure S16**). XPS further pointed towards the complete oxidation of the clusters to  $\text{CuI}$  and  $\text{AgI}$  after 7 days (directly after deposition some  $\text{CuI}$  species could still be observed, which is an effect of purity of the Ar used as carrier gas, **Figure S16**). The coordination structure and oxidation state of the Cu atom in the as-synthesized catalysts was further investigated with X-ray absorption spectroscopy (XAS, **Figure 36E-H**). The pseudo radial distribution function extracted from the extended X-ray absorption fine structure (EXAFS) spectra excluded the presence of  $\text{Cu}_2\text{O}$ ,  $\text{Cu}(\text{OH})_2$  and or metallic Cu species corroborating the XPS results. Further, a Cu-Cu scattering event in the second coordination shell of CuO could be discerned to a higher and lesser degree for the NCB-, respectively GO-based catalysts (**Figure 36E-F**). The Cu coordination numbers of  $3 \pm 0.6$ , respectively  $\text{Cu } 2 \pm 0.4$  (vs 4 in the bulk) agrees with the small particle size and further indicates a slightly stronger support interaction with

GO than with NCB. This is most likely due to the higher density of ligation sites on the GO-support (heteroatom content  $\sim 50\%$  vs  $\sim 30\%$  for NCB). Further, by considering Cu phthalocyanine ( $\text{CuPc}$ ) and Cu acetylacetonate ( $\text{Cu}(\text{acac})_2$ ) as a reference, the ligation site of the clusters could be probed showing a strong contribution from Cu-N and Cu-O bonds in the first coordination sphere. In the case of Cu-NCB, these are most likely pyrrolic and pyridinic N and  $\text{NO}_x$ . For the Cu-GO, this is either from  $\text{NO}_x$  or C=O or  $\text{COO}^-$  species. Linear combination analysis of the near edge structure (XANES) spectra puts their relative contribution  $>28\%$  (**Figure 36G-H**). We note that XANES analysis is limited by the lack of suitable references as all references available are of bulk materials, which are known to differ strongly by reduction of particle size.<sup>45</sup> Therefore, ongoing research is going towards the simulations of XANES spectra of CuO, Cu<sub>2</sub>O and Cu clusters in the relevant size ranges to substitute the bulk reference spectra and improve our understanding of the cluster-support interaction.

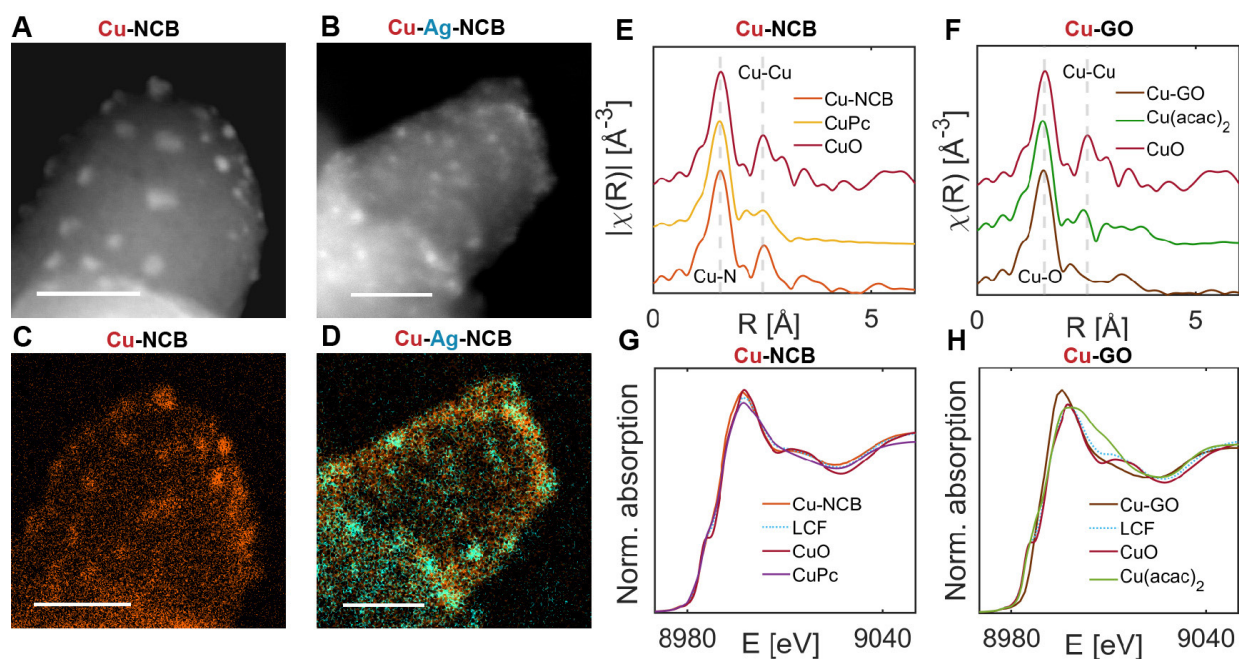


**Figure 36.** Advanced characterization of the as-synthesized Cu(-Ag) oxide clusters immobilized on heteroatom doped carbonaceous support. (A-B) STEM-HAADF images of the Cu and Cu-Ag-NCB catalyst. (C-D) STEM-EDXS elemental maps of the images in A and B showing Cu in orange and Ag in turquoise. Scale bars indicate 10 nm. (E-F) Pseudo radial distribution functions extracted from the EXAFS spectra of the Cu-NCB and -GO catalyst, respectively. CuO, CuPc and Cu(acac)<sub>2</sub> were used as a reference. (G-H) XANES spectra of the Cu-NCB and -GO catalyst, respectively. A linear combination fit (LCF) of the CuO and CuPc and Cu(acac)<sub>2</sub> reference spectra puts the contribution of the ligation sites to catalyst structure at 48% (Cu-GO) and 28% (Cu-NCB), respectively.

### 6.3. Electrochemical screening of the Cu(-Ag) oxide cluster carbonaceous support composite electrodes.

We subjected our Cu(-Ag)-NCB/GO GDL composites to a series of electrochemical screening tests to determine their activity in CO<sub>2</sub>RR. Electrochemically speaking, the cluster support composites differ in two major ways: 1) NCB and GO are respectively a good and poor CO<sub>2</sub>RR electrocatalyst for the production of CO,<sup>36,37</sup> which could explain differences in performance by means of tandem-effects upon the introduction of the clusters<sup>38</sup> and 2) have different support-cluster interactions of varying strength, i.e. via N- and NO<sub>x</sub>-ligation sites in the case of NCB and C=O,OH and COOH groups for GO, respectively, which may affect the performance, i.e. similarly to what has been observed for atomically precise ligand capped Au clusters.<sup>39</sup> Further, since support effect have been invoked to explain performance differences in Cu<sub>3-4</sub>-cluster-NCB/GO based composites in the past,<sup>28,29</sup> we deemed it of utmost importance to carefully deconvolute the contribution of the support from the cluster based composites. Therefore, before we investigated the effect of the introduction of clusters, we first determined the activity of the supports themselves.

As expected, the NCB catalyst showed

good selectivity (>90%) for CO, even at modest overpotential of 600 meV (**Figure S20A**) whereas the GO support was poorly selective for CO<sub>2</sub>RR and produced H<sub>2</sub> as a majority product at all potentials tested (**Figure S20B**). Some HCOO<sup>-</sup> could be detected in the catholyte but never more than 20% of the current was directed towards this product. Further, even though several acid washing steps had been performed, trace amounts of Mn leftover from the graphite oxidation step could not be fully excluded, which may explain the observed CO as a minority product.<sup>40</sup> Nevertheless, the strongly differentiating CO activities (2 mA cm<sup>-2</sup> vs 40 μA cm<sup>-2</sup> for NCB and GO, respectively) ensures the exclusion of CO-coverage effects in case of the cluster-GO composites. Finally, material degradation for potentials more cathodic than -1.1 V vs RHE could be observed for either support offering the upper limit for the potential screening of the clusters-based composites (**Figure S21**).

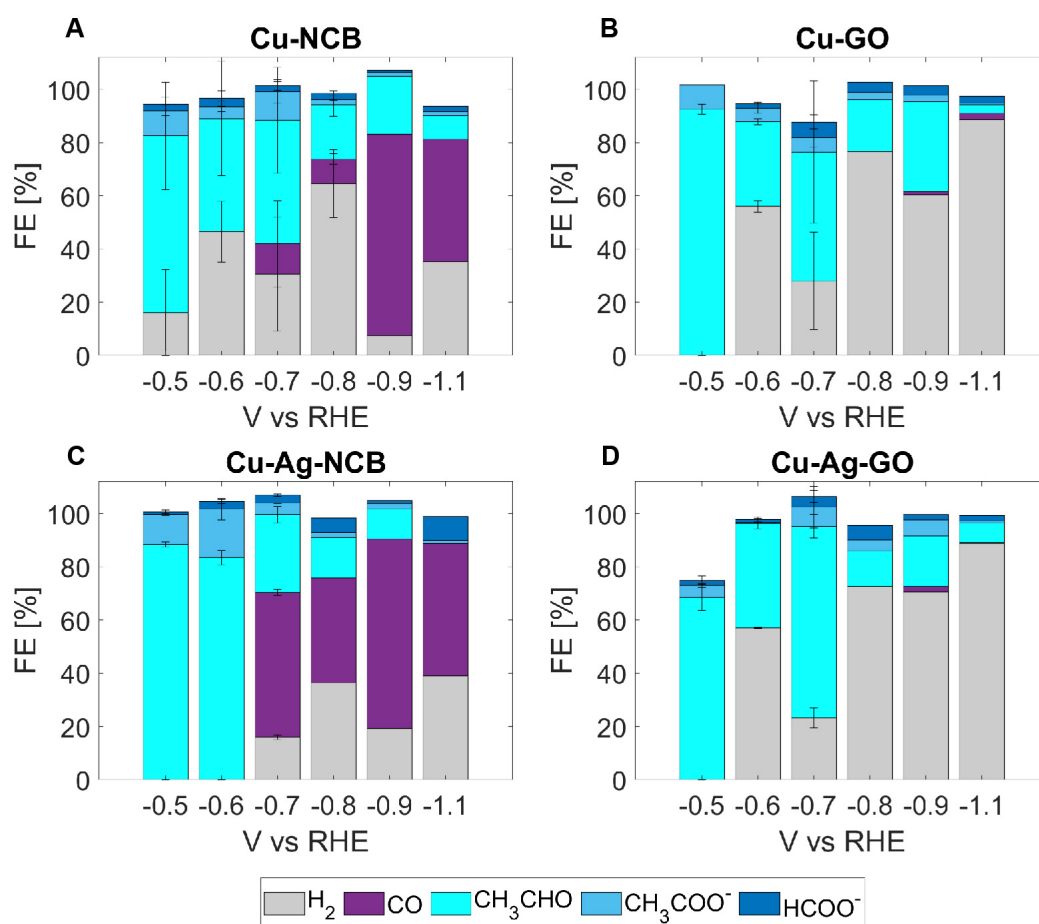


**Figure 37.** (A-B) Selectivity screening of Cu-NCB and Cu-GO GDL composites, respectively. (C-D) Selectivity screening of Cu-Ag-NCB and Cu-Ag-GO GDL composites, respectively. All electrochemical reactions were carried out in  $\text{CO}_2$  saturated 0.1M  $\text{KHCO}_3$  electrolyte in Nafion® membrane separated H-cell. Chronoamperometry was carried out in a cathodic potential window of -0.5 to -1.1 V vs RHE (half-cell potential) with 100 and lastly 200 meV increment (iR-drop corrected) using an Ag/AgCl reference electrode. A Pt foil ( $1 \text{ cm}^2$ ) was used as counter electrode. Gaseous products were quantified via gas chromatography. Liquid products were detected using  $^1\text{H-NMR}$  and quantified using the Kuhl et al. protocol.<sup>10</sup> For the lower overpotential experiments (<800 meV), liquid products were collected for at least 3 hrs for reasonable statistics. For all other potentials, FEs were averaged for a minimum of 30 min. Error bars represent standard deviations of at least two independent measurements. The less than 100% FE observed for the Cu-Ag-GO-GDL at -0.5 V vs RHE stems from unquantifiable gaseous products due to dilution of the  $\text{CO}_2$  stream ( $\text{H}_2$  most likely).

With the activity of the supports quantified, the effect of the introduction of Cu(-Ag) clusters could be investigated. **Figure 37** shows the chronoamperometry experiments performed to determine the selectivity as function of potential, support and type of cluster. Independently of the support (**Figure 37A-B**), acetaldehyde could be observed at any potential between -0.5 and -1.1 V vs RHE upon the introduction of Cu oxide clusters. As well as acetate, two electron transfers less reduced than acetaldehyde, as a minor product (<10%) and formate (<10%) at higher overpotential. Only for the NCB based samples was CO a notable product and especially at high overpotential which stems clearly from the support activity. Further, especially at lower overpotentials (more cathodic than -0.8 V vs RHE), significant acetaldehyde selectivity's could be reported. For Cu-NCB-GDL at -0.5 V vs RHE, an acetaldehyde selectivity of  $66\pm 20\%$  was determined. At the same potential, for Cu-GO, the FEs was as high as  $92\pm 2\%$ . For the NCB based catalyst enhancement of the overpotential by 100-200 meV, put the acetaldehyde FEs in the 40-50% range. Interestingly, for Cu-GO, the

selectivity decreased to around 30% at -0.6 V vs RHE to then increase to nearly 50% at -0.7 V vs RHE. We assign this to a phase-transition of the GO support at -0.6 V vs RHE (i.e. -1.2 V vs Ag/AgCl) absent for NBC.<sup>41</sup> Further enhancement of the overpotential reduced the acetaldehyde selectivity independent of the support but remained >10% upto -0.9 V vs RHE. Interestingly, upon the introduction of 8 at.% Ag into the clusters, a similar trend could be observed as for pure Cu oxide clusters (**Figure 37C-D**). However, for the Cu-Ag-NCB catalyst, at -0.5 V vs RHE the selectivity towards acetaldehyde was as high as  $88\pm 1\%$  and  $83\pm 3\%$  a 100 meV more cathodic. The  $C_{2+}$  selectivity was approximately 100% for either potentials. For the Cu-Ag-GO catalyst, again the selectivity dropped at -0.6 V vs RHE but more importantly, a ~70% selectivity could be maintained at -0.7 V vs RHE.

## 6.4. Resistance against potential cycling

An optimal catalyst is not only selective, it remains stable for long hours of operation and is indifferent to start-stop cycles.<sup>42</sup> Therefore, we subjected one of our catalysts, the Cu-NCB GDL catalyst, to a stress test (**Figure 38**). First, we took a previously screened catalyst sample, exposed it to air for several hours, and then ran the operation again (**Figure 38A**, cycle 2). Notably, neither the current density ( $200 \mu\text{A cm}^{-2}$ ) nor the acetaldehyde selectivity (40-50%) changed. We then repeated this process for a second time but extended the reaction time 10-fold and let it run for nearly 30 hrs (**Figure 38A**, cycle 3). After an initial stage of equilibration (first 3 hrs), a stable performance was obtained equivalent to the first and second cycle. To determine the reason of this remarkable resistance against start-stop cycles, we investigated the nature of our catalysts post-catalysis using EXAFS and XANES (**Figure 38B-E**). Interestingly, the EXAFS spectra showed that the clusters had not only reduced fully upon applied potential,<sup>43</sup> they had retained their metallic state even after exposure to air and independently of the support, i.e.

NCB or GO (**Figure 38B-C**). Similar to the pre-catalysis samples, Cu-N and Cu-O contributed significantly to the overall signal, which was confirmed by XANES linear combination analysis, and is suggested to originate from the cluster-support interaction (**Figure 38D-E**). However, post catalysis, the majority of the EXFAS intensity originated from a Cu-Cu single scattering event of metallic Cu for either catalyst. Fitting of the Cu coordination shell estimates a Cu-NCB, -GO catalyst Cu coordination number of  $5.6 \pm 0.9$  and  $4.8 \pm 0.8$  (versus 12 in the bulk), respectively.<sup>44</sup> We translate that into an average particle size of 1.0 and 0.9 nm,<sup>45,46</sup> respectively, which is excellent agreement with a reduced CuO particle size of 1.6 nm (**Figure 36**). We, therefore, conclude that the recyclability of the Cu(-Ag) cluster-supported catalysts, is a direct result of their in situ transformation towards a metallic species, and their subsequent resistance towards oxidation.<sup>47</sup>



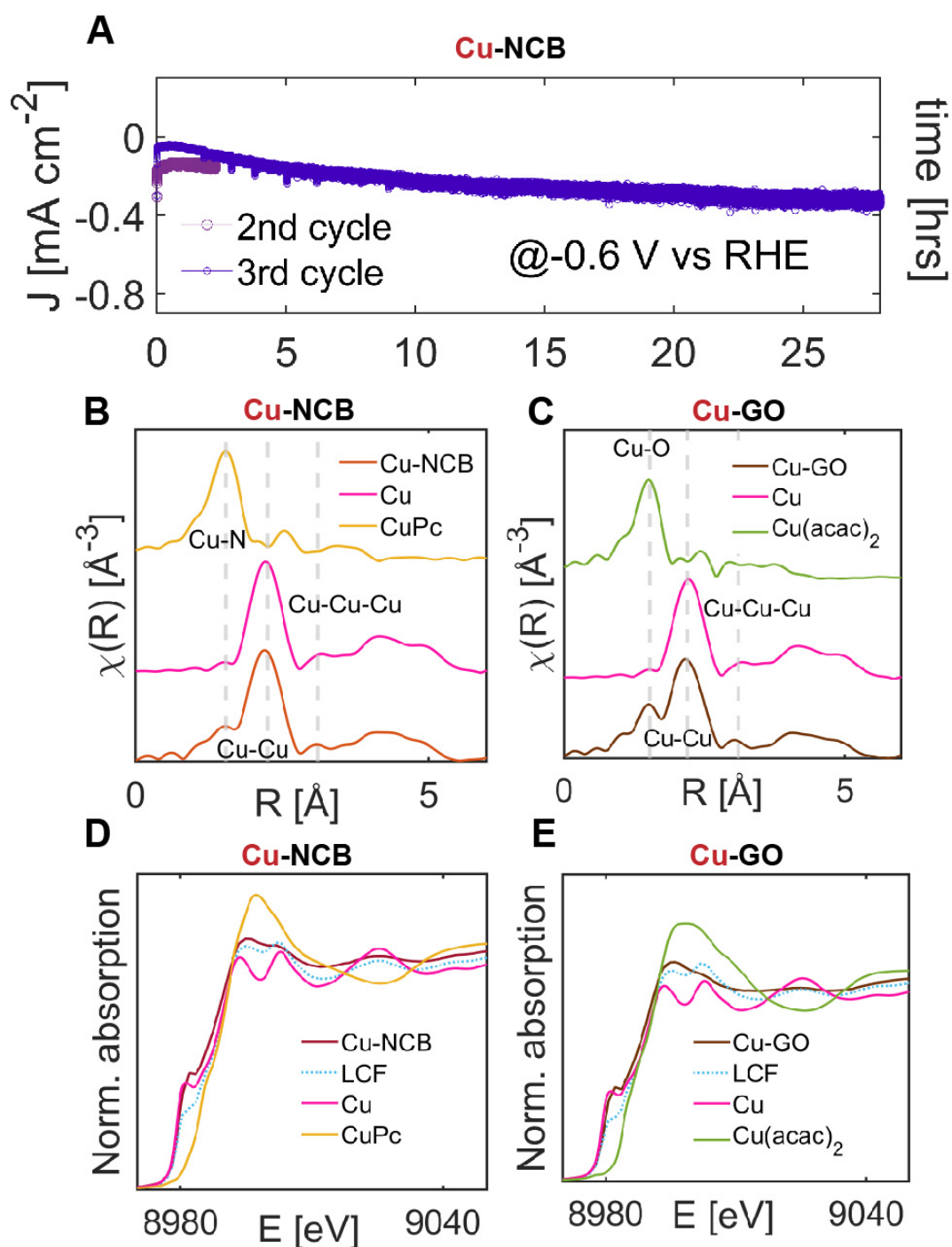


**Figure 38.** (A) Stress test of the Cu-NCB GDL at -0.6 V vs RHE in 0.1 M  $\text{KHCO}_3$ . (B-C) Pseudo radial distribution functions extracted from the EXAFS spectra of the Cu-NCB and -GO catalyst, respectively, after catalysis and exposure to air. Cu, CuPc and  $\text{Cu}(\text{acac})_2$  were used as a reference. (D-E) XANES spectra of the Cu-NCB and -GO catalyst, respectively, after catalysis and exposure to air. A linear combination fit (LCF) of the Cu and CuPc and  $\text{Cu}(\text{acac})_2$  reference spectra puts the contribution of the ligation sites to catalyst structure at 40% and 30%, respectively.

## 6.5. Conclusions

We have developed a scalable production and immobilization method of bimetallic Cu-based clusters of sizes  $\sim 1$  nm. We show that such composite materials have unique catalytic properties and show high selectivity towards acetaldehyde ( $>90\%$ ) in the electrochemical conversion of  $\text{CO}_2$ . We show that our catalysts retain their in situ formed metallic nature post catalysis, and demonstrate that this feature offers resistance against potential cycling. We

propose our catalyst production method as a platform technology that may offer researchers an entirely new class of catalyst to screen for activity in various electrochemical reaction such as water splitting, oxygen evolution, nitrogen reduction etc.

## 6.6. References

1. Barton, J. L. Electrification of the chemical industry. *Science* **368**, 1181–1182 (2020).
2. *Health Assessment Document for Acetaldehyde: Review Draft*. (1987).
3. Smidt, J. *et al.* Katalytische Umsetzungen von Olefinen an Platinmetall-Verbindungen Das Consortium-Verfahren zur Herstellung von Acetaldehyd. *Angewandte Chemie* **71**, 176–182 (1959).
4. Jira, R. Acetaldehyde from Ethylene—A Retrospective on the Discovery of the Wacker Process. *Angewandte Chemie International Edition* **48**, 9034–9037 (2009).
5. Smidt, J. *et al.* The Oxidation of Olefins with Palladium Chloride Catalysts. *Angewandte Chemie International Edition in English* **1**, 80–88 (1962).
6. Imbao, J., van Bokhoven, J. A., Clark, A. & Nachttegaal, M. Elucidating the mechanism of heterogeneous Wacker oxidation over Pd-Cu/zeolite Y by transient XAS. *Nat Commun* **11**, 1118 (2020).
7. Fan, L. *et al.* Strategies in catalysts and electrolyzer design for electrochemical CO<sub>2</sub> reduction toward C<sub>2</sub>+ products. *Science Advances* **6**, eaay3111.
8. Luna, P. D. *et al.* What would it take for renewably powered electrosynthesis to displace petrochemical processes? *Science* **364**, (2019).
9. Nitopi, S. *et al.* Progress and Perspectives of Electrochemical CO<sub>2</sub> Reduction on Copper in Aqueous Electrolyte. *Chem. Rev.* **119**, 7610–7672 (2019).
10. Kuhl, K. P., Cave, E. R., Abram, D. N. & Jaramillo, T. F. New insights into the electrochemical reduction of carbon dioxide on metallic copper surfaces. *Energy Environ. Sci.* **5**, 7050–7059 (2012).
11. Hori, Y., Murata, A., Takahashi, R. & Suzuki, S. Electroreduction of carbon monoxide to methane and ethylene at a copper electrode in aqueous solutions at ambient temperature and pressure. *J. Am. Chem. Soc.* **109**, 5022–5023 (1987).
12. Hori, Y., Murata, A. & Takahashi, R. Formation of hydrocarbons in the electrochemical reduction of carbon dioxide at a copper electrode in aqueous solution. *J. Chem. Soc., Faraday Trans. 1* **85**, 2309–2326 (1989).
13. Hori, Y., Takahashi, I., Koga, O. & Hoshi, N. Electrochemical reduction of carbon dioxide at various series of copper single crystal electrodes. *Journal of Molecular Catalysis A: Chemical* **199**, 39–47 (2003).
14. Hori, Y. Electrochemical CO<sub>2</sub> Reduction on Metal Electrodes. in *Modern Aspects of Electrochemistry* (eds. Vayenas, C. G., White, R. E. & Gamboa-Aldeco, M. E.) 89–189 (Springer, 2008). doi:10.1007/978-0-387-49489-0\_3.
15. Takahashi, I., Koga, O., Hoshi, N. & Hori, Y. Electrochemical reduction of CO<sub>2</sub> at copper single crystal Cu(S)-[n(111)×(111)] and Cu(S)-[n(110)×(100)] electrodes. *Journal of Electroanalytical Chemistry* **533**, 135–143 (2002).
16. Piqué, O., Low, Q. H., Handoko, A. D., Yeo, B. S. & Calle-Vallejo, F. Selectivity Map for the Late Stages of CO and CO<sub>2</sub> Reduction to C<sub>2</sub> Species on Copper Electrodes. *Angewandte Chemie International Edition* **60**, 10784–10790 (2021).

17. Schouten, K. J. P., Qin, Z., Pérez Gallent, E. & Koper, M. T. M. Two Pathways for the Formation of Ethylene in CO Reduction on Single-Crystal Copper Electrodes. *J. Am. Chem. Soc.* **134**, 9864–9867 (2012).
18. Li, C. W. & Kanan, M. W. CO<sub>2</sub> Reduction at Low Overpotential on Cu Electrodes Resulting from the Reduction of Thick Cu<sub>2</sub>O Films. *J. Am. Chem. Soc.* **134**, 7231–7234 (2012).
19. Chen, Z. *et al.* Grain-Boundary-Rich Copper for Efficient Solar-Driven Electrochemical CO<sub>2</sub> Reduction to Ethylene and Ethanol. *J. Am. Chem. Soc.* **142**, 6878–6883 (2020).
20. Wang, Y. *et al.* Catalyst synthesis under CO<sub>2</sub> electroreduction favours faceting and promotes renewable fuels electrosynthesis. *Nat Catal* **3**, 98–106 (2020).
21. Zhu, C. *et al.* Product-Specific Active Site Motifs of Cu for Electrochemical CO<sub>2</sub> Reduction. *Chem* **7**, 406–420 (2021).
22. Timoshenko, J. *et al.* Steering the structure and selectivity of CO<sub>2</sub> electroreduction catalysts by potential pulses. *Nat Catal* **5**, 259–267 (2022).
23. Batchelor, T. A. A. *et al.* High-Entropy Alloys as a Discovery Platform for Electrocatalysis. *Joule* **3**, 834–845 (2019).
24. Ma, S. *et al.* Electroreduction of Carbon Dioxide to Hydrocarbons Using Bimetallic Cu–Pd Catalysts with Different Mixing Patterns. *J. Am. Chem. Soc.* **139**, 47–50 (2017).
25. Hoang, T. T. H. *et al.* Nanoporous Copper–Silver Alloys by Additive-Controlled Electrodeposition for the Selective Electroreduction of CO<sub>2</sub> to Ethylene and Ethanol. *J. Am. Chem. Soc.* **140**, 5791–5797 (2018).
26. Zhong, M. *et al.* Accelerated discovery of CO<sub>2</sub> electrocatalysts using active machine learning. *Nature* **581**, 178–183 (2020).
27. Koolen, C. D., Luo, W. & Züttel, A. From Single Crystal to Single Atom Catalysts: Structural Factors Influencing the Performance of Metal Catalysts for CO<sub>2</sub> Electroreduction. *ACS Catal.* 948–973 (2022) doi:10.1021/acscatal.2c03842.
28. Karapinar, D. *et al.* Electroreduction of CO<sub>2</sub> on Single-Site Copper-Nitrogen-Doped Carbon Material: Selective Formation of Ethanol and Reversible Restructuration of the Metal Sites. *Angewandte Chemie International Edition* **58**, 15098–15103 (2019).
29. Xu, H. *et al.* Highly selective electrocatalytic CO<sub>2</sub> reduction to ethanol by metallic clusters dynamically formed from atomically dispersed copper. *Nat Energy* **5**, 623–632 (2020).
30. Su, X. *et al.* Complementary Operando Spectroscopy identification of in-situ generated metastable charge-asymmetry Cu<sub>2</sub>–CuN<sub>3</sub> clusters for CO<sub>2</sub> reduction to ethanol. *Nat Commun* **13**, 1322 (2022).
31. Reinmann, R. & Akram, M. Temporal investigation of a fast spark discharge in chemically inert gases. *J. Phys. D: Appl. Phys.* **30**, 1125 (1997).
32. Schwyn, S., Garwin, E. & Schmidt-Ott, A. Aerosol generation by spark discharge. *Journal of Aerosol Science* **19**, 639–642 (1988).

33. Maisser, A., Barmounis, K., Attoui, M. B., Biskos, G. & Schmidt-Ott, A. Atomic Cluster Generation with an Atmospheric Pressure Spark Discharge Generator. *Aerosol Science and Technology* **49**, 886–894 (2015).
34. Lee, D. C., Yang, H. N., Park, S. H. & Kim, W. J. Nafion/graphene oxide composite membranes for low humidifying polymer electrolyte membrane fuel cell. *Journal of Membrane Science* **452**, 20–28 (2014).
35. Yang, F. *et al.* Highly Efficient CO<sub>2</sub> Electroreduction on ZnN<sub>4</sub>-based Single-Atom Catalyst. *Angewandte Chemie International Edition* **57**, 12303–12307 (2018).
36. Hursán, D. *et al.* Morphological Attributes Govern Carbon Dioxide Reduction on N-Doped Carbon Electrodes. *Joule* **3**, 1719–1733 (2019).
37. Hursán, D. *et al.* CO<sub>2</sub> Conversion on N-Doped Carbon Catalysts via Thermo- and Electrocatalysis: Role of C–NO<sub>x</sub> Moieties. *ACS Catal.* **12**, 10127–10140 (2022).
38. Meng, D.-L. *et al.* Highly Selective Tandem Electroreduction of CO<sub>2</sub> to Ethylene over Atomically Isolated Nickel–Nitrogen Site/Copper Nanoparticle Catalysts. *Angewandte Chemie International Edition* **60**, 25485–25492 (2021).
39. Li, S. *et al.* Boosting CO<sub>2</sub> Electrochemical Reduction with Atomically Precise Surface Modification on Gold Nanoclusters. *Angewandte Chemie International Edition* **60**, 6351–6356 (2021).
40. Feng, J. *et al.* A Mn–N<sub>3</sub> single-atom catalyst embedded in graphitic carbon nitride for efficient CO<sub>2</sub> electroreduction. *Nat Commun* **11**, 4341 (2020).
41. Gutić, S. J. *et al.* Electrochemical tuning of capacitive response of graphene oxide. *Phys. Chem. Chem. Phys.* **20**, 22698–22709 (2018).
42. Cofell, E. R. *et al.* Potential Cycling of Silver Cathodes in an Alkaline CO<sub>2</sub> Flow Electrolyzer for Accelerated Stress Testing and Carbonate Inhibition. *ACS Appl. Energy Mater.* **5**, 12013–12021 (2022).
43. Beverskog, B. & Puigdomenech, I. Revised Pourbaix Diagrams for Copper at 25 to 300°C. *J. Electrochem. Soc.* **144**, 3476 (1997).
44. Ravel, B. & Newville, M. ATHENA, ARTEMIS, HEPHAESTUS: data analysis for X-ray absorption spectroscopy using IFEFFIT. *J. Synchrotron Rad* **12**, 537–541 (2005).
45. Frenkel, A. Solving the 3D structure of metal nanoparticles. *Zeitschrift für Kristallographie - Crystalline Materials* **222**, 605–611 (2007).
46. Marinkovic, N. S., Sasaki, K. & Adzic, R. R. Determination of Single- and Multi-Component Nanoparticle Sizes by X-ray Absorption Spectroscopy. *J. Electrochem. Soc.* **165**, J3222 (2018).
47. Cook, A. W., Jones, Z. R., Wu, G., Scott, S. L. & Hayton, T. W. An Organometallic Cu<sub>20</sub> Nanocluster: Synthesis, Characterization, Immobilization on Silica, and “Click” Chemistry. *J. Am. Chem. Soc.* **140**, 394–400 (2018).

## 6.7. Supporting Information

### Note S1. Experimental part related to support synthesis

As catalyst support, a selection of materials was chosen based on their activity in the  $\text{CO}_2\text{RR}$ , overall conductivity, wettability, high-surface area, diverse heteroatom functionalities, scalability and overall economics from inhouse developed<sup>1</sup> as well as the literature inspired syntheses (**Figure S1**).<sup>2,3, 4,5,6</sup> In brief, the materials produced which were N-edge functionalized (**Figure S1A,B**) were synthesized by mixing graphene nanoplatelets (Graphene Supermarket AO-4, 1 g) or multiwalled carbon nanotubes (PlasmaChem GmbH, 1g) with urea (Sigma Aldrich >99%, 3 g) and ball milled at 500 rpm for 48 hr at 20:1 ball ( $\text{ZrO}_2$ ) to reactant mass ratio under nitrogen atmosphere.<sup>5,6</sup> The products were washed and collected in i-PrOH reaching a concentration of 30 mg mL<sup>-1</sup>. The N-doped carbon black based material was synthesized via a protocol adapted from Yang et al. (**Figure S1C**).<sup>4</sup> In brief, Vulcan carbon black (FuelCellStore, 900 mg) was oxidized by means of mixing with an aqueous  $\text{HNO}_3$  solution (Sigma Aldrich  $\geq 65\%$ , 30 mL) and heated to 80 °C whilst stirring under reflux for 3 hrs. The oxidized carbon black was collected with

50 mL of water and washed until neutral pH  $\sim 6.8$  was reached. The washed product was dried overnight under vacuum of which 150 mg was mixed with urea in a mortar (Sigma Aldrich >99%, 1.5 g). The mixture was placed in a ceramic boat and heated to 800 °C in 80 min, kept for 60 min at 800 °C and then cooled naturally to r.t. all under Ar atmosphere. The 500 mg of NCB-NP were washed and collected with i-PrOH reaching a concentration of 30 mg mL<sup>-1</sup>. Graphene oxide nanoparticles were produced according to a previously reported synthesis (**Figure S1D**).<sup>1</sup>

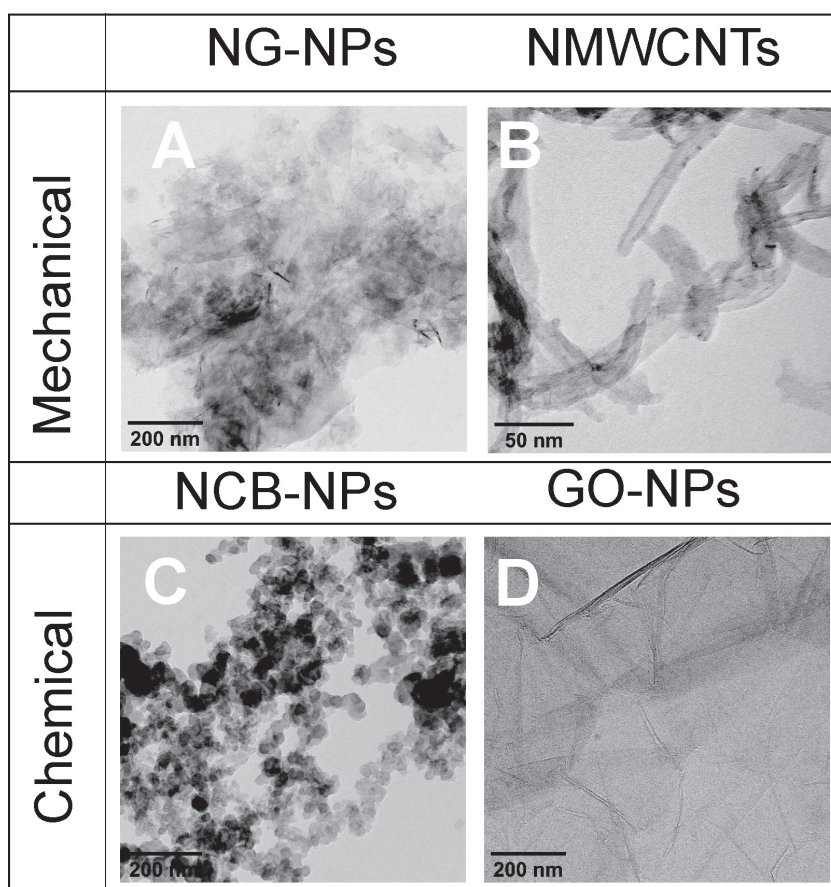


**Figure S1.** BF-TEM images of the carbonaceous support materials synthesized for cluster immobilization. A-B) Produced via the mechanical route i.e. ball milling that are nitrogen rich: NG-NPs<sup>5</sup>, NMWCNTs.<sup>5,6</sup> C-D) Produced via chemical routes i.e. pyrolysis and oxidation: NCB-NPs<sup>4</sup> and GO-NPs<sup>1</sup>, respectively. A) N-edge functionalized graphene nanoparticles. B) N-edge functionalized multiwalled carbon nanotubes. C) N-doped carbon black nanoparticles. D) Graphene oxide nanoparticles.

## Note S2. Experimental part related to cluster production

In order to achieve a scalable synthesis of metal oxide clusters of controllable size, composition and (surface) loading, we investigated the production of metal oxide clusters via spark ablation, in which two metal electrodes of arbitrary composition are ablated via a spark generated plasma (>5000 K, Ar) to produce particles in the aerosol.<sup>7,8,9,10,11</sup> Traditionally, spark ablation has been used to produce nanoparticles of a single element in the size range 5-20 nm (i.e. C, Ag, Pd, Zr, and Nb).<sup>7,8</sup> More recently, multicomponent materials have been produced as well including immiscible mixtures and high-entropy alloys on various substrates but all of sizes > 5 nm.<sup>12,9,10</sup> On

the other hand, spark ablation has also been used to produce atomically precise metal (oxide) clusters (<2 nm) but only of single element (Ag, and Au) and purely in the aerosol and more importantly, not at practically relevant production levels (~pg/hrs).<sup>13,11</sup> In here, we have achieved a scalable synthesis of Cu(Ag) metal oxide clusters <2 nm with a 6-orders higher mass production rate (μg/hrs). To produce such clusters of well-defined size and composition, and especially at high production rates, a highly specific spark generator configuration was chosen that optimized a set of parameters to control 1) the size, 2) the production rate and finally 3) the composition (**Figure S2**).



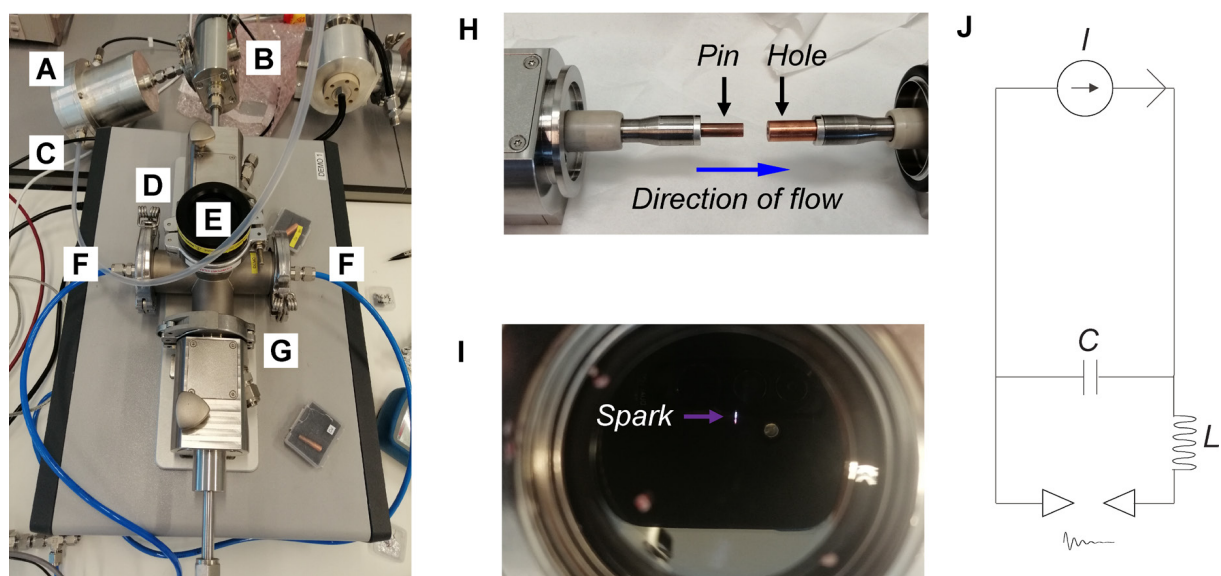


**Figure S2.** Description of the spark ablation and electrostatic deposition experimental set-up, operation, and electrical components. (A) Faraday cup used to collect either negatively or positively charged particles from the aerosol. The measured current (via an electrometer) allows to determine the number of ions hitting the cup per unit of time giving a measure of the ablation rate (cluster production rate). (B) Deposition chamber allowing for a filter deposition in which the entire aerosol flow is passed through a substrate as well as an electrostatic deposition method<sup>14</sup> in which a bias is applied to a substrate and as such only particles of opposite polarity are adhered to it. (C) Aerosol exhaust. (D) Positive electrode (grounded). (E) Spark chamber. (F) Carrier gas (Ar) flow inlet. Direction of flow is from (E) to (B). (G) Negative electrode. (H) Pin-to-hole configuration of the electrode set-up of the spark ablator showing two Cu electrodes. Exchanging the pin or negative electrode for Ag allows for the production of bimetallic clusters. (I) Picture of the spark in operation. (J) Resistance-inductance-capacitance (RLC) electrical circuit, in which  $I$  denote the power supply.  $C$  denote(s) the capacitor,  $L$  denotes the inductor needed to store potential energy via the magnetic field needed for the oscillatory nature of the spark. The spark is indicated by the damped exponential with a  $\sim 100$  ns time constant of the oscillation of the spark between the grounded and negative electrode.

## Note S2.1. Controlling the particle size

The first objective, was to reduce the particle size, which can be estimated based on Eq. 1:

$$D \approx \left( \frac{3\beta V_{eff} \dot{m}}{\rho \pi Q^2} \right)^{1/3} \quad (1)$$

in which  $Q$  carrier gas flow rate in this case Ar [ $\text{m}^3 \text{s}^{-1}$ ],  $V_{eff}$  the effective volume in the spark chamber [ $\text{m}^3$ ],  $\beta$  the coalescence kernel [ $\text{m}^3 \text{s}^{-1}$ ], which is rate at which two particles coalesce, the mass production rate [ $\text{kg s}^{-1}$ ] and  $\rho$  the density of the material ablated [ $\text{kg m}^{-3}$ ].<sup>15,16,9</sup> Therefore, three parameters needed to be optimized: 1) the  $V_{eff}$  should be kept at a minimum, 2) the flow rate should be maximized and, finally, 3) the mass production rate should be minimized. To keep the effective volume as small as possible, we opted for a dual-mixed flow geometry using two inlets (**Figure S2A-G**) and a pin-to-hole configuration (**Figure S2H**).<sup>17</sup> Further, we chose a gas flow rate of a factor of 2.5 higher with respect to a conventional nanoparticle spark generated synthesis ( $\sim 6 \text{ nm Au}$ )<sup>15</sup>, effectively reducing the particle size by a factor  $\sim 2$ . And lastly,

we reduced the ablation rate, which is given by Eq. 2:

in which  $\Delta m = \Delta m f \approx E_s c f$  (2) the electrode mass or ablated mass [ $\text{kg}$ ] and  $f$  the repetition frequency of the spark [ $\text{s}^{-1}$ ], which roughly equates to the product of the energy per spark ( $E_s$ ) and  $c$ , a material dependent constant [ $\text{kg J}^{-1}$ ], by reducing the energy per spark (**Figure S2I**). The  $E_s$  can be determined via Eq. 3:

$$E_s = \frac{1}{2} C U^2 \quad (3)$$

in which  $U$  denoted down-voltage [V] and  $C$  the capacitance [F] (**Figure S2J**). By bringing the energy per spark down by an order of magnitude (1 nF), the particle size should be reduced further by an estimated factor of  $\sim 2.2$ , effectively pushing the particle size in to the cluster regime ( $\sim 1 \text{ nm}$ ).

## Note S2.2. Optimizing the ablation rate

The second objective, was to enhance the production rate. Therefore, we maximized the spark repetition frequency to  $\sim 10$  MHz by enhancing the charging current of the capacitor banks whilst maintaining a stable spark and preventing continuous plasma formation, which would destroy the size distribution as the well-defined nature of the particles is a direct consequence of the pulsating nature of the spark (1 mA, **Figure S2K**).<sup>18</sup> Further, as the ratio between

positively and negatively charged particles differs in the cluster regime as well as their most frequently observed size<sup>11</sup>, we investigated the effect of charge as well. **Figure S3** shows the effect of capacitance and cluster charge on both the particle size and production rate for a Cu-Cu electrode configuration (i.e. **Figure S2H**).

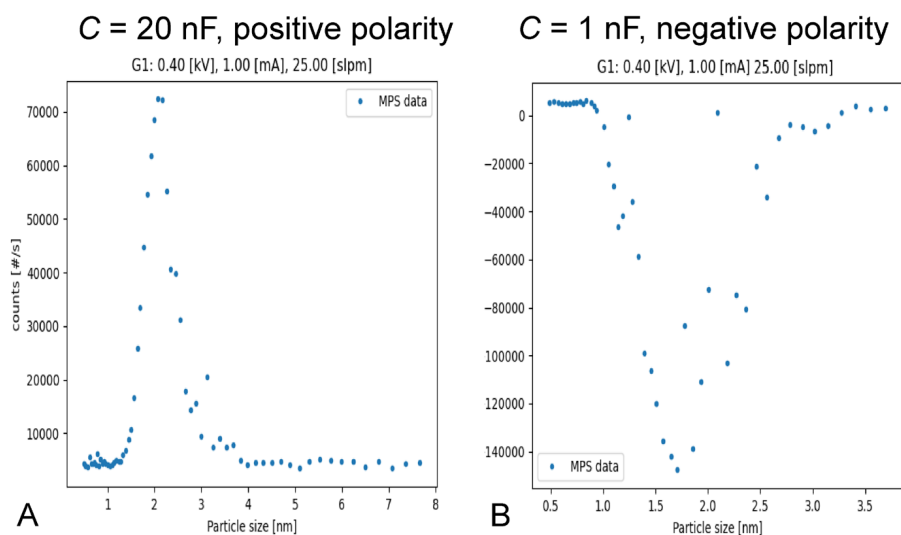


**Figure S3.** Size distributions of charged clusters produced in the aerosol as measured by a differential mobility analyzer (DMA) to determine the particle mobility (and thus size) and the production rate measured via the Faraday cup depicted in **Figure S2A** and an electrometer. The voltage scan of the DMA is converted to a particle size. The current measured by the electrometer is converted to a number concentration and thus the production rate (min losses). (A) The Cu oxide positively charged particle size distribution with an average size of  $\sim 2.1$  nm, a  $7 \times 10^5 \text{ s}^{-1}$  production rate, at 0.4 kV spark discharge voltage, 1 mA charging current, 25 lpm aerosol gas flow and 20 nF capacitance. (B) The Cu oxide size distribution of negatively charged particles with the average size of 1.6 nm and double the production rate at 1 nF capacitance but all other parameters kept the same ( $1.4 \times 10^6 \text{ s}^{-1}$ ).

### Note S2.3. Controlling the particle composition

The third and final objective was to control the particle composition by mixing in a second element. This can be achieved simply by switching out either the pin or the hole electrode for one of a different element (in this case Ag).<sup>10</sup> Since the negatively charged electrode will have the highest relative ablation rate due to its attraction

of the  $\text{Ar}^+$  ions existing in the plasma resulting in rapid ion bombardment<sup>19</sup>, and we need a majority Cu for a good electrochemical performance, we opted to swop this electrode. **Figure S4** shows the size distribution with a Cu-pin, Ag-hole configuration.

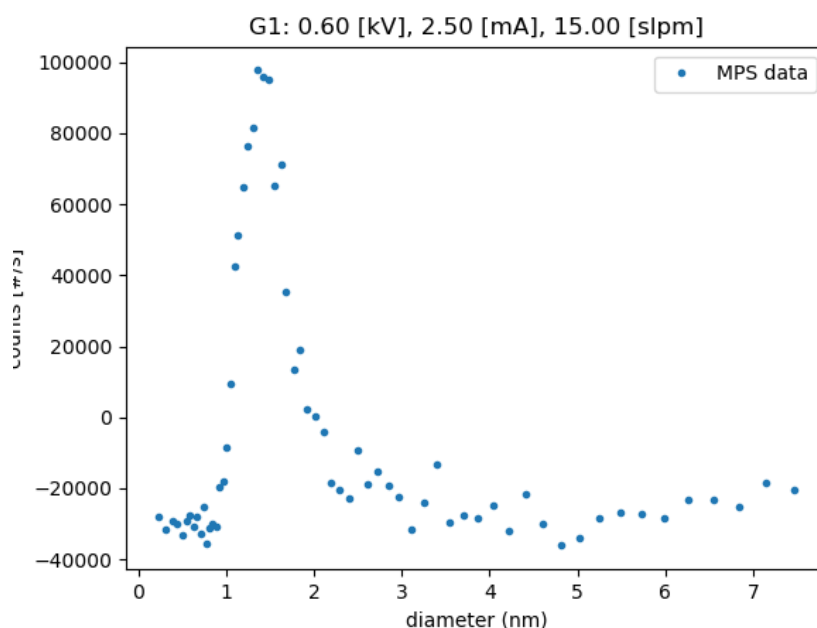


**Figure S4.** Size distribution and production rate of the positively charged Cu-Ag oxide clusters with an average size of 1.5 nm, which showed the smallest size and highest production rate whilst maintaining a stable spark.

## Note S3. Experimental part related to electrostatic precipitation deposition.

In order to accurately deposit the metal oxide clusters on a substrate with a well-defined spot size to control the loading/dispersion on various substrates, we opted for the use of electrostatic precipitation.<sup>14</sup> Since metal oxide clusters carry for the large part a charge, they are well suited to be extracted from the aerosol using an applied bias. Therefore, we placed a TEM grid coated with support material orthogonal to the particle beam (to minimize diffusion deposition) in the deposition chamber indicated in **Figure S2B**. By applying a bias of (+/-)60 V, all the particles of opposite polarity could thereby be deposited on to the TEM grid by concentrating the particle beam into a spot size equal to the TEM grid diameter. An optimized loading of 1.0 mg cm<sup>-2</sup> MWCNTs, 0.27 mg cm<sup>-2</sup> NG-NPs, 0.13 mg cm<sup>-2</sup> NCB-, 0.050 mg cm<sup>-2</sup> GO-NPs support was used for uniform sub-monolayer coating of the TEM grid (**Figure S1**). The particle spot size can be determined via Eq. 4:

$$r_{spot} = \sqrt{\frac{Q}{\pi V_d}} \quad (4)$$

in which  $Q$  is the aerosol flow rate [m<sup>3</sup> s<sup>-1</sup>] and  $V_d$  is the particle velocity [m s<sup>-1</sup>], which can be estimated based on the particle mobility (measured via the DMA) and the electric field applied. The projected 2D coverage of such an electrostatic precipitation deposition can then be estimated via Eq. 5:

$$coverage = \frac{N_p 4\pi r_p^2 t_d}{4\pi r_{spot}^2} \quad (5)$$

in which  $N_p$  denotes the particle production rate [s<sup>-1</sup>],  $r_p$  the particle radius [m], and  $t_d$  the deposition time [s]. For the electrostatic precipitation experiments, we report coverage in the form of partial monolayers as determined for a 2D projection on a flat surface. The actual coverage is factors smaller due to the added depth-profile of the 3D surface.

## Note S4. Experimental part related to cluster immobilization.

Since the clusters produced have >70% of their atoms at the surface, which are highly undercoordinated, they are extremely reactive and agglomerate and sinter easily. Therefore, cluster immobilization is no mean task. Here, we have studied the stability of (bi)metal oxide clusters on various carbonaceous supports: N-doped carbon black NPs (NCBNPs), graphene oxide NPs (GONPs), N-edge functionalized graphite NPs (NGNPs), and finally N-edge functionalized multiwalled carbon nanotubes (NMWCNTs). The synthesis of these substrates is described elsewhere. Here we report the cluster immobilization and stabilization via the electrostatic precipitation deposition study, described in **Note S3**, instead. We observed a deposition equivalent of 0.5 ML of CuO and CuAgO clusters in 2D projection with BF-TEM on all four supports (**Figure S5**). For NCB, GO and NG, coated with CuO, no apparent particles could be observed (**Figure S5A, C-D**), which is a direct result of the low thickness contrast and low density of CuO. Instead, for the NMWCNTs-based sample, particle agglomeration had occurred as particles >20 nm could be distinguished (**Figure S5B**). Interestingly, for the CuAgO particles, a similar effect could be discerned as here larger particles could be observed

likewise (**Figure S5F**). Contrarily, particle agglomerates were absent for the NCB, NG, and GO coated materials with particles <2 nm clearly visible (**Figure S5E, G-H**).

To further investigate the nature of the particles (or the absence thereof) deposited on the various supports as well as their apparent agglomeration when deposited on NMWCNTs, we conducted a STEM-HAADF/EDXS study. Here, we selected one unstable material, MWCNT, and a stable one, NCB, and investigated both the CuO as well as CuAgO functionalization more thoroughly. **Figure S6** shows the outcome of CuO deposition on NCB. Indeed, a homogenous distribution of Cu particles ~1.5 nm can be observed at the particle surface comparing well with the measured size prior to deposition.

Instead, for the mass equivalent CuO deposition on the MWCNTs, larger agglomerates >10 nm are directly visible in the STEM-HAADF image (**Figure S7**). STEM-EDXS further confirms the Cu nature of the particles.

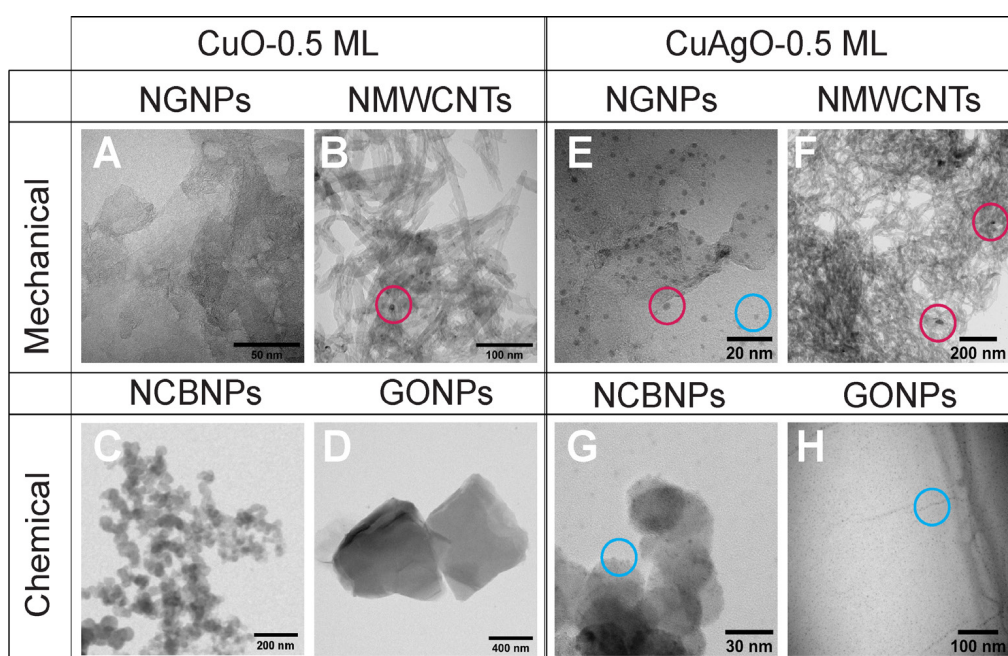


**Figure S5.** BF-TEM images of the electrostatic precipitation deposition of 0.5 mL equivalent of 1.6 nm CuO and 1.5 nm CuAgO clusters on four different carbonaceous supports. (A-D) NGNPs and NMWCNTs (produced mechanochemically) and NCBNPs and GONPs (produced chemically) coated with CuO clusters, respectively. No apparent particles can be observed with BF-TEM other than in (B). This is due to the small particle size, low relative density of CuO ( $6.31 \text{ g cm}^{-3}$ ) and therefore low contrast in bright-field mode. Instead, in (B), particle agglomeration had occurred resulting in the observed particle size  $>20 \text{ nm}$ . (E-H) NGNPs, NMWCNTs, NCBNPs, and GONPs coated with CuAgO clusters, respectively. Particles  $<2 \text{ nm}$  could clearly be observed for NCB, NG and GO based supports and indicated by the blue circles. However, the particle size distribution for the NG-NPs indicated some form of sintering as the mean size shifted from  $\sim 1.5$  to  $2.1 \pm 0.6 \text{ nm}$  ( $>2 \text{ nm}$  particle indicated by red circle). Further, for the NMWCNTs, particle agglomerates  $>20 \text{ nm}$  could be observed similar to the CuO coated system confirming the high surface mobility on carbon nanotubes (red circles, respectively).

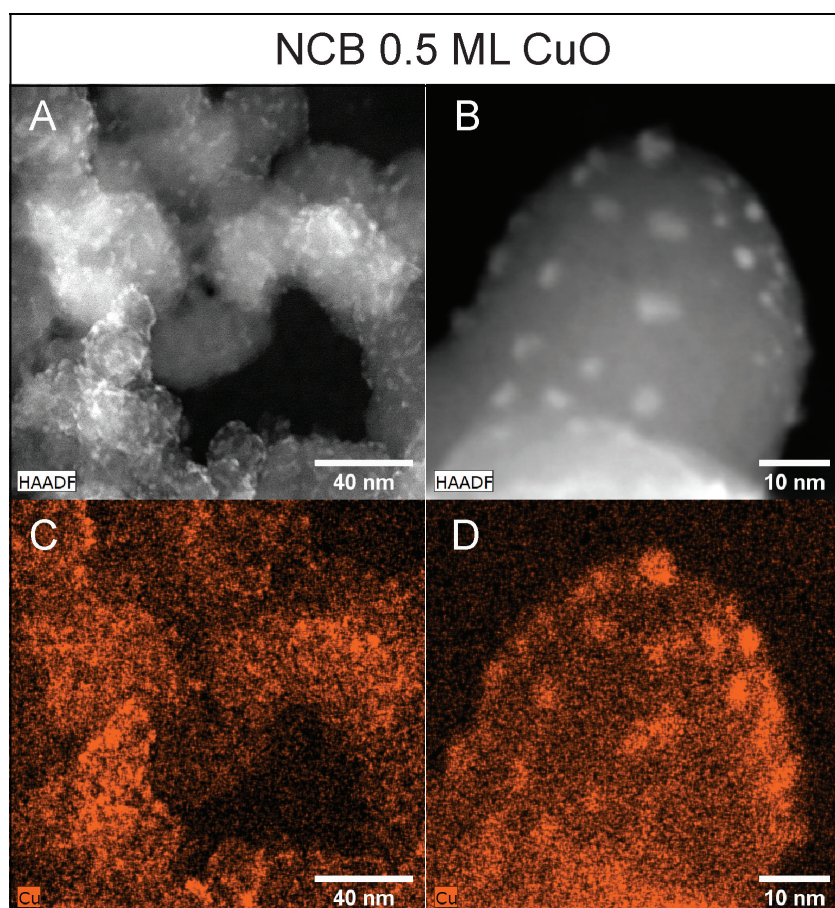


**Figure S6.** Advanced EM investigation of the 0.5 ML of CuO clusters electrostatically precipitated on the NCB support. (A-B) STEM-HAADF image at 0.45 and 1.25 MX magnification, respectively, showing a homogeneous distribution of higher contrasting particles at the amorphous carbon substrate surface. The average particle size of  $1.5 \pm 0.5$  nm compares well to the 1.6 nm determined by the DMA prior to deposition. (C-D) STEM-EDXS Cu elemental map of the images depicted in (A-B) confirming the Cu nature of the particles.



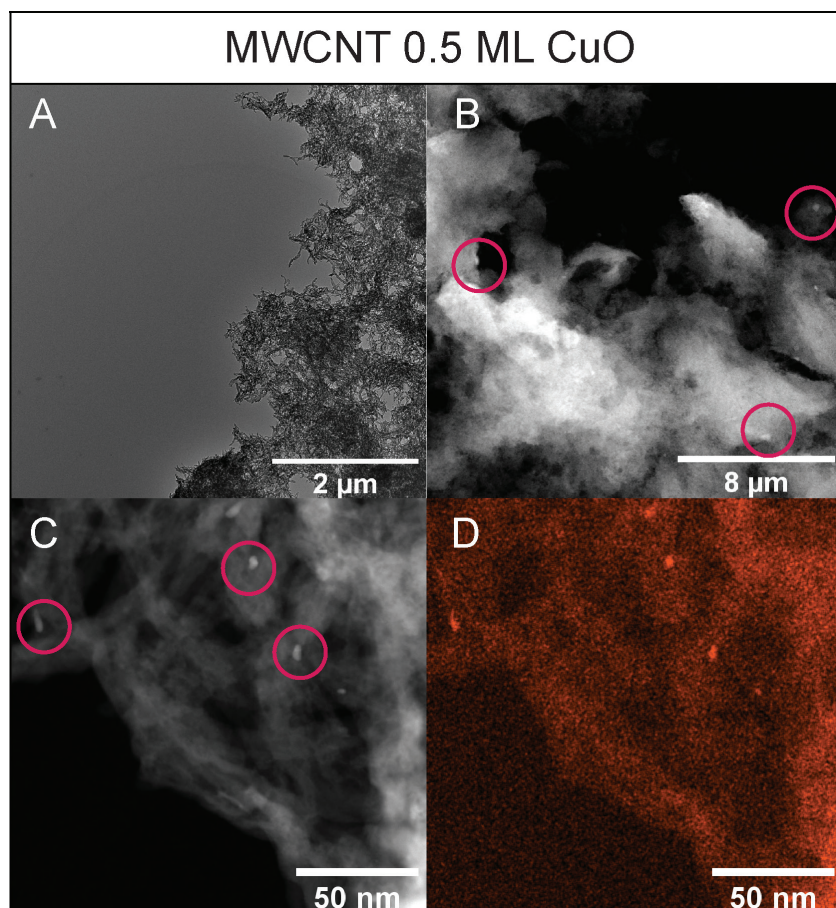


**Figure S7.** Advanced EM investigation of the 0.5 ML of CuO clusters electrostatically precipitated on the MWCNT support. (A) BF-TEM image of the substrate. (B) STEM-HAADF image of the coated substrate with >10 nm agglomerates visible indicated by the red circles. (C) STEM-HAADF image with clearly identifiable agglomerates. (D) STEM-EDXS elemental map of the image in (C) showing the Cu nature of the agglomerates.

**Figure S8** shows the outcome of CuAgO deposition on NCB. The average cluster size determined with STEM-HAADF of  $1.4 \pm 0.33$  nm overlays well with the DMA determined  $\sim 1.5$  nm (**Figure S8A**). Therefore, we can conclude that the particles produced by the spark have been successfully deposited without agglomeration. The high N-content in the NCB samples as well as the high surface area (average C-NP size  $\sim 50$  nm) facilitate immobilization and stabilization of the clusters (**Figure S8B**). STEM-EDXS puts the composition of the CuAgO clusters at  $\text{Cu}_{0.42}\text{Ag}_{0.08}\text{O}_{0.5}$  (**Figure S7C**). Further, a second particle mode could be detected that was rich in Ag (**Figure S8D-F**). However, its relative abundance was about two orders smaller and could therefore be neglected in the electrochemical performance considerations (**Figure S8G-F**).

**Figure S9** shows the outcome of CuAgO deposition on MWCNTs. Similar to what could be observed in BF-mode, STEM-HAADF pointed towards various agglomerates  $> 20$  nm (**Figure S9A,C**). STEM-EDXS suggested Ag-species as the most mobile as most agglomerates were rich in Ag (**Figure S9B,**

**D**). Cu instead, showed stronger interaction with the support and remained relatively well dispersed, similar to what had been observed for CuO clusters. Finally, as a control experiment, we acquired a STEM-EDX spectrum confirming the absence of both Cu and Ag in the uncoated MWCNTs (**Figure S9E, F**).

An attempt was made to explain the weaker bonding of the clusters to the MWCNTs by investigating the work function of the supports arguing that stronger bonding should occur for the support with the lowest binding energy (**Figure S10**). Interestingly, the secondary electron cut-offs (SECO) of the support materials, which is equivalent to the work function, could not explain the trend. Following the work function, bonding to the MWCNTs should be second best to NCB supported clusters.

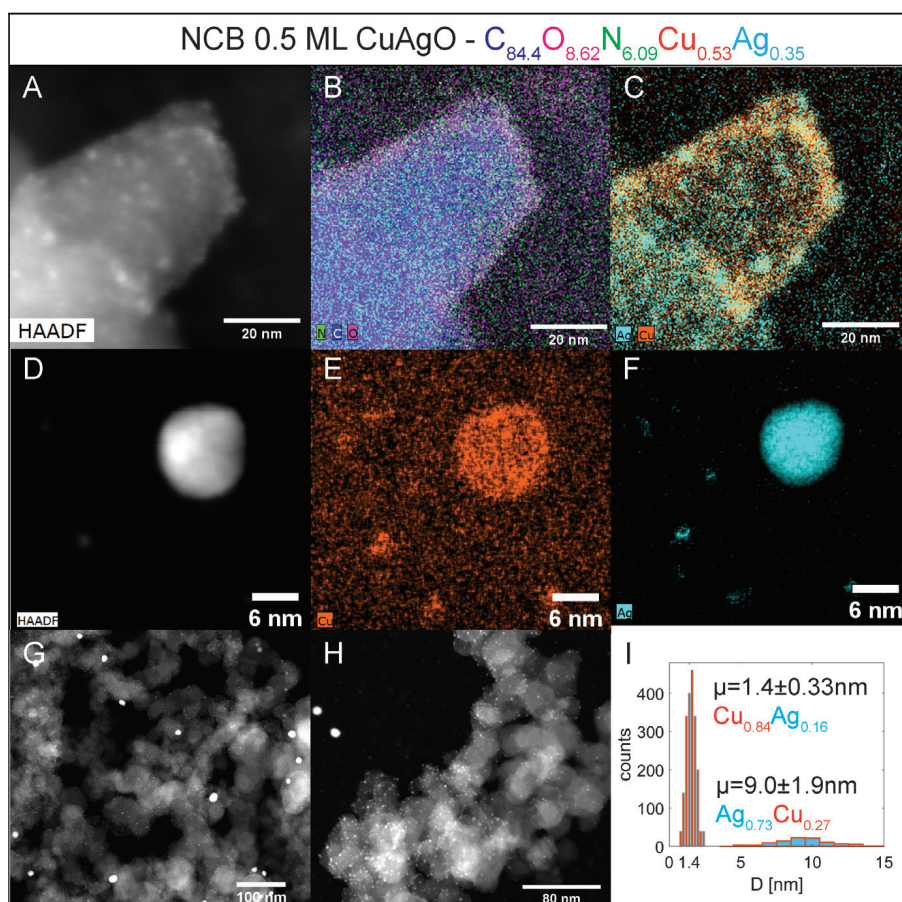


**Figure S8.** Advanced EM investigation of the 0.5 ML of CuAgO clusters electrostatically precipitated on the NCB support. The TEM grid used was of Au to minimize interference. The composition offered in the title was determined by STEM-EDXS analysis. Note that the grid contains C as well. (A) STEM-HAADF image of the CuAgO clusters with average size of  $1.4 \pm 0.33$  nm. The measured size distribution compares well to the one measured via the DMA at 1.5 nm. (B) STEM-EDXS elemental map of the HAADF image in (A) showing N, C, O, in green, blue, and magenta, respectively. The N doping is as high as 6 at. %. (C) STEM-EDXS elemental map of the HAADF image in (A) of Cu and Ag in orange and turquoise, respectively. Determined Cu:Ag ratio  $\sim 5:1$ . (D) STEM-HAADF image of large  $9 \pm 1.9$  nm particle. (E) STEM-EDXS elemental map of the HAADF image in (D) showing Cu in orange. (F) STEM-EDXS elemental map of the HAADF image in (D) showing Ag in turquoise. Determined Cu:Ag ratio:  $\sim 1:2.7$ . This particle represents the second mode that is being produced at the 0.6 kV, 2.5 mA, and 15 lpm spark generator settings. (G) STEM-HAADF low-magnification image showing the relative abundance of the Ag rich particle. (H) STEM-HAADF image showing the high relative abundance of the CuAgO clusters. (I) Quantification of the relative abundance of both particle modes by observing a 630x630 nm area. Nearly 2-order larger abundance of CuAgO clusters vs Ag-rich NP. Average Cu:Ag composition calculated considering both relative abundance and particle mass is 2.1:1, which compares well to the composition determined via XPS (see **Figure S16**, **Table S1**).

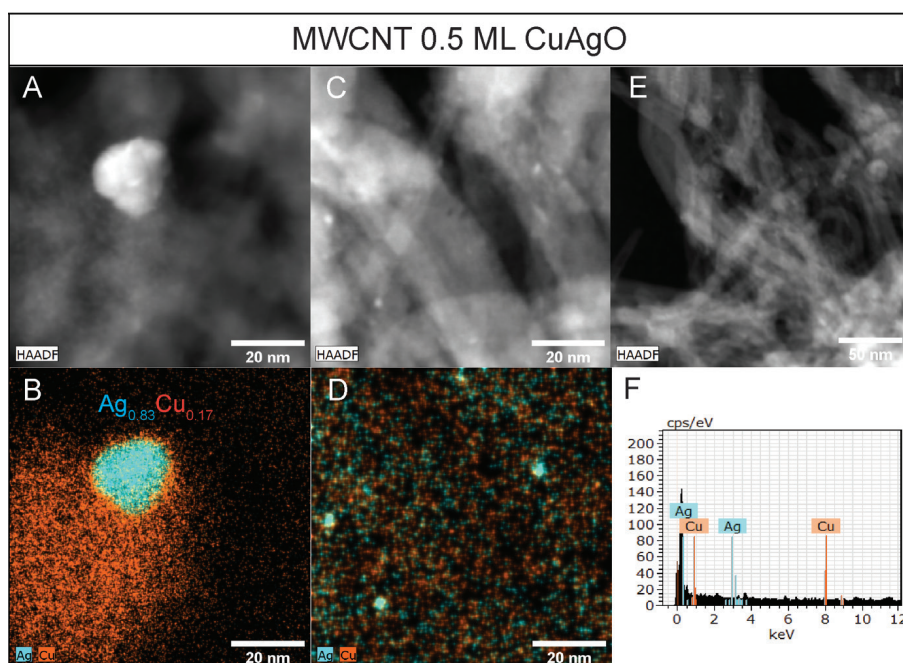


**Figure S9.** Advanced EM investigation of the 0.5 ML of CuAgO clusters electrostatically precipitated onto the MWCNT support. (A) STEM-HAADF image of agglomerate >20 nm. (B) STEM-EDXS elemental map of the image in (A) with Cu in orange and Ag in turquoise. The particle composition is given in the inset. (C) STEM-HAADF image of > 2 nm particles. (D) STEM-EDXS elemental map of the image in (C), which shows the high Ag content in the particles. (E) STEM-HAADF image of uncoated MWCNTs. (F) STEM-EDXS spectrum of the image in (E) showing the absence of both Cu and Ag prior to deposition.

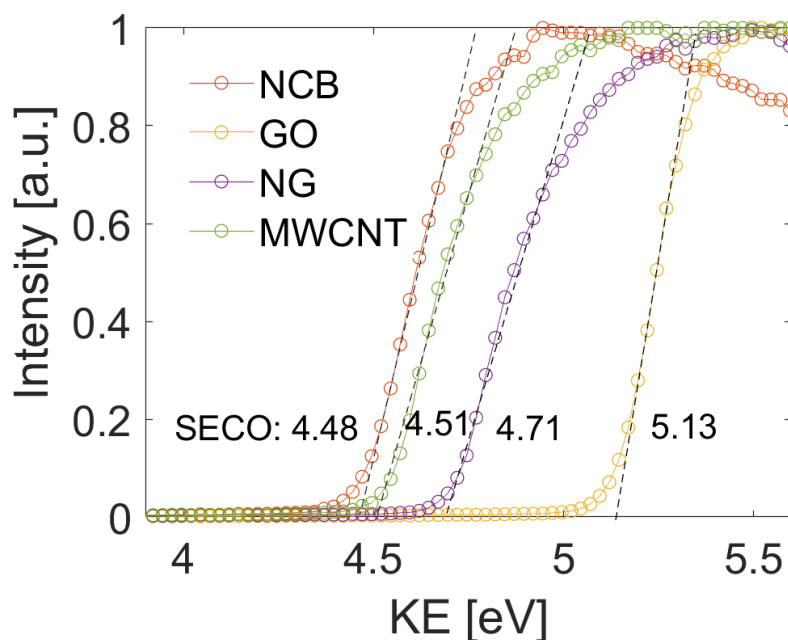


**Figure S10.** Secondary electron cut-off measured with XPS of the heteroatom doped carbonaceous supports.

Instead, we explain the agglomeration of the CuO/CuAgO clusters on the MWCNT substrate by their poor adhesion. The MWCNTs produced in this study, consist of rolled-up graphene nanosheets with possible amine, imines and amides, bond at their tips. The majority of the structure, however, is highly-crystalline, graphene (**Figure S11**). Dietsche et al. showed that in order to stabilize  $\text{Ag}_{13}$  clusters on highly-ordered graphite, defects introduced by sputtering were necessary.<sup>20</sup> Further, both Cu and Ag are fully oxidized as determined by XPS (**Figure S16**). And Ag clusters  $\sim 5$  nm on (110)  $\text{TiO}_2$  have shown to undergo Ostwald ripening at room temperature when exposed to  $\text{O}_2$  as determined by STM proposing a potential growth pathway.<sup>21</sup>

It was argued that  $\text{Ag}_2\text{O}$  was the relevant species to undergo surface diffusion due to its higher mobility than its metallic counterpart. This explains the larger Ag-rich agglomerates observed for the CuAgO MWCNTs coated materials vs the CuO coated ones. Upon the failure of  $\text{Ag}_2\text{O}$  to find a stable ligation site,  $\text{Ag}_2\text{O}$  diffuses rapidly over the surface and agglomerates. Instead, the Cu oxides bond relatively well to the surface and stays better dispersed. Nevertheless, for their high relative instability, we have excluded MWCNTs for any further consideration. Likewise, due the shift in particle size distribution of roughly 33% larger of the CuAgO clusters on NG-NP support, we have excluded them as well.

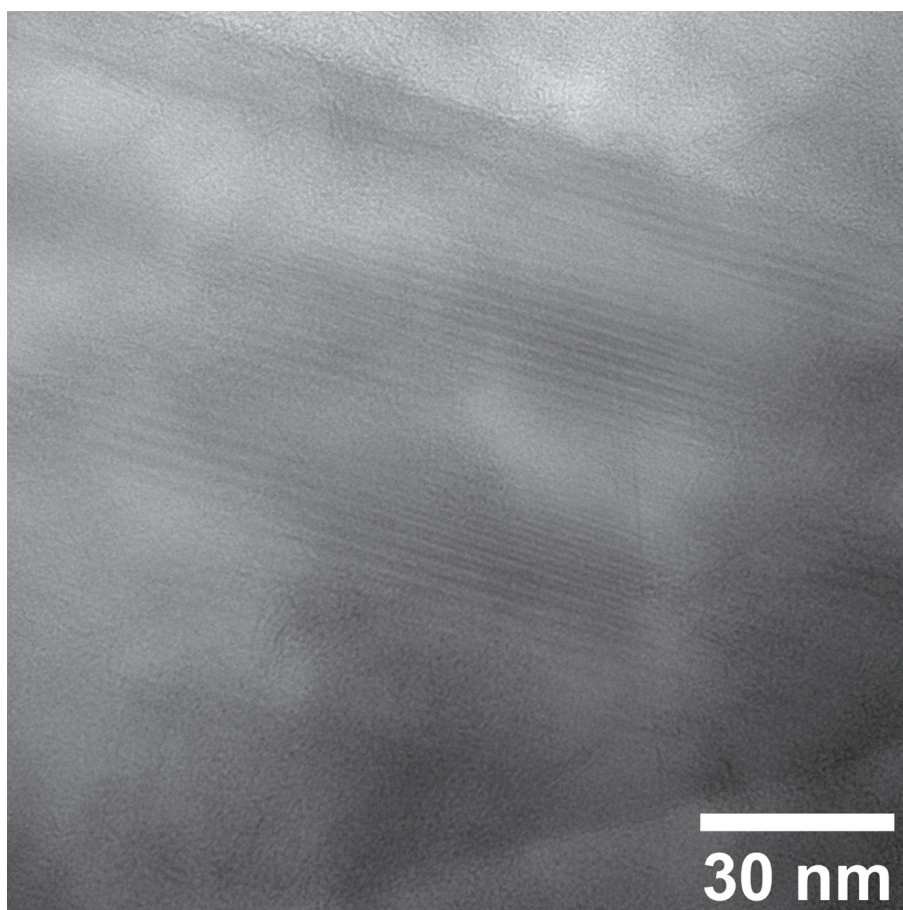


**Figure S11.** BF-TEM image of the bare MWCNTs. Lattice fringes can be discerned showing the crystalline nature of the nanotubes.

## Note S5. Experimental part related to cluster composite electrode production.

In order to test the metal oxide clusters in the electrochemical CO<sub>2</sub> reduction reaction, it is adamant that the cluster carbonaceous support composite will be scaled. Further, for potential flow and membrane assembled electrode cell configurations, the use of a gas diffusion layer support is highly advantageous. Further, to ensure homogeneous cluster coverage and good exposure to the electrolyte, cluster deposition via filtration in which the aerosol gas is directly flowed through a porous support is optimal. Therefore, we designed a Toray TGP-H-60 carbon paper-based gas diffusion electrode with a carbonaceous

support catalyst layer air brushed on top (**Figure S12**).

In order to achieve homogeneous coverage of the carbonaceous heteroatom doped support NPs on the carbon paper, a loading study was performed at different mass loadings for the GO-, NG-, and NCB-NPs based catalyst support inks at 1 mg mL<sup>-1</sup> (**Figure S13**).

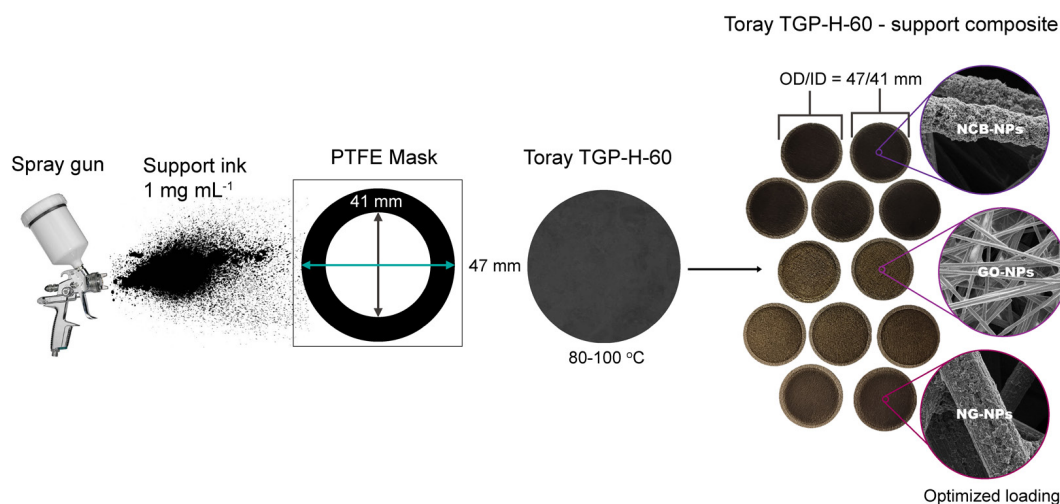


**Figure S12.** Air brush experiment to produce heteroatom-doped carbonaceous support-carbon paper composites. Ink was consisted of 3:1 isopropanol:H<sub>2</sub>O in case of the NCB-, NG-NPs based inks and pure H<sub>2</sub>O for the GO-NPs based ink to prevent flocculation. The carbon paper was heated to 80, and 100 °C, respectively to facilitate solvent evaporation. All inks were sonicated for 30 min prior to spraying.

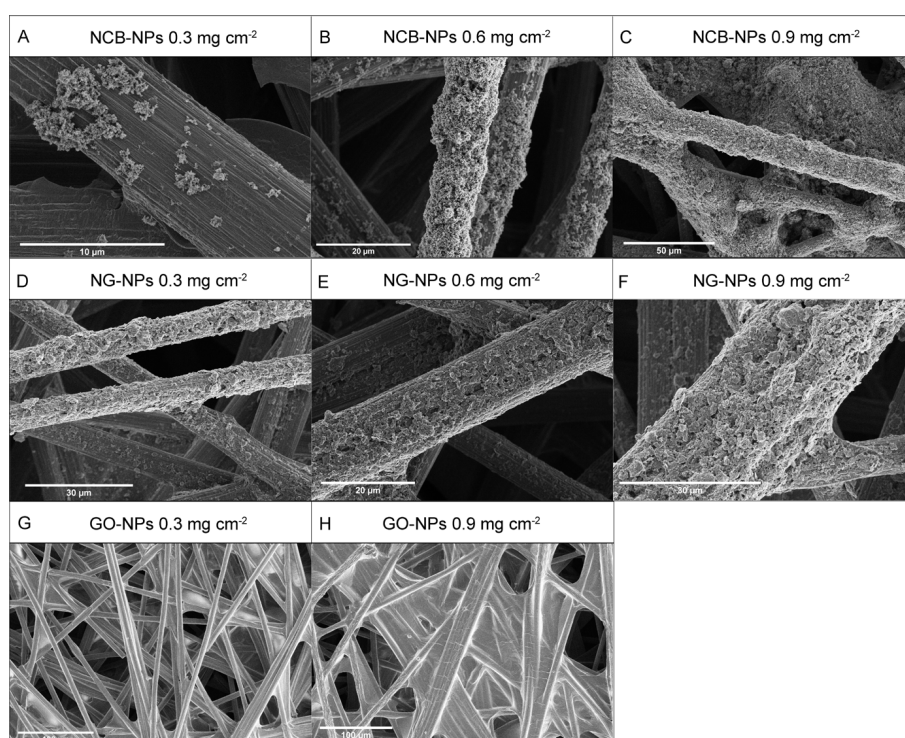


**Figure S13.** Loading study of the airbrushed heteroatom doped carbonaceous support. (A-C) SEM images of NCB-NPs coated on carbon paper at 0.3, 0.6 and 0.9 mg cm<sup>-2</sup>. (D-F) SEM images of NG-NPs coated on carbon paper at 0.3, 0.6 and 0.9 mg cm<sup>-2</sup>. (G-H) SEM images of GO-NPs coated on carbon paper at 0.3 and 0.9 mg cm<sup>-2</sup>. Optimal loading was achieved at 0.3 mg cm<sup>-2</sup> for the GO-NPs, and 0.6 mg cm<sup>-2</sup> for the NCB-, NG-NPs-based composites in that pore blockage was prevented whilst maintaining good coverage allowing for facile aerosol filtration and electrolyte penetration. All cluster immobilization experiments were performed at the optimized catalyst support loading.



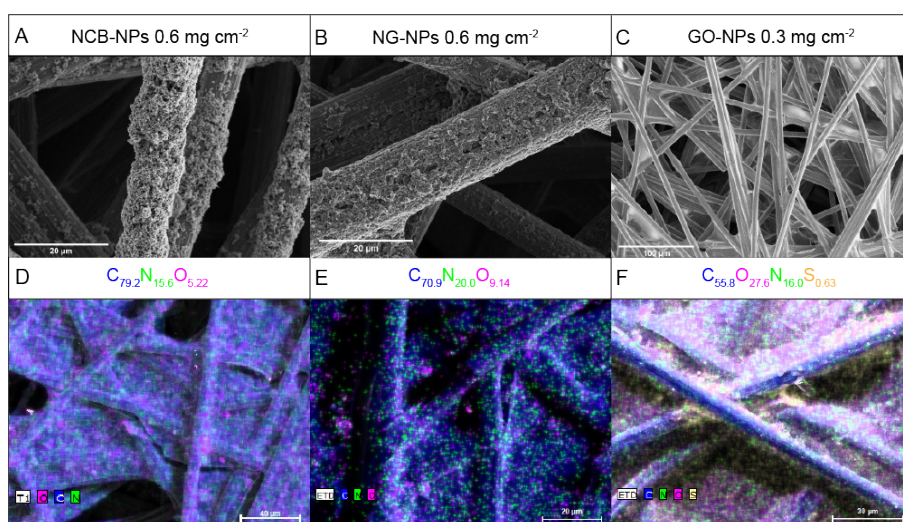


**Figure S14.** Composition study using SEM-EDXS. (A-C) SEM images of the composite materials produced in **Figure S13**. (D-F) SEM-EDXS elemental maps of the composite materials depicted in A-C in which pixels in blue, green, magenta, and yellow depict C, N, O and S, respectively.

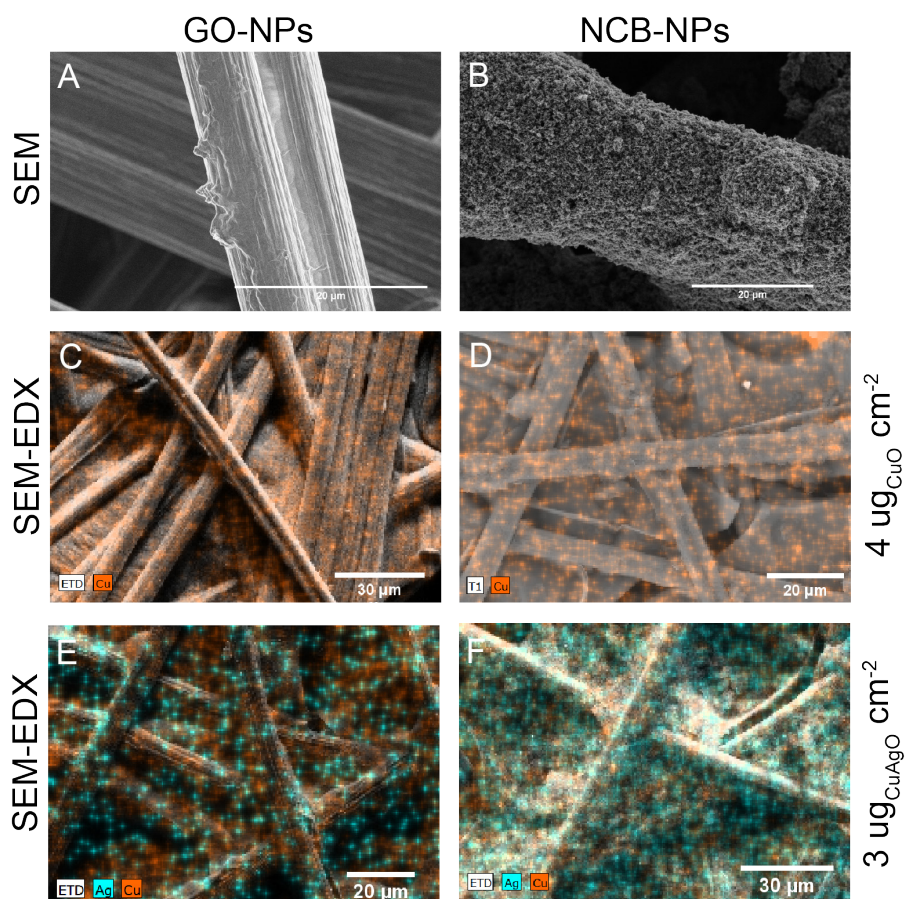


**Figure S15.** Filtration of metal oxide clusters produced via spark ablation on heteroatom doped carbonaceous support composited. Deposition time in all instances 10 hrs. (A,B) SEM image of the Cu oxide cluster coated GO- and NCB-NP composites showing no clear difference with uncoated samples in **Figure S13**. This is due to the fact that the cluster size is below the limit of detection of SEM. (C-D) SEM-EDXS elemental map of the Cu oxide cluster coated GO-, NCB-NP coated composites, respectively, clearly showing a homogenous Cu signal (in orange) proving the successful coating step. Ablation rate determined mass loading of  $4 \text{ ug}_{\text{CuO}} \text{ cm}^{-2}$ . (E-F) SEM-EDXS elemental maps of the CuAg oxide cluster coated GO- and NCB-NP coated composite materials, respectively, showing a homogeneous distribution of Cu and Ag indicated in orange and turquoise, respectively. Ablation rate estimated mass loading of  $3 \text{ ug}_{\text{CuAgO}} \text{ cm}^{-2}$ .

## Note S6. Experimental part related to cluster characterization using XPS.

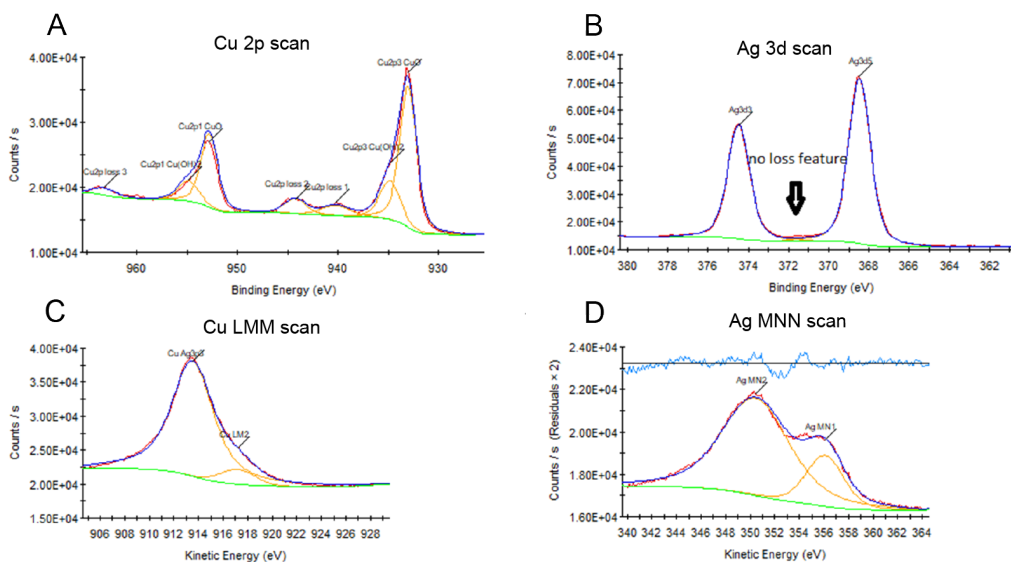
To investigate the oxidation state of both Cu and Ag in the bimetallic clusters excluding the influence of the support we deposited an equivalent amount of CuAg oxide clusters as indicated in **Figure S15** on pure carbon paper and performed XPS (**Figure S16**). To determine the oxidation state after deposition, we performed XPS measurements on the composite 2 hrs (directly) after production (**Figure S16A-D**) and after 7 days (**Figure S16E-H**). Fitting of the Cu 2p and Cu LMM Auger spectrum suggested the presence of both CuO as well as Cu(OH)<sub>2</sub> with the CuO the majority species

at no less than 65 at.%. Determination of the Auger parameter for Ag based on the MNN Auger spectrum of Ag indicated Ag<sub>2</sub>O as the produced species. The high relative presence of -OH species in Cu suggest the oxidation of the clusters had already happened prior to deposition meaning in the aerosol. This can be understood from the following. In air, ~21% is O<sub>2</sub> and ~78% N<sub>2</sub>. This, leaves <1 % for H<sub>2</sub>O. Instead, in Ar, the relative ratio between O<sub>2</sub> and H<sub>2</sub>O is ~1:1, explaining the relatively high OH content in the clusters.

CuAgO clusters	CuAg composition
4 μg cm <sup>-2</sup>	
XPS	Cu <sub>78</sub> Ag <sub>32</sub>
STEM-EDX	Cu <sub>75</sub> Ag <sub>35</sub>

**Table S1.** Composition of the CuAgO clusters as deposited on pure carbon paper (**Figure S16**) containing two modes of particles: clusters of ~1.5 nm and particles of ~9 nm (**Figure S9**). XPS surface composition and the weighted STEM-EDX composition (Cu<sub>84</sub>Ag<sub>16</sub> and Ag<sub>73</sub>Cu<sub>27</sub> 132:1) shows matching results with <5% error showing the extreme conformity of the particle beam produced with the spark.

2 hrs after deposition



7 days after deposition

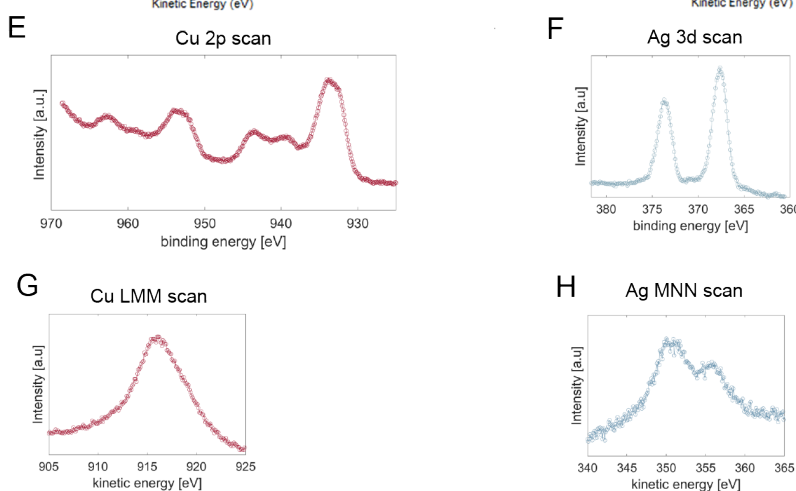


**Figure S16.** XPS study of the oxidation state of the CuAg oxide clusters deposited on carbon paper, 2 hrs (A-D) and 7 days after deposition (E-H). (A) Cu 2p spectrum of the CuAg oxide clusters. Fitting of the 2p spectrum suggests a combination of both CuO (933 eV) and Cu(OH)<sub>2</sub> (935 eV) species, with the relative composition of CuO between 65-75 at.% and 25-35 at.% for Cu(OH)<sub>2</sub>. (B) Ag 3d spectrum showing no loss feature. From the 3d spectrum alone, it is not possible to determine the oxidation state of Ag. (C) Cu LMM Auger spectrum showing a combination of the Ag3p3 peak and the Cu LMM Auger peak. Position of the Cu Auger peak estimated at 917 eV through a fit. (D) Ag Auger spectrum showing the two MNN Ag peaks. The peak position MN1 at 356 eV used to determine the Auger parameter. Auger parameter of Ag of 724, which is much lower than metallic Ag proving the oxidized state of Ag after deposition. (E) Cu 2p spectrum of the CuAg oxide clusters 7 days after production. (F) Ag 3d spectrum 7 days after production showing again no loss feature. (G) Cu LMM Auger spectrum again showing the presence of the Ag3p3 peak. (H) Ag MNN Auger spectrum with the Auger parameter estimated at 718 eV confirming the oxidized state of Ag.

## Note S7. Evaluation of the electrochemical performance in the CO<sub>2</sub>RR

### 7.1. Note S7.1. Cathode preparation.

Conical pieces of Toray TGP-60r carbon paper coated with 0.6 or 0.3 mg cm<sup>-2</sup> of NCB or GO respectively and functionalized with ~4 μg cm<sup>-2</sup> Cu(-Ag) clusters were cut out

with a geometrical surface area of 0.5 cm<sup>2</sup>. Finally, 20 μL of 0.83 wt% Nafion dispersed in *iso*-propanol were added as binder.

### 7.2. Note S7.2. Electrochemical measurements.

The electrodes were evaluated in a commercial gas-tight H-cell from Gaoss Union using constant potential mode controlled by a potentiostat (Autolab PGSTAT302N). All measurements were carried out in 0.1 M KHCO<sub>3</sub>, which functioned as both catholyte and electrolyte (25 mL per chamber). Chambers were kept separate by means of a cation exchange (Nafion) membrane. Prior to electrochemical testing, the electrolyte was saturated with CO<sub>2</sub> by bubbling at 25 mL·min<sup>-1</sup> for at least 15 min. Also, during any measurement, CO<sub>2</sub> was bubbled through the catholyte continuously to ensure sufficient CO<sub>2</sub> supply during the measurement. A Pt wire was used as counter electrode for the oxygen reduction reaction. An Ag/AgCl electrode was used as

reference. All measurements were carried out at -1.1 V vs RHE. The value of the potential versus Ag/AgCl was converted to the scale of the reversible hydrogen electrode (RHE) using the equation: E (versus RHE) = E (versus Ag/AgCl (3 M KCl)) + 0.21 V + 0.059 \* pH. The potential was mathematically compensated for the ohmic resistance that was determined by the electrochemical impedance spectroscopy (EIS). The FEs and currents were repeatedly measured on three individual electrodes for each material evaluated.

### Note S7.3. Quantification of the gaseous products

Gas products were analysed online (10 min interval) using a gas chromatography (GC, SRI Instrument 8610C) with the auto-sampling loop (1 ml) connected to CO<sub>2</sub> off-gas of the H-cell catholyte chamber. H<sub>2</sub> was

analysed using thermal conductive detector (TCD) and CO, CH<sub>4</sub>, and C<sub>2</sub>H<sub>4</sub> were analysed using flame ionization detector (FID) with a methanizer.

### 7.2. Note S7.2. Electrochemical measurements.

Quantification of the liquid products was achieved according to a previously reported method and a derivation of the Kuhl *et al* method.<sup>22,23</sup> In brief, the liquid products of all electrodes were quantified using nuclear magnetic resonance (NMR, Bruker 400 MHz AVIII HD). **Figure S17** shows a typical 1D <sup>1</sup>H NMR spectrum obtained for a standard solution containing typical liquid products from the CO<sub>2</sub>RR and the internal standards (phenol and DMSO) as indicated by the arrows. The peak area ratio of a given

product to that of the internal standard, as obtained by peak fitting using MestReNova software, was used to determine the concentration of the products. Identical NMR acquisition parameters were used for all measurements. In addition, the water peak was suppressed using the solvent suppression function. The acquisition time of d1 was 5 s and the number of scans was 260. Products with peaks with chemical shifts than larger water (> 5 ppm) were quantified using phenol, all others with DMSO.

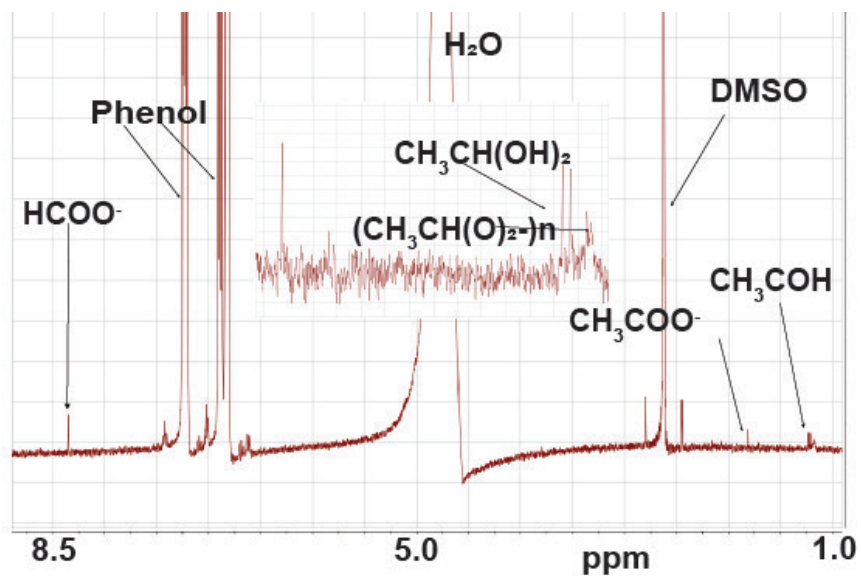


**Figure S17.** Typical  $^1\text{H-NMR}$  spectrum taken of a catholyte aliquot after  $\text{CO}_2\text{RR}$  using a Cu-Ag-NCB-GDL catalyst at 0.9 V vs RHE for 1 hrs. The catholyte contains three  $\text{CO}_2\text{RR}$  products: formate, acetate and acetaldehyde. The acetaldehyde exist a hydrated form<sup>23</sup> and a less soluble aggregate i.e. metaldehyde resulting in peak broadening and shift to lower ppm values. Any multimer of acetaldehyde forms chemically and is base catalyzed. See **Figure S18** for a typical NMR spectrum of metaldehyde.

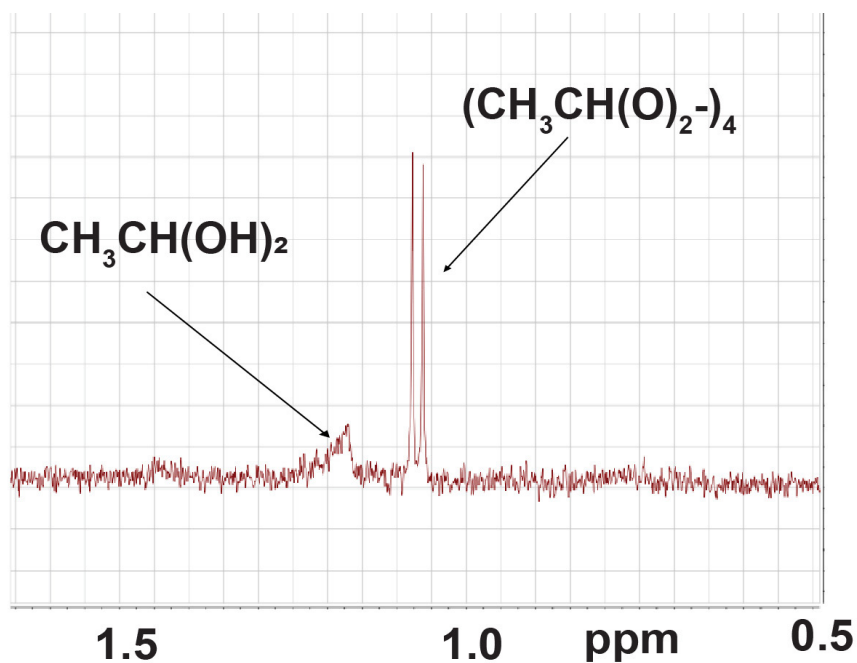


**Figure S18.**  $^1\text{H-NMR}$  spectrum of metaldehyde dissolved in 0.1 M  $\text{KHCO}_3$ .

## 7.5. Note S7.5. Calculation of the faradaic efficiency

The faradaic efficiency (FE) was calculated for gas and liquid products, using

$$\text{FE} = \frac{nFC_i v P}{jRT}$$

and

$$\text{FE} = \frac{nFC_i V}{Q},$$

respectively, where  $n$  is the number of transferred electrons to produce one molecule of product  $i$ ,  $F$  is the faradaic

constant,  $C_i$  is the concentration of the product as determined by GC or NMR,  $v$  is the flow rate of  $\text{CO}_2$ ,  $P$  and  $T$  are the pressure (101325 Pa) and temperature (22 °C) of the gas sampled by the GC sample loop, respectively,  $j$  is the total current when sampling,  $R$  is the gas constant,  $V$  is the volume of the electrolyte, and  $Q$  is the total charge transferred to produce the target product.

## Note S7.6 Determination of the support activity in $\text{CO}_2\text{RR}$ .

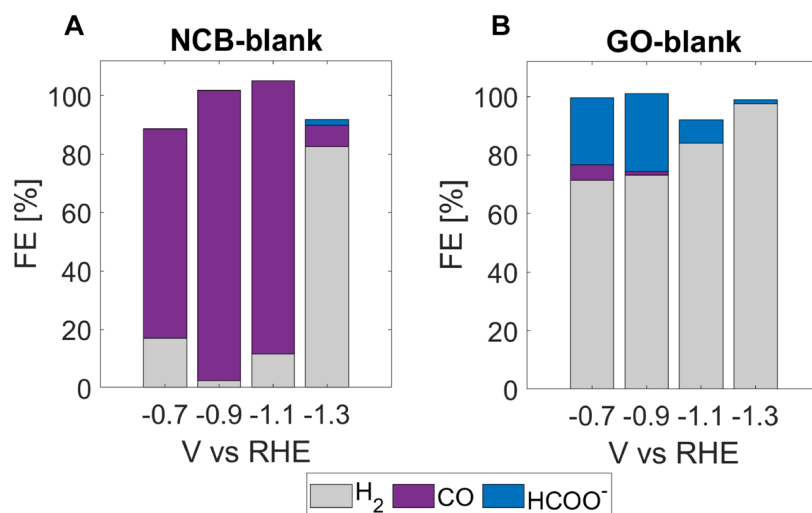


**Figure S19.** (A) Selectivity as a function of potential of the as-synthesized NCB-GDL composite. (B) Selectivity as a function of potential as the as-synthesized GO-GDL composite. All measurements were performed in  $\text{CO}_2$  saturated 0.1 M  $\text{KHCO}_3$ . The reaction was let to equilibrate for 10 min before the first sampling of the gas products was performed. An average over 30 min has been reported. Several washing steps with  $\text{HNO}_3$  was performed to remove trace metal species from the supports.



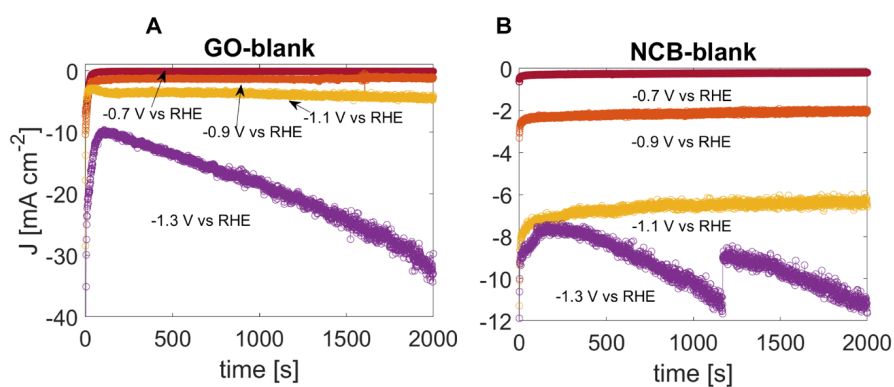


**Figure S20.** (A) Geometrical current density as a function of potential of the as-synthesized GO-GDL composite. (B) Geometrical current density as a function of potential as the as-synthesized NCB-GDL composite.

	H <sub>2</sub>	CO	CH <sub>3</sub> CHO	CH <sub>3</sub> COO <sup>-</sup>	HCOO <sup>-</sup>
Cu_NCB_0.5V	16.09	0.00	66.43	9.50	2.50
Cu_NCB_0.6V	46.50	0.00	42.53	4.50	3.08
Cu_NCB_0.7V	30.49	11.49	46.44	10.78	2.15
Cu_NCB_0.8V	64.60	9.17	20.51	1.88	2.46
Cu_NCB_0.9V	7.41	75.75	21.83	1.49	0.79
Cu_NCB_1.1V	35.18	46.02	8.94	1.56	2.00
Cu_NCB_0.5V_STD	16.09	0.00	20.27	1.96	2.50
Cu_NCB_0.6V_STD	11.42	0.00	21.54	1.95	2.87
Cu_NCB_0.7V_STD	21.38	16.25	19.86	4.43	1.58
Cu_NCB_0.8V_STD	12.80	1.98	4.30	0.21	0.82

**Table S1.** Faradaic efficiencies of Cu-NCB per potential and product.

	H <sub>2</sub>	CO	CH <sub>3</sub> CHO	CH <sub>3</sub> COO <sup>-</sup>	HCOO <sup>-</sup>
Cu_GO_0.5V	0.00	0.00	92.55	9.18	0.00
Cu_GO_0.6V	56.02	0.00	31.84	5.08	1.69
Cu_GO_0.7V	27.98	0.00	48.46	5.34	5.98
Cu_GO_0.8V	82.60	0.00	19.57	2.81	3.75
Cu_GO_0.9V	60.46	1.03	33.89	2.35	3.74
Cu_GO_1.1V	88.58	2.50	3.20	0.52	2.61
Cu_GO_0.5V_STD	0.00	0.00	1.87	0.02	0.00
Cu_GO_0.6V_STD	2.12	0.00	1.16	1.85	0.60
Cu_GO_0.7V_STD	18.34	0.00	26.81	3.47	2.76

**Table S2.** Faradaic efficiencies of Cu-GO per potential and product.

	H <sub>2</sub>	CO	CH <sub>3</sub> CHO	CH <sub>3</sub> COO <sup>-</sup>	HCOO <sup>-</sup>
CuAg_NCB_0.5V	0.00	0.00	88.42	11.34	0.83
CuAg_NCB_0.6V	0.00	0.00	83.45	18.25	2.85
CuAg_NCB_0.7V	15.98	54.36	29.26	4.32	3.04
CuAg_NCB_0.8V	36.32	39.58	15.06	1.92	5.44
CuAg_NCB_0.9V	19.28	71.17	11.34	2.00	1.14
CuAg_NCB_1.1V	39.06	49.72	0.00	1.21	8.99
CuAg_NCB_0.5V_STD	0.00	0.00	0.97	0.40	0.83
CuAg_NCB_0.6V_STD	0.00	0.00	2.66	3.99	0.81
CuAg_NCB_0.7V_STD	0.91	1.12	3.16	0.09	0.44

**Table S3.** Faradaic efficiencies of Cu-Ag-NCB per potential and product.

	H <sub>2</sub>	CO	CH <sub>3</sub> CHO	CH <sub>3</sub> COO <sup>-</sup>	HCOO <sup>-</sup>
CuAg_GO_0.5V	0.00	0.00	68.48	4.56	1.88
CuAg_GO_0.6V	57.04	0.00	39.20	0.46	1.10
CuAg_GO_0.7V	23.21	0.00	72.03	7.21	4.04
CuAg_GO_0.8V	72.54	0.00	13.52	4.06	5.51
CuAg_GO_0.9V	70.59	1.98	19.05	5.95	2.21
CuAg_GO_1.1V	88.88	0.25	7.35	0.68	2.09
<b>D</b>					
CuAg_GO_0.5V_ST	0.00	0.00	4.95	0.80	1.62
<b>D</b>					
CuAg_GO_0.6V_ST	0.25	0.00	1.97	0.23	0.88
<b>D</b>					
CuAg_GO_0.7V_ST	3.75	0.00	4.40	7.84	2.30
<b>D</b>					

**Table S4.** Faradaic efficiencies of Cu-Ag-GO per potential and product.

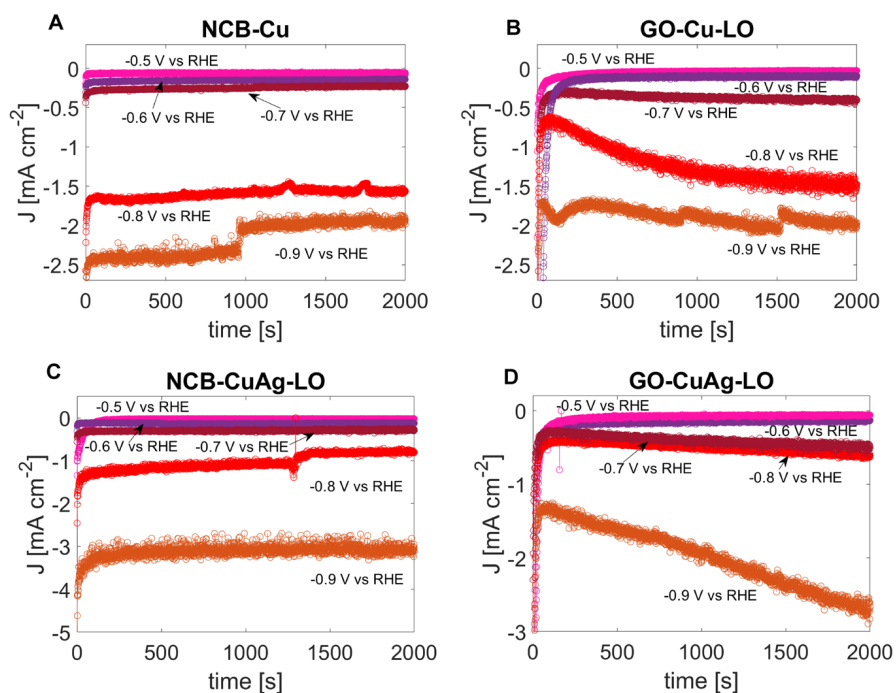


**Figure S21.** Geometrical current densities as a function of potential for the screened Cu-(ag)-NCB/GO GDL catalysts at low overpotential.



## S8. References

1. Lee, D. C., Yang, H. N., Park, S. H. & Kim, W. J. Nafion/graphene oxide composite membranes for low humidifying polymer electrolyte membrane fuel cell. *Journal of Membrane Science* **452**, 20–28 (2014).
2. Zhang, J., Xia, Z. & Dai, L. Carbon-based electrocatalysts for advanced energy conversion and storage. *Science Advances* **1**, e1500564 (2015).
3. Duan, X. *et al.* Metal-Free Carbon Materials for CO<sub>2</sub> Electrochemical Reduction. *Advanced Materials* **29**, 1701784 (2017).
4. Yang, F. *et al.* Highly Efficient CO<sub>2</sub> Electroreduction on ZnN<sub>4</sub>-based Single-Atom Catalyst. *Angewandte Chemie International Edition* **57**, 12303–12307 (2018).
5. Fouda, A. N., Duraia, E. S. M. & Almaqwashi, A. A. Facile and scalable green synthesis of N-doped graphene/CNTs nanocomposites via ball milling. *Ain Shams Engineering Journal* **12**, 1017–1024 (2021).
6. Jeon, I.-Y. *et al.* Direct nitrogen fixation at the edges of graphene nanoplatelets as efficient electrocatalysts for energy conversion. *Sci Rep* **3**, 2260 (2013).
7. Schwyn, S., Garwin, E. & Schmidt-Ott, A. Aerosol generation by spark discharge. *Journal of Aerosol Science* **19**, 639–642 (1988).
8. Peineke, C., Attoui, M. B. & Schmidt-Ott, A. Using a glowing wire generator for production of charged, uniformly sized nanoparticles at high concentrations. *Journal of Aerosol Science* **37**, 1651–1661 (2006).
9. Feng, J., Ramlawi, N., Biskos, G. & Schmidt-Ott, A. Internally mixed nanoparticles from oscillatory spark ablation between electrodes of different materials. *Aerosol Science and Technology* **52**, 505–514 (2018).
10. Feng, J. *et al.* Unconventional Alloys Confined in Nanoparticles: Building Blocks for New Matter. *Matter* **3**, 1646–1663 (2020).
11. Maisser, A. *et al.* Characterization of atmospheric-pressure spark generated atomic silver and gold clusters by time-of-flight mass spectrometry. *Journal of Aerosol Science* **156**, 105780 (2021).
12. Tabrizi, N. S., Xu, Q., van der Pers, N. M. & Schmidt-Ott, A. Generation of mixed metallic nanoparticles from immiscible metals by spark discharge. *J Nanopart Res* **12**, 247–259 (2010).
13. Maisser, A., Barmponis, K., Attoui, M. B., Biskos, G. & Schmidt-Ott, A. Atomic Cluster Generation with an Atmospheric Pressure Spark Discharge Generator. *Aerosol Science and Technology* **49**, 886–894 (2015).

14. Preger, C., Overgaard, N. C., Messing, M. E. & Magnusson, M. H. Predicting the deposition spot radius and the nanoparticle concentration distribution in an electrostatic precipitator. *Aerosol Science and Technology* **54**, 718–728 (2020).
15. Feng, J., Biskos, G. & Schmidt-Ott, A. Toward industrial scale synthesis of ultrapure singlet nanoparticles with controllable sizes in a continuous gas-phase process. *Sci Rep* **5**, 15788 (2015).
16. Feng, J. *et al.* General Approach to the Evolution of Singlet Nanoparticles from a Rapidly Quenched Point Source. *J. Phys. Chem. C* **120**, 621–630 (2016).
17. Megyeri, D., Kohut, A. & Geretovszky, Z. Effect of flow geometry on the nanoparticle output of a spark discharge generator. *Journal of Aerosol Science* **154**, 105758 (2021).
18. Feng, J. Scalable Spark Ablation Synthesis of Nanoparticles: Fundamental Considerations and Application in Textile Nanofinishing. (Delft University of Technology, 2016). doi:10.4233/UUID:FB6C0122-587B-471D-8009-B52EF9B69B07.
19. Voloshko, A., Itina, T. E., Voloshko, A. & Itina, T. E. *Nanoparticle Formation by Laser Ablation and by Spark Discharges — Properties, Mechanisms, and Control Possibilities*. *Nanoparticles Technology* (IntechOpen, 2015). doi:10.5772/61303.
20. Dietsche, R. *et al.* Comparison of electronic structures of mass-selected Ag clusters and thermally grown Ag islands on sputter-damaged graphite surfaces. *Appl. Phys. A* **90**, 395–398 (2008).
21. Lai, X., St.Clair, T. P. & Wayne Goodman, D. Oxygen-induced morphological changes of Ag nanoclusters supported on TiO<sub>2</sub>(110). *Faraday Disc.* **114**, 279–284 (1999).
22. Zhang, J., Luo, W. & Züttel, A. Crossover of liquid products from electrochemical CO<sub>2</sub> reduction through gas diffusion electrode and anion exchange membrane. *Journal of Catalysis* **385**, 140–145 (2020).
23. Kuhl, K. P., Cave, E. R., Abram, D. N. & Jaramillo, T. F. New insights into the electrochemical reduction of carbon dioxide on metallic copper surfaces. *Energy Environ. Sci.* **5**, 7050–7059 (2012).

Chapter 7

# Conclusions and perspectives

## 7.1. Conclusions

With the aim to offer design strategies to improve the selectivity towards liquid fuels of electrocatalysts in the CO<sub>2</sub>RR, various well-defined Cu-based electrocatalyst were prepared using wet-chemical and physical processes. Further, they were systematically investigated for their electrochemical performance in CO<sub>2</sub>RR, which was correlated to their materials properties as probed via SP-ICP-MS, XAS, STEM-HAADF and other more conventional characterization techniques. Hereby, it could be concluded that alloying Cu with Ag improved the selectivity of Cu towards liquid fuels such as acetic acid, acetaldehyde and ethanol for particles >10 nm, e.g. the bulk. And further, that interfaces of Cu-(Ag) (100) and (111) surfaces have especially high selectivity for liquid fuels, in agreement with what is known for bulk single crystals. Finally, upon the reduction of particle size beyond the size limit in which metallicity breaks down, the cluster size regime, electrocatalyst performances differ distinctly from the bulk and can be by nature of a more precisely defined active site (or series of active sites) have much higher selectivity for specific products than for bulk catalysts.

In Chapter 2, three decades worth of experimental data on the CO<sub>2</sub>RR were critically reviewed. From here it was concluded that:

- 1) metal nanoparticle catalyst >10 nm behave as bulk materials (electronics and facet controlled reactivity) but can benefit from higher surface to mass ratios,
- 2) ultrasmall particles (1 nm ≤ X ≤ 10 nm) may have significantly increased activities in comparison to bulk materials as based on their higher degree of undercoordination but may be negatively affected in CO<sub>2</sub>RR performance by enhancement of the parasitic HER ,
- 3) cluster catalysts can produce hydrocarbons and perform C-C coupling and can show uniquely high selectivity for multicarbon products, and
- 4) single-atom catalysts cannot form C-C bonds but do show high selectivities for single carbon products such as CH<sub>4</sub>, MeOH, CO and HCOO<sup>-</sup>.

In Chapter 3, facilitated by Chapter 2, a selection of catalyst from potentially promising size regimes (NP > 10 nm and clusters < 1 nm) was made forming the basis of this thesis.



In Chapter 4, the full picture of the ensemble of multimetallic NPs was made accessible by means of the development of a novel protocol, based on SP-ICP-MS, in which composition distribution could be obtained at the single-particle level but with ensemble representative statistics in a matter of minutes. This allowed to study the chemistry of a galvanic exchange reaction that made it possible to introduce Ag and Pd in Cu lattices of shaped NPs. The method was successfully applied to four shapes of NPs (Au spheres and Cu cubes, truncated octahedra and tetrahedra) and three Cu-based surface-alloy NPs (CuAg, CuPd and CuPdAg). The author argues that this technique can find use in materials science, materials chemistry, (nano)physics, (nano) photonics, catalysis and electrochemistry.

In Chapter 5, facilitated by the work developed in Chapter 4, a low-temperature non-equilibrium synthesis of shape-controlled NSA with up to three components, was designed independently of component miscibility. This facilitated the deeper understanding and deconvolution of the effect of facet and composition in the CO<sub>2</sub>RR to show improved selectivity

of Cu-Ag alloys towards C<sub>2+</sub> liquid fuels. Further, machine learning was used to guide the synthesis of Cu-Ag-Pd NSAs with high C<sub>2+</sub> selectivity and phase stability. The author expects the low-temperature non-equilibrium synthesis to be advantageous for researchers seeking nanomaterials of specific spatial atomic arrangements in a range of applications.

In Chapter 6, a scalable production and immobilization method was discussed for Cu-based bimetallic clusters of <150 atoms, which have unique catalytic properties for electrochemical conversion of CO<sub>2</sub> to acetaldehyde with high selectivity (>90%). Further, this type of catalyst also exhibits resistance against potential cycling due to its in situ formed metallic nature, which remains even after air exposure and is a unique property of cluster catalysts. The author argues that this production method offers a platform technology for screening different catalysts for various electrochemical reactions beyond CO<sub>2</sub>RR such as nitrogen reduction reaction and OER.

## 7.2. Perspectives

Although the results discussed in this thesis offer significant improvements in design strategies for electrocatalysts with enhanced CO<sub>2</sub>RR selectivity towards liquid fuels over the conventional, achievements were solely made at the lab scale and, therefore, using a limited range of reaction environments. For their application in CO<sub>2</sub>RR as a mature technology, performance metrics will need to be assessed at various length scales and

under various reaction conditions beyond the discussed. Therefore, the author attempts to provide a perspective on which specific metrics will need to be reevaluated at more industrially relevant conditions to assess the technology readiness level of the obtained results and discussed in the previous. Below such perspectives are provided.

### 7.2.2. Catalyst stability as a function of reaction environment

The performance in various electrolytes and pH environments has not yet been established for the Cu-based catalyst mentioned i.e. only 0.1 M KHCO<sub>3</sub> electrolyte (pH 6.8) has been tested. Therefore, further scientific objectives could be to establish catalyst performance as a function of pH and the nature of the electrolyte i.e. KOH, CsOH, NaOH, CsHCO<sub>3</sub> and NaHCO<sub>3</sub> at various ionic strengths. As it has been reported that the nature of the electrolyte, its pH and the specific cation all influence CO<sub>2</sub>RR performance, which carries disadvantages and advantages relative to an aimed at product, electrolyte screening will need to be attempted with a specific product in

mind.<sup>1</sup> Further, current densities reported have been limited due to the requirement of CO<sub>2</sub> to dissolve to achieve electrochemical conversion in the presently used H-cell configuration and the overall low solubility of CO<sub>2</sub> in aqueous solutions. Therefore, extension of the performance screening of the discussed catalysts in different gas-fed reaction designs will be needed to determine and evaluate structure-activity relationships at more industrially relevant current densities. Two types of reactor design are particularly of interest, namely the zero-gap cell and the solid-state device of which some specifics are discussed below.<sup>2,3</sup>

### 7.2.3. Electrolyzer design

In the field of CO<sub>2</sub> electrolysis, two major schools of thought exist with respect to the electrolyzer design (**Figure 39**) that could enable industrial scale. The first, is based on the so called zero-gap electrolyzer design in which the cathode and anode are sandwiched in between an ion exchange membrane (**Figure 39A**).<sup>2</sup> The second, is based on a solid-state device in which the cathode is operated without contact to any liquid electrolyte. Instead a solid polymer electrolyte is used to shuttle ions to perform CO<sub>2</sub> electrolysis (**Figure 39B**).<sup>3</sup>

The zero-gap electrolyzer design has two major advantages: 1) the sandwich structure allows to reduce the cell resistance by making the cell thinner thereby lowering the overall cell potential and improve the energy efficiency and 2) it easily

allows for stacking of the cells offering an easy avenue to increase electrode surface area, pressurized operation and increase conversion. However, the zero-gap design has two major disadvantages that need consideration: 1) it requires alkaline anolyte to run the reaction at high current densities, which traps CO<sub>2</sub> as carbonates, which lessens the conversion and floods the cathode overtime i.e. stops the reaction and 2) in case of liquid products, cross-over via the ion exchange membrane may occur resulting in the need for purification steps and even loss of product via reoxidation at the anode.

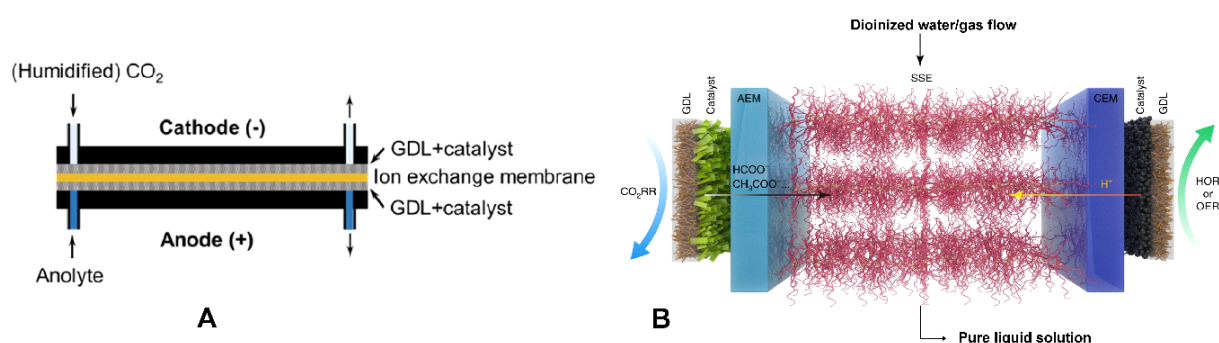


**Figure 39.** (A) Zero-gap cell with the ion exchange membrane either cation exchange membrane (CEM) or anion exchange membrane (AEM). (B) A solid-state device in which ions shuttling occurs through a solid-state electrolyte (SSE). Adapted and reprinted with permission from Ref. <sup>2</sup> and Ref. <sup>3</sup>.

Since this thesis discusses by and large the production of liquid fuels, salt formation may be a significant issue as OH<sup>-</sup> formation and reaction with CO<sub>2</sub> to form carbonates is relatively large for C-C coupled products. In example, in case of acetaldehyde three moles of carbonate could cross-over per one mole of acetaldehyde formed enhancing the rate of salt formation 3-fold as compared to CO evolution and could significantly reduce CO<sub>2</sub> conversion. This may in turn significantly thwart long-term operation of the zero-gap design and would require further scrutiny. Potential avenues to address these issues are purging of the cathode with pure H<sub>2</sub>O and or switching of the electrolyte to pure H<sub>2</sub>O with periodically infused cations to maintain high selectivity and conversion.<sup>4,5</sup> Further, cross-over of liquid product through the ion exchange membrane to the anode could result in significant loss of product. Also, here optimization would be needed of which optimized electrolyte flow and or operation at elevated temperatures may offer some lenience.

An alternatively solution could be sought in

the solid-state device design as it has two major operational advantages over the zero-gap design: 1) since the cathode is never into direct contact with liquid electrolyte, flooding is not possible. Further, degradation processes based on corrosion/dissolution well-known for Cu based catalysts<sup>6</sup> are strongly inhibited extending the life time of the catalyst.<sup>7</sup> And 2) cross-over of products to the anode side is prevented by a steady-stream of gas or water vapor through the solid-electrolyte layer collecting the products before reoxidation can occur. On top of that, cross-over of CO<sub>3</sub><sup>2-</sup> can be circumvented by its recombination with H<sup>+</sup> to form CO<sub>2</sub> which can then be reused, thereby, extending its conversion.<sup>8</sup> Also, several disadvantages exist regarding this technology: 1) it lacks maturity, i.e. its components, i.e., solid electrolyte, although commercially available, have never been used for electrolysis (originate from battery tech) and, therefore, the durability cannot be assessed, 2) cations are absent in the solid-sate device, which may reduce CO<sub>2</sub>RR over HER selectivity, and 3) the AEM, SSE, CEM three-component configuration limits

the cell thinness and increases thereby the overall cell potential.

Although major advantages and disadvantages exist for either cell design, performance metrics of the catalyst discussed in this thesis would require extension on and revalidation of in either type of reactor designs before their technology readiness level can be assessed beyond the lab scale. Therefore, future studies should be aimed at testing the developed catalysts in such gas-fed electrolyzers to confirm obtained results and raise the technology readiness level to the pilot scale.

## 7.3. References

- (1) Monteiro, M. C. O.; Dattila, F.; Hagedoorn, B.; García-Muelas, R.; López, N.; Koper, M. T. M. Absence of CO<sub>2</sub> Electroreduction on Copper, Gold and Silver Electrodes without Metal Cations in Solution. *Nat Catal* **2021**, *4* (8), 654–662. <https://doi.org/10.1038/s41929-021-00655-5>.
- (2) Endrődi, B.; Bencsik, G.; Darvas, F.; Jones, R.; Rajeshwar, K.; Janáky, C. Continuous-Flow Electroreduction of Carbon Dioxide. *Progress in Energy and Combustion Science* **2017**, *62*, 133–154. <https://doi.org/10.1016/j.pecs.2017.05.005>.
- (3) Xia, C.; Zhu, P.; Jiang, Q.; Pan, Y.; Liang, W.; Stavitski, E.; Alshareef, H. N.; Wang, H. Continuous Production of Pure Liquid Fuel Solutions via Electrocatalytic CO<sub>2</sub> Reduction Using Solid-Electrolyte Devices. *Nat Energy* **2019**, *4* (9), 776–785. <https://doi.org/10.1038/s41560-019-0451-x>.
- (4) Endrődi, B.; Kecsenovity, E.; Samu, A.; Darvas, F.; Jones, R. V.; Török, V.; Danyi, A.; Janáky, C. Multilayer Electrolyzer Stack Converts Carbon Dioxide to Gas Products at High Pressure with High Efficiency. *ACS Energy Lett.* **2019**, *4* (7), 1770–1777. <https://doi.org/10.1021/acsenergylett.9b01142>.
- (5) Endrődi, B.; Samu, A.; Kecsenovity, E.; Halmágyi, T.; Sebők, D.; Janáky, C. Operando Cathode Activation with Alkali Metal Cations for High Current Density Operation of Water-Fed Zero-Gap Carbon Dioxide Electrolysers. *Nat Energy* **2021**, *6* (4), 439–448. <https://doi.org/10.1038/s41560-021-00813-w>.
- (6) Huang, J.; Hörmann, N.; Oveisi, E.; Loiudice, A.; De Gregorio, G. L.; Andreussi, O.; Marzari, N.; Buonsanti, R. Potential-Induced Nanoclustering of Metallic Catalysts during Electrochemical CO<sub>2</sub> Reduction. *Nature Communications* **2018**, *9* (1), 3117. <https://doi.org/10.1038/s41467-018-05544-3>.
- (7) Zhu, P.; Xia, C.; Liu, C.-Y.; Jiang, K.; Gao, G.; Zhang, X.; Xia, Y.; Lei, Y.; Alshareef, H. N.; Senftle, T. P.; Wang, H. Direct and Continuous Generation of Pure Acetic Acid Solutions via Electrocatalytic Carbon Monoxide Reduction. *Proceedings of the National Academy of Sciences* **2021**, *118* (2), e2010868118. <https://doi.org/10.1073/pnas.2010868118>.
- (8) Kim, J. Y. ‘Timothy’; Zhu, P.; Chen, F.-Y.; Wu, Z.-Y.; Cullen, D. A.; Wang, H. Recovering Carbon Losses in CO<sub>2</sub> Electrolysis Using a Solid Electrolyte Reactor. *Nat Catal* **2022**, *5* (4), 288–299. <https://doi.org/10.1038/s41929-022-00763-w>.

# Curriculum Vitae



## **Cedric David Koolen**

Doctoral Candidate and Safety Engineer  
Ecole Polytechnique Fédérale de Laussane (**EPFL**)

MSc. Physical Chemistry & MSc. Chemistry

e-mail: [cedric.koolen@epfl.ch](mailto:cedric.koolen@epfl.ch)

phone: +41762025649 | +31613015890

Adress: Rue de conthey 6, 1950 Sion, Switzerland

## Personal Data

Year and place of birth: 1994, Purmerend, the Netherlands.

Languages: Dutch<sup>\*\*\*</sup>, English<sup>\*\*</sup> and German (B1), French (B1)<sup>\*\*</sup> (\*native-speaker, \*\*used in teaching).

IT Skills: Microsoft Office, Matlab, Adobe Illustrator, Blender, Image processing software.

## Education (3 degrees, 3.3 GPA)

Present – 2020      Doctoral Assistant, Laboratory of Materials for Renewable Energy, Institute of Chemical Sciences and Engineering, École Polytechnique Fédérale de Lausanne – Valais-Wallis, Sion, Switzerland and Empa Materials Science & Technology, Dübendorf, Switzerland.

2020 – 2019      Candidacy exam, Laboratory of Nanochemistry for Energy, Institute of Chemical Sciences and Engineering, École Polytechnique Fédérale de Lausanne – Valais-Wallis, Sion, Switzerland.

2019 – 2017      Master of Science Physical Chemistry, Faculty of Science, Lund University, Lund, Sweden.

2018 – 2015      Master of Science Chemistry, track Molecular Design, Synthesis & Catalysis, Faculty of Science, University of Amsterdam & VU University, Amsterdam, the Netherlands.

2015 – 2012      Bachelor of Science Pharmaceutical Sciences, Faculty of Science, VU University, Amsterdam, the Netherlands.

2012 – 2006      Grammar school, Sint Ignatius Gymnasium, Amsterdam, the Netherlands.



## Research experience (5 universities, 7 laboratories)

2021	Visiting PhD student, Materials for Energy Conversion and Storage, Department of Chemical Engineering, TU Delft, Delft, the Netherlands.
Present – 2020	Plasma-based techniques for the synthesis and characterization of metal catalysts for eCO <sub>2</sub> RR, Laboratory of Materials for Renewable Energy, Institute of Chemical Sciences and Engineering, École Polytechnique Fédérale de Lausanne – Valais-Wallis, Sion, Switzerland and Empa Materials Science & Technology, Dübendorf, Switzerland.
2020 – 2019	Multimetallic Nanocrystals for CO <sub>2</sub> RR, Laboratory Nanochemistry for Energy, Institute of Chemical Sciences and Engineering, École Polytechnique Fédérale de Lausanne – Valais-Wallis, Sion, Switzerland.
2019 – 2018	Master of Science research project physical chemistry, title: Anisotropic Dynamics of Dense Colloidal Ellipsoids, Division of Physical Chemistry, Faculty of Science, Lund University, Lund, Sweden.
2018 – 2017	Master of Science research project chemistry, title: Preparation and Characterization of Functionalized Ellipsoidal Hematite Particles, Division of Physical Chemistry & Van 't Hoff Institute of Molecular Sciences, Faculty of Science, Lund University & University of Amsterdam, Lund, Sweden.
2018 – 2017	Research Project Air Pollution, Van 't Hoff Institute of Molecular Sciences, Faculty of Science, University of Amsterdam, Amsterdam, the Netherlands.
2015	Bachelor of Science research project (five months), title: Investigation into the Weak Interactions Involving Halogens in Protein-Ligand Binding, Division of Theoretical Chemistry, Faculty of Science, VU University, Amsterdam, the Netherlands.

## Publications (4 1<sup>st</sup> author, 7 total contributions, average impact factor: 13.0)

- 2023 From single crystal to single atom: structural factors influencing the performance of metal catalysts for CO<sub>2</sub> electroreduction, **Koolen, C. D.**; Luo, W.; Züttel, A., *ACS Catal.* **2023**, 13, XXX, 948–973
- 2022 High-throughput Sizing, Counting and Elemental Analysis of Anisotropic Multimetallic Nanoparticles with Single-Particle Inductively Coupled Plasma Mass Spectrometry **Koolen, C. D.**; Torrent, L.; Agarwal, A.; Meili-Borovinskaya, O.; Gasilova, N.; Li, M.; Luo, W.; Züttel, A, *ACS Nano*, **2022**.
- 2022 Tandem effect of Ag@C@Cu catalysts enhances ethanol selectivity for electrochemical CO<sub>2</sub> reduction in flow reactors, Zhang, J.; Pham, T. H. M.; Ko, Y.; Li, M.; Yang, S.; **Koolen, C. D.**; Zhong, L.; Luo, W.; Züttel, A, *Cell Reports Physical Science* **2022**, 3 (7), 100949.
- 2022 Ensuring the environmental sustainability of emerging technologies, M.-V. Florin, R. Buchs, Acknowledged: **Koolen, C. D.**; EPFL Risk Governance Center (IRGC), Lausanne, Switzerland.
- 2021 Colloidal Nanocrystals as Electrocatalysts with Tunable Activity and Selectivity, Guntern, Y.T.; Okatenko, V.; Pankhurst, J.; Varandili B.; Iyengar, P.; **Koolen, C.D.**; Stoian, D.; Vavra, J.; Buonsanti, R., *ACS Catal.*, **2021**, 11, 3, 1248–1295.
- 2019 Zet aanpak luchtvervuiling weer terug op de kaart, **Koolen, C.D.** and Rothenberg, G., *Tijdschrift Milieu*, **2019**, 3, 8-9.
- 2019 Air Pollution in Europe, **Koolen, C.D.** and Rothenberg, G., *ChemSusChem*, **2019**, 12, 164-172.

## Manuscripts in preparation (4 1<sup>st</sup> author, 2 corresponding author)

- 2023 A machine-learning based algorithm for the determination of nanoparticle shape via inductively coupled plasma mass spectrometry, **Koolen, C. D.**; Koolen, S.R.J., Torrent, L.; Agarwal, A.; Tanner, M.; Gasilova, N.; Menin, L.; Luo, W.; Züttel, A., *in preparation*.
- 2023 Scalable synthesis of CuAg oxide clusters via spark ablation for the highly selective electrochemical conversion of CO<sub>2</sub> to acetaldehyde. **Koolen, C.D.**; Zijlstra, B.; Winzely, M.; Zhang, J.; Pfeiffer, T.; Vrijburg, W.; Li, M.; Boshuizen, B.; Agarwal, A.; Ko, Y.; Bornet, A.; Herranz Salaner, J.; Safonova, O.; Schmidt-Ott, A.; Luo, W.; Züttel, A., *in preparation*.
- 2023 Low-temperature non-equilibrium synthesis of anisotropic multimetallic nanosurface alloys for the electrochemical CO<sub>2</sub> reduction reaction, Koolen, C.D.; Oveisi, E.; Zhang, J.; Li, M.; Pedersen, J.K.; Rossmeisl, J.; Luo, W.; Züttel, A., *submitted to Nature Synthesis*.

## Patents

- 2023 Conductive or semi-conductive clusters produced via spark ablation, **Koolen, C. D.**, Züttel, A. *patent pending*.
- 2021 Sizing and counting of (an)isotropic polyelemental inorganic nanoparticles using single-particle inductively-coupled plasma mass spectrometry, **Koolen, C. D.**, *patent pending*.

## Teaching experience (500+ students, 500+ hrs)

2022	Analytical Separation Methods, bachelor course École Polytechnique Fédérale de Lausanne, Lausanne, Switzerland.
2022	Chemistry and Analytical Laboratory I, bachelor course École Polytechnique Fédérale de Lausanne, Lausanne, Switzerland.
2021	Thermodynamics of energy conversion and storage, master course École Polytechnique Fédérale de Lausanne, Sion, Switzerland.
2020	Nanomaterials for Chemical Engineering Applications, master course École Polytechnique Fédérale de Lausanne, Sion, Switzerland.
2019	Semester project Dominic Brullmann Master Materials Science and Engineering, École Polytechnique Fédérale de Lausanne, Sion, Switzerland.
2019	Colloidal Synthesis of Nanoparticles and their Energy Applications, Doctoral Course École Polytechnique Fédérale de Lausanne, Sion, Switzerland.
2016	Computational (Pharmaco)chemistry, Bachelor of Science course in Pharmaceutical Sciences and Chemistry, Faculty of Science, VU University, Amsterdam, the Netherlands.

## **Achievements (>30,000 USD in grants received)**

2022	Bronze medal Suisse Romande Toastmaster Prepared Speech Novice Competition, Nyon, Switzerland.
2021	EPFL Travel Grant (2,000 CHF), Institute of Chemical Sciences and Engineering, École Polytechnique Fédérale de Lausanne, Lausanne, Switzerland.
2019 – 2018	Undergraduate Excellence Scholarship (100,000 SEK), Department of Chemistry, Lund University, Lund, Sweden.
2018	Niels Bohr Institute Travel Grant (15,000 DKK), Niels Bohr Institute, University of Copenhagen, Copenhagen, Denmark.
2018	Röntgen-Ångström-Cluster Travel Grant (20,000 SEK), Deutsches Elektronen-Synchrotron (DESY), Hamburg, Germany.
2017	Erasmus plus mobility grant (€ 2,000), University of Amsterdam, Amsterdam, the Netherlands.
2015	Bronze medal best Pharmaceutical Sciences Bachelor project, VU University, Amsterdam, the Netherlands.
2016 – 2014	National Scholarship of the Netherlands (€ 12,000), Ministry of Education, Culture and Science, Hoofddorp, the Netherlands.

## **Schools (only PhD level courses) and Conferences**

2022	ACS Fall Meeting, Chicago, United States of America.
2021	ILMAC 2021, Basel, Switzerland.
2019	NanoGe Fall Meeting, Berlin, Germany.
2018	Graduate School on Neutron Scattering including final exam (two weeks), The Nordic Neutron Science Programme and the Swedish Neutron Education for Science & Society Programme, Tartu, Estonia.
2018	RACIRI Summer School including poster presentation (one week), Advanced Materials Design at X-ray and Neutron Facilities, Röntgen-Angström-Cluster/loffe-Röntgen-Institute, Rügen, Germany.

## **Notable experiences and volunteering**

Present – 2021	Toastmaster, Toastmaster International Lausanne, Lausanne, Switzerland.
2018 – 2017	Member of the Board, Lunds Universitets Roddklub, Malmö, Sweden.
2017 – 2016	Commis de Cuisine at Suitehotel & Restaurant Posthoorn (one Michelin star), Monnickendam, the Netherlands.
2013 – 2012	Fundraiser for several Dutch NGO's such as 'Het Longfonds', Amsterdam, the Netherlands.



Ce document a été imprimé au Centre d'impression EPFL,  
imprimerie climatiquement neutre, certifiée myClimate depuis  
2017, sur papier Nautilus® SuperWhite, 100% recyclé et issu  
de déchet de consommation, certification FSC™ et Blue Angel.



[repro.epfl.ch](http://repro.epfl.ch)